



HAL
open science

Performance evaluation of vehicle radiofrequency communication systems: contribution to the modelling approach

Jessen Narrainen

► **To cite this version:**

Jessen Narrainen. Performance evaluation of vehicle radiofrequency communication systems: contribution to the modelling approach. Other. INSA de Rennes, 2017. English. NNT : 2017ISAR0007 . tel-01579510

HAL Id: tel-01579510

<https://theses.hal.science/tel-01579510>

Submitted on 31 Aug 2017

HAL is a multi-disciplinary open access archive for the deposit and dissemination of scientific research documents, whether they are published or not. The documents may come from teaching and research institutions in France or abroad, or from public or private research centers.

L'archive ouverte pluridisciplinaire **HAL**, est destinée au dépôt et à la diffusion de documents scientifiques de niveau recherche, publiés ou non, émanant des établissements d'enseignement et de recherche français ou étrangers, des laboratoires publics ou privés.

Thèse

UNIVERSITE
BRETAGNE
LOIRE

THESE INSA Rennes
sous le sceau de l'Université Bretagne Loire
pour obtenir le titre de
DOCTEUR DE L'INSA RENNES
Spécialité : Electronique et Télécommunications

présentée par

Jessen NARRAINEN

ECOLE DOCTORALE : *MATISSE*

LABORATOIRE : *IETR*

Performance evaluation
of vehicle radiofrequency
communication systems:
contribution to the
modelling approach

Thèse soutenue le 07.03.2017
devant le jury composé de :

Martine LIENARD

Professeur, Université de Lille 1 / Présidente

Jean-Marc LAHEURTE

Professeur, Université de Paris-Est Marne-La-Vallée / Rapporteur

Rodolphe VAUZELLE

Professeur, Université de Poitiers/ Rapporteur

Raffaele D'ERRICO

Ingénieur de recherche, CEA-LETI / Examineur

Philippe BOUTIER

Ingénieur de recherche, Renault SAS/ Co-encadrant de thèse

Philippe BESNIER

Directeur de recherche CNRS, IETR / Directeur de thèse

Xavier BUNLON

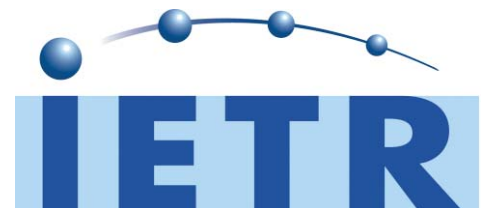
Responsable d'équipe RF / CEM, Renault SAS/ Examineur

Performance evaluation of vehicle radiofrequency communication systems: contribution to the modelling approach

Jessen NARRAINEN



En partenariat avec



REMERCIEMENTS

Cette thèse a été effectuée dans le cadre d'une Convention Industrielle de Formation par la Recherche (CIFRE) entre la société Renault et l'Institut d'Electronique et des Télécommunications de Rennes (IETR).

J'adresse mes sincères remerciements à Monsieur Philippe Besnier, Directeur de recherche CNRS, pour avoir assuré la direction de cette thèse et pour m'avoir donné l'opportunité de réaliser ces travaux de thèse au sein de l'IETR. Je le remercie particulièrement pour le suivi sans faille de cette thèse, sa disponibilité, ainsi que pour les échanges fructueux durant ces trois dernières années.

Je tiens à remercier Martine Gatsinzi Ibambé, Ingénieure R & AE, mon encadrante Renault pendant les premiers dix-huit mois de la thèse. Elle a guidé mes premiers pas chez Renault. Je lui suis très reconnaissant pour ses conseils, son aide et son soutien.

Je souhaite témoigner toute ma reconnaissance à Philippe Boutier, Référent RF chez Renault, qui a su parfaitement prendre la suite de l'encadrement de la dernière partie de la thèse. Je voudrais lui adresser de chaleureux remerciements pour la confiance qu'il m'a accordée, mais aussi pour son enthousiasme, sa joie de vivre et la manière unique avec laquelle il a su encadrer mon travail.

J'exprime particulièrement ma gratitude à Xavier Bunlon, chef d'équipe de l'équipe CEM/RF, chez Renault, pour l'accueil dans son équipe, ses conseils et sa précieuse aide technique qu'il a su apportée pendant la thèse.

J'adresse ma reconnaissance à Madame Martine Liénard, Professeur à l'Université de Lille 1, de m'avoir fait l'honneur de présider mon jury de thèse.

Ensuite, j'exprime toute ma gratitude à Monsieur Jean-Marc Laheurte, Professeur à l'Université Paris Est Marne-la-Vallée, et Monsieur Rodolphe Vauzelle, Professeur à l'Université de Poitiers, pour avoir accepté d'être les rapporteurs de mes travaux et pour l'attention qu'ils ont accordée à la lecture de ce mémoire.

Mes remerciements s'adressent également à Monsieur Raffaele D'Errico, Ingénieur de recherche au CEA-Leti, pour avoir accepté d'examiner mes travaux de thèse.

Un grand merci à tout le personnel technique et administratif de l'INSA de Rennes, du laboratoire et de chez Renault pour leur aide et leur bonne humeur. Je remercie toutes les personnes que j'ai rencontrées au cours de ces trois années de thèse et qui ont apportées leur pierre à l'édifice. Je remercie, notamment, tous les membres de l'équipe CEM-RF, ainsi que les collègues de l'IETR pour leur accueil et leur amitié.

Je terminerai enfin en adressant des remerciements remplis de tendresse et d'affection à ma famille et mes proches. Je tenais à adresser un immense merci à mes parents et ma sœur Yovane pour leur soutien sans faille tout au long de ma scolarité. Merci pour tout ce que vous avez fait pour moi, je ne saurai l'oublier. Je profite pour embrasser mes nièces, Meïssa et Emna, à qui je souhaite bonheur et succès dans leur vie. Je remercie aussi mon beau-frère Sativen et son frère Krisnen pour leurs conseils et encouragements. Enfin, un merci tout particulier à Julie. Merci pour ton extrême patience, merci pour ta présence, tes encouragements et pour tout le reste...

TABLE OF CONTENTS

REMERCIEMENTS	II
TABLE OF CONTENTS	IV
Résumé étendu	VIII
Chapter 1 : Introduction	1
Chapter 2 : Context and objectives of this work	4
2.1 Outline of V2X communications systems and general principle	5
2.1.1 Targeted applications of V2X communications.....	6
2.1.1.1 Road-safety applications.....	6
2.1.1.2 Traffic management applications	8
2.1.1.3 ADAS.....	9
2.1.1.4 Infotainment applications	9
2.1.2 General principles of this communication	10
2.1.2.1 Standardization and harmonization of V2X communication systems.....	10
2.1.2.2 Frequency band allocation and their characteristics	10
2.1.2.3 Messages dedicated to V2X communications.....	11
2.1.2.4 The IEEE 802.11p standard.....	11
2.1.3 Integration of V2X systems in the vehicle and importance of upstream studies	13
2.2 Overview of previous research works: The 2008 -2012 period	13
2.2.1 Achievements of different simulation blocks.....	14
2.2.1.1 PHYsical layer following the IEEE 802.11p standard	14
2.2.1.2 Propagation modelling using “normalized” channel (Ohio & GT).....	16
2.2.1.3 Validation and performance evaluation	18
2.2.1.4 Antenna Integration.....	18
2.2.2 Limitations of previous work.....	19
2.3 Main objectives of this thesis	20
2.3.1 Propagation channel modelling (A new philosophy)	20
2.3.2 Antenna integration	21
2.4 References	23
Chapter 3 : Generation of virtual driving scenarios.....	24
3.1 A state of the art	24
3.1.1 Wireless propagation channel.....	24
3.1.2 Propagation of electromagnetic waves.....	25
3.1.2.1 Free-space attenuation	25
3.1.2.2 Reflection	26
3.1.2.3 Diffraction	27
3.1.3 Channel characteristics	28
3.1.3.1 Large-scale fading or slow-fading	29
3.1.3.2 Short-scale fading or fast-fading.....	30
3.1.3.3 Channel impulse response.....	30
3.1.3.4 PDP (power delay profile).....	32
3.1.3.5 Time-dispersive characteristics	32
3.1.3.6 Doppler spectrum.....	33

3.1.4	Specificity of vehicular channels	35
3.1.5	Typical V2X environments	36
3.1.6	V2X channel sounding or channel measurements	37
3.1.6.1	Channel sounding techniques	37
3.1.6.2	Vehicular channel measurement results	37
3.1.7	Channel modelling	41
3.1.7.1	Deterministic channel (Ray-tracing)	41
3.1.7.2	Stochastic channel models	41
3.1.7.3	Geometry-based stochastic channel	42
3.1.8	Conclusions	43
3.2	Channel modelling method adopted	44
3.2.1	Principle of the GBSCM method in FEKO	45
3.2.1.1	Description of the scatterers in the simulation	45
3.2.1.2	Description of the generic setting	47
3.2.1.3	Ray-tracing using the UTD module in FEKO	48
3.2.1.4	Generation of time-sequences	48
3.2.2	CIR and PDP construction and extraction of different parameters	50
3.2.2.1	Channel response	50
3.2.2.2	Power delay profile	52
3.2.3	Extraction of channel parameters	53
3.2.3.1	RMS delay spread	53
3.2.3.2	Angular spread	54
3.2.3.3	Doppler spectrum	54
3.3	Channel responses from arrangement of location and numbers of surrounding simple scatterers	56
3.3.1	Analytical model to study the distribution of the scattering elements	56
3.3.1.1	Implementation of the analytical model	56
3.3.1.2	Quick glance on UTD theory	57
3.3.1.3	Conclusion	60
3.4	Description of the different simulated configurations	60
3.4.1	Configuration for rural-like channel	62
3.4.1.1	Suggestion of the number and laws of distributions of the scatterers	62
3.4.1.2	Analytical method and FEKO simulation results	63
3.4.2	Configuration for highway-like channel	66
3.4.2.1	Suggestion of the number and laws of distributions of the scatterers	66
3.4.2.2	Analytical method and FEKO simulation results	67
3.4.3	Configuration for urban-like channel	70
3.4.3.1	Suggestion of the number and laws of distributions of the scatterers	70
3.4.3.2	Analytical method and FEKO simulation results	71
3.5	Summary of the simulation results	73
3.6	Conclusions	75
3.7	References	76
Chapter 4 : Antenna integration		81
4.1	Computation electromagnetic techniques	81
4.1.1	FEKO software tool	82
4.1.1.1	MoM and MLFMM	83
4.1.1.2	Meshing criteria	84
4.1.2	Numerical model of the vehicle	84
4.1.3	Measurement facility	84
4.2	A state of the art on V2X antenna integration	86
4.2.1	Antenna design at 5.9 GHz	86
4.2.2	Numerical methods to integrate V2X antennas	87

4.2.3	Impacts of antenna on V2X communication performance	87
4.2.4	Conclusions.....	88
4.3	Representation of the antenna on the vehicle	89
4.3.1	Roof- antenna case.....	90
4.3.1.1	<i>Canonical vehicle structure</i>	<i>90</i>
4.3.1.2	<i>The Mégane IV numerical model</i>	<i>92</i>
4.3.1.3	<i>Measurement of a $\lambda/4$ monopole antenna of the roof of the Mégane IV.....</i>	<i>94</i>
4.3.2	On-board antenna case	96
4.3.2.1	<i>Simulation</i>	<i>96</i>
4.3.2.2	<i>Measurement.....</i>	<i>96</i>
4.3.3	Conclusions.....	97
4.4	Complete EM simulation including the influence of near-field elements.....	98
4.4.1	Defining the far-field zone.....	98
4.4.1.1	<i>Full-scale model.....</i>	<i>99</i>
4.4.1.2	<i>Quarter-scale model.....</i>	<i>102</i>
4.4.1.3	<i>Conclusions.....</i>	<i>103</i>
4.4.2	Limitations of using far-field pattern in the presence of near-field elements and a proposed method to mitigate their effect	104
4.4.2.1	<i>Conclusions.....</i>	<i>107</i>
4.5	References	108
Chapter 5 : Modelling of the IEEE 802.11p PHY layer		110
5.1	Description of the PHY layer	110
5.1.1	The transmitted packet structure	110
5.1.2	Architecture of the transmitter	111
5.1.3	Receiving process	112
5.1.4	Computer implementations	113
5.2	Time sequences generation	114
5.3	Simulation results with different antennas	115
5.3.1	Antennas under test.....	115
5.3.1.1	<i>Patch antennas</i>	<i>115</i>
5.3.1.2	<i>Omnidirectional antennas.....</i>	<i>116</i>
5.3.1.3	<i>Antenna configurations and use cases.....</i>	<i>118</i>
5.3.2	Performance in terms of received power	119
5.3.3	Performance in terms of PER	121
5.4	Simulation results with different PHY layer parameters	122
5.5	Conclusions	125
5.6	References	127
Chapter 6 : Field tests.....		128
6.1	Presentation of the Scoop@f project.....	128
6.2	Technical equipment in the Renault car.....	129
6.3	Experimental setup.....	130
6.3.1	Vehicles	130
6.3.2	Antennas	131
6.3.2.1	<i>Shark-fin antennas</i>	<i>131</i>
6.3.2.2	<i>Patch antenna</i>	<i>132</i>
6.3.2.3	<i>Summary of antenna used in the measurement campaigns.....</i>	<i>132</i>
6.3.3	Modem	133
6.3.3.1	<i>Physical description.....</i>	<i>133</i>
6.3.3.2	<i>Sensitivity of the modem.....</i>	<i>133</i>
6.3.4	Global setup	134

6.4	log data processing	136
6.4.1	Evaluation of PER and distance in post-processing.....	136
6.5	Scenario	137
6.6	Performance results	138
6.6.1	Changing parameters: Antennas	139
6.6.2	Changing parameters: DATA rate and packet length.....	140
6.7	Comparison between simulation and measurements	143
6.7.1	Configuration for the new rural scenario.....	143
6.7.2	Measurement results: RSSI for each antenna configuration	144
6.7.3	Measurement results: PER results for each antenna configuration under different PHY layer parameters	146
6.7.3.1	Measurement results	146
6.7.3.2	Simulation results.....	146
6.8	References	149
General conclusions		150
Perspectives		153
Appendix. A Matlab implementation of the PHY layer		154
Appendix. B WinProp results		157
Appendix. C A second measurement campaign		162
List of figures		164
List of tables		169
Publications		171

RESUME ETENDU

Introduction et contexte

Le cadre général de cette thèse porte sur les communications véhicule à véhicule (V2V) ou véhicule à infrastructure (V2I). L'objectif principal de ce type de communication est d'améliorer la sécurité routière et d'optimiser la fluidité du trafic. L'évolution de ces nouvelles technologies permettra d'introduire des applications qui amélioreront l'information pour la détection des situations dangereuses pour les usagers de la route. Différents cas d'usages sont résumés dans le rapport produit par l'European Telecommunication Standard Institute (ETSI) [1].

Les travaux de recherche sur les communications V2X au cours des dernières années ont été accompagnés d'efforts de normalisation dans le contexte des systèmes de transport intelligents coopératifs (C-STI). En Europe, l'ETSI travaille à l'élaboration d'une norme pour les systèmes STI coopératifs, en collaboration avec le Comité européen de normalisation (CEN) [2]. L'harmonisation des standards assure principalement l'interopérabilité des équipements et des systèmes et de ce fait encourage l'innovation, l'ouverture et le développement des marchés [3]. La Figure 1 nous montre les différentes bandes de fréquences attribuées aux communications V2X en Europe.

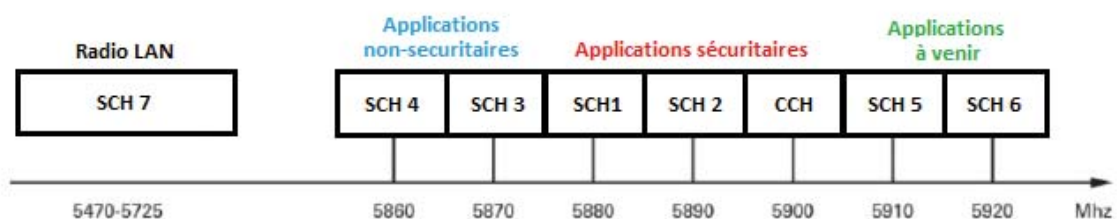


Figure 1 : Allocations de fréquences en Europe.

Les caractéristiques des différents canaux en termes de puissance maximale de sortie, de bande passante et de limite de densité de puissance spectrale sont données dans le rapport EN 302 571 de l'ETSI, mis à jour en mars 2016.

Le protocole de communication dans le cadre de systèmes V2X se base sur le standard 802.11p qui n'est qu'une adaptation de l'IEEE 802.11a dédiée au WIFI. Les caractéristiques et les changements apportés dans ce nouveau standard sont détaillés dans [4].

Motivation et organisation de la thèse

Les performances de systèmes de communication embarqués dépendent principalement de la configuration des antennes, du type de récepteurs utilisés (modem) et du canal de propagation. L'intégration de ces systèmes de communications sans fil dans les véhicules est actuellement source de complexités quant au positionnement et à la sélection de la ou des antennes requises et de l'architecture électrique et électronique. Il faut de plus maîtriser les coûts et les délais de développement tout en garantissant une qualité optimale des services vendus. Par conséquent, trouver la configuration d'antenne la plus favorable afin d'assurer la meilleure performance est une tâche fastidieuse.

Le sujet de la thèse se concentre précisément sur l'élaboration d'une méthode et d'un outil de simulation robuste et fiable pour optimiser les choix technologiques d'antennes et leurs

implantations à bord. Il permettra de limiter ainsi le recours aux prototypes et aux essais de roulage. L'évaluation de cette performance en termes de bilan de liaison ou de taux d'erreur paquet suppose la prise en compte la plus adaptée possible du triptyque : canal de propagation / antenne / protocole de communication dans la simulation.

La suite de ce résumé étendu compile les résultats essentiels obtenus au cours de cette thèse. Ces résultats sont essentiellement articulés en quatre parties. Dans un premier temps (Chapitre 3 de la thèse), nous nous sommes focalisés sur l'édification d'une stratégie de simulation électromagnétique en situation dynamique permettant de reproduire les effets rencontrés dans différents types d'environnement de type urbain, rural ou autoroutier par exemple. Afin de reproduire des chemins de propagation dont les temps d'étalement et la distribution angulaire sont ajustables, nous avons recours à des éléments de diffraction/réflexion très simples. Il est montré, en particulier, qu'un modèle analytique brut, basé sur la théorie uniforme de diffraction au premier ordre, permet d'évaluer leur agencement pour reproduire un canal de propagation aux caractéristiques particulières.

La deuxième partie de la thèse traite de l'intégration d'antennes dans nos modèles de canaux de propagation précédemment développés. Il a été constaté qu'il est particulièrement utile de simplifier la maquette numérique du véhicule complet lors d'une simulation électromagnétique de l'antenne intégrée à bord de ce véhicule. De plus, dans cette section, nous étudions la limite de la validité de substitution d'une antenne intégrée à bord d'un véhicule uniquement par son diagramme de rayonnement dans les modèles de canaux de propagation. Cette étude doit nous permettre de déduire que les interactions électromagnétiques avec les éléments se situant dans le champ-proche ne sont plus valides. Ainsi, une stratégie de correction doit être trouvée.

L'évaluation des performances d'antennes, en termes de taux d'erreurs paquet, après l'implémentation de la couche physique du standard 802.11p, est au cœur de la troisième partie de cette thèse. Des résultats de simulation, pour chaque configuration d'antenne, sont donnés pour plusieurs combinaisons de paramètres de couche PHY tels que le débit et la longueur de paquet.

La dernière partie de ce manuscrit traite de la présentation d'une campagne de mesure qui a été réalisée principalement dans un environnement de type rural. Les essais de roulage ont pour but de démontrer la capacité des méthodes de simulation à faire un choix approprié d'installation d'antenne.

Modélisation des canaux de propagation

Cette partie sera consacrée exclusivement à la définition des modèles de canaux de propagation. Ils sont en général élaborés selon différentes méthodes. Certains sont issus de campagnes de mesure [5], d'autres de calculs purement déterministes [6]. Ces derniers sont réalisés avec un simulateur à tracé de rayon 3D. Ces modèles nécessitent une description complète de l'environnement à simuler et peuvent être coûteux en temps de simulation. Une troisième famille de méthode, appelée géométrique-stochastique (Geometrically-Based Stochastic Channel Model) [7], autorise une approche plus souple en termes de modélisation de canaux aux statistiques variables suivant les scénarios envisagés. L'aspect géométrique de ces modèles permet de calculer la contribution des trajets, décrivant l'interaction entre l'onde qui se propage et les diffuseurs, grâce à un tracé de rayon. Notre but est de s'attacher à créer des scénarios de roulage virtuels qui représenteraient des situations discriminées en termes d'étalement des retards, d'angles

d'arrivée, de spectres Doppler. De manière préliminaire, nous montrons comment les méthodes de type GBSCM peuvent moduler les caractéristiques d'un canal de propagation. Les modèles simulés pourront ensuite servir de cas test pour étudier les choix technologiques d'antennes et leur emplacement dans les véhicules.

Nous souhaitons représenter un scénario où deux véhicules sont en situation dynamique. La modulation des caractéristiques du canal s'effectuera par l'utilisation de diffuseurs plans parfaitement conducteurs. Les diffuseurs font 1.5 m x 2 m de dimension et sont donc très grands par rapport à la longueur d'onde à la fréquence centrale de communication soit 5,9 GHz. Les variables dans chaque configuration seront le nombre de diffuseurs et leur positionnement par rapport aux antennes). Cependant, l'emplacement (c'est-à-dire la distribution statistique appropriée) et le nombre de diffuseurs doivent d'abord être déterminés, ce qui a été fait après un processus de tâtonnement. Dans ce travail, nous introduisons un modèle analytique simple afin de façonner rapidement ces caractéristiques. Une fois sélectionnée, l'approche de modélisation du canal de propagation basée sur la méthode GBSCM est utilisée pour simuler des scénarios de conduite virtuelle sous le logiciel électromagnétique FEKO. Un ensemble d'environnements rencontrés dans un contexte V2V peut être préparé selon ce processus à deux étapes. FEKO, basé sur la théorie uniforme de diffraction, est ensuite utilisé afin d'effectuer un tracé de rayon avec le nombre maximal d'interactions (réflexion et diffraction) limité à 3. Cependant, FEKO n'est pas adapté pour simuler des scénarios variant dans le domaine temporel. Afin, d'obtenir une séquence temporelle, plusieurs scénarios statiques (snapshots) successifs doivent être simulés. Des séries de 1000 « snapshots » sont créées pour représenter le dynamisme.

Sur la figure 1, nous avons un schéma représentant l'environnement simulé. La distance, D , entre l'émetteur Tx et le récepteur Rx est fixée à 300m. Les diffuseurs sont disposés sur les lignes espacées entre elles de 8m. Les diffuseurs, dont le nombre total est N , peuvent être répartis en deux sous-groupes : N_{INT} , ceux se trouvant entre le Tx et Rx et N_{OUT} , le nombre de diffuseurs placés en avant de Tx ($y < 0$) et après le Rx ($y > 0$).

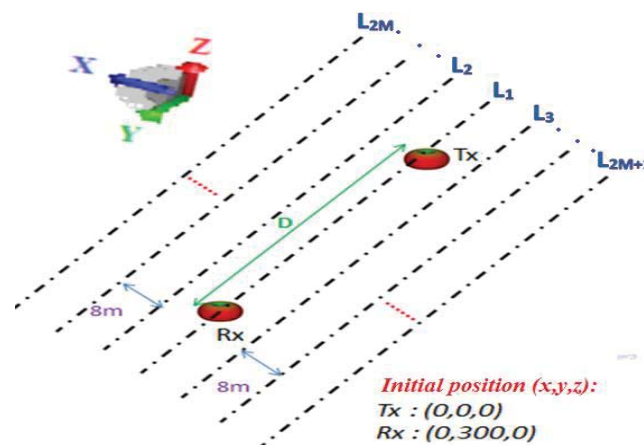


Figure 2 : Schéma généralisé représentant l'environnement simulé.

Description des trois configurations simulées et les résultats obtenus

Dans cette sous-section, nous allons décrire trois configurations qui représentent trois scénarios distincts en termes de caractéristiques des canaux de propagation. Dans ce résumé, les résultats, issus des simulations de FEKO, sont donnés en termes d'étalement de retard et de la distribution des angles d'arrivée. Les spectres Doppler correspondant à chaque configuration sont donnés dans le chapitre 3 de ce manuscrit.

Le minimum et le maximum des quantiles à 10%, 90% ainsi que la moyenne des étalements de retard au sens RMS (τ_{RMS}) pour les différentes réalisations de chacune des trois configurations ont été retenus et reportés dans le tableau 1 à la fin de cette section. Les angles d'arrivée sur le récepteur sont ici calculés par construction géométrique pour chaque trajet. Il est important de noter l'orientation angulaire du scénario simulé parce qu'un trajet en vue directe provenant de l'émetteur arrivera avec un angle de 270° sur le récepteur. Nous évaluons la probabilité d'occurrence, par intervalle de 5° , pour chacune de nos trois configurations sur toute la durée du dynamisme (une seule réalisation).

Configuration rurale

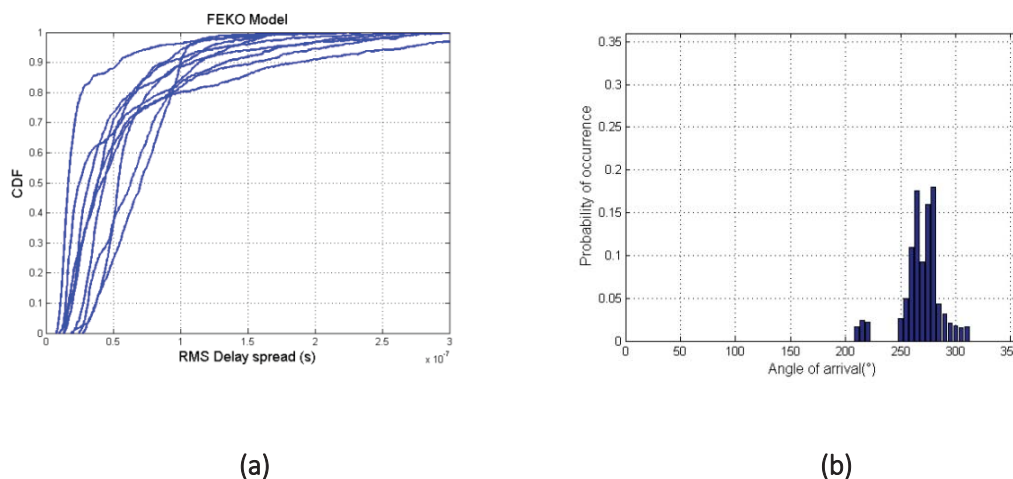


Figure 3 : Résultat issu de la simulation FEKO pour la configuration rurale : (a) étalement des retards et (b) distribution angulaire.

Dans la première configuration, 33 N_{INT} diffuseurs, répartis sur 11 lignes, sont positionnés intégralement dans l'intervalle $y \sim [20, 280]$.

L'étalement des retards pour 10 différentes configurations de type rural sont donnés dans la Figure 3(a). Nous avons un quantile à 10% qui varie entre 11 et 37 ns selon les réalisations. Nous obtenons un quantile minimum à 90% de 55 ns et un maximum à 90% de 154 ns. L'étalement des retards moyen oscille entre 26 ns et 87 ns.

N'ayant pas de diffuseurs de type N_{OUT} , le tracé de rayon effectué par simulation sur FEKO présente un étalement angulaire sectoriel, comme nous pouvons constater sur la Figure 3(b), ce qui est représentatif d'un scénario rural. Dans ce dernier, il y a très peu de bâtiment. Le mécanisme de

propagation dominant reste le trajet direct augmenté les réflexions/diffractions sur l'habitable des voitures. Il y a, donc, une dispersion angulaire très faible en zone rurale.

Configuration autoroute

La deuxième configuration contient 33 N_{INT} diffuseurs dans l'intervalle $y \sim [20,280]$ et 22 N_{OUT} diffuseurs qui sont équitablement positionnés avant le Tx ($y \sim [-220,-20]$) et après le Rx ($y \sim [320,520]$).

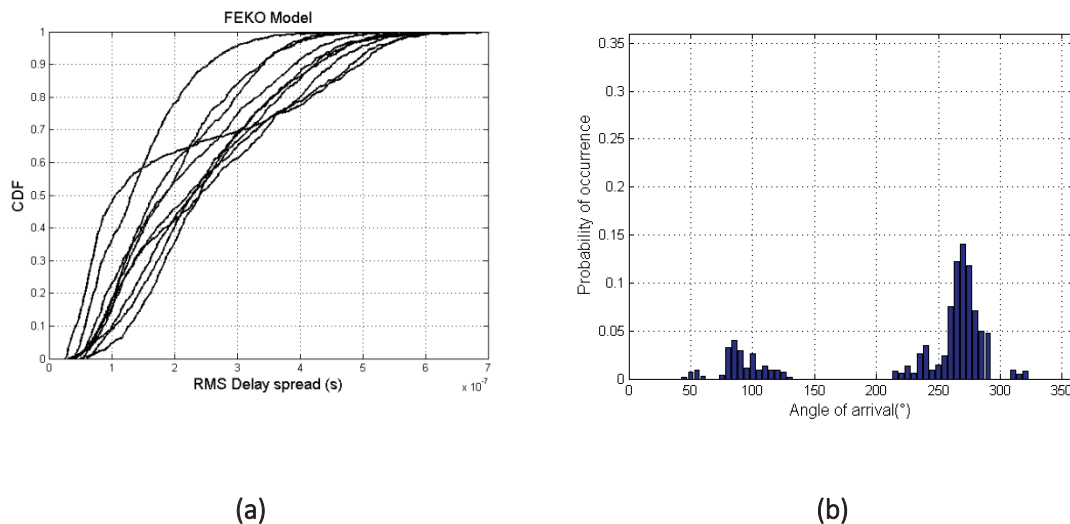


Figure 4 : Résultat issu de la simulation FEKO pour la configuration autoroute : (a) étalement des retards et (b) distribution angulaire.

Les étalements des retards pour 10 différentes configurations de type autoroute sont donnés dans la Figure 4(a). Nous avons un quantile à 10 % qui varie entre 43 et 128 ns selon les réalisations. Nous obtenons un quantile minimum à 90% de 254 ns et un maximum à 90 % de 553 ns. L'étalement de retard moyen oscille entre 144 ns et 271 ns. Ces valeurs sont aussi affichées dans le tableau 1.

Dans cet environnement de propagation, nous avons un plus grand étalement angulaire que dans la configuration précédente dû à la présence des 22 diffuseurs N_{OUT} (Figure 4b). Généralement, les éléments contribuant aux trajets multiples sont plus nombreux dans un environnement autoroute (forte densité de véhicules, panneaux, barrières, mur de séparation de voie) comparé à un scénario rural.

Configuration urbaine

Dans ce dernier cas, 46 diffuseurs sont répartis sur 7 lignes. Des lignes avec les indices suivants ont été utilisées : (L_i , où $i = 1, 4, 5, 10, 11, 20$ et 21). Par conséquent, la distance perpendiculaire entre les lignes où les diffuseurs sont placés et l'axe Tx-Rx est augmentée. Il y a 18 diffuseurs N_{IN} . 28 diffuseurs de N_{OUT} ont été répartis également sur les 7 lignes. Il est important de noter que dans cette configuration proposée, l'axe Tx-Rx (L_1) est exempt de diffuseurs N_{IN} . Donc, le récepteur se trouve donc en ligne de vue de l'émetteur. La présence des éléments de type N_{OUT} dans l'axe Tx-Rx

induisent des réflexions spéculaires avec des distances de propagation plus grandes, arrivant t ainsi plus tardivement sur le récepteur.

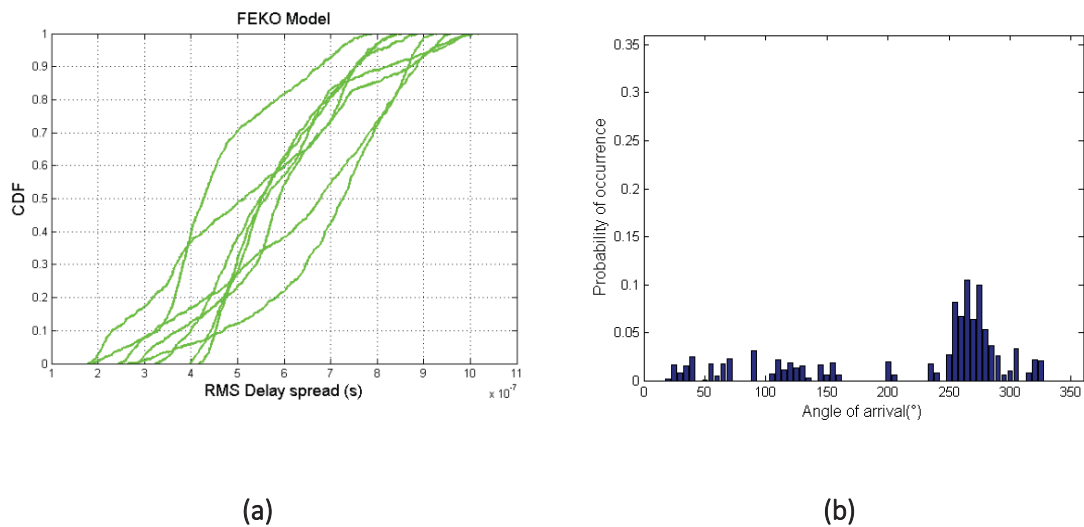


Figure 5 : Résultat issu de la simulation FEKO pour la configuration urbaine : (a) étalement des retards et (b) distribution angulaire.

La valeur minimale pour le quantile à 10% est de 267 ns tandis que la valeur de seuil maximale de 10 % est de 470 ns. Les valeurs moyennes de l'étalement de retard se situent entre 459 ns et 676 ns. Les critères supérieurs fixés à 90% de la distribution cumulée vont de 754 ns à 884 ns.

Une augmentation de la distance perpendiculaire entre les diffuseurs et les véhicules nous a permis d'enrichir de façon significative la répartition angulaire approchant ainsi d'une représentation équitable d'un tel scénario urbain où la présence de bâtiments et la forte densité de trafic assurent une multitude de trajets.

Comparaison des résultats de simulation avec les résultats issus de la littérature

A travers la littérature, nous avons repéré quelques campagnes de sondage de canal qui ont été réalisées pour extraire les réponses impulsionnelles et ainsi les différentes caractéristiques déterminantes d'un canal de propagation selon les principaux environnements considérés : rural, autoroute et urbain respectivement [10]. Le tableau 2 résume les spectres d'étalement des retards observés selon chaque scénario :

Table 1 : Statistiques sur l'étalement de retard obtenues à partir de la simulation

RMS-ds (ns)	Rural	Highway	Urban
10 th percentile	11 – 37	43 - 128	444 – 691
Mean RMS-ds	26 – 87	144 - 271	803 – 959
90 th percentile	55 -184	254 - 553	996 – 1340

Table 2 : Statistiques sur l'étalement de retard obtenues à partir de la littérature.

RMS-ds (ns)	Rural	Highway	Urban
10th percentile	20 [32]	30	30
Mean RMS-ds	22 - 52 [25]	41 [25] – 247	47-373
90th percentile	150	340	1100

Les résultats obtenus à partir de nos simulations (tableau 1) sont proches des résultats obtenus à partir des différentes campagnes de mesure (tableau 2) même si nous constatons que les valeurs des quantiles à 10% et celles des τ_{RMS} moyens pour la configuration urbaine sont relativement élevées.

Intégration d'antennes

Dans la première partie ce chapitre, nous voulons montrer les altérations que subissent un diagramme de rayonnement lorsqu'une antenne est intégrée à bord d'une voiture, compte tenu des interactions entre celle-ci et l'antenne correspondante. Idéalement, une simulation avec une méthode rigoureuse doit être exécutée avec une description complète du véhicule. Malheureusement, en raison des contraintes dues aux limitations des moyens de calcul disponibles, un compromis sur la précision des résultats simulés doit être effectué afin de réduire le temps de calcul et de satisfaire les exigences de mémoire. De ce fait, il est alors nécessaire de déterminer le niveau de description suffisant, pour déterminer de manière suffisamment fiable le diagramme de rayonnement de l'ensemble. Dans ce résumé, l'exemple d'une antenne patch placée sur la lunette arrière du véhicule sera considéré. D'autres cas de positionnement d'antenne pourront, bien sûr, être suivis dans le chapitre 4 de la thèse.

Le cas d'une antenne patch située à l'intérieur de l'habitacle

L'antenne patch, développée dans [15], a été utilisée pour analyser l'exemple d'une antenne placée à bord d'un véhicule. Le modèle numérique, illustré à la Figure 6, prenant en compte le hayon a été utilisé dans notre simulation. Le pare-brise arrière était représenté sous forme de verre avec une permittivité relative de 4,5. La Figure 6 nous montre la distribution des courants de surface affichée avec une dynamique de 90 dB sur deux points de vue différents.

Simulation

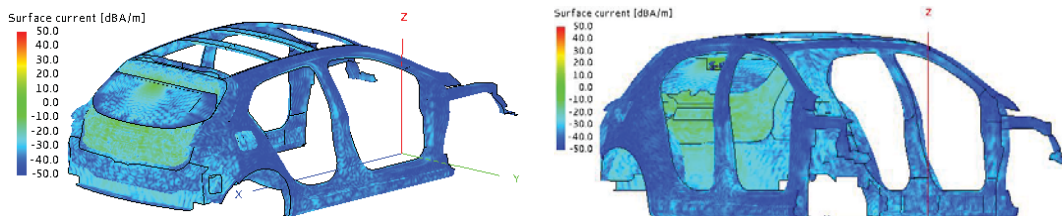


Figure 6 : Distribution des courants surfaciques.

Measurement



Figure 7 : La configuration de mesure d'une antenne patch sur la lunette arrière.

La configuration de mesure est illustrée à la Figure 7. Nous pouvons y voir la Mégane IV placée sur le plateau tournant de la chambre anéchoïque. L'emplacement de l'antenne patch est encadré en rouge. Une couche de mousse de polystyrène a été utilisée comme support pour s'assurer que l'antenne patch reste dans une position verticale avec le lobe majeur du diagramme de rayonnement pointant bien dans le plan azimutal.

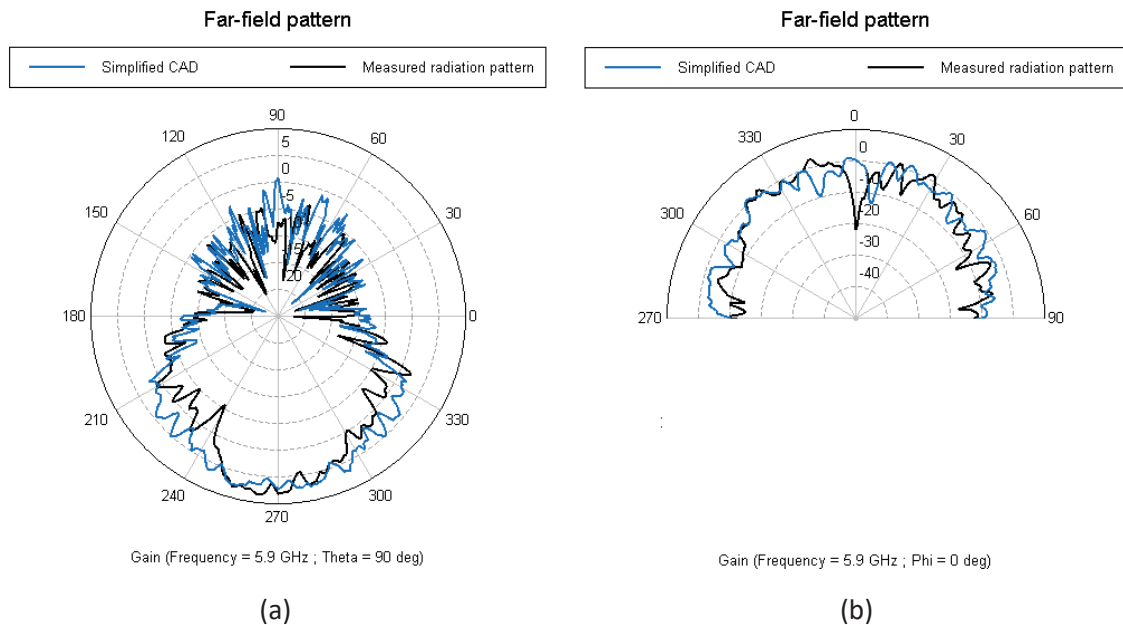


Figure 8 : Diagramme de rayonnement d'une antenne patch intégrée sur la lunette arrière de la Mégane IV dans (a) le plan azimutal (b) et le plan d'élévation

Il existe une bonne corrélation entre les diagrammes de rayonnement à la fois dans le plan azimutal et le plan d'élévation comme on peut le constater sur la Figure 8(a) et Figure 8(b) respectivement. Il faut noter que le diagramme de rayonnement de l'antenne mesurée, dans notre chambre anéchoïque, caractérise le champ uniquement dans l'hémisphère supérieure. Dans les applications automobiles, il n'est pas très intéressant de caractériser le champ de rayonnement vers le sol.

Représentation d'antenne dans le modèle de propagation

En ce qui concerne la représentation de l'antenne intégrée sur le véhicule dans un environnement de propagation, il faut recourir à des méthodes asymptotiques car l'échelle d'un scénario complet est très grande par rapport à la longueur d'onde. Dans ce cas, la substitution du système rayonnant par une source ponctuelle peut avoir une forte influence sur la précision des résultats. À notre connaissance, aucun travail n'a été recensé dans la littérature pour étudier la précision de l'utilisation directe d'un diagramme de rayonnement dans un canal de propagation. Le remplacement du système rayonnant (antenne intégrée à bord d'un véhicule) par son seul diagramme de rayonnement doit être manipulé avec précaution, en particulier dans les cas où des éléments de diffraction se trouvent à proximité de l'élément rayonnant. Ainsi, une technique pour rétablir ou maintenir les interactions avec les éléments en champ-proche doit être trouvée. Cela fera, donc, l'objet de la deuxième partie de ce chapitre.

Détermination du champ-lointain

La première étape pour mener à bien cette étude est de définir un critère pour lequel nous pouvons supposer être en champ-lointain. La distance, appelée D_{\min} , sera le rayon de référence délimitant la zone champ-proche. Ce niveau du champ électrique est évalué à chaque distance. Celui-ci est normalisé à la distance considérée et peut être exprimé en volt (ou dBV). Ce champ normalisé est comparé au niveau du champ rayonné normalisé à 1 m. Ces deux observables ont exactement les mêmes valeurs au-delà de la frontière champ-proche/champ-lointain. Un critère d'acceptabilité de 1 dB est fixé pour estimer D_{\min} . A partir des résultats, détaillés dans la section 4.4.1 de la thèse, nous avons conclu que la distance D_{\min} est de 60 m pour les véhicules à échelle 1 et de 5 m pour des véhicules à échelle $\frac{1}{4}$.

L'objectif de mener l'étude sur une structure du véhicule à échelle réduite est d'observer l'impact de la taille de la voiture sur la frontière entre le champ proche et le champ lointain. De plus, les dimensions réduites conduisent à un modèle numérique plus léger qui peut donc être inclus dans un modèle de canal de propagation simulé pour étudier l'effet des éléments de champ proche sans dépasser les limitations de mémoire de nos moyens de calcul.

Correction d'erreur sur la représentation d'une antenne intégrée dans un modèle de canal.

Un scénario de propagation, contenant 25 éléments diffractant, a été conçu pour cette étude. L'environnement complet a été réduit à l'échelle $\frac{1}{4}$ pour s'adapter aux limitations de ressources de calcul. En effet, dans cette section, toutes les simulations seront effectuées avec la méthode, dites rigoureuse, MLFMM. La méthodologie pour étudier l'influence des éléments en champ-proche sur la puissance reçue en utilisant un diagramme de rayonnement est décrite comme suit :

- Cas 1: MLFMM avec l'émetteur et récepteur représentés par leur diagramme de rayonnement.

Dans le premier cas, nous utilisons un point source pour représenter l'antenne d'émission et une antenne virtuelle parfaitement adaptée comme antenne de réception. Elles sont respectivement représentées par le diagramme de rayonnement d'un monopole situé sur le toit d'une maquette numérique d'un véhicule.

- Cas référence: MLFMM avec le Tx modélisé par son diagramme de rayonnement tandis que Rx est simulé par son système rayonnant complet (antenne + véhicule).

Dans notre cas pris comme référence, seule l'antenne de transmission est représentée par son diagramme de rayonnement. A la réception, l'élément rayonnant complet est considéré. En effet, nous incorporons dans le canal de propagation, la maquette numérique du véhicule avec l'antenne sur le toit. La puissance dissipée à travers cette antenne nous donnera la puissance reçue.

- Cas 2: MLFMM avec Tx modélisé par son diagramme de rayonnement et Rx par son diagramme de rayonnement incluant les éléments en champ-proche.

Comme dans les deux cas précédents, le Tx est toujours modélisé par son diagramme de rayonnement. Par contre, dans ce cas-ci, les éléments de diffraction se trouvant dans la zone champ-proche entourant le point de réception, sont inclus dans la simulation a priori du diagramme de rayonnement. La puissance reçue dans ce cas, nous laissera déterminer si l'inclusion des éléments de champ-proche permet de réduire l'écart par rapport au cas de référence.

Table 3 : Résultat des puissances reçus (en dB) pour les 3 cas étudiés.

Scenario No.	Cas 1	Cas de référence	Cas 2	Différence en dB (Case 1 - Cas de référence)	Différence en dB (Case 2- Cas de référence)
1	-91.9	-85.2	-81.9	-6.7	3.3
2	-82.5	-83.4	-83.4	0.9	0
3	-83.3	-81.9	-82.6	-1.4	-0.7
4	-86.8	-81.9	-84.0	-4.9	-2.1
5	-81.5	-86.8	-85.7	5.3	1.1
6	-88.1	-83.0	-82.8	-5.1	0.2
7	-87.9	-81.5	-82.2	-6.4	-0.7
8	-82.8	-83.3	-83.3	0.5	0
9	-88.7	-83.9	-82.9	-4.8	1
10	-90.4	-84.0	-82.3	-6.4	1.7
11	-89.1	-83.9	-82.3	-5.2	1.6
12	-92.0	-82.1	-78.2	-9.9	3.9
13	-86.1	-89.9	-88.1	3.8	1.8
14	-87.0	-85.4	-83.6	-1.6	1.8
15	-87.9	-84.1	-83.0	-3.8	1.1
16	-82.5	-83.4	-83.4	0.9	0
17	-86.1	-85.2	-85.2	-0.9	0
18	-88.6	-81.5	-79.4	-7.1	2.1
19	-88.8	-83.7	-82.4	-5.1	1.3
20	-88.4	-85.1	-84.6	-3.3	0.5

Dans le tableau 4-4, les résultats obtenus à partir des 20 canaux de propagation tirés au hasard sont répertoriés. Les puissances reçues pour le cas 1, le cas 2 et le cas de référence sont exprimés en dB. Les puissances enregistrées pour le cas 1 et le cas 2 sont alors rapportées à la situation de

référence. Ces rapports sont également exprimés en dB. Dans des conditions parfaites, c'est-à-dire en l'absence de diffuseurs de champ proche, on s'attend à ce que le rapport de puissance entre le cas 1 et le cas de référence approche 1 (0 dB). Les lignes du tableau en bleu sont des scénarios particuliers où les éléments de champ proche étaient absents. En passant, nous pouvons remarquer que le rapport de puissance, comme prévu, pour le cas 1 vis-à-vis du cas de référence pour ce scénario particulier sont intrinsèquement petits, car les interactions en champ proche sont mineures. Globalement, notre méthode pour limiter les erreurs dues aux interactions de champ proche est efficace car nous réduisons considérablement le rapport de puissance quand nous simulons nos canaux de propagation avec le cas 2. Le scénario 14 est en fait la seule exception.

Chaîne de simulation complète

In fine, le chaînage des simulations du triptyque du canal de propagation / antenne / protocole de communication est effectué à l'issue de l'incorporation de la couche physique du standard IEEE 802.11p. Cette dernière a été implémentée lors des travaux d'une précédente thèse entre le groupe Renault et l'IETR [10]. Plusieurs jeux de simulation permettent de distinguer les performances en termes de taux d'erreur paquet (TER) selon le type et la position des antennes en émission ou en réception.

Le simulateur de la couche PHY peut être divisé en trois parties : l'émetteur, le canal bruité et le récepteur respectivement.

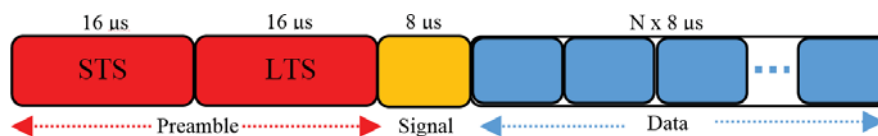


Figure 9 : La structure du paquet transmis selon le standard IEEE 802.11p.

La structure du paquet transmis est donnée dans la Figure 9. Dans l'implémentation de la couche PHY, nous assumons une synchronisation parfaite à la réception. De plus, l'hypothèse que les paramètres de transmission sont connus est émise. Le nombre, N , de symboles de données transmises est tributaire de la longueur du paquet et du débit.

Nous utilisons la réponse de canal pour évaluer le PER. Les séquences temporelles obtenues à partir des simulations FEKO ont été échantillonnées à $400 \mu\text{s}$ tandis que la période d'échantillonnage des communications V2X, travaillant dans une bande passante de 10 MHz, est de 100ns. Par conséquent, une interpolation doit être effectuée afin d'obtenir la fréquence d'échantillonnage correcte, conduisant à une durée totale de la séquence de 0,4 ms. Après interpolation, nous divisons la séquence temporelle en séquences plus petites correspondant à la durée de la longueur de paquet souhaitée.

La puissance moyenne reçue de chaque paquet est évaluée avant d'être rapportée au niveau du seuil de sensibilité pour calculer le SNR. Ensuite, l'algorithme de Monte Carlo est utilisé pour estimer la performance en terme TER de chaque paquet reçu pour l'ensemble du scénario de roulage. Chaque paquet est passé 2000 fois dans le simulateur de la couche PHY fournissant un résultat significatif pour le TER de l'ordre de 5×10^{-3} .

Dans ce résumé, nous présentons les performances de 5 configurations d’antennes dans un environnement de type autoroute. Les diagrammes d’antennes de ces 5 configurations considérées sont donnés dans le chapitre 5. Nous exprimons la qualité de la communication dans chaque configuration en fonction d’un pourcentage de succès sur temps de trajet du couple Tx/Rx. En effet, nous considérons une communication réussie dans le cas où le PER est en dessous de 0.1.

Suite aux résultats, tabulés ci-dessous, nous pouvons en déduire que la configuration d’antenne 1 (Config. 1) nous procure les meilleurs résultats. Nous avons jusqu’à 74 % de réussite dans le cas d’une modulation en Mode 5 et une taille de paquet de 1000 octets. Ensuite, nous pouvons déduire que Config. 4 est moins performante que Config. 2. Nous pouvons aussi rajouter que le bilan de liaison entre l’émetteur et le récepteur est tellement mauvais en utilisant Config. 3 et Config. 5 dans un scénario autoroute que la probabilité de succès est 0% dans ces deux configurations d’antennes.

Table 4 : Résumé des résultats issus de la simulation pour les 5 configurations d’antenne selon différents paramètres de la couche PHY.

Canal de propagation de type autoroute						
	Mode 1, 200 octets	Mode 1, 1000 octets	Mode 3, 200 octets	Mode 3, 1000 octets	Mode 5, 200 octets	Mode 5, 1000 octets
Config. 1	100 %	100 %	100 %	100 %	91 %	74 %
Config. 2	90 %	68 %	32 %	11 %	0 %	0 %
Config. 3	0 %	0 %	0 %	0 %	0 %	0 %
Config. 4	47 %	33 %	6 %	3 %	0 %	0 %
Config. 5	0 %	0 %	0 %	0 %	0 %	0 %

Campagne de mesure

Dans la dernière partie, une campagne de mesure a été réalisée dans un environnement rural. Dans ce résumé nous allons nous focaliser sur la confrontation des résultats issus de ces tests de roulage ainsi que ceux obtenus à partir de nos résultats de simulation. Les détails de cette campagne de mesure peuvent être retrouvés dans le chapitre 6 de ce document.

La puissance reçue, en roulage, pour des distances inter-véhicules avoisinant les 300 m sont présentés pour 4 configurations d’antennes sur la Figure 10. En outre, sur la Figure 11, nous pouvons voir les distributions des puissances reçues, issues de la simulation, pour les 4 configurations d’antennes utilisées en mesure.

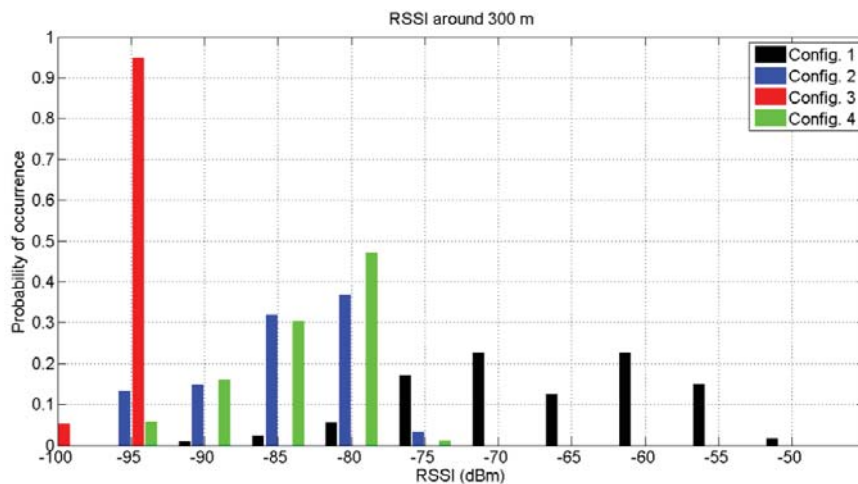


Figure 10 : Puissances reçues, obtenues à partir de la campagne de mesure, pour des distances inter-véhicules avoisinant 300 m

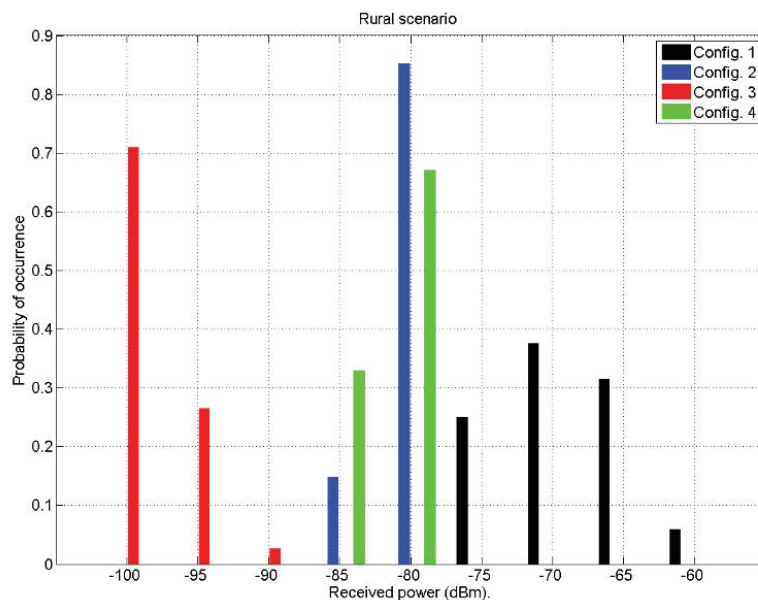


Figure 11 : Puissances reçues, obtenues à partir de la simulation pour des distances inter-véhicules de 300 m

La représentation de l'histogramme est illustrée avec une largeur de barre de 5 dBm. En comparant les deux résultats, nous constatons qu'il existe une bonne corrélation entre le RSSI obtenu dans les essais de roulage et les résultats de simulation extraits de FEKO.

En outre, les résultats des TER, pour les 4 configurations d'antennes considérées, sont calculés à partir des données obtenues de la campagne de mesure. Ils seront confrontés à des résultats de simulation obtenus sous FEKO. Les tableaux 5 et 6 résument ces deux séries de résultats. Le TER moyen est évalué pour les communications qui se sont produites à des distances inter-véhicules autour de 300 m (275 m à 325 m). De plus, on calcule également la probabilité d'obtenir une communication réussie sur la durée de la communication (tabulée entre parenthèses). Nous émettons l'hypothèse qu'un TER de moins de 10% est favorable à une bonne communication entre l'émetteur et le récepteur.

Config. 1 confirme les résultats de mesure, bien que les résultats de la simulation montrent des performances inférieures lors de la transmission en mode supérieur. Néanmoins, Config. 1 est clairement la configuration d'antenne la plus performante, que ce soit en simulation ou en essais sur le terrain. Sous Config. 2, Config. 4, les résultats de simulation ne permettent pas de distinguer les performances entre ces deux configurations. Pendant les mesures, ces deux configurations d'antenne affichent cependant des performances différentes suivant le mode de transmission, bien qu'elles présentent les mêmes faiblesses que dans les simulations. La troisième configuration d'antenne, Config. 3, affiche les pires performances de communication à la fois dans les campagnes de mesure et dans la simulation. En outre, dans ce dernier cas, cette configuration n'est pas favorable aux communications V2V lorsque la distance entre véhicules est à 300 m quel que soit le mode de transmission.

Table 5 : Résultats mesurés obtenus avec les 4 configurations d'antenne. TER moyen et entre parenthèses taux de transmission avec TER <10%

Canal de propagation de type rural – Résultats mesurés				
	Mode 1, 200 bytes	Mode 1, 1000 bytes	Mode 5, 200 bytes	Mode 5, 1000 bytes
Config. 1	0.04 (89 %)	0.04 (93 %)	0.00 (100 %)	0.01 (100 %)
Config. 2	0.08 (84 %)	0.11 (83 %)	0.20 (63%)	0.86 (0 %)
Config. 3	0.54 (14 %)	-	-	-
Config. 4	0 (100 %)	0.11 (84 %)	0.36 (39 %)	0.17 (70 %)

Table 6 : Résultats simulés obtenus avec les 4 configurations d'antenne. TER moyen et entre parenthèses taux de transmission avec TER <10%

Canal de propagation de type rural – Résultats simulés				
	Mode 1, 200 bytes	Mode 1, 1000 bytes	Mode 5, 200 bytes	Mode 5, 1000 bytes
Config. 1	0.00 (100%)	0.00 (100%)	0.15 (79%)	0.21 (76%)
Config. 2	0.00 (100%)	0.00 (100%)	1.00 (0 %)	1.00 (0 %)
Config. 3	1.00 (0 %)	1.00 (0 %)	1.00 (0 %)	1.00 (0 %)
Config. 4	0.00 (100%)	0.01 (100%)	1.00 (0 %)	1.00 (0 %)

Nous avons constaté que les tendances attendues des performances de communication en termes de PER sont globalement prévisibles à partir de notre modèle bien que nous ayons obtenu des résultats surprenants dans certains cas, ce qui nécessitera une enquête plus approfondie.

Références

- [1] ETSI - EN 302 637-2 Intelligent Transport Systems (ITS) – Vehicular Communications – Basic set of applications – Part 2: Specification of cooperative awareness basic service.
- [2] CEN- TS 17423: 2014 Systèmes de transport intelligents – Systèmes coopératifs – Exigences des applications STI, 2014.
- [3] J. Jääskeläinen, “Towards globally harmonized standards in cooperative ITS”, Workshop ETSI TC ITS, Vienna, Austria, 5-6 Feb. 2013.
- [4] 802.11p-2012 IEEE Standard for Information Technology – Telecommunications and Information Exchange between Systems – Local and Metropolitan Area Networks – Specific Requirements Part 11, Wireless LAN Medium Access Control (MAC) and Physical Layer (PHY) Spec, 2012.
- [5] A. Paier, J. Karedal, N. Cznik, H. Hofstetter, C. Dumard, T. Zemen, F. Tufvesson, C. Mecklenbrauker, A. Molisch, " First car-to-car and car-toinfrastructure radio channel measurement at 5. 2 GHz," in Proc IEEE 18th International Symposium on Personal, Indoor and Mobile Radio Communications, PIMRC 2007, August 2007.
- [6] J. Maurer , T. Fügen , T. Schäfer and W. Wiesbeck "A new inter-vehicle communications (IVC) channel model", Proc. IEEE 60th VTC, vol. 1, pp.9 -13 2004.
- [7] J. Karedal , F. Tufvesson , N. Czink , A. Paier , C. Dumard , T. Zemen , C. F. Mecklenbräuker and A. F. Molisch "A geometry-based stochastic MIMO model for vehicle-to-vehicle communications", IEEE Trans. Wireless Commun., vol. 8, no. 7, pp.3646 -3657 2009.
- [8] A. Molisch et al., “A survey on vehicle-to-vehicle propagation channels”, IEEE Wireless Communications, vol.16, no.6, pp.12 - 22, Dec. 2009.
- [9] M. Ibambe Gatsinzi, F. Jouvie, X. Bunlon and A. Azoulay, “Study of a 5.8 GHz frequency band patch antenna integrated into a vehicle for automotive DSRC applications,” 2007 International Conference on Electromagnetics in Advanced Applications, Torino, 2007, pp. 543-546.
- [10] I. Ivan, “Vehicle to Vehicle communication systems performance evaluation: A simulation approach combining physical layer implementation, propagation channel model and antenna properties”, PhD dissertation, Renault SAS – IETR, INSA de Rennes, 2012.

Chapter 1 : INTRODUCTION

The general framework of this Ph.D. thesis deals with Vehicle to Vehicle (V2V) or Vehicle to Infrastructure (V2I) communications.

This communication is firstly dedicated to reinforce security through exchange of information between vehicles in case of unexpected events. Other applications are also foreseen including infotainment. In order to be available on demand, this communication service must be guaranteed in such a way that the communication link is provided whatever the relative position of the vehicles, and their environment, as long as they are in the vicinity of each other. Therefore, a single-hop coverage must be ensured at a significant distance, typically hundreds of meters before allowing the information to spread at larger distances through multi-hop vehicle to vehicle communications. Bearing information pertaining to security aspects, this communication should fulfill highest quality requirements to be able to transmit messages with high reliability under high dynamic environmental conditions.

In consequence, a precise and effective knowledge of every component of the communication system, their behavior in different driving environments and their performance are necessary to evaluate V2V communications. The purpose of this PhD thesis is precisely to elaborate a design strategy to fulfil the above conditions. The communication link between cars depends on several parts of the communication chain and there is a need to study each of them separately before plugging all the independent blocks together:

- The transmitter architecture and in particular the maximum transmitted power allowed.
- The transmitting antenna including its antenna pattern according to its specific position on board the vehicle.
- The electromagnetic propagation channel which is in general unknown and represented by a set of possibilities.
- The receiving antenna, given,
- The receiver architecture and in particular its sensitivity.

For harmonization purposes, V2X systems lie on a new communication protocol, namely the IEEE 802.11p which uses the 5.9 GHz frequency band. This worldwide ITS (Intelligent Transport Systems) standard is derived from the existing and well-known IEEE 802.11a, with the physical (PHY layer) and medium-access layer (MAC layer) adapted to support low-latency communication among vehicles. The IEEE 802.11p PHY layer is based on the orthogonal frequency division multiplexing (OFDM) modulation with 52 subcarriers, while the actual payload is contained in 48 subcarriers. The remaining 4 subcarriers are used as pilot carriers for frequency and phase synchronization at the receiving end. Therefore, the transmitter and receiver, code and decode the transmitting signal according to this standard.

Furthermore, the effectiveness and reliability of these applications rely upon the properties of the propagation channel and the antenna performance. Thus, a sound understanding of these parameters has to be performed within the frequency band dedicated to vehicular communications.

The Integration of such a communication system in a vehicle involves the proper choice of modems and, above all, that of antennas including their location on-board vehicles. The selection of integrated antennas may rely upon series of measurement campaigns in real conditions but this can quickly reveal to be costly as the implementation of such functional validations is time-consuming due to the high number of test cases to evaluate.

The most reasonable strategy consists in developing a simulation tool to provide guidance to engineers before experimental validations. This is the purpose of this Ph.D. thesis which is a continuation of a former one undertaken in the period between 2008-2012 which was mainly devoted to the physical layer description and the emulation of standard propagation channels.

In this work, several unsolved problems are addressed and further studied:

- Simulation strategy of multiple types of propagation channels which can take into account realistic antenna pattern.
- Performance, in terms of radiation pattern, of antennas implemented on-board vehicles (and not only the intrinsic antenna pattern).
- Production of a complete simulation tool combining the first two items and the physical layer description.
- Production of a field-test with vehicles.

The continuation of the manuscript is organized as follows: **Chapter 2** gives a more detailed description of the context and the motivation of this thesis. The outlines and the general principles of V2X communication systems are presented. Furthermore, the targeted applications and the details of the standard of the communication protocol are outlined. Finally, an overview of the achievements from previous works are succinctly presented before exposing the main objectives of our work.

Chapter 3 focuses on the elaboration of a propagation channel modeling strategy. We propose a novel simulation method, based on a geometry-based stochastic channel model, to produce channel responses with variable characteristics. The simulated channel properties rely on the adjustment of the number and spatial distribution of simple diffracting elements around the transmitter and receiver. We show, in particular, that it is possible to pre-determine virtual driving scenarios with an arrangement of these elements such that their characteristics can emulate those of environments such as rural, highway and urban in terms of RMS-delay spread, angular spread and the Doppler spectrum.

Chapter 4 is dedicated to the description of the behavior of antennas on board the vehicles. In particular, the performance of the integrated antenna is determined by seeking to simplify the CAD of the vehicle in order to speed up the simulations. On the other hand, it is also sought to represent the antenna by its radiation pattern, which lead us to examine the limit of validity of this approach, particularly in the situation where the scatterers are located in the vicinity of the vehicle.

Chapter 5 presents the implementation of the complete tool after the embodiment of the PHY layer and the propagation channel response including integrated antenna pattern. Simulation results in terms of power received and packet error rate (PER) will be given for each antenna and driving environment configuration.

In the last chapter, **Chapter 6**, a description of a measurement campaign carried out to validate the simulation tool is presented and conclusions about the performance of different antenna sets are given.

Finally, we will end up with general conclusions summing up of all the works presented in the manuscript. Moreover, perspectives and future works pertaining to the scope of V2X communication systems will be stated in order to have a clear vision on the completion and improvement of this thesis project.

Chapter 2 : CONTEXT AND OBJECTIVES OF THIS WORK

Along with the increase of road traffic and the burst in wireless communication technologies, the interest in V2X communications has significantly raised. V2X communications englobe both Vehicle to Vehicle communications (V2V) and Vehicle to Infrastructure communications (V2I). The main objective of this communication system is to reduce the number of road accidents and to eliminate the excessive cost due to traffic collisions. The World Health Organisation (WHO) recently published (2015) in its global status report in road safety that 1.25 million deaths occur due to road accidents each year [1]. It is the first cause of deaths of those aged 15-29 years. According to l'Observatoire National Interministériel de la Sécurité Routière, 3461 people died due to road traffic accidents in France in 2015 [2]. It accounts a slight rise (+2.3%) as compared to the previous year. The following graph give an indication of the evolution of the number of death casualties in France annually:

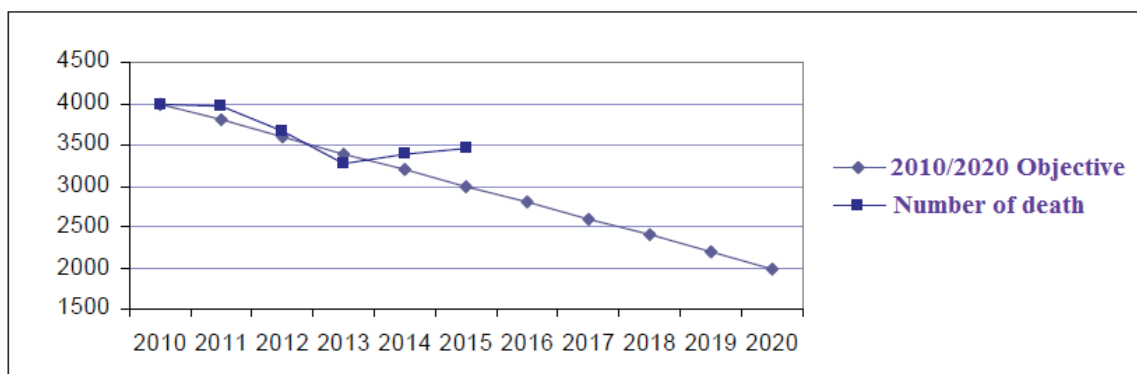


Figure 2-1 : Annual death toll due to road accidents in France.

If preventive measures are not taken, those breathtaking figures should increase and road death is likely to become the third-leading cause of death in 2020, climbing from ninth place in 1990. As reported by the National Highway Traffic Safety Administration [3], V2X system has the potential to help drivers avoid or minimize up to 80 percent of crashes involving unimpaired drivers and such a technology should be the next major safety breakthrough. V2X communications has the potential to take a huge leap towards making our roads safer. Their economic benefits that come along motivates each party, be it car manufacturers, researchers or OEM (Original Equipment Manufacturer) to develop this system.

In this chapter, we will put forward the general principle and targeted applications of V2X communication systems. Afterwards, we will describe the different standards of V2X communication systems before pointing out the numerous conception problems. Finally, we will end up this subsection with a focus on the global integration of V2X systems in the vehicle and the importance of upstream studies.

2.1 OUTLINE OF V2X COMMUNICATIONS SYSTEMS AND GENERAL PRINCIPLE

V2X communication systems form a special class of wireless networks, known as vehicular ad hoc networks or VANETs (Figure 2-2). VANETs provide communication among nearby vehicles and between vehicles and nearby roadside equipment. Each equipped vehicle will have a wireless communication equipment to provide ad hoc network connectivity. Such networks comprise of sensors and on board units (OBU) installed in the car as well as road side units (RSU). The data collected from the sensors on the vehicles can be displayed to the driver, sent to the RSU or even broadcasted to other vehicles depending on its nature and importance. V2V communication uses multi-hop communication (multicasting/broadcasting) for transmission of data. V2I communication uses single-hop communication (RSU broadcasts message to the vehicles in range). VANETs offer the potential for fast and accurate driving information (e.g. traffic, accidents and emissions) that would otherwise be more difficult to disseminate. Possible applications for such networks can be generally classified as safety and non-safety applications.

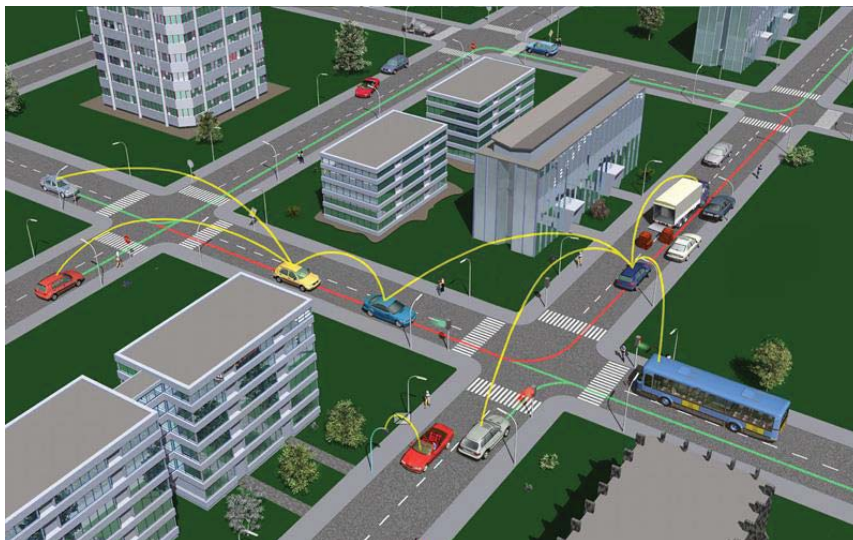


Figure 2-2 : V2X ad-hoc network environment [4]

2.1.1 Targeted applications of V2X communications

Even though Intelligent Transport Systems (ITS) will have, without any ounce of doubt, a great potential in the near future, there are many research challenges and issues that need to be tackled in order to uphold the emergence of safe ITS applications. Recent technological advancements in wireless communications in the transport systems were accompanied with a deployment of a wide range of targeted applications pertaining to V2X communication systems. V2X applications can be regrouped into four main categories: (i) Road safety, (ii) Traffic management, (iii) Advanced driver assistance systems (ADAS) and (iv) Infotainment (blending between information and entertainment). The European project DRIVE C2X has been mainly established to prepare the European Field Operational Tests and have thus opted several use cases to be prioritized in the assessment of these field tests [5]. It has successfully ended in 2014. The different use-cases were summarized in the basic set of applications defined in the ITS technical report produced by ETSI [6]. The different ITS applications can be grouped into four main categories as shown in Figure 2-3.

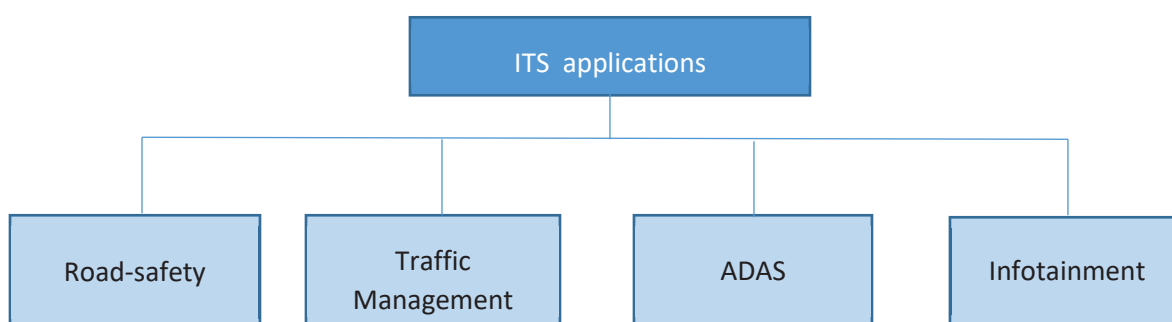


Figure 2-3 : Main categories of ITS applications.

2.1.1.1 Road-safety applications

This category of application remains the priority amongst ITS applications. They will exploit data collected from local ITS entities (including vehicles, surrounding environment, road-side units, ...) to gather appropriate information in order to reduce traffic accidents. Applications pertaining to road safety can be further clustered among the following ones:

- Road Hazard warning

The concept of this set of applications is the inter-exchange of road hazards' information identified by drivers or on-board vehicle sensors to its surrounding so that other drivers approaching those hazards could be notified of an elevated risk in advance. A short list of Road Hazard warning applications may include: Emergency electronic brake lights, wrong way driving warning, stationary vehicle warning, signal violation warning and roadwork warning [3]. An illustrated example of stationary vehicle warning is given in Figure 2-4. In this particular example, any vehicle that is dangerously immobilized on the road following an accident or breakdown may alert other approaching vehicles of the risk associated to this dangerous situation.

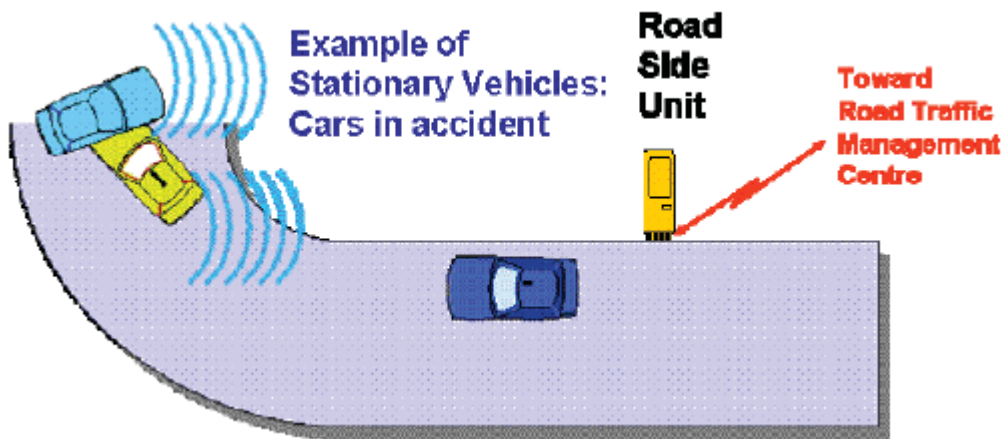


Figure 2-4 : Example of Road Hazard Warning.

- Cooperative collision warning

Cooperative collision warning alerts the drivers potentially under imminent crash risk so that they can avoid an accident via prompt reaction. An example of this set of application is “merging traffic turn collision risk warning” cited in [3] and illustrated in Figure 2-5(a). The objective of such an application is to assist the driving to make a safer right turn by providing information of presence, position and movement of incoming vehicles from the left side. In the case of obstructed line of sight by obstacle (such as fallen trees or objects, etc.) we should rely on Road-Side Unit to be capable to relay signal and to provide notifications about collision risks. Moreover, “co-operative forward collision warning” also falls in the cooperative collision avoidance applications. As presented in Figure 2-5(b), this use-case is based on co-operation between vehicles in order to alert the driver in a hazardous situation, where the current movement pattern of vehicles may lead to a crash. This can obviously avoid longitudinal collisions. Other cooperative collision warnings may be listed as: “Vulnerable road user Warning”, “Pre-crash sensing warning” and “Across-traffic turn collision risk warning”.

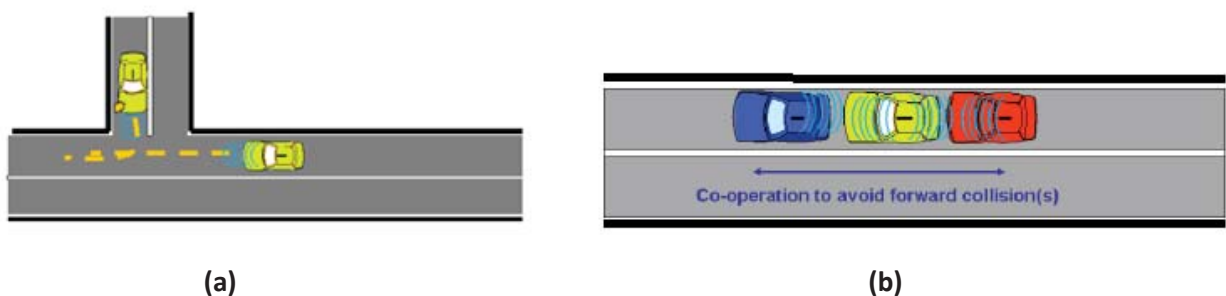


Figure 2-5 : Examples of Cooperative collision warning: (a) merging traffic turn collision risk warning and (b) co-operative forward collision warning.

- Co-operative awareness warning

Co-operative awareness warning are time-triggered messages responsible to produce and maintain awareness between vehicles and RSU present in the ad-hoc network. Several applications such as “slow vehicle warning”, “Motorcycle warning” and “Emergency vehicle warning” are offered within this class of application. Figure 2-6 presents the “Emergency vehicle warning” use case. The emergency vehicle notifies the surrounding vehicles to form a corridor and to provide a clear path and eventually could communicate with RSU to set the traffic light to green. This allows emergency vehicles to reduce their response time and to avoid collision with other vehicles.

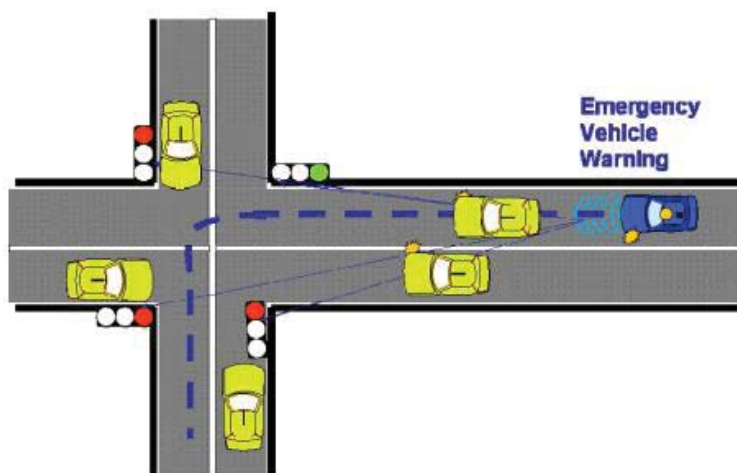


Figure 2-6 : Example of Co-operative awareness warning.

2.1.1.2 Traffic management applications

The main objective of traffic management applications is to improve traffic fluidity by reducing travel time and traffic congestion. These applications provide information such as road condition status and recommended itineraries to the user. These pieces of information are usually disseminated by RSU. Traffic management applications include “Traffic light optimal speed advisory”, “Enhanced route guidance and navigation” and “Co-operative flexible lane change”. The latter, illustrated in Figure 2-7 is a use case considering the flexible allocation of a dedicated lane (for example, reserved to public transport) to some vehicles which can get a permanent or temporary access right under specific conditions.

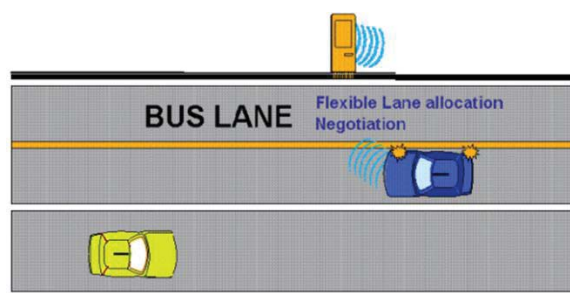


Figure 2-7 : Example of traffic management applications.

2.1.1.3 ADAS

Advanced driver assistance systems (ADAS) fall into several categories depending on their purpose to extend the driver's field of vision, to warn of a loss of alertness, or to provide electronic co-driving functions, anti-collision systems or parking aids. Thus, ADAS enable better situational awareness and control to make driving easier and safer. ADAS technology can be based upon systems local to the car, that is, "vehicle resident systems" like vision/camera systems, sensor technology, or can be based on smart, interconnected networks as in the case of V2X systems. V2X communications technologies can aid ADAS by helping to "extend a vehicle's field of vision and to gather information that cannot be obtained by on-board sensors. For example, at intersections with poor visibility, information about oncoming vehicles and pedestrians detected by sensors alongside the road will be conveyed via RSU, and information about approaching vehicles will be conveyed via V2V communications. Furthermore, in newly-developed feature like adaptive cruise control (ACC) allows preceding and following vehicles to maintain safe distances between one another on highways. ACC uses forward-facing millimeter-wave radar to detect inter-vehicular distances and relative speeds. In Figure 2-8, several ADAS applications developed by Renault is depicted.



Figure 2-8 : ADAS applications developed by Renault.

2.1.1.4 Infotainment applications

Infotainment provides comfort and convenience applications for the users in order to enhance their driving experience. Such application can offer local-based services such as points of interest notifications (nearby filling station, public transport management, medical center, etc.), video streaming and multimedia facilities.

2.1.2 General principles of this communication

2.1.2.1 Standardization and harmonization of V2X communication systems

Research works on V2X communications over the last years were accompanied by standardization efforts in the context of cooperative intelligent transport systems (C-ITS) [7]. The initial driving forces for the technology are the USA and Europe. These activities have led to a globally harmonized set of standards in Europe and the United States. Standardization of ITS is of utmost importance to ensure interoperability between different equipment and system, regardless of their brands and models.

The main standardization committee in the USA is the Institute of Electrical and Electronics Engineers (IEEE). They proposed a Wireless Access in Vehicular Environments (WAVE) V2X protocol stack reserved for future ITS applications [8]. In Europe, the European Telecommunications Standards Institute (ETSI) is working towards a global standard for cooperative ITS systems together with the European Committee for Standardization (CEN) [9]. Also, the International Organization for Standardization Technical Committee 204 (ISO TC204) is contributing to harmonize the standards globally.

The need to satisfy the low latency and high mobility, both intrinsic criteria of V2X communications, pushed for an evolution of the classic Wi-Fi standard towards an adapted IEEE 802.11p exclusively dedicated to such type of communications. Different channels in the 5.9 GHz band have been reserved in Europe and North America. It was in June 2000 that IEEE brought a new modification to the existing 802.11a, to enable two terminals to directly communicate between themselves, without any support of a network infrastructure, in a rapidly changing environment.

2.1.2.2 Frequency band allocation and their characteristics

In Figure 9, we can see the different frequency bands allocated to ITS-G5 in Europe. They are distributed into three principal sub-band. In a first place, ITS-5GA (from 5,875 to 5,905 GHz) is reserved for safety-related applications. This sub-band is further divided into three channel of 10 MHz bandwidth each: the Control Channel (CCH) and two service channels, SCH1 and SCH2 respectively. The ITS-G5B frequency band (from 5,855 to 5,875 GHz) is available for non-safety applications such as road traffic management, fleet management, infotainment and so on. The ITS-G5D band (from 5,905 to 5,925 GHz) is set aside to forthcoming ITS applications. The last sub-band, ITS-G5C, is not dedicated to ITS systems but can be used to share the spectrum with radio local networks (RLAN) and Wi-Fi [8].

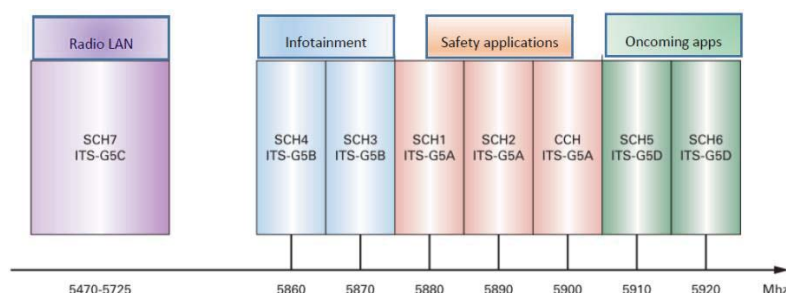


Figure 2-9 : Dedicated frequency bands to V2X communications in Europe.

Since January 2009, (ETSI) has been working on a draft version, the ETSI EN 302 571 standard, which gives us the characteristics of the different channels pertaining to maximum output power, channel spacing and the power spectral density limit. The last up-to-date version of this document has been published in March 2016. European frequency allocation bands dedicated to ITS systems and their corresponding characteristics are resumed in Table 2-1.

Table 2-1 : Characteristics of V2X channels.

Channel	Center frequency	Channel spacing	Default data rate	Tx power limit	Tx power density limit
CCH	5900 MHz	10 MHz	6 Mb/s	33 dBm EIRP	23 dBm/MHz
SCH1	5880 MHz	10 MHz	6 Mb/s	33 dBm EIRP	23 dBm/MHz
SCH2	5890 MHz	10 MHz	12 Mb/s	23 dBm EIRP	13 dBm/MHz
SCH3	5870 MHz	10 MHz	6 Mb/s	23 dBm EIRP	13 dBm/MHz
SCH4	5860 MHz	10 MHz	6 Mb/s	0 dBm EIRP	-10 dBm/MHz

2.1.2.3 Messages dedicated to V2X communications.

The two primary standardized messages for the V2V and V2I communications are the cooperative awareness messages (CAM) and the decentralized environment notification messages (DENM). The CAMs are periodically broadcasted beacons used to maintain awareness of the surrounding vehicles. These are single-hop messages sent with an adaptive frequency of 1-10 Hz. The CAMs include information such as position, type and direction. The DENMs are event-triggered multi-hop warning messages which are generated by the ITS applications in order to alert neighboring vehicles about potential hazards like bad weather conditions or brutal slowdown.

2.1.2.4 The IEEE 802.11p standard

The IEEE 802.11p dedicated to V2X systems is an adaptation of the well-known WLAN IEEE 802.11a. The different changes in the characteristics of the physical layer are well resumed in Table 2-2. In the 802.11p standard, the allocated channel bandwidth is halved resulting in a 10 MHz channel bandwidth. The carrier spacing is thus reduced by half while the symbol length is doubled ($2 \times 4\mu\text{s}$). The cyclic prefix also doubles, making the system more robust to inter-symbol interference. This increase in the cyclic duration makes the 802.11p standard better suited for V2X environments which tend to have high delay spreads. Besides, the reduction of the channel bandwidth has the direct consequence of reducing the transmitted data rates by half, thus improving the reliability of the communication. Binary Phase Shift Keying (BPSK), Quadrature Phase Shift Keying (QPSK), 16-Point Quadrature Amplitude Modulation (16-QAM), and 64-Point Quadrature Amplitude Modulation (64-QAM) modulation schemes are available allowing 27 Mbps data rate at maximum.

Table 2-2 : Comparison between the 802.11p and 802.11a PHY layer parameters.

Parameter	IEEE 802.11p	IEEE 802.11a
Num. of sub-carrier (N_{SC})	48	48
Num. of pilot sub-carrier	4	4
Num. of sub-carrier STS	12	12
STS duration (T_{STS})	1.6 μs	0.8 μs
Short training sequence duration (T_{short})	16 μs ($10 \times T_{STS}$)	8 μs ($10 \times T_{STS}$)
Num. of sub-carrier LTS	53	53
LTS duration (T_{LTS})	6.4 μs	3.2 μs
Long training sequence duration (T_{long})	12.8 μs ($2 \times T_{LTS}$)	8 μs ($T_{GI2} + 2 \times T_{LTS}$)
Freq. between sub-carrier (Δf)	0.15625 MHz (= 10 MHz/64)	0.3125 MHz (= 20 MHz/64)
Time FFT (T_{FFT})	6.4 μs ($1/\Delta f$)	3.2 μs ($1/\Delta f$)
PLCP preamble ($T_{preamble}$)	32 μs ($T_{short} + T_{long}$)	16 μs ($T_{short} + T_{long}$)
OFDM symbol period (T_{signal})	8 μs ($T_{GI} + T_{FFT}$)	4 μs ($T_{GI} + T_{FFT}$)
Guard interval period (T_{GI1})	1.6 μs	0.8 μs
Training symbol duration (T_{GI2})	3.2 μs	1.6 μs
Symbol interval (T_{sym})	8 μs	4 μs
Time slot	13 μs	9 μs

2.1.3 Integration of V2X systems in the vehicle and importance of upstream studies

In the development and deployment of communication-based V2X systems, there will be many challenges to overcome since the performance of these systems are strictly related to the antenna configuration, the type of receivers and the fast changing environment. The integration of these wireless communication systems in vehicles are inevitable sources of complexities regarding vehicle design aspects on the positioning of the required number of antennas and the electrical and electronic architecture to choose the best technologies. Therefore, finding the most favorable antenna configuration together with the best developed V2X receivers in order to ensure the best performance is a tedious task. A possible solution is the employment of measurement campaigns, but they are expensive, time consuming, and provide no repeatability.

So, the development of robust and precise simulation tools can be helpful for equipment specifications in upstream development phase in order to validate the performance of the communication systems in different driving conditions. Indeed, a complete simulation tool can turn out to be a preliminary phase that can allow a rough selection between numerous combinations of configurations (V2X receiver implementation, adequate diversity techniques to be adopted, antenna positions, antenna technologies, etc.). Therefore, for the simulation tool to be optimized, it should include the complete communication chain for V2X systems, taking into account all the parameters influencing the quality of service: the V2X modems, antenna configurations and the propagation channel between the communicating devices.

2.2 OVERVIEW OF PREVIOUS RESEARCH WORKS: THE 2008 -2012 PERIOD

This thesis is the continuity of a previous research work undergone by Renault in collaboration with the Institut d'Electronique et Télécommunications de Rennes (IETR) in the frame of the Ph. D thesis of Iulia Ivan. The initial studies focused on the V2X systems and help to bring to light the important role played by the V2X receiver technologies in rapidly changing environment due to the high mobility of both transmitter and receiver [10].

The thesis has enabled to develop a first strategy towards a complete embodiment of a simulation chain englobing the V2X receiver physical layer implementation, normalized propagation channels models and finally antenna integration. Important milestones have been reached since most parts of the complete simulation chain are readily available since then. Nevertheless, many hindrances need to be tackled. In the next sub-sections, we will take a quick glance at the different blocks of the simulation chain developed in the previous work.

2.2.1 Achievements of different simulation blocks

2.2.1.1 PHYSical layer following the IEEE 802.11p standard

For accurate system performance evaluation, correct modeling of the communication system's physical layer is required. The implementation was performed according to the IEEE 802.11p standard dedicated to V2X communication systems. In this subsection, we briefly describe the transmission and reception chain, including all simplification hypothesis made in the implementation.

Modulation schemes

Based on OFDM, the IEEE 802.11p standard offers data payload communication capabilities of 3 Mb/s to 27 Mb/s depending on the different modulation schemes used. The modulation parameters and the corresponding data payload or data rate are summed up in Table 2-3. Of course lower data rates will most likely be chosen for safety applications, since they require a high reliability.

Table 2-3 : Modulation coding schemes as per IEEE 802.11p standard

Modulation Coding scheme (Mode)	Modulation	Coding rate	Coded bits per subcarrier (N_{BPSC})	Coded bits per OFDM symbol (N_{CBPS})	Data bits per OFDM symbol (N_{DBPS})	Data rate (Mb/s)
1	BPSK	1/2	1	48	24	3
2	BPSK	3/4	1	48	36	4.5
3	QPSK	1/2	2	96	48	6
4	QPSK	3/4	2	96	72	9
5	16-QAM	1/2	4	192	96	12
6	16-QAM	3/4	4	192	144	18
7	64-QAM	2/3	6	288	192	24
8	64-QAM	3/4	6	288	216	27

Transmitter and Receiver structure

Figure 2-10 represents the general block diagram of both the transmitter and the receiver. As mentioned earlier, some simplification hypothesis were made notably in the computer implementation of the receiver where the frequency and time synchronization were considered perfect. Based on the channel estimation technique, the performance of two types of receivers were investigated: the conventional receiver (with simple channel estimation based on the two

training symbols), and the receiver with perfect CSI (channel state information), i.e. with channel impulse response perfectly known. These channel estimation schemes can be considered as best case scenario (receiver with perfect CSI), and the worst case scenario (the conventional receiver).

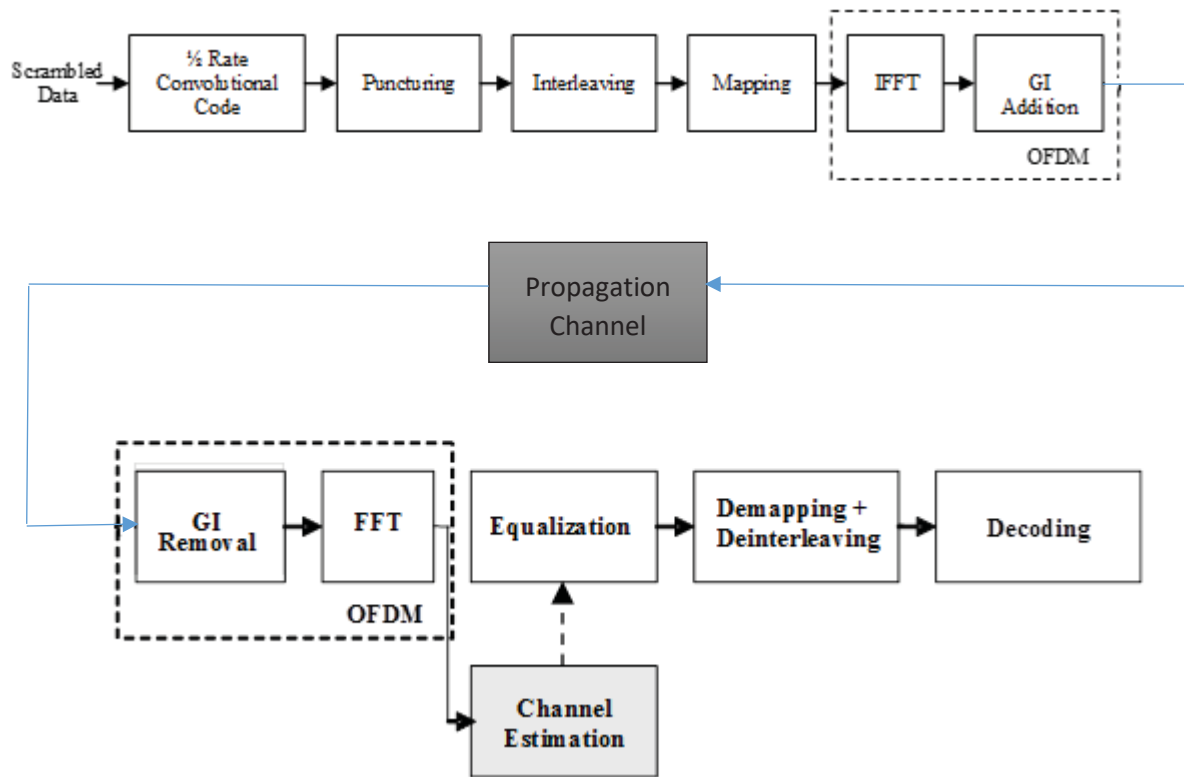


Figure 2-10 : The Transmitter and Receiver block diagram.

IEEE 802.11p transmitted packet structure

The frame of the transmitted packet is given in Figure 2-11. Assuming perfect synchronization at the receiver and known transmission parameters, the packets generated contain neither the short-training sequence (STS) nor the SIGNAL symbol. Therefore, the preamble of simulated transmitted packet consists only of the long-training sequence (LTS) $[T_1, T_2]$ and the guard interval (GI2). The number, N , of DATA symbols transmitted is a function of the packet length and the data rate

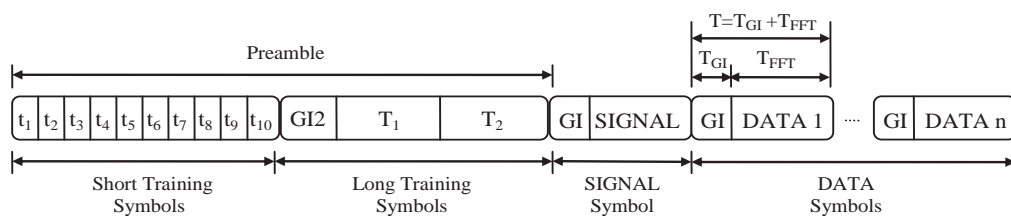


Figure 2-11 : IEEE 802.11p transmitted packet structure.

2.2.1.2 Propagation modelling using “normalized” channel (Ohio & GT)

In this subsection, a brief description of the propagation channel models chosen in [10] will be given. The authors deemed it judicious to use two tapped-delay line propagation channel models due to reduced computational complexity and their current availability in the open literature. Appropriate definitions and explanations about different types of propagation channel models will be given in chapter 3.

Georgia Tech Channel Model (Model 1)

The first model was proposed in the preliminary version of the IEEE 802.11p standard. The main objective of this model was to enable equipment certification tests using a radiofrequency channel emulator. The model is thus adjusted to satisfy the constraints imposed by this kind of equipment. So, the model was based on the tapped delay line (TDL) structure and consisted of taps (or delay bins), with the tap amplitude PDF being either Ricean or Rayleigh. Furthermore, each tap contains N unresolvable paths that have different types of Doppler spectra, e.g., flat shape, round shape, classic 3 dB shape, and classic 6 dB shape. This allows one to synthesize almost arbitrary Doppler spectra for each tap. The propagation channel was modeled for the six following scenarios:

- three for V2V communications:
 - V2V – Expressway Oncoming
 - V2V – Urban Canyon Oncoming
 - V2V – Expressway Same Direction with Wall
- three for V2I communications (or R2V – Roadside to Vehicle communications):
 - R2V – Urban Canyon
 - R2V – Expressway
 - R2V – Suburban Street
- Description of a channel model : V2V – Expressway Oncoming

Table 2-4 presents an example of a channel model proposed in [11] **Error! Reference source not found.** for a Vehicle to Vehicle – Expressway Oncoming scenario. The model was described with 4 taps and 11 paths. The first path of the first tap represents the Line of sight (LOS) and is thus modeled as a Rician distribution, with Rician K factor of -1.6 dB. The “Frequency Shift” represents the central frequency of the Doppler spectrum, “Fading Doppler” is the width of the spectrum, and “LOS Doppler” denotes the frequency of the peak corresponding to the LOS component. The possible spectral shapes for each path are: Classical 3 dB - C3, Classical 6 dB - C6, Rounded, and Flat.

Table 2-4 : Example of channel model in an Expressway-oncoming environment for V2V communications [11].

Tap No.	Path No.	Relative Path Loss (dB)	Delay Value (ns)	Rician K (dB)	Frequency Shift (Hz)	Fading Doppler (Hz)	LOS Doppler (Hz)	Modulation	Fading Spectral Shape
1	1	0.0	0	-1.6	1451	60	1452	Rician	Round
1	2	-24.9	1	<i>n/a</i>	884	858	<i>n/a</i>	Ray	Round
1	3	-25.5	2	<i>n/a</i>	1005	486	<i>n/a</i>	Ray	Round
2	4	-13.1	100	<i>n/a</i>	761	655	<i>n/a</i>	Ray	C3
2	5	-7.5	101	<i>n/a</i>	1445	56	<i>n/a</i>	Ray	Round
3	6	-28.9	200	<i>n/a</i>	819	823	<i>n/a</i>	Ray	C3
3	7	-29.3	201	<i>n/a</i>	1446	75	<i>n/a</i>	Ray	Flat
3	8	-35.6	202	<i>n/a</i>	124	99	<i>n/a</i>	Ray	Round
4	9	-25.7	300	<i>n/a</i>	1437	110	<i>n/a</i>	Ray	Flat
4	10	-34.4	301	<i>n/a</i>	552	639	<i>n/a</i>	Ray	C3
4	11	-27.4	302	<i>n/a</i>	868	858	<i>n/a</i>	Ray	C6

Ohio University channel model (Model 2)

This model is based on measurement campaigns that were carried out in the state of Ohio for the following scenarios [12]:

- UIC – Urban Antenna Inside Car
- UOC – Urban Antenna Outside Car
- SC – Small City
- OHT – Open-Area High Density Traffic
- OLT – Open-Area Low Traffic Density

Except for the UIC scenario where the receiving antenna was placed on the dashboard, inside the car-body, all the other measurements were performed with omnidirectional antennas placed on the roof-top of vans. The particularity of this model was that the fading amplitudes were fitted with the Weibull distribution. Furthermore, inter-tap correlation and the non-stationarity were considered. The latter was modeled by a persistence process through a first-order two-state Markov chain. Nevertheless, this model has two major inconveniences. Firstly, the Doppler spectra has neither been analyzed nor modelled in sufficient details. In addition, no clues were provided pertaining to the determination of the phase distribution of the Weibull method. This piece of information is essential to the generation of complex coefficients of the fading channel (i.e. both

amplitude and phase). So the authors carried out a tedious work to overcome those uncertainties regarding the phase distribution. In [10], two methods for generating Weibull fading envelope and phase are given. Thus, time-sequences following Weibull distribution were successfully obtained and could be used for PER/BER performance evaluation.

2.2.1.3 Validation and performance evaluation

In the first place, the implementation of the physical layer had to be validated in order to ensure a correct evaluation of the PER performance evaluation in different propagation channel conditions. The second part of this study was dedicated to a deeper analysis of the physical layer with more emphasis given to the influence of the phase distribution and then to the main parameters of the propagation channel.

Below, simulation results with a receiver with perfect Channel State Information (pCSI) are given in Figure 2-12(a) and 2-12(b). All environments pertaining to both Model 1 and Model 2 were simulated with transmission mode 3 and a packet length of 1000:

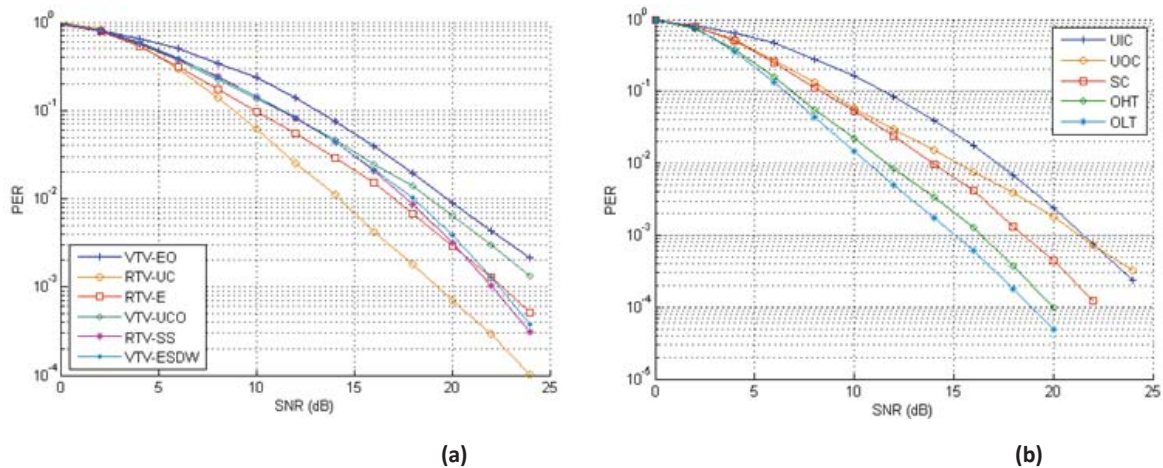


Figure 2-12 : PER performance vs. SNR with perfect CSI for all considered scenarios in: (a) Model 1 (b) Model 2.

Those results show that the PER is influenced mainly by the Rician K-factor of the first-tap and the RMS delay-spreads for the Model 1. For Model 2, the shape factor and the RMS delay-spreads impact most the performance. More simulation results can be found in the third chapter of [10].

2.2.1.4 Antenna Integration

The propagation channel models described in section 2.2.1.2 are based on measurement results with on-roof omnidirectional antennas. So, to integrate antennas in the simulation chain, information pertaining to the distribution of angles of arrivals on the receiving antenna is compulsory. The authors elaborated a method using the ray-tracing module of the electromagnetic simulator FEKO to develop a deterministic highway scenario which allows to generate time sequences of the propagation channel with different receiving antennas. In this work, three methods to integrate the antenna radiation pattern were proposed. In the first method, the deterministic highway scenario had to be simulated each time a new antenna radiation pattern had to be simulated. The second method consisted of simulating the highway scenario once and storing all the information concerning received rays at the point of reception. Thus, a posteriori integration can be performed with any radiation pattern afterwards, rendering the simulation

computationally less expensive. The last proposed method tried to reproduce random sequences of propagation channel with parameters associated to a particular environment. Statistical parameters were extracted from deterministic simulation of a particular scenario from FEKO simulations. The third method was shown to give good results as compared to deterministic simulation and have the advantage of being less demanding regarding time consumption.

2.2.2 Limitations of previous work

As it can be noted, the previous work lead to a first strategy towards the elaboration of a complete simulation tool including the transmitter/receiver, antenna and propagation channel model. Nevertheless, question marks still remain and problems such as antenna integration in our propagation models is in need of better understanding. First of all, the authors used propagation channel models that were available in the literature. These models were developed in such a format that they can be directly implemented in a radiofrequency channel emulator. The aim was mainly to validate the physical layer of the IEEE 802.11p standard dedicated to V2X communications. These propagation channel models considered isotropic antennas and cannot be adapted to different antenna configurations as they do not pertain information about the angular distribution of the received signals. Therefore, after validating the PHY layer of the standard of the communication, the authors developed a deterministic propagation channel model to emulate a highway scenario using the UTD module of the electromagnetic simulator FEKO. Deterministic approaches such as ray-tracing methods describe site-specific realistic simulations. In these approaches, accurate parameters such as dimensions and electromagnetic (EM) properties of multipath contributors present in the scenario should be included. However, in the UTD module of FEKO only metallic plates can be used to model the scenario making realistic on-map driving environment difficult to reproduce. Moreover, they require time-consuming modeling of the environment to be simulated and are therefore computationally expensive. So, if we were to use the same electromagnetic simulator, another philosophy of channel modelling other than pure deterministic propagation channel models should be adopted. Another limitation of this preliminary work deals with the problem of antenna integration on vehicle. Though a general and efficient strategy was proposed to perform a propagation simulation at once, the antenna pattern alone is in general very different from the pattern once installed on-board the vehicle. Moreover, interaction with the vehicle may not be in the far-field, due to its large size with regard to the wavelength. There is therefore a need for a methodology to handle the problem of simulating efficiently the performance of various antennas in several positions on a vehicle.

2.3 MAIN OBJECTIVES OF THIS THESIS

In this section, we shall put forward the main objectives of this thesis. The goal is to come up with a complete and effective simulation tool that can cope with our need, that is, to anticipate V2X performance under different antenna technologies and their implementation in different driving environments. A strengthening of the simulation chain developed in previous works must be done and a better understanding of the interactions of the antenna and its surroundings must be reached.

In this thesis, we shall develop a complete simulation tool that will englobe the complete communication chain for V2V communications. A method to correctly and adequately embed each of the individual simulation blocks needs to be worked upon. To be able to reach such a goal without much predicaments, good care should be taken to consolidate the different individual blocks leading to the complete communication chain: the physical layer of the communication standard, the propagation channel models, and finally the method of antenna integration. In the following subsections, the emphasis will be placed on a new philosophy on propagation channel modelling and on the different methods of integrating the antenna in our propagation channel.

2.3.1 Propagation channel modelling (A new philosophy)

In order to evaluate a communication system, we need to model the propagation channel of the relevant environments pertaining to that communication. The most encountered approaches, in the literature, for modelling V2V communications' propagation channels are: deterministic, stochastic and geometry-based stochastic methods. In this thesis, we propose a Geometry-Based Stochastic Channel Modelling (GBSCM) approach to build up propagation channel simulations to assess the performance of vehicle-to-vehicle wireless communications (V2V). The Geometry-Based Stochastic Channel Modeling (GBSCM) method is a combination of both the deterministic and stochastic approaches. In this method, scatterers are placed randomly (according to suitable statistical distribution) around the transmitter and receiver. Scatterers in GBSCM are often represented by simple geometric shapes with uniform materials. Then, simplified ray-tracing is performed to evaluate the corresponding channel impulse response. This approach is numerically cheaper than purely deterministic method and enables to intrinsically model the non-stationary behavior as it includes the dynamic nature of the environment. Moreover, such a technique allows us to define different types of scenario that may encompass the above-mentioned propagation model 1 and 2 without sticking to any particular too standardized description. Taking into account its numerous advantages, many researchers focused their attention on the GBSCM as an approach to simulate V2V propagation channels. Our proposed methodology allows the simulation of dynamic scenarios, with an electromagnetic simulator, to emulate typical propagation environments (rural, highway and urban-like propagation channels). Simple metallic plates are used to represent scatterers in the simulated geometric configurations. The common characteristics defining a propagation channel such as delay spread, angle of arrival distribution and the delay-Doppler spectrum are obtained through adjustment of the number and location of those simple metallic plates. In chapter 3, a complete state-of-art in V2X propagation channel modelling will be given together with explanations on how we chose the GBSCM technique. In the same way, more details on our proposed methodology will be included in the same chapter.

Through dynamic scenarios, such simulations could directly provide different channel responses that may be incorporated in a complete V2V communication simulation tool including antenna integration and the physical layer modelling of modems.

2.3.2 Antenna integration

To characterize the different propagation channel models, antennas with isotropic radiation pattern were used. These radiation patterns were obtained by simulating perfect dipoles. However, our aim is to compare the performance of different antennas in different driving environment. Therefore, we should be able to correctly integrate our antenna model in our propagation channel model. The main goal of this part is to find a way to find a liable method to represent at best the antenna implemented on the vehicle in our propagation channel model simulation.

The ideal solution would be to define a new calculating procedure that remains valid for all antenna models and under all installation configurations in or on the vehicle. A rapid brainstorming may lead to the following clues:

- Use of the radiation pattern of the antenna only

It simply consists of substituting the emitting and receiving antennas by their far-field radiation pattern in our propagation models. This can be a temporary solution at upstream stages of conception when digital mock-up of project vehicle is not yet available and where suppliers can share with us their antenna models. Even though, this procedure can give us a quick view of the communication performance of the antenna, these preliminary results cannot be taken for granted as the radiation pattern of the antenna might considerably change when implanted onto the vehicle.

- Use of the radiation pattern of the antenna implanted onto the vehicle

Here also we follow the same procedure as above with a single difference: substitution of the resulting radiation pattern of the integrated antenna on the vehicle model. A fine meshing of the antenna and numerical model of the whole vehicle is required in simulation to obtain the radiation pattern through an electromagnetic simulator. At high operating frequency, the numerical model of such complex system can lead to a high number of meshes increasing the need in terms of computational resources. It can be, thus, particularly valuable to substitute the whole vehicle with a simulation of the antenna in a simplified representation of the vehicle. It will be then necessary to determine a sufficient level of description of the near environment of the implanted antenna to obtain a liable radiation pattern of the whole system.

Looking at the two above antenna integrations solutions, questions may be raised as to the integrity of representing the antennas directly by their far-field radiation pattern in the propagation channels models. It is important to study the impact of the presence of whatever element in the near-field zone of the radiating object albeit supposing to know the far-field region limit. If we substitute directly the “antenna + vehicle system” with a radiation pattern, the interactions with the elements in the near-field region will no longer be valid. On the other side, it is unconceivable to model the whole vehicle and antenna together while simulating the transmitting/receiving communication link with a rigorous method due to insufficient hardware resources. It will all depends on the degree of approximation that we are ready to tolerate. Chapter

4 will deal with those methods of antenna integration techniques and we will try to bring answers to all these interrogations.

2.4 REFERENCES

- [1] World Health Organization (WHO). Global Status Report on Road Safety 2013; Technical Report; World Health Organization (WHO): Geneva, Switzerland, 2013.
- [2] <http://www.securite-routiere.gouv.fr/la-securite-routiere/l-observatoire-national-interministeriel-de-la-securite-routiere>.
- [3] www.nhtsa.gov
- [4] CAR-2-CAR : <https://www.car-2-car.org>
- [5] <http://www.drive-c2x.eu/project>
- [6] ETSI - EN 302 637-2 Intelligent Transport Systems (ITS) – Vehicular Communications – Basic set of applications – Part 2: Specification of cooperative awareness basic service.
- [7] K. Evensen, “Harmonization of C-ITS standards: EU-US initiatives. Workshop ETSI TC ITS, Berlin, Germany, 12-13 fév. 2014.
- [8] 802.11p-2012 IEEE Standard for Information Technology – Telecommunications and Information Exchange between Systems – Local and Metropolitan Area Networks – Specific Requirements Part 11, Wireless LAN Medium Access Control (MAC) and Physical Layer (PHY) Spec, 2012.
- [9] CEN- TS 17423: 2014 Systèmes de transport intelligents – Systèmes coopératifs – Exigences des applications STI, 2014.
- [10] I. Ivan, “Vehicle to Vehicle communication systems performance evaluation: A simulation approach combining physical layer implementation, propagation channel model and antenna properties”, PhD dissertation, Renault SAS – IETR, INSA de Rennes, 2012.
- [11] G. Acosta and M. A. Ingram, “Six time- and frequency-selective empirical channel models for vehicular wireless LANs,” 1st IEEE International Symposium on Wireless Vehicular Comm., Sept 2007.
- [12] I. Sen and D. W. Matolak, “Vehicle-vehicle channel models for the 5-GHz band,” IEEE Trans. Intelligent Transportation Systems, vol. 9, 2008, pp. 235–245.

Chapter 3 : Generation of virtual driving scenarios

scenarios

3.1 A STATE OF THE ART

3.1.1 Wireless propagation channel

A wireless communication normally consists of a transmitter, a receiver and a wireless channel in between them. The latter is known as the propagation channel and refers to the physical medium between the transmitter (Tx) and the receiver (Rx). In a wireless communication, the electromagnetic wave radiated from the Tx will be subjected to many physical phenomena depending on the type of environment. The basic mechanisms of propagation which are free-space attenuation, reflection, diffraction and scattering (diffusion) will enable the transmitted signal to arrive at the receiver with different paths as illustrated in Figure 3-1. Each different path arriving on the receiver will be attenuated, delayed, depolarized and phase-shifted. In many cases, this multipath propagation makes it possible for a sufficient amount of energy to reach the receiver, so that the communication link is feasible. This is especially so when the direct signal is blocked. The impinging waves combine vectorially at the receiver, leading to either constructive or destructive addition depending on the relative phases among the incoming total signal components. The resulting signal amplitude variation is known as small-scale fading [1]. On the other hand, large-scale fading is due to path loss of the transmitted signal as a function of distance and shadowing by large objects such as buildings and hills. We will elaborate on both type of fading in coming subsections.

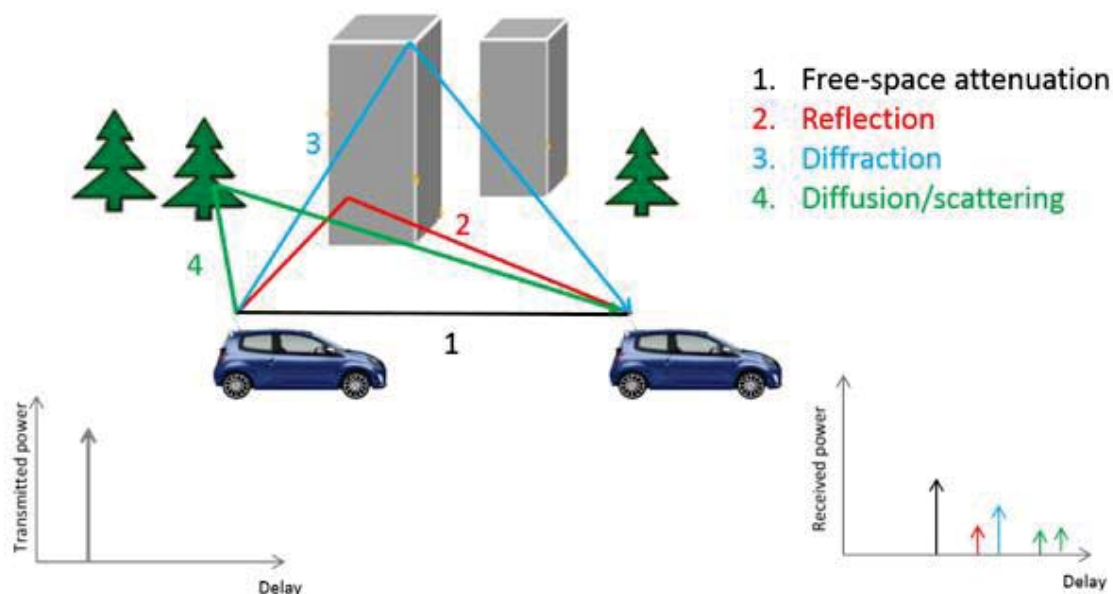


Figure 3-1 : Example of a wireless propagation channel

A reliable knowledge of the propagation channel is the foundation of a wireless communication system design and analysis. This is the reason why a good physical understanding of the behavior of electromagnetic waves in a channel is very important to enable accurate predictions of system performance and to mitigate the effect of fading. In the next section, we will focus on the basic mechanisms of propagation.

3.1.2 Propagation of electromagnetic waves

The basic mechanisms that affect the propagation of electromagnetic waves in a channel are: free-space attenuation, reflection, diffraction and scattering [2].

3.1.2.1 Free-space attenuation

Free-space attenuation represents the simplest model for signal propagation. It assumes that the transmitter is in the line-of-sight of the receiver, i.e., there is no obstruction between them. Under these assumptions, the power of the received signal falls off with the square of the distance separating the transmitter and the receiver. The well-known Friis model is used to estimate the link budget in this case [1]:

$$P_{rec} = P_t \times G_t \times G_r \times \left(\frac{\lambda}{4\pi d_{Tx-Rx}} \right)^2 \quad (\text{Eq. 3.1})$$

where P_t is the transmitted power, G_t and G_r the transmitted antenna gain and the receiving antenna gain respectively. λ is the wavelength of the transmitted signal and d_{Tx-Rx} is the separation distance between the transmitter and receiver. This version of the Friis formula, given in (Eq. 3.1), ignores any polarization mismatch.

It must be noted that this relation is valid only in the case where the distance between the transmitter and the receiver is sufficiently large enough to ensure that the receiving antenna can be considered in the far-field of the transmitting antenna. A receiver is situated in the far-field when the distance d_{Tx-Rx} is larger than the Fraunhofer distance which is governed by the largest dimension of the emitting antenna D and the wavelength of the emitted signal [3]:

$$d_{Tx-Rx} = \frac{2D^2}{\lambda} \quad (\text{Eq. 3.2})$$

We will show in chapter 4 that this approximation does not stand for antennas integrated on vehicles where the largest dimension of the antenna is other than that of the antenna solely.

However, free-space propagation is the theoretical reference case. In real conditions of propagation, the transmitted electromagnetic wave will interfere with the environment of the transmission system as per the different cited mechanisms.

3.1.2.2 Reflection

Reflection occurs when a propagating electromagnetic wave impinges upon an obstruction with dimensions very large compared to the wavelength of the propagating wave [1]. Specular reflection exists if the interacting surface, is totally smooth or if at least the irregularities on the surface medium are negligible as compared to the wavelength. In case the obstacle is a perfect electric conductor, there is no transmission of the wave through the medium, i.e., all the energy is reflected. Else, there is occurrence of refraction. The latter is the description of how the wave is transmitted through an obstacle. Reflection and refraction are subject to Snell-Descartes and Fresnel laws. The coefficients of reflection and refraction are functions of the material properties of the medium, and generally depend on the wave polarization, the angle of incidence, and the frequency of the propagating wave. They are given below for the parallel polarization, i.e., the electric-field is in the plane of the incidence of the incoming wave.

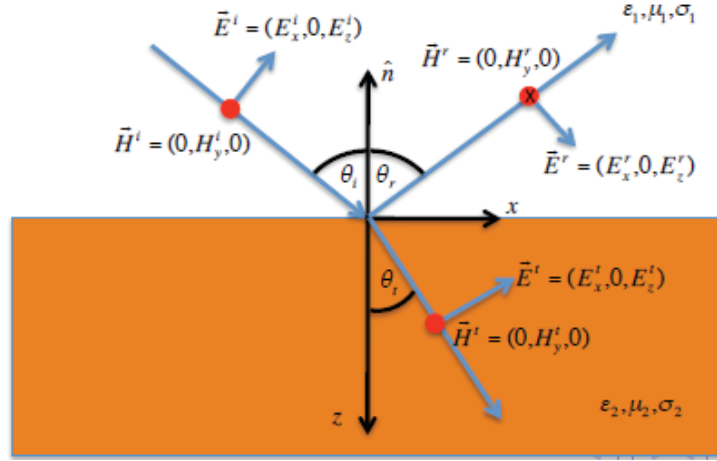


Figure 3-2 : Reflection and transmission

$$\Gamma_{\parallel} = \frac{-\eta_1 \cos \theta_i + \eta_2 \cos \theta_t}{\eta_1 \cos \theta_i + \eta_2 \cos \theta_t} \text{ and}$$

(Eq. 3.3)

$$T_{\parallel} = \frac{2 \eta_2 \cos \theta_i}{\eta_1 \cos \theta_i + \eta_2 \cos \theta_t}, \text{ where } \theta_t = \sin^{-1} \left(\frac{\gamma_1}{\gamma_2} \sin \theta_i \right)$$

In the configuration presented in Figure 3-2, the electric field is in the (\hat{n}, x) plane. Γ_{\parallel} is the reflection coefficient and T_{\parallel} is the transmission coefficient for the parallel polarization. η_1 and η_2 are the wave impedances in medium 1 and medium 2 respectively while γ_1 and γ_2 are the attenuation constants in these respective media. A complementary set of equations is obtained for the perpendicular polarization of the electric field with regard to the incident plane [4].

3.1.2.3 Diffraction

Diffraction occurs when the radio path between a transmitter and a receiver is obstructed by a surface that has sharp edges. The waves produced by the obstructing surface are present throughout the space and even behind the obstacle, giving rise to bending of waves around the diffracting object, even when a line-of-sight path does not exist between the transmitter and the receiver. At high frequencies, diffraction depends on the geometry of the object as well as the amplitude, phase and polarization of the incident wave and the point of diffraction.

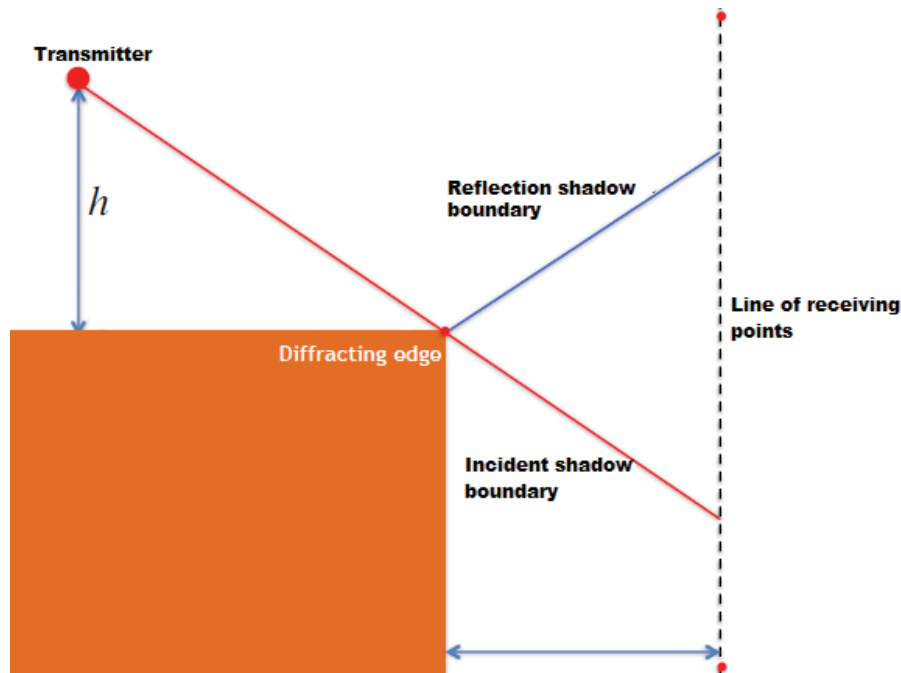


Figure 3-3 : Diffraction.

Diffraction losses are commonly modelled using the well-known knife edge diffraction method based on the Fresnel-Kirchoff diffraction parameter [5].

Diffraction can be also characterized using the geometrical theory of diffraction (GTD) which is an extension of Geometrical Optics (GO) for predicting diffracted field in a shadow region caused by an edge [6]. The geometry of this model is shown in Figure 3-3, where the diffracting object is assumed to be asymptotically thin. However, GTD cannot be applied to the neighborhood of the transition regions. So, to solve this problem Kouyoumjian and Pathak developed the Uniform Theory of Diffraction (UTD) to overcome these singularities and calculate field in the transition regions [7]. The UTD principle will be described in more details later in this chapter.

Scattering

Scattering occurs when a wave is spread in several directions after encountering an object significantly smaller than its wavelength [1]. It can also occur when the transmitted wave encounters a dense medium where the number of small obstacles (relative to the wavelength) per unit volume is large. In such medium the electromagnetic field is said to be diffused. The observed phenomenon corresponds to the superposition, be it constructive or destructive, of a high number

of random diffractions. In this case, the behavior of the scattered waves are dealt with statistical notions and is referred as diffusion. Diffused or scattered waves are produced by rough surfaces, small objects, or by other irregularities in the channel as shown in the Figure 3-4 (b). In practice, foliage, street signs, lamp posts and stairs within buildings can induce scattering in a mobile communication systems.

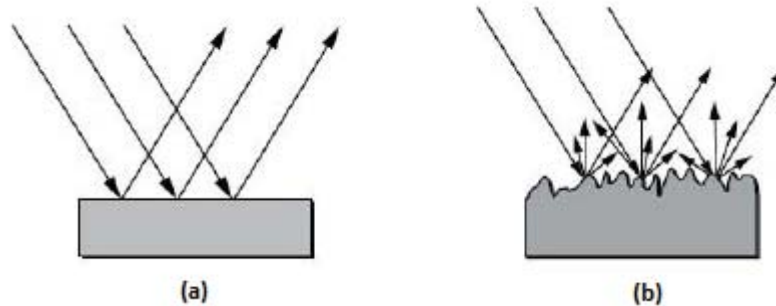


Figure 3-4 : Difference between specular reflection on a smooth surface (a) and scattering of a rough surface (b).

3.1.3 Channel characteristics

An incident electromagnetic wave will interact differently in changing propagation channels. A wireless propagation channel can be characterized with several statistical channel metrics which have been widely adopted in the literature: path loss, time-dispersive characteristics, Doppler spectrum and angular spectrum being among the most common ones. Particular propagation channels bearing the same range of values of these characteristics can thus be bunched up in several subgroups or categories.

In practice, the two most important parameters to characterize any wireless channel are the large-scale fading (slow fading) and the small-scale fading (fast-fading). Large-scale fading explains the variation in the received signal due to the motion over large areas. The path loss describes how the average received power tends to decrease with the distance between the Tx and the Rx and the presence of very large scatterers such as mountains, hills and buildings. On the other side, small-scale fading statistics describe how the instantaneous received power fluctuates over space, time and frequency due to interference between multipath components. This fading is due to scattering from nearby objects and thus is termed small-scale fading. Fast fading can be observed down to half-wavelength distances. Figure 3-5 illustrates how slow fading and fast fading influence the received power over distance.

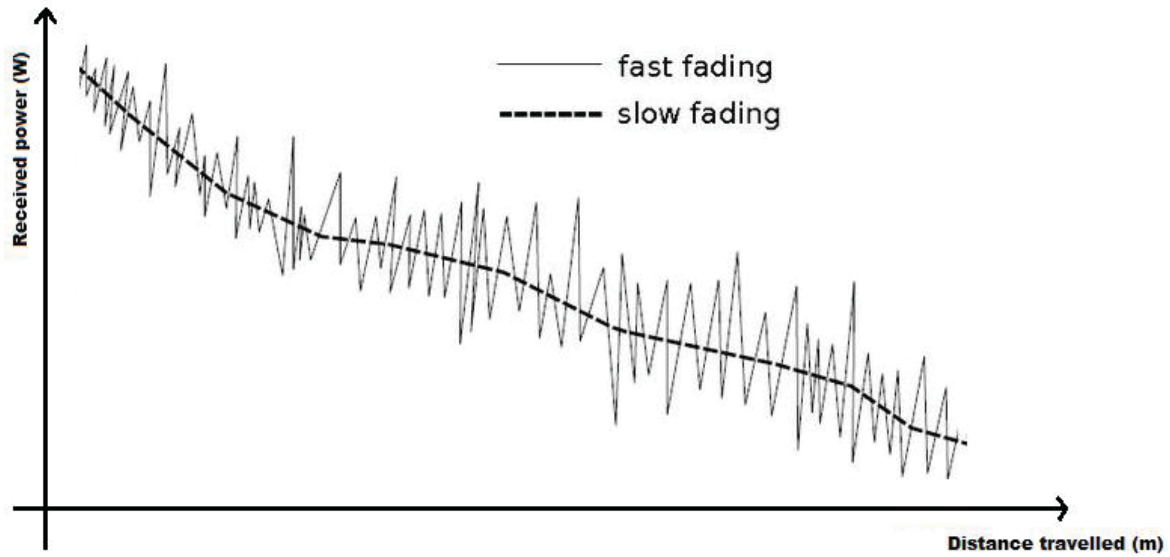


Figure 3-5 : Illustration of fast fading (short-term scale) and slow fading (long-term scale)

3.1.3.1 Large-scale fading or slow-fading

The large-scale fading represents the average attenuation of the received signal power. Large-scale fading can be described in terms of distance dependent path loss and statistical variations about the mean produced by shadowing or objects obstructing the propagation path [2].

When expressed in dB, the instantaneous path loss can be considered as the sum of the mean path loss, shadow fading and small scale fading as follows [2]:

$$PL(d) = L(d) + X\sigma + F \quad (\text{Eq. 3.4})$$

where $PL(d)$, $L(d)$, $X\sigma$ and F denote the instantaneous path loss, the mean path loss, shadow fading and small scale fading associated with the Tx-Rx (transmitter and receiver) separation distance d , respectively. Here, $X\sigma$ represents the variation around the mean of the path loss according to a zero-mean random variable with a standard deviation of σ . Large scale fading, referring to the total effect combining the mean path loss and shadow fading shown in (Eq. 3.4), characterizes signal strength variation over large distances. Typically, the mean path loss $L(d)$ is assumed to be deterministic and is log-dependent on the Tx-Rx separation distance d as follows:

$$L(d) = L_0 + 10n \cdot \log_{10}(d) \quad (\text{Eq. 3.5})$$

where L_0 is a constant which accounts for system losses and n is the path loss exponent depending on the specific propagation environment. For instance in free space propagation $n = 2$ while in environments with obstructions n tends to have larger values.

Table 3-1 below sums up some examples of path loss exponents for indoor and cellular communications [1].

Table 3-1 : Path loss exponents in different propagating conditions

Environment	Path loss exponent, n
Free space	2
Urban area cellular radio	2.7 to 3.5
Shadowed urban cellular radio	3 to 5
In building line-of-sight	1.6 to 1.8
In building non-line-of-sight	4 to 6

Large scale fading characteristics are very useful for determining the coverage area or evaluating system performance. A propagation environment where there is absence of direct wave path from the transmitter to the receiver is known as NLOS channel (non line-of-sight). On the other way round, LOS (line of sight) scenarios are referred when there is occurrence of a direct path. Naturally, the attenuation factor is higher in NLOS conditions.

3.1.3.2 Short-scale fading or fast-fading

The presence of different obstructing objects in a wireless propagation channel can create a constantly varying environment that impacts the amplitude, phase and time of arrival of the transmitted signal. This can lead to various replicas (multipath components) of the transmitted signal arriving at the receiver at slightly different time, resulting in the superposition of those multipaths at the receiver. Superposition of these attenuated, delayed and phase-shifted versions of the transmitted signal combine either constructively or destructively to give a resultant signal. Multipath and movement of the receiver over a small area bring rapid fluctuations in the received signal termed as short-term fading or fast-fading. Major factors impacting fast-fading are: multipath propagation, speed of the transmitter or receiver, speed of surrounding objects in the propagating environment and the bandwidth of the communication.

The most important effects of fast-fading are [1]:

- Rapid changes in signal strength over a small distance or time duration,
- Random frequency modulation due to varying Doppler shifts on the different multipath components,
- Time dispersion (or frequency selectivity in the frequency domain) caused by the different paths arriving with different delays on the receiver.

3.1.3.3 Channel impulse response

The impulse response is used to describe completely the behavior of a channel in the time domain. The impulse response is defined as the response of a channel to a theoretically infinitely short pulse with unit energy described by a Dirac function (distribution). In order to measure the impulse response of the channel, a very narrow pulse is transmitted. The impulses corresponding to

multipath arrive at the receiver with different delays and with different attenuations depending upon the nature of the propagation mechanism.

As in a propagation environment, the transmitter, the receiver or scatterers in the channel can be mobile, the impulse channel response is generally considered as a linear time-variant filter. The filtering nature of the channel is caused by the summation of the amplitudes and delays of the multipath signal arriving at any time instant. The impulse response is an important characterization of the channel since it may be used to analyze and compare the performance of different wireless communication systems.

The time-variant channel impulse response can be written as the superposition of all multipath components:

$$\tilde{h}(\tau, t) = \sum_{i=0}^{N-1} a_i(t) \cdot \delta(\tau - \tau_i(t)) \quad (\text{Eq. 3.6})$$

where $a_i(t)$ and $\tau_i(t)$ represent the complex amplitude and excess delay respectively of the i th multipath component at time t . It is useful to discretize the multipath delay axis τ of the impulse response into equal time delay segments called delay bins, each bin having a time delay width equal to $(\tau_{i+1} - \tau_i) = \Delta\tau$ and $\tau_i = i\Delta\tau$ for $i \in \{0, 1, 2, \dots, N-1\}$, where N represents the total number of possible equally-spaced multipath components, including the first arriving component.

The time-varying baseband impulse response of a multipath channel illustrated in Figure 3-6 can be expressed as:

$$\tilde{h}_b(\tau, t) = \sum_{i=0}^{N-1} a_i(\tau, t) \exp[j(2\pi f_c \tau_i(t) + \varphi_i(\tau, t))] \delta(\tau - \tau_i(t)) \quad (\text{Eq. 3.7})$$

where $a_i(\tau, t)$ and $\tau_i(t)$ are the real amplitudes and excess delays, respectively, of the i th multipath component at time t . The phase term $2\pi f_c \tau_i(t) + \varphi_i(\tau, t)$ in the above equation represents the phase shift due to free space propagation of the i th multipath component, plus any additional phase shifts which are encountered in the channel.

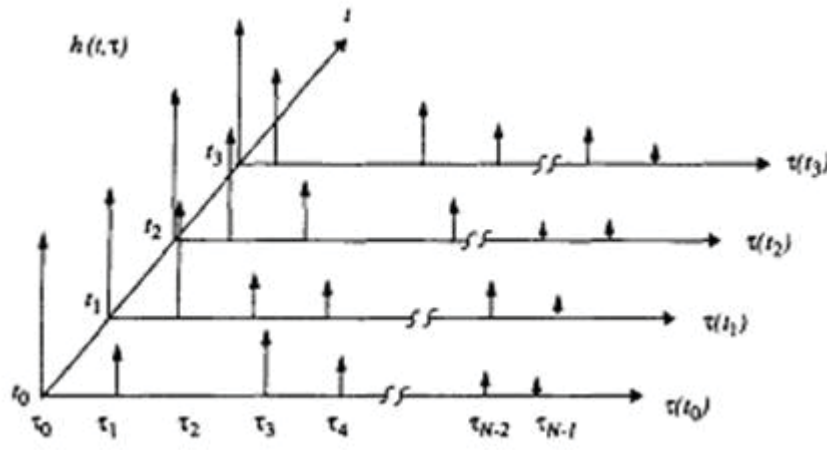


Figure 3-6 : Example of a time-varying channel impulse response [1].

3.1.3.4 PDP (power delay profile)

The power delay profile is a function of time delay, which gives the signal power received through a multipath channel as a function of time delay. It is obtained by taking the spatial average of $|\tilde{h}(\tau, t)|^2$ over a local area. By making several local area measurements of $|\tilde{h}(\tau, t)|^2$ in different locations, it is possible to build an ensemble of power delay profiles, each one representing a possible small-scale multipath channel state.

$$P(\tau) = \langle |\tilde{h}(\tau, t)|^2 \rangle = \left\langle \left| \sum_i^N a_i(t) \delta(\tau - \tau_i(t)) \right|^2 \right\rangle \quad (\text{Eq. 3.8})$$

where $|\tilde{h}(\tau, t)|^2$ is the square modulus of the time-varying channel impulse response and $\langle \rangle$ stands for spatial averaging.

Several small scale multipath channel parameters such as mean excess delay, RMS delay spread, and excess delay spread which define the channels' time dispersive properties can be obtained from the power delay profile.

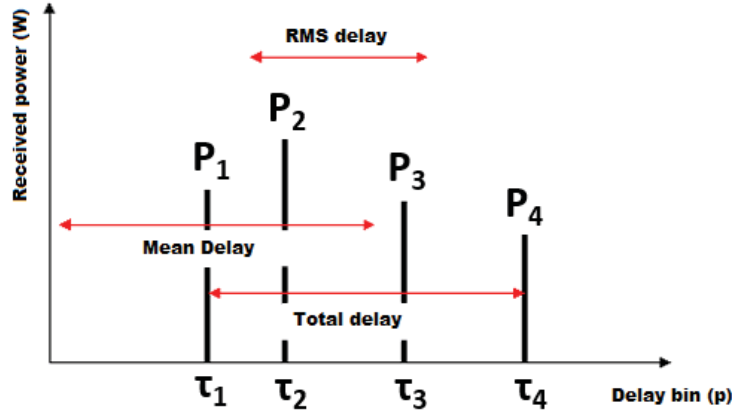


Figure 3-7 : Power delay profile of a single snapshot

3.1.3.5 Time-dispersive characteristics

Root mean square delay spread (RMS-ds)

The root mean square delay spread (RMS-ds) quantifies the time dispersive character of the propagation channel. As the name suggests, the RMS-ds (σ_τ) is defined as the square root of the second central moment of the PDP:

$$\sigma_\tau = \sqrt{\frac{\sum_{p=0}^{P-1} P_p \tau_p^2}{\sum_{p=0}^{P-1} P_p} - (\bar{\tau})^2} \quad (\text{Eq. 3.9})$$

with P_p ($p \in \{0, \dots, P-1\}$) the average power at each discretized delay bin, τ_p , and $\bar{\tau}$ the mean excess delay or the first moment of the PDP, defined as:

$$\bar{\tau} = \frac{\sum_{p=0}^{P-1} P_p \tau_p}{\sum_{p=0}^{P-1} P_p} \quad (\text{Eq. 3.10})$$

Maximum excess delay

The maximum excess delay is defined as the time delay between the first and the last received multipath component. The signal strength of the last multipath component must be higher than a certain threshold, differentiating it from the thermal noise.

Coherence time and coherence bandwidth

Coherence time is a statistical measure of the time duration over which the channel impulse response is almost invariant. When channel has a long coherence time, it is said to be slow faded. Essentially it is the minimum time duration over which two received signals are affected differently.

The RMS-ds is analogous to another parameter defined in the frequency domain, the coherence bandwidth (Bc). Coherence bandwidth is a statistical parameter that characterizes the frequency domain channel response, and indicates the range of frequencies over which two frequency components have a strong potential for amplitude correlation. Although an exact analytical relationship between the RMS-ds and the coherence bandwidth does not exist, they are inversely proportional to one another.

3.1.3.6 Doppler spectrum

The frequency domain dual of the PDP is the Doppler power spectrum. The latter provides information about the spectral broadening produced by the different Doppler shifts of the multipath components. Techniques for spectral estimation can be divided into non-parametric and parametric methods. Among different methods for estimating the Doppler power spectrum based on measurements results, the simplest are the periodogram method and the Welch's method [8]. They are both common non-parametric estimators. We briefly describe these methods hereafter.

An estimate of the power spectrum by using the periodogram method is obtained by simply performing the discrete-time Fourier transform of the measured samples, and appropriately scaling the magnitude square of the result:

$$\hat{S}_p(k) = \frac{1}{N} \sum_n^{N-1} \left| h_p[n] \exp\left(\frac{-j2\pi nk}{N}\right) \right|^2 \quad (\text{Eq. 3.11})$$

where \hat{S}_p is the Doppler spectrum for each simulated delay bin, p. The inverse of the sampling time is given by k and h_p represents the channel impulse response corresponding to delay bin p. Finally, N gives the total number of sample.

The Welch method is a refined version of the periodogram estimator and was developed and presented for signal analysis in 1967 [9]. It globally takes a signal, divides it into segments and performs a FFT on each block. Eventually, an averaging is done over all modified periodogram estimates. The Welch estimation method uses a hamming windowing technique to emphasize the information in the center of the segment to the detriment of the edges. The Doppler spectrum of the simulated channel paths computed with Welch method is given by:

$$\hat{S}_p^w(k) = \frac{1}{M} \sum_{m=1}^M \left(\frac{1}{N_s} \sum_n^{N_s-1} \left| h_p[n + (m-1) * N_s] \exp\left(\frac{-j2\pi(n + (m-1) * N_s)k}{N_s}\right) \right|^2 \right) \quad (\text{Eq. 3.12})$$

Where M is the number of segments and N_s the different number of sample in each segment.

3.1.4 Specificity of vehicular channels

In order to have robust tools to evaluate V2X communications performance and to bring future enhancements to V2X systems, a sound knowledge of vehicular propagation channel is needed. In the past, much effort has been focused on cellular channel between a static base-station and a mobile receiver. However, vehicular channels differ from traditional cellular communication channel in many ways [10]. These differences can be summed up as follows:

- Height level between the transmitter and receiver

On the opposite of cellular channel where the Tx (usually a static base station) is relatively much higher than the Rx, in V2X communications both the Tx and the Rx are normally at about the same height and in similar environment. This implies differences in the main propagation mechanisms of multipath components. For example, in a V2V propagation environment, scattering occurs both around the Tx and the Rx while in cellular communication the area around the base station is usually free of scatterers. This can lead to a significant difference in the angles of arrival (AoA) or angles of departure (AoD) distribution of the propagating waves between the two categories of channel.

- Mobility of the channel

Typical vehicular channel environments exhibit high mobility as both the Tx and Rx are dynamic as well as a significant number of mobile reflectors and/or scatterers. On the other hand, in a cellular channel, either the Tx or the Rx is static. Also, moving scatterers in the environment have small impacts on the channel characteristics. Channel fluctuations are much more important in V2X channels and hence suffer from more severe fading effect than the classic cellular channels [10], [11]. Moreover, in vehicular channels the probability of link obstructions increases due to the movement of interacting objects and the use of relatively low-height antenna. Given the dynamic nature of the V2V physical environment, the channel may be statistically non-stationary [12], [13], [14] and therefore traditional wide-sense stationary uncorrelated scattering (WSSUS) [15] channel models may not be applicable even for short duration. Non-stationarity is maybe the most important specificity that differentiates a vehicular channel to a conventional cellular one. The region where the channel may be considered non-stationary can be modelled by a birth/death process to account for the appearance and disappearance of taps [16]. Nevertheless, this method to overcome non-stationarity issues does not account for the “drift” of scatterers into different delay bin and can also produce sudden appearance and disappearance of strong multipath components.

- Frequency of communication

As compared to cellular channels with main operating frequencies between 700 MHz and 2100 MHz, the 5.9 GHz central carrier frequency dedicated to V2X communication systems can be considered to be relatively high. Hence, V2X transmitted signals bear higher attenuation and specific propagation mechanisms such as diffraction are less efficient.

Given all these specificities of vehicular channels, it is of utmost importance to study and characterize their behavior in terms of fading statistics since the channel properties have large impacts on of the quality service of the communication system.

3.1.5 Typical V2X environments

The propagation channel characteristics of V2V channels will differ according to the surrounding environment in which the communication takes place. The most common encountered scenarios for V2X communications are [10]:

- Rural environments

In a rural environment, we have typically a single lane in each direction with few or no buildings. Usually, in rural scenario, vegetation could act as some scatterers but the main propagation mechanisms remain LOS and diffraction due to terrain changes. Traffic density is normally light and average velocities range from 16 m/s to 20 m/s.

- Highway environments

Highways tend to have two to four lanes in each direction usually with guardrails and middle wall separating the direction of travel. The traffic density can be high during peak hours. The average velocity ranges from 30 m/s to 35 m/s. There is a higher number of scatterers in a highway environment as compared to rural areas.

- Urban environments

Urban areas are characterized by wider streets with the presence of tall buildings alongside the roads. There is a dense traffic in urban environment and velocities are limited to 13 m/s in such scenarios. An urban channel bears strong multipath due to the high buildings and billboards. These walls generate rich reflections.

Although the classification of different traffic environments is somehow arbitrary as there exists sometimes large variations in the properties of the above described scenarios all around the world, the channel characteristics of these typical V2X environments are often distinct and distinguishable from each other.

3.1.6 V2X channel sounding or channel measurements

All propagation channel models, hypothetically, are built upon wireless channel measurement results. For example, the model parameters of stochastic channel models are derived from extensive measurement campaigns. Furthermore, ray-tracing models need to be confronted against results extracted from measurement data. Recent wireless applications such as V2X communications systems require channel sounders to be able to capture the fast time-varying, wideband and double-directional propagation channel.

3.1.6.1 Channel sounding techniques

The measurement setup used to characterize the transfer function of a wireless channel, be it in the time-domain or frequency domain, is referred to as a channel sounder. The latter can be classified as narrowband measurement or wideband measurement. Narrowband channel sounders can be used to characterize a channel by its path loss, Doppler shift and fading statistics (small- and large-scale fading). Measurements using narrow-band measurement systems can be performed using a sine wave generator together with vector signal/network analyzer [17], [18] or spectrum analyzer [19]. Since the channel response is measured at a single carrier frequency, the time resolution of a narrowband channel sounder is infinity, meaning that it is impossible to characterize the time-selectivity of wideband channels. Therefore, to obtain time-variant channel impulse responses and other parameters derived from it, such as delay spread or excess delay, wideband measurement campaigns are required. The most common wideband channel sounding technique in the time-domain consists of transmitting a pseudo-noise (PN) sequence and estimating the channel impulse response as a result of a cross-correlation between the received signal and the transmitted PN sequence. This technique is often referred as the correlative channel sounding. The latter has been widely used for wideband vehicular channel measurements. The time resolution of a correlative channel sounder and the maximum resolvable delay are related to the chip duration and the length of the PN sequence respectively. A different wideband sounding principle is multitone sounding, which is based on sounding signals similar to those of OFDM systems [20]. Sounding with multitone signals requires more complicated equipment, but provides channel characterization that is of equal quality in all parts of the considered bandwidth, while PN based sounding is less accurate near the band edges [21]. Another popular channel sounding technique by means of vector network analyzers (VNAs), usually used for the measurement of impulse responses in indoor environments, is not feasible for vehicular channels as the coherence time is smaller than the acquisition time of the VNA. VNA based channel measurement setups can in principle cover any bandwidth (mostly limited by the antenna bandwidth), but since the frequency points are measured sequentially over a long time span, the method is limited to time invariant channels. Another drawback of this technique is in its limitation of the separation distance of the transmitter and the receiver as both ends need to be connected to the VNA through cables.

3.1.6.2 Vehicular channel measurement results

In the subsection, we will make a survey of measuring campaigns that have been carried out around the 5 GHz frequency band in typical V2V environments. This work will act as a database for later comparisons with results obtained from simulated propagation channel models. In a first place, a focus will be made principally on narrowband channel characteristics. Basically, we will see

how path loss parameters are extracted from measurement campaigns. Results pertaining to Doppler spectrum and delay spreads will be given after.

Large-scale measurement results

Path loss is one of the most important parameters used when estimating a link budget. V2V path loss models differ from classic fixed to mobile path loss models. Many research works suggest that dual-slope path loss models fit the measured data obtained in V2V propagation environments with much more accuracy than single-slope models. A dual-slope model is characterized by a path loss exponent γ_1 and a standard deviation σ_1 within a certain distance from the emitter, known as critical distance (d_c) or breakpoint and a path loss exponent γ_2 and a standard deviation σ_2 at a distance greater than d_c . Based on this model, the path loss (in dB scale) can be estimated as:

$$PL(d) = \begin{cases} PL(d_0) + 10\gamma_1 \log\left(\frac{d}{d_0}\right), & d_0 \leq d \leq d_c \\ PL(d_0) + 10\gamma_1 \log\left(\frac{d_c}{d_0}\right) + 10\gamma_2 \log\left(\frac{d}{d_0}\right), & d > d_c \end{cases} \quad (\text{Eq. 3.13})$$

where d is the distance between the transmitter and receiver, $PL(d_0)$ is the average path loss for a reference distance d_0 .

In 1991, Green and Hata [22] estimated the critical distance as $d_c = \frac{2\pi \times h_T \times h_R}{\lambda_c}$ where h_T and h_R are the height of the transmitting and receiving antennas respectively. λ_c represents the wavelength at the carrier frequency f_c . Yet, in [23] Xia et al. proposed a critical distance of $d_c = \frac{4 \times h_T \times h_R}{\lambda_c}$ which seemed to be more efficient in vehicular channel. However, it was noticed that the critical distance is in fact related to the propagation characteristics of the environment and may bear important differences according to the considered scenario: rural, highway or urban. So, the breakpoint or critical distance is an adjustable parameter based on observations. A summary of the values of the different parameters for single-slope and dual-slope models for V2X channels are presented in Table 3-2 for various propagation environments.

In [28] path loss characterization for V2I communications at 5.9 GHz were carried out in urban areas for different height of antennas. In this particular measuring campaigns, authors obtained path loss exponents ranging from 1.79 to 3.71. Besides, authors in [29] gave radio propagation parameters for dual path loss model in V2V urban scenarios for line of sight and obstructed line of sight (OLOS).

Table 3-2 : Path loss model (single and dual slope) parameters for typical V2X environments

Typical environment	Path loss model parameters
Rural/suburban	$\gamma = 1.59$ $\sigma = 2.1$ dB [24]
	$\gamma = 1.79$ $\sigma = 3.3$ dB [25]
	$\gamma = 1.53$ $\sigma = 3.5$ dB [27]
	$\gamma_1 = 2.3$ $\sigma_1 = 3.2$ dB $\gamma_2 = 4$ $\sigma_2 = 0.4$ dB $d_c = 226$ m [26]
Highway	$\gamma = 1.77$ $\sigma = 3.1$ dB [24]
	$\gamma = 1.85$ $\sigma = 3.2$ dB [25]
	$\gamma = 1.77$ $\sigma = 2.8$ dB [27]
	$\gamma_1 = 1.9$ $\sigma_1 = 2.5$ dB $\gamma_2 = 4$ $\sigma_2 = 0.9$ dB $d_c = 220$ m [26]
	$\gamma_1 = 2.0$ $\sigma_1 = 5.9$ dB $\gamma_2 = 4$ $\sigma_2 = 6.6$ dB $d_c = 220$ m [30]
Urban	$\gamma = 1.68$ $\sigma = 1.7$ dB [24]
	$\gamma = 1.61$ $\sigma = 3.4$ dB [25]
	$\gamma = 1.68$ $\sigma = 3.2$ dB [27]
	$\gamma = 1.79 - 3.7$ [28]
	LOS : $\gamma_1 = 1.84$ $\sigma_1 = 4.15$ dB $\gamma_2 = 2.85$ $\sigma_2 = 4.15$ dB $d_c = 165$ m [29]
	OLOS : $\gamma_1 = 1.53$ $\sigma_1 = 6.67$ dB $\gamma_2 = 2.74$ $\sigma_2 = 6.67$ dB $d_c = 165$ m [29]

Divergence between results illustrates that the path loss parameters are strongly dependent on the propagation environment, the measurement techniques used, the physical characteristics of vehicles and the antenna heights.

Small-scale measurement results

V2V propagation channels display higher Doppler spreads compared to the traditional cellular radio channels, due to the high relative velocities between the TX and RX vehicles and due to the presence of moving scatterers (or multiple reflective objects). Moreover, due to the non-uniformity of AoA distribution of multipath components, the Power Doppler Spectrum of V2V channels can differ from classical bathtub spectrum. Doppler spread values between 100–300Hz have been reported in [25], [19] for highway and in [31] for urban environment. Tan et al. [31] presented Doppler values close to 1000Hz for highway environments. In [25], Kunisch et al. noticed large variations in the Doppler spread during measurement campaigns not only due to the high mobility of the transmitter and receiver but also the mobile scattering environment which changes rapidly. Scenario in which the transmitting and receiving vehicles were driving in the same direction showed lower RMS Doppler spread than measurements carried out in oncoming driving scenarios, i.e., vehicles travelling in the opposite directions. Doppler shift rising up to 1107 Hz were reported in [33] where measurements were carried out in an oncoming highway scenario in Lund, Sweden.

Statistics pertaining to time dispersive characteristics such as RMS delay spread and maximum excess delay have been extracted from numerous measurement campaigns. In [16] authors put forward the results of RMS delay spread in different regions. In the urban scenario, the mean RMS delay spread ranges from 126 ns to 236 ns with a maximum reaching 1330 ns. In highway scenario with light traffic density they obtained a mean RMS-ds of 53 ns while this channel characteristics raised to 127 ns when traffic was denser. Measurement campaigns were performed in Helsinki by authors in [34]. The mean RMS delay spread extracted from measured data were 165 ns for highway environment and 373 ns in urban configurations. Paier et al. [33] obtained a mean RMS-ds of 242 ns for a highway scenario. In rural environment, the lowest delay spread of 20-60 ns were observed [31], [25]. In the light of all results obtained from the literature regarding RMS delay spreads, we can infer that the smallest delay value is observed in rural environments and the largest values in urban environments [35]. Table 3-3 below, given in [10], presents a summary of the time dispersive character of typical V2V propagation scenarios in terms of 10%, 90% and the mean RMS delay of results observed from the several measurement campaigns carried out.

Table 3-3 : Summary of RMS-ds results extracted from different measurement campaigns.

RMS-ds (ns)	Rural	Highway	Urban
10th percentile	20 [32]	30 [34]	30 [34]
Mean RMS-ds	22 [31]-52 [25]	41 [25] – 247 [33]	47 [25]-373 [34]
90th percentile	150 [32]	340 [33]	1100 [34]

3.1.7 Channel modelling

In order to evaluate wireless system performance by simulation and to analyze the impact of antennas and to improve physical layer processing algorithms of receiver, the wireless propagation channel model is required. Channel modelling always implies a trade-off between accuracy and simplicity of use. The most encountered techniques to model V2V communications' propagation channels are: deterministic, stochastic and geometry-based stochastic channel methods.

3.1.7.1 Deterministic channel (Ray-tracing)

Deterministic approaches such as ray-tracing methods describe site-specific realistic simulations. These approaches provide meaningful interpretation of the channel if accurate parameters such as dimensions and electromagnetic properties of multipath contributors present in the scenario are included. Wiesbeck et al. were pioneer for ray tracing for V2X systems [19], [36], [37], with Virtual Drive simulation tool.

Another commercial software, WinProp [39], was developed in parallel by AWE communications (refer to Appendix B). The computation of interaction losses along each ray is based on the Fresnel coefficients for reflection and transmission, and on the Uniform Geometrical Theory of Diffraction (UTD) for diffraction. The algorithm supports an arbitrary number of reflections, diffractions and transmissions/penetrations for each ray path, but in practice only two reflections, one diffraction and zero transmission are considered (more interactions did not show to considerably improve the computation accuracy). Scattering on rough surfaces is also included in the model. Scattering objects are divided into small triangles, and each triangle is modelled as a Lambertian source [40].

Ray tracing has also been used to investigate the effects of different antenna positions on the vehicles [38]. Furthermore, for the prediction of the radio channel at an arbitrary crossroad scenario, researchers of TU Braunschweig have developed a ray-optical channel model especially designed for vehicular communications in the 5.9 GHz frequency band [35]. Such a deterministic model easily allows investigating any desired scenario without a need to carry out expensive and complex measurements. In [41], [42] the contributors compared important channel metrics, namely channel gains and PDPs, to that obtained from both channel sounder measurements and the simulation results using the same ray-optical channel model developed in TU Braunschweig. They found good accuracy of the channel model as far as the present physical phenomena of wave propagation are captured by their implemented algorithms.

Although they offer the most accurate simulation, their applications are limited as they are numerically too intensive to process even though real efforts are made to speed up the computation using parallel programming and GPU computing.

3.1.7.2 Stochastic channel models

Stochastic approaches, like Tapped-Delay Lines (TDL), consist in modelling channels according to some of their parameters like delay, Doppler frequency, and angular spread. Each tap is described by those aforementioned parameters based on the wide-sense stationary uncorrelated scattering (WSSUS) assumption [15]. The channel impulse response is obtained by means of a finite impulse response filter with a discrete number of taps.

The parameters of the TDL channel model are described in a stochastic manner. Acosta-Marum and Ingram [44], provided empirical models for vehicular communications for three V2V models and another three for V2I communications. Depending on the fading distributions of the taps (or delay bin), the channel amplitudes would be modelled with either Rician distribution in case of strong LOS component or Rayleigh in NLOS situation. The models have been derived from channel measurements at 5.9 GHz in different environments (expressway, urban canyon and suburban streets).

In Sen & Matolak [16] propose stochastic models based on the TDL technique in five propagation environments: UIC – Urban Antenna Inside Car, UOC – Urban Antenna Outside Car, SC – Small City, OHT – Open-Area High Traffic Density, OLT – Open-Area Low Traffic Density. These models introduce the Weibull distribution to model the amplitude of taps variations. The main drawback of V2V stochastic models based on the TDL representation is the non-stationary behavior of the vehicular channel. To overcome this problem, the authors have proposed a birth/death (on/off) process to consider the non-stationarity persistence using a two-state first-order Markov chain.

Their low computational complexity and high flexibility make them attractive. However, V2V channels are widely-known to have a non-stationary behavior [45] and hence the WSSUS assumption no longer stands. Therefore, TDL models are not totally adequate to reproduce V2V channel models.

3.1.7.3 Geometry-based stochastic channel

The GBSCM method [49] is a combination of both the deterministic and stochastic approaches. In this method, scatterers are placed randomly (according to suitable statistical distribution) around the transmitter and receiver. Scatterers in GBSCM are often represented by simple geometric shapes with uniform materials. Then, simplified ray-tracing is performed to evaluate the corresponding channel impulse response. This approach is numerically cheaper than purely deterministic method and enables to intrinsically model the non-stationary behaviour as it includes the dynamic nature of the environment. Taking into account its numerous advantages, many researchers focused their attention on the GBSCM as an approach to simulate V2X propagation channels. Some of these models can be classified in regular-shaped GBSCM, where the scatterers are placed on regular shapes like ellipses [50], or a two-ring configuration [51]. A series of papers by Zajic et. al [52], [53] proposed a 3D model based on placement of scatterers on a two cylindrical-shaped pattern. On the other hand, irregular-shaped GBSCM tends to reproduce the physical reality of the simulated configuration by a more realistic placement of the scatterers. A good example of an irregular-shaped GBSCM approach can be found in [49] and is adapted in [54] and [55], where a highway environment was modelled. Three types of scatterers were distinguished representing mobile discrete (transmitter, receiver and other vehicles), static discrete (road signs, etc) and diffuse scatterers respectively. The channel impulse response, obtained after simplified ray-tracing is divided into four parts: 1) the LOS component, 2) discrete components stemming from reflections off mobile scatterers, 3) discrete components stemming from reflections off static scatterers and 4) diffuse components. Thus, this model requires signal model parameters that the authors extracted from measured data. Although this model is useful and accurate, it remains quite complex and requires much effort to set up.

3.1.8 Conclusions

In the first part of chapter 3, a succinct description of wireless propagation channel is given. The main propagation mechanisms occurring when an electromagnetic wave travels from the transmitter to the receiver were defined and illustrated. Propagation channel characteristics such as path loss, delay spread, Doppler spread and angular spread are environment-dependent, i.e., they pertain to certain range of values that are intrinsic to particular situation or scenario. Afterwards, focus was driven to V2X channel communications and it was found that they could be categorized into three main types of environment: rural, highway and urban.

Furthermore, the concept of channel modelling and its approaches were described and emphasis was placed on their corresponding advantages and drawbacks. Gathering experience from previous research works available in the literature, it is not easy to say if there is a modelling method which outstands the other techniques. The choice of the appropriate approach depends on the requirements of the application and the ease of implementation of each method. For instance, pure stochastic model using classical tapped-delay-lines technique is simple to set up and can be implemented onto standard RF channel emulator to test V2X receivers. However, this model does neither take into account the non-stationary behavior of vehicular channels nor includes any information about the distribution of the angles of arrivals on the receiving antenna. Particularly, the angular spread can prove to be an important factor and therefore a mandatory parameter when dealing with antenna integration in the propagation channel models.

Deterministic channel modelling may offer the most accurate simulation results if all the electromagnetic properties are available and all the obstacles in the propagating environment are properly designed. The accuracy of the results will also depend on the liability of the software tool in its capacity to predict and compute all rays arriving at the receiver. To sum up, deterministic modelling method can prove to be a good solution if ray-tracing algorithms in the software tool are correctly executed and if effective parallel processing techniques are implemented to reduce computational time.

Nowadays, many researchers are steering toward GBSCM methods to model V2X communication propagation channels. It has the advantage of being flexible and considers intrinsically the non-stationarity of this type of environment. This approach can be seen as a combination of both deterministic and stochastic model method to enhance the efficiency of V2X system communication modelling.

The objective of this thesis work is to adopt an approach that can help us to create, in a flexible and efficient way, propagation scenarios in which we can easily integrate the properties of antennas. Therefore, we need a modeling technique that produce channels that are distinguishable, in terms of their intrinsic characteristics, from each other and hence can be employed to test the performance of several antennas in each of them. Taking into account all the aims and constraints of this work, the choice of a GBSCM approach is almost imperative.

Rather than emulating a specific propagation channel with parameters extracted from costly measurement campaigns, we aim at a direct and simple approach to emulate characteristics of different families of propagation channel pertaining to the V2V context. However, it remains to show that such a model can serve to construct channels that are as diverse as the three typical V2V environments suggested earlier. Therefore, we propose in next section, a GBSCM method using a ray tracing technique to emulate channel responses that are distinguishable from each other and can be associated to rural, highway and urban environment.

3.2 CHANNEL MODELLING METHOD ADOPTED

In this chapter, we introduce a new geometry-based stochastic channel method to get typical channel responses of various propagation channels through a standard electromagnetic simulator. Our aim is to simulate virtual driving scenarios that can be distinguished in terms of their channel properties such as RMS delay spread, angles of arrival and Doppler spectrum. The main contributions of our proposed method are the following:

- Only a unique type of scatterers is used in our model.
- A generic physical setting is developed and the number and position of scatterers can be easily (though empirically) adjusted in order to obtain channel impulse responses pertaining to different V2V environments.
- Random positioning of scatterers according to suitable statistical distributions within correct intervals ensures that the channel response falls in some prescribed propagation channel category.
- An analytical model is therefore introduced to reach a satisfying distribution of scatterers in a much faster way, thus preselecting configurations pertaining to channel parameters such as those from measured experiments available in the open literature or other sources.
- A set of random realizations of dynamic scenarios is performed to ensure that the parameters of the channel response remain within the range of models known from literature or acquired from experiments.
- Models are developed with a well-known and liable EM simulator. The facility and accuracy for the integration of realistic antenna pattern also motivated the use of this software. That will further enable virtual testing of antenna performance analysis according to their type and placement within the car body (see chapter IV).

Through dynamic scenarios, such simulations could directly provide different channel responses that may be incorporated in a complete V2V communication simulation tool including antenna integration and the physical layer modelling of modems.

3.2.1 Principle of the GBSCM method in FEKO

In this section, our proposed method will be elaborated. In a first place, we will describe the type of scatterers used in our simulated configurations and then we will present the generic setting set in place to create our virtual driving scenarios. Afterwards, we will focus on how the generation of time-sequences of our simulated configurations are produced and how channel responses and power-delay profiles are constructed from the time-varying simulations. Finally, we will describe the extraction of different channel parameters.

3.2.1.1 Description of the scatterers in the simulation

In our proposed GBSCM method, we wish to simulate dynamic scenarios representing two vehicles in motion. The main idea is to use simple perfect electric conducting (PEC) plates as simple scatterers to emulate essential characteristics defining a V2V propagation channel. It should be noted that we do not have the claim to match exactly the statistics of our simulated propagation channels with those obtained from measuring campaigns but wish only to establish a sufficient resemblance. Moreover, we limited ourselves at producing scenarios that are distinguishable from each other. This is the main reason why we used simple metallic plates as scatterers, which have no intention to represent any physical object in particular.

For V2X systems operating at frequencies around 5.9 GHz, the wavelength is about 5 cm. The chosen dimensions of the 2D scatterers are 1.5m x 2m and are thus large compared to the wavelength at the central frequency of 5.9 GHz dedicated to V2V communications. A preliminary parametric study was carried out to evaluate the precision of high frequency asymptotic method as compared to rigorous simulation method. Simple configurations were simulated using the size of the scatterers as parametric variable to compare the received power using the Uniform Theory of Diffraction and the power obtained using the Multi-Level Fast Multipole Method (MLFMM). In Figure 3-8, an example of a simulated configuration to test the precision of the high-frequency approximation method is given.

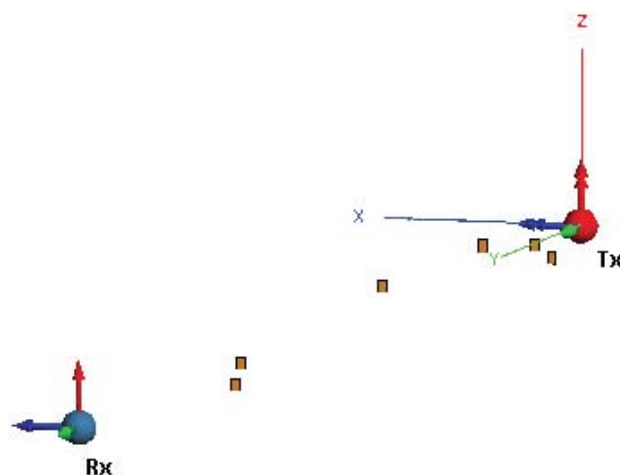


Figure 3-8 : Simulated configuration to test the precision of the UTD module

Table 3-4 and Table 3-5 resume two random sets of simulations results. Here, we compare the received power across a perfect matched antenna for the two different methods when the size of the scatterers are made to vary. The relative error, clearly suggests us that the precision of the UTD method reaches an acceptable criterion when the size of the scatterers are about 30λ to 40λ .

Table 3-4 : First set of simulation results of the parametric study to test the precision of the UTD module.

Size in wavelength	Power received in Watt		Relative error
	MLFMM	UTD	
$3.75 \lambda \times 5 \lambda$	4.3548E-10	3.5782E-09	7.2
$7.5 \lambda \times 10 \lambda$	5.8217E-10	4.0413E-09	5.9
$15 \lambda \times 20 \lambda$	5.3518E-10	1.9360E-09	2.6
$30 \lambda \times 40 \lambda$	5.1016E-10	6.0438E-10	0.16

Table 3-5 Second set of simulation results of the parametric study to test the precision of the UTD module.

Size in wavelength	Power received in Watt		Relative error
	MLFMM	UTD	
$3.75 \lambda \times 5 \lambda$	4.3011E-10	5.4629E-09	11.7
$7.5 \lambda \times 10 \lambda$	5.6359E-10	3.6612E-09	5.5
$15 \lambda \times 20 \lambda$	5.4801E-10	1.5797E-09	1.9
$30 \lambda \times 40 \lambda$	2.8373E-10	1.9148E-10	0.3

The method being based on a unique type of scatterer, the only variables that are made to change from one configuration to another are the number of metallic plates and their probabilistic locations with respect to the antennas. In the next section, a complete description of the generic setting of our configurations is given.

3.2.1.2 Description of the generic setting

Outline of the general representation of the simulated configuration

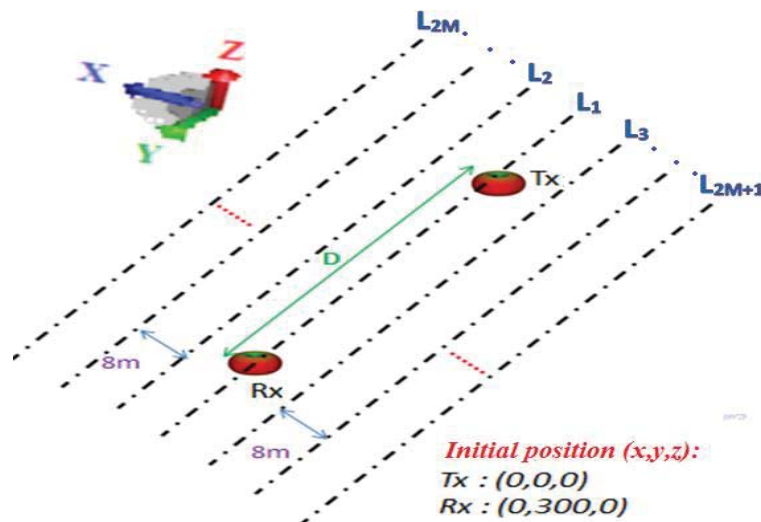


Figure 3-9 : Diagram outlining the general representation of the simulated configurations

Figure 3-9 shows a general representation of the simulated environment. In the Cartesian coordinate system (O,x,y,z) the transmitter T_x , located at the origin and the receiver $R_x(0, y=D, 0)$, represented by their respective radiation patterns, are separated by a distance D of typically 300 m. The scatterers are distributed along $2M+1$ lines $L_1, L_2, \dots, L_{2M+1}$ spaced 8m from each other. The number of lines $2M+1$ is adjusted according to different scenarios. The total number N of scatterers is divided in two sub-parts, N_{IN} those lying between the antennas (T_x and R_x) and N_{OUT} those lying before the T_x ($y < 0$) and beyond the R_x ($y > 300$). N_{OUT} scatterers have a clustering effect of producing multipath components with higher delays. Regarding the high number of scatterers in our simulation, we opt for an automatic and randomized positioning. The y -coordinates of the scatterers are drawn from a discrete uniform distribution within specific bounds for each configuration. Thus, each scatterer is randomly placed according to some constraints pertaining to its position. If those constraints are well adapted it can be proved that the propagation channel characteristics are held within some prescribed values. Due to the random positioning of the scatterers, a need for numerous realizations of each configuration is necessary in order to verify the repeatability of our results.

Transmitter and Receiver representation

The vehicles (both transmitting and receiving) are virtually represented by the radiation pattern of an antenna. In our simulations, they are represented by the radiation pattern of a perfect dipole. The isotropy in the azimuthal plane was the reason why we opt for a simple dipole in a first place to characterize each of our simulated propagation channel.

3.2.1.3 Ray-tracing using the UTD module in FEKO

The complete geometry of each configuration is written in the EDITFEKO files format (*.pre) via a Matlab program. The transmitted antenna is represented as an impressed source. The input format is a (*.ffe) file in which the antenna radiation pattern is described in spherical coordinates (θ , φ) with its phase located at the origin of the local coordinates imposed by the user. The two most important parameters of the ray-tracing module is the number of interactions to be considered and the type of interactions to be taken into account. The maximum number of interaction gives the maximal number of physical propagating phenomena a particular ray is subjected to before arriving at the receiving point. For example, the parameter is set to 2, a ray can have 2 reflections, or 1 reflection and a diffraction. If set to 0, only direct rays are taken into account. We have set this parameter to 3, which represents a very good trade-off between the computation time and the accuracy of the obtained results.

The following type of ray interaction is available in the UTD module:

- GO (direct and reflected rays, shadowing): Direct, reflected rays, and shadow regions are taken into account.
- Edge and wedge diffracted rays: Diffraction on edges and wedges are taken into account. The ray may include an arbitrary number of reflections, but only one diffraction.
- Corner diffraction terms: It takes into account corner diffractions
- Double diffractions and diffraction/reflection: Double diffraction on edges and wedges, and combinations of reflections are taken into account.
- Cone tip diffraction: Tip diffractions at the tip of a cone are taken into account.

The receiving antenna is defined as an ideal one that is decoupled from the model and should ideally be in the far field of radiating structures (so that incident plane wave approximations are applicable). In chapter 4, we will investigate the influence of the presence of obstacles in the near-field region of the antenna. Furthermore, FEKO computes the power received by this ideal antenna assuming a perfect match, i.e. conjugate complex load. The relative phase of the received signal is also printed to the *.out file, which indicates the relative phase of either the voltage or the current through the termination impedance (which is an ideal conjugate complex load).

3.2.1.4 Generation of time-sequences

Once our generic setting corresponding to a particular configuration is designed, ray-tracing is performed by a specific module of the electromagnetic simulator FEKO, based on the Uniform Theory of Diffraction (UTD). However, FEKO is not designed to simulate time-variant scenarios. Therefore, to obtain a time-sequence, successive static scenes called snapshots must be created to simulate a dynamic scenario.

In each snapshot, the positions of the transmitter (Tx) and the receiver (Rx) change while in the first place the scatterers positioned in configuration remains static. The new positions of both Tx and Rx are calculated as a function of their corresponding speed and the sampling time between consecutive snapshots. The sampling time in our simulations was chosen so that the maximum resolvable Doppler shift satisfies the following criteria:

$$T_{\text{samp}} \leq 2 \cdot \text{Max. resolvable Doppler shift.}$$

From measurement campaign in the literature [33], the maximum shift measured in an environment with the highest mobility was 1107 Hz measured in a highway scenario in Helsinki. So, a sampling time of 400 μs was considered in our work. It corresponds to a resolvable bandwidth of $1/T_{\text{samp}} = 2500$ Hz, leading to a maximum resolvable Doppler shift of 1250 Hz.

Example of a highway configuration

For highway configuration, a speed of 30 m/s was assigned to both vehicles. The change in position of the Tx and Rx corresponds to a distance travelled of 0.0120 m from one snapshot to the other. Therefore, to have a tolerable time sequence duration we opted for 1000 snapshots for each configuration leading to a total distance travelled of 12 m in a highway situation. The generation of the 1000 successive static configurations is automated with a Matlab program, which writes directly the position of the scatterers as well as the modified position of the Tx and Rx in the FEKO simulation file. (*.pre files). The simulation parameters are given in Table 3-6.

Table 3-6 : Simulation parameters of a highway configuration

Tsamp (μs)	Average vehicle speed (m/s)	No. of files for one time sequence	Time sequence duration (s)	Average distance travelled by the vehicles (m)
400	30	1000	0.4	12

Simulations in FEKO are performed in the frequency domain. A continuous wave with power of 1 W is transmitted at the frequency f_0 , and after post-treatment, we extract the received power and the phase at this same frequency from the "*.out" file. However, for V2X communications, we are dealing with a wideband channel. Considering the control channel (CCH), the channel response must be evaluated over the 10 MHz bandwidth. In the following subsection a description of the method used to simulate the propagation channel models over the whole bandwidth is given before presenting the channel impulse response (CIR) computation method. All simulations are based on the modelled scenario previously described in this section.

3.2.2 CIR and PDP construction and extraction of different parameters

3.2.2.1 Channel response

As seen in previous chapters, V2X communication systems are based on an IEEE 802.11p OFDM physical layer. FEKO simulations are performed for the 64 subcarrier frequencies, equally spaced over the 10 MHz bandwidth around 5.9 GHz, of the 802.11p OFDM signal. The IEEE 802.11p standard specifies the arrangement of the given 64 subcarriers of the OFDM signal as shown in Figure 3-10. 52 subcarriers are useful subcarriers (data + pilot) which are assigned numbers from -26 to 26. The pilot signals are embedded into the subcarriers of -21, -7, 7 and 21 as shown in Figure 2. The rest of subcarriers are null carrier which are allocated in the beginning (0) and middle (27 to 37) of the band to eliminate the effect of null carriers in the data subcarriers.

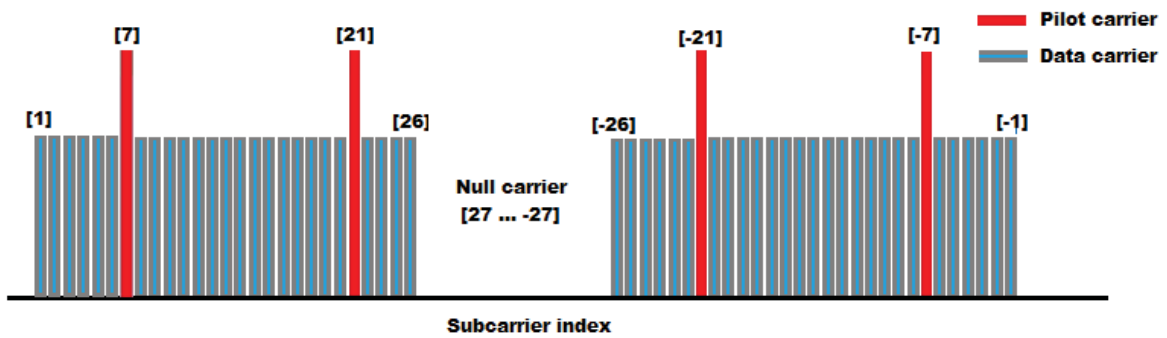


Figure 3-10 : Frequency domain representation of an OFDM signal

So a snapshot of a propagation channel configuration in FEKO is simulated over the 64 subcarriers covering the 10 MHz bandwidth around the central frequency of 5.9 GHz.

$$f_i = 5.895 \times 10^9 + \frac{\Delta f}{2} + (i + 32) \bmod 64 \cdot \Delta f, i \in \{0, \dots, N - 1\} \quad (\text{Eq. 3.14})$$

where Δf represents the subcarrier frequency spacing given by, $\Delta f = 10 \text{ MHz}/64 = 0.15625 \text{ MHz}$. The index i corresponds to the IFFT input represented in with $i=0$ on the central frequency (Figure 3-11).

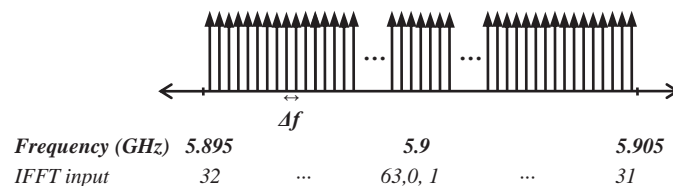


Figure 3-11 : $N=64$ simulation frequencies.

The power received at each frequency, $PR_i, i \in \{0, \dots, (N-1)\}$ thus obtained for one snapshot is plotted in Figure 3-12.

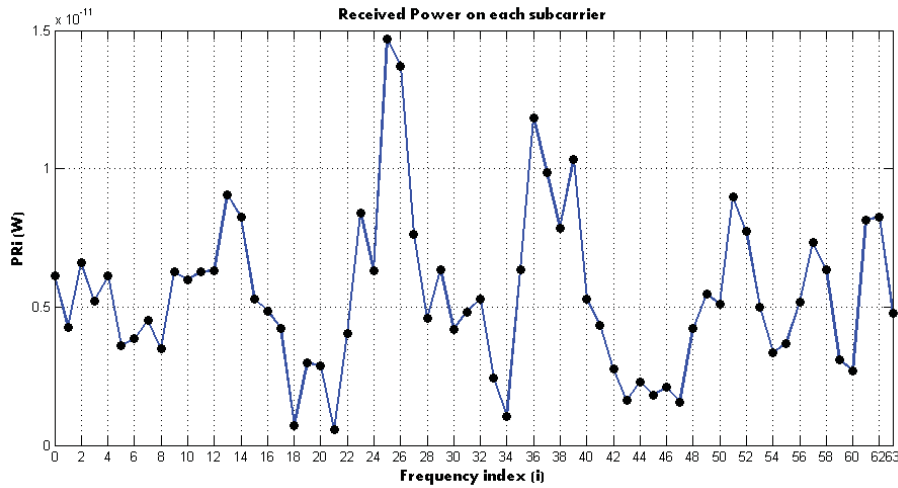


Figure 3-12 : Power received on each subcarrier frequency (example).

Therefore the impulse response is calculated from the discrete inverse Fourier transform of the frequency response.

$$\tilde{h}(t, \tau_p) = \frac{1}{\sqrt{N}} \sum_{i=0}^{N-1} PR_i \exp\left(\frac{j2\pi ip}{N}\right), \quad p \in \{0, \dots, N - 1\}$$

In section 3.1.3, we stated that it is useful to discretize the multipath delay axis τ of the impulse response into equal time delay segments called delay bins. Here, p represents the delay bin, and the time duration between two delay bins is given as one over the total channel bandwidth of the communication ($T_s = 1/10 \text{ MHz} = 100 \text{ ns}$). The time-domain representation after IFFT is displayed in Figure 3-13, as a function of the delay bin (p).

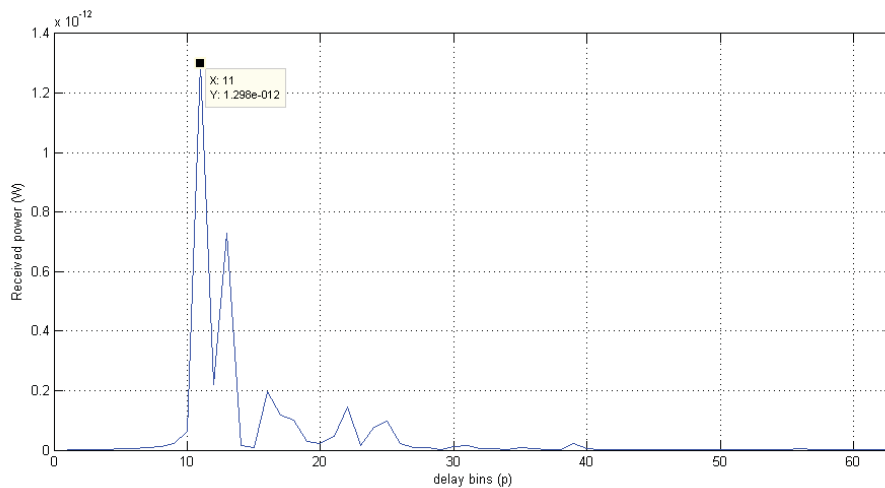


Figure 3-13 : The channel response in time domain against the delay bins (example).

3.2.2.2 Power delay profile

The power delay profile (PDP) is calculated as the squared amplitude of the channel response and is hence represented by $|\tilde{h}(t, \tau_p)|^2$. The Power delay profile of a snapshot of a particular simulated highway configuration is given in Figure 3-14. The maximum resolvable delay obtained in time domain, is equal to one over the frequency spacing, i.e. $1/\Delta f = 6.4 \mu s$.

Figure 3-14 illustrates an example of the variation of the PDP as a function of time, given 1000 simulated snapshots over 12 meters for the same highway configuration.

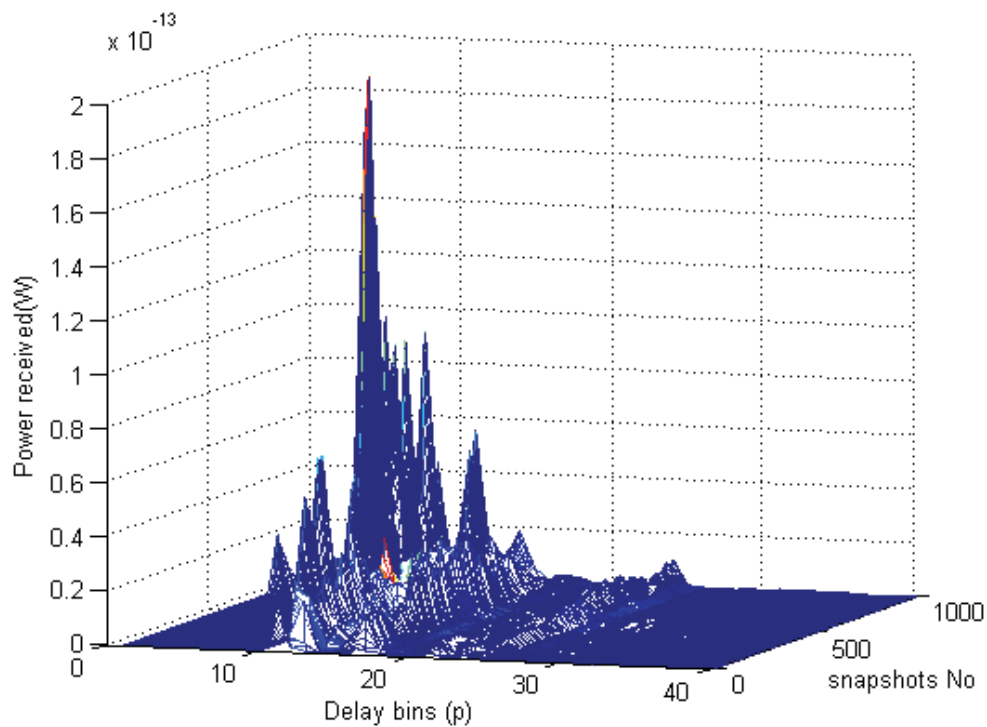


Figure 3-14 : PDP of a simulated highway configuration.

3.2.3 Extraction of channel parameters

Our goal is to simulate virtual driving scenarios based on different GSBCM configurations that can be distinguished in terms of their channel properties such as RMS delay, angles of arrival and Doppler spectrum. So, in this section we will describe how each of these parameters was extracted from post-processing of the simulated results obtained from FEKO.

3.2.3.1 RMS delay spread

To calculate the time dispersive character of the propagation channel, only the part of the channel response in time domain after the delay bin corresponding to the first multipath component arriving on the receiving antenna is taken into account. Let us consider the case where the first signal impinging on the receiver arrived in the d^{th} delay bin. In such case the PDP is given as:

$$|\tilde{h}(t, \tau_p)|^2 \text{ where } p \in \{d, \dots, N - d\} \text{ and } N \text{ is the total number of subcarriers}$$

Keeping up with the previous example where the first signal arrived in the 11th delay bin, the PDP used to extract the time dispersive characteristics is presented in Figure 3-15. The latter simply represents the result of a time-shift. Of course, the total power received remains unchanged, since there is no energy received prior to the 11th delay bin. We chose, by convention, to describe the time delay domain independently of the Tx-Rx distance.

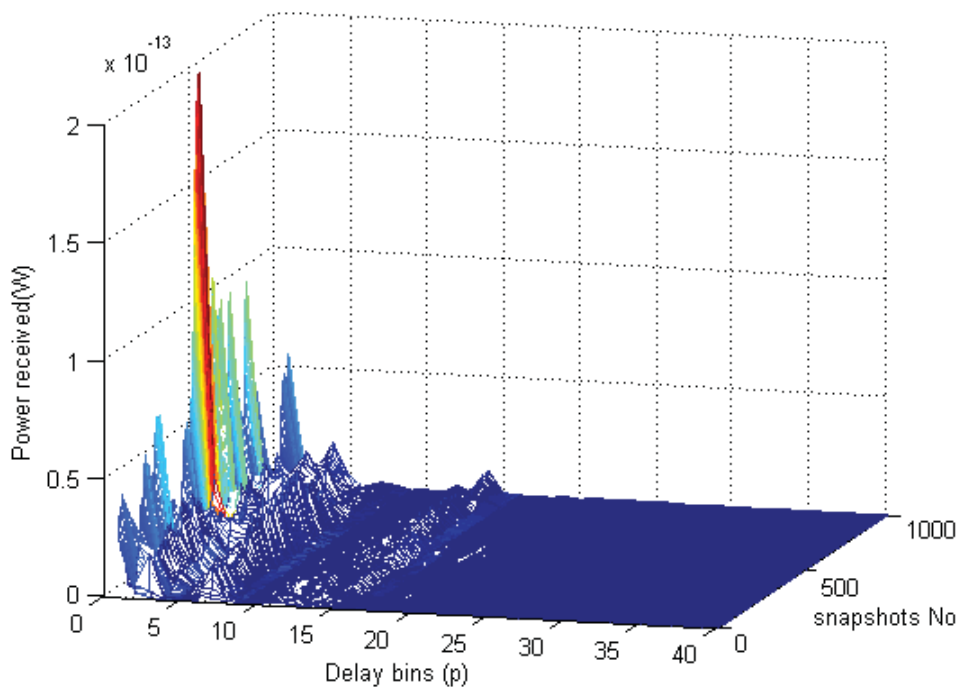


Figure 3-15: PDP after the elimination of delay bins prior to the first arriving component.

So, for all configuration the RMS-ds is evaluated for every snapshot. Therefore for every simulated scenario an empirical cumulative density function (cdf) or probability density function of the time-varying RMS-ds is given.

3.2.3.2 Angular spread

In V2V communications, scatterers found in the environment are about at the same height as the antennas resulting in multipath components arriving mainly in the azimuthal plane. Thus, the angular spread in the elevation plane is neglected.

The angles of arrival (AOA) on the receiver are calculated by geometric reconstruction of each ray. In the UTD module in FEKO an additional output file having a (*.dbg) extension can be requested. This optional file contains a large amount of additional data concerning the modeled geometry. Furthermore, detailed information of each propagating ray is included in this file. The electric field components E_x , E_y , and E_z at every interacting points are provided for every single ray path. A high number of reflecting or diffracting scatterers in the modeled geometry can make the file to become very large.

Figure 3-16 represents a snapshot of a simulated rural configuration with some ray-tracing. It is important to take into consideration the angular orientation of the simulated scenario. According to our chosen coordinate system, a path from the transmitter with a line of sight (LOS) will arrive with an angle of 270° on the receiver.

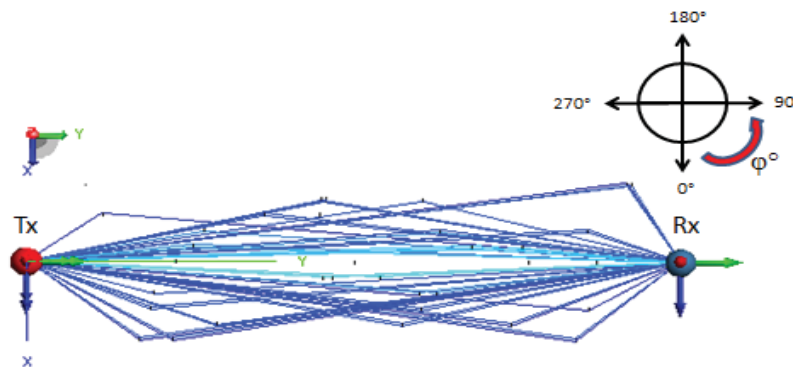


Figure 3-16 : Angular orientation of the Rx with respect to the Tx

We evaluate the probability of occurrence, with an angle step of 5° , for each simulated configurations over the whole time-sequence duration (1000 snapshots).

3.2.3.3 Doppler spectrum

Delay-Doppler spectrum

We are in a dynamic context when we consider V2V communications. So, it is deemed judicious, if not mandatory, to characterize the associate Doppler spectrum. In this sub-section, we will calculate the delay-Doppler spectrum to model the spectral broadening produced by the different Doppler shifts of the multipath components for our simulated configurations. The periodogram method [9] is used to estimate the delay-Doppler spectrum. The latter is obtained by performing the discrete-time Fourier transform of the respective simulated channel impulse responses and scaling the magnitude of the square of the result:

$$S_p(k) = \frac{1}{\sqrt{N_{sample}}} \left| \sum_{n=0}^{N_{sample}-1} \tilde{h}(\tau_p)[n] \exp\left(\frac{-j2\pi nk}{N_{sample}}\right) \right|^2 \quad (\text{Eq. 3.15})$$

where k is the inverse of the sampling time. $\tilde{h}(\tau_p)$ is the impulse response in the delay bin p . In our simulations, delay bins correspond to time-intervals of 100 ns in the delay domain. We also took a sampling time (T_{samp}) of 400 μs leading a resolvable bandwidth of $1/T_{\text{samp}} = 2500$ Hz. S_p is the Doppler spread associated to the delay bin p . Therefore, with our periodogram method, we have a Doppler spectrum for set of paths regrouped in each delay bin.

Doppler shifts

It can be noted that the Doppler shift for a path arriving from the T_x impacting the scatterer P, with an angle φ_{T_x} and arriving on the R_x with an angle of φ_{R_x} is given by:

$$v(\varphi_{T_x}, \varphi_{R_x}) = \frac{1}{\lambda} [(V_{T_x} - V_P) \cos \varphi_{T_x} + (V_{R_x} - V_P) \cos \varphi_{R_x}] \quad (\text{Eq. 3.16})$$

where λ is the wavelength, V_{T_x} , V_P and V_{R_x} the respective speed of the transmitter T_x , the scatterer P and the receiver R_x . Finally, φ_{T_x} and φ_{R_x} are the angle of departure and arrival respectively.

3.3 CHANNEL RESPONSES FROM ARRANGEMENT OF LOCATION AND NUMBERS OF SURROUNDING SIMPLE SCATTERERS

Now that all techniques of channel characteristics extraction have been presented, we will put forward the choice of the distribution of scatterers in our model in order to mimic characteristics of driving scenarios pertaining to common V2V environments. The aim of the next sections is to introduce three geometric configurations which differ from each other in terms of number and placement of simple scatterers around the transmitter T_x and receiver R_x . These configurations will be simulated with the prospect to represent three distinct scenarios (rural, highway and urban) in terms of their channel properties. We used an empirical method to select the appropriate number and location of scatterers following some basic rules to create poor or rich multipath environment or to modify angular spread of incoming waves on the R_x .

The empirical adjustment of scatterers in the scene around the T_x and the R_x can be, however, time consuming since it is based on a trial and error process associated with a series of multiple bounces ray-tracing calculations. An analytical model is therefore introduced to reach a satisfying distribution of scatterers in a much faster way. In subsection 3.3.1, a description of the analytical model, based on the Uniform Theory of Diffraction is given. The basic modelling of diffractive interactions is recalled in a first place.

3.3.1 Analytical model to study the distribution of the scattering elements

This analytical method aims at defining the number and convenient distribution of scatterers in our generic physical setting based on the targeted RMS delay and angular spread. It would of course be an initial step towards a rough estimation of these parameters. Preselected configurations would then be simulated in electromagnetic simulator FEKO using the Uniform Theory of Diffraction module as ray-tracing method (see section 3.4). Our simplified analytical propagation model is thus based on a one-interaction UTD method. Moreover, paths that could normally be masked by other diffracting plates are not cancelled out. Three types of propagation phenomena were considered: Edge\Wedge diffractions, corner diffractions and reflection in case of line-of-sight configurations.

3.3.1.1 Implementation of the analytical model

The generic setting previously introduced was implemented in Matlab. The scatterers, of the same unique type as considered in subsection 3.2.1.1, are placed according to our empirical method to define suitable distributions of these diffractive elements around the transmitting and receiving antennas to emulate channel responses corresponding to those obtained from channel sounding measurement campaigns available in the literature. All scatterers are rectangular PEC plates. The analytical tool was developed to carry out a simple one-bounce ray-tracing without taking into consideration visibility or masking effects. The complex electric-field strength is calculated at the receiving end and is used to build a channel impulse response based on the delays caused by excess propagating distance of each ray.

3.3.1.2 Quick glance on UTD theory

In 1962, Keller proposed a method for calculating electromagnetic field diffraction in approximation, known as the geometrical theory of diffraction (GTD) [6]. GTD can calculate diffraction around obstacles in the total field using the diffraction theory. We refer to the situation depicted in Figure 3.3 (section 3.1.2.2). The total field, received from the transmitter, includes the incident ray field, the composition of all possible reflection ray and diffraction field from top of the obstacle. However, GTD exhibits a singular behavior at the ray-shadow boundary, both at the Incident Shadow Boundary (ISB) and Reflected Shadow Boundary (RSB) as shown in Figure 3-3. In 1970, diffracted field expression is derived by P.H. Pathak and R.G. Kouyoumjian, they improved Keller's geometrical theory of diffraction of the field to overcome the singularity and discontinuity at shadow boundaries, and introduced the uniform geometrical theory of diffraction (UTD). In the following section, we will show how the continuity is ensured throughout the optical boundaries. UTD and its modifications [7] eliminate this inaccuracy and enable to compute diffracted field on a dielectric as well as perfectly conducting wedge. Capability of computing both field magnitude and phase makes this approach suitable for use in area where multipath occurs.

Our analytical model takes into account rays that undergo reflection upon hitting the center of the scatterer, diffraction from both horizontal and vertical edge and diffraction from the four corners of each of the rectangular corners. The received field from each interactive point will be governed by the propagation mechanism it underwent.

- **For an incident ray in case of Line of sight**

$$E_{rec} = E_0 \cdot \exp^{-jkd} \cdot \frac{1}{d}, \quad (\text{Eq. 3.17})$$

Where, E_{rec} is the received electric-field strength and E_0 is the transmitted electric-field strength. k represents the free-space wavenumber while d gives the separation distance between the transmitter and receiver.

- **In case of reflection**

$$E_{rec} = E_0 \cdot R \cdot \exp^{-jkd_r} \cdot \frac{1}{d_r}, \quad (\text{Eq. 3.18})$$

Where E_{rec} is the received electric-field strength, E_0 is the transmitted electric-field strength and k the free-space wavenumber. d_r is the total distance between the Tx and the scatterer and from scatterer to the Rx. R represents the Fresnel reflection coefficient.

- **For edge/wedge diffraction**

Two cases are to be distinguished. The received E-field depends on its polarization, either perpendicular or parallel to the plane of incidence of the incoming ray.

$$E_{rec} \frac{\perp}{\parallel} = E_0 \cdot \exp^{-jks'} \cdot \frac{1}{s'} \cdot D \frac{\perp}{\parallel} \cdot \sqrt{\frac{s'}{s(s'+s)}} \cdot \exp^{-jks} \quad (\text{Eq. 3.19})$$

where, E_{rec} is the received electric-field strength,

- E_0 is the transmitted electric-field strength,
- k is the free-space wavenumber,
- s' is the path length from the Tx to the point of diffraction,
- s is the path length from the point of diffraction to the Rx,
- D_{\parallel}^{\perp} is an angle and polarization-dependent diffraction coefficient

The expression of the UTD perfectly electrically conducting edge/wedge diffraction coefficient, D_{\parallel}^{\perp} developed by [7] is given as :

$$D_{\parallel}^{\perp} = \frac{-\exp^{-j\frac{\pi}{4}}}{2n\sqrt{2\pi k}} \times \left\{ \begin{array}{l} \cot\left(\frac{\pi + (\phi - \phi')}{2n}\right) \times F(kLa^+(\phi - \phi')) \\ + \cot\left(\frac{\pi - (\phi - \phi')}{2n}\right) \times F(kLa^-(\phi - \phi')) \\ \mp \cot\left(\frac{\pi + (\phi + \phi')}{2n}\right) \times F(kLa^+(\phi + \phi')) \\ \mp \cot\left(\frac{\pi - (\phi + \phi')}{2n}\right) \times F(kLa^-(\phi + \phi')) \end{array} \right\} \quad (\text{Eq. 3.20})$$

$$L = \begin{cases} \frac{s's}{s' + s} & \text{for spherical waves} \\ s & \text{for plane waves} \end{cases} \quad (\text{Eq. 3.21})$$

$$a^{\pm}(\chi) = 2 \cos^2\left(\frac{2n\pi N^{\pm} - \chi}{2}\right) \text{ where } \chi = \phi \pm \phi' \quad (\text{Eq. 3.22})$$

N^{\pm} is the smallest integer that satisfies the following equation:

- $2\pi n N^+ - \chi = \pi$ (Eq. 3.23)
- $2\pi n N^- - \chi = \pi$

$$F(X) = \sqrt{X} \exp^{jX} \int_{\sqrt{X}}^{\infty} \exp^{-ju^2} du \quad (\text{Eq. 3.24})$$

ϕ' and ϕ are the angle of incidence and the angle of diffraction respectively. They are clearly represented in Figure 3-17. The wedge angle, β , is described by $n = 2 - \left(\frac{\beta}{\pi}\right)$ where β is the angle between the 0th-face and nth-face of the diffracting object. Thus for a right-angled wedge, $\beta = \frac{\pi}{2}$ and therefore $n = 1.5$. In our case, for $n=2$ as all the scatterers are metallic plates for which $\beta = 0$.

The transition function $F(X)$ cancels the singularity of the cotangent functions and thus is used to correct Keller's non-uniformity at ISB and RSB. Outside the Geometrical Optics shadow-boundary transition regions, the $F(X)$ function becomes unity, and the UTD result reduces automatically to the GTD.

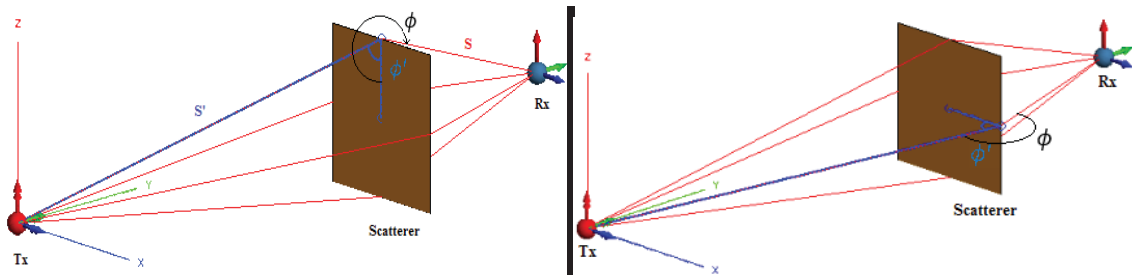


Figure 3-17 Horizontal and vertical edge diffraction in UTD module of FEKO

As it can be seen the diffraction is given for both parallel and perpendicular polarizations. Thus, the diffracted electric field impacted on a scatterer will be geometry-dependent as whether the edge containing the point of interaction is perpendicular or parallel to the polarization of the impacting wave.

Corner diffraction

It is important to consider corner diffraction in UTD applications as all diffracting structures are in practice of finite-length. A corner is formed when a finite edge is truncated. In this situation, the fields diffracted by an edge abruptly fade at the corner. The diffraction coefficient for an edge is no longer valid since it lies on the hypothesis of its infinite length. A UTD corner-diffraction coefficient must be, therefore, figured out to compensate for this edge-diffraction discontinuity and evaluate the corner-diffracted fields. In [56] Sikta and Burnside respectively developed a heuristic corner diffraction coefficient. One major flaw in the coefficient, revealed by [57], is that it does not show unicity for certain backscatter angles near normal incidence. However, Sikta and Burnside's coefficient of corner diffraction is successful for many plate geometries and may be used with caution.

$$E_{rec} \frac{\perp}{\parallel} = E_0 \cdot \exp^{-jks'} \cdot \frac{1}{s'} \cdot \frac{j}{8\pi k \cos \beta} \cdot \sqrt{\frac{s'}{s(s'+s)}} \cdot \exp^{-jks} \times \left\{ \left| F \left(\frac{1}{2\pi \cos^2 \beta} \right) \right| \mp \frac{1}{\cos \Psi} \left| F \left(\frac{\cos^2 \Psi}{2\pi \cos^2 \beta} \right) \right| \right\} \quad (\text{Eq. 3.25})$$

The total diffracted field from a corner consists of terms for each of the adjoining edges. Therefore, eight terms are needed for the rectangular plate. β is the angle between the incident ray and the tangent to the edge and ψ is the angle of diffraction. Figure 3-18 brings clarity regarding the geometric representation of the angles.

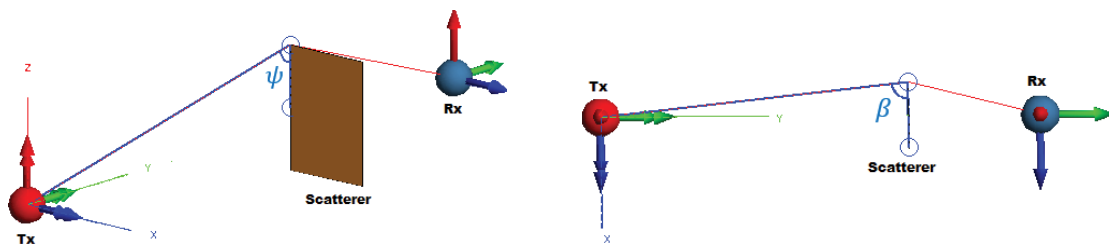


Figure 3-18: Corner diffraction in UTD module of FEKO

3.3.1.3 Conclusion

The UTD perfectly electrically conducting edge/wedge diffraction coefficient from [8] was used to calculate the electric-field strength of the contributions of each scatterers. Moreover, corner diffractions were calculated using the heuristic corner diffraction coefficient developed by Sikta and Burnside in [56]. Therefore, each scatterer present in the configuration comes up with at least 16 interactions (8 from edges and 8 from corners). The electric field strength of reflected rays from our PEC scatterers placed within the $T_x - R_x$ axis in case of LOS were calculated using the reflection coefficient of -1. Each interacting point is easily obtained since scatterers are simple rectangular PEC plates. Hence, path lengths from T_x to scatterers and from scatterers to R_x as well as corresponding angles of incidence and diffracted angles are easily evaluated and substituted in each formulae. The complex electric field strength of each contributed ray is calculated as well as its associated path length. At the end, a power delay profile is obtained from which the RMS delay spread can be derived. Angular spread is calculated as the angle of arrival of every contribution on the R_x . All calculations are performed in terms of a few seconds to get a general trend of the channel parameters. This enables a quick pre-selection or the rejection of the GBSCM candidate model as shown in the next section 3.4.

3.4 DESCRIPTION OF THE DIFFERENT SIMULATED CONFIGURATIONS

In this section, the three simulated configurations retained to represent virtual driving scenarios in rural, highway and urban areas will be presented. As stated earlier, the analytical tool serves as a quick prediction to preselect configurations that are eligible to represent those typical environments at least with respect to channel characteristics such as RMS delay spread and the angular spread. Delay spread resulting from the analytical method are compared to those obtained from measurement campaigns available in the literature and listed in section 3.1.6.2. Furthermore, angle of arrival distribution is also studied and if the latter is proved meaningful to represent its corresponding scenario, only then the preselected setting would be designed and executed in a three-bounced ray-tracing in FEKO UTD module. Classical distributions of angle of arrival in V2X context are rather scarce in the literature. Therefore we chose to perform an indicative comparison with results from a narrowband deterministic commercial ray-tracing software (WinProp). AoA probability density functions are required to integrate different antenna patterns in our propagation channel models. Intuitively, we expect to obtain the highest angular spread in urban scenario followed by highway environment with rural areas having poor AoA distribution. These hypotheses make sense when comparing fixed to mobile communications in these same scenario. A brief description of Winprop software is presented in Appendix B together with the definition of each simulated scenario.

Following detailed description given in previous sections, channel responses both in frequency and time domain for each preselected configuration are evaluated. From these responses, the corresponding PDP is constructed from which the time-dispersive characteristics are extracted. These results were expected to remain within satisfactory bounds. From geometric reconstruction, the angular spread at the receiving end will also be calculated and be compared to previous results.

Figure 3-19 represents a block diagram that summarizes the engaged pathway to obtain virtual driving scenarios:

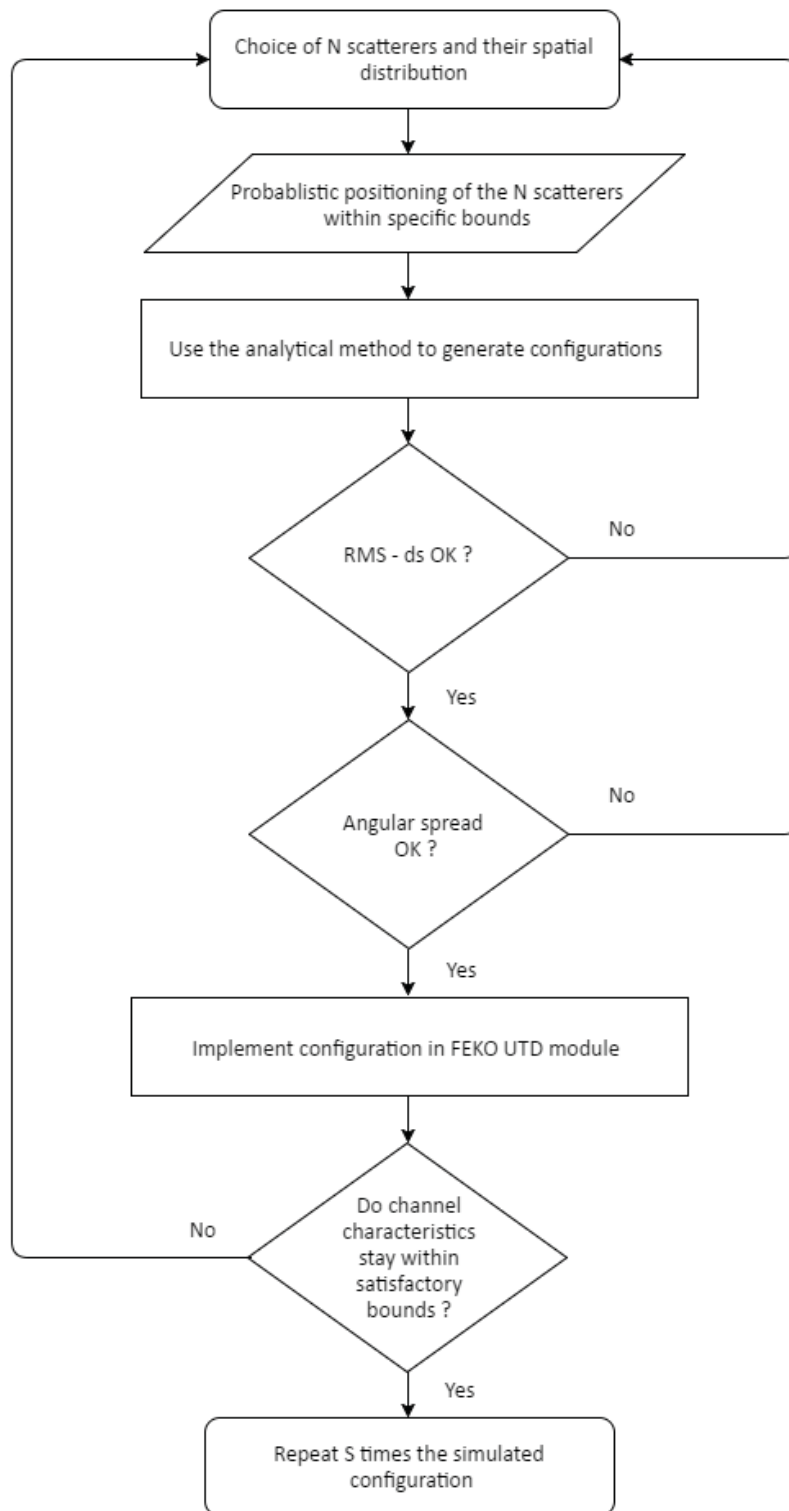


Figure 3-19 : Flow chart of the steps to obtain virtual driving scenarios.

3.4.1 Configuration for rural-like channel

The first configuration is destined to emulate a rural-like propagation channel. After a bunch of simulation with our analytical tool we came up with a physical setting representing an NLOS rural environment. In the next subsections, we will suggest the number and the laws of distribution of scatterers in this scenario.

3.4.1.1 Suggestion of the number and laws of distributions of the scatterers

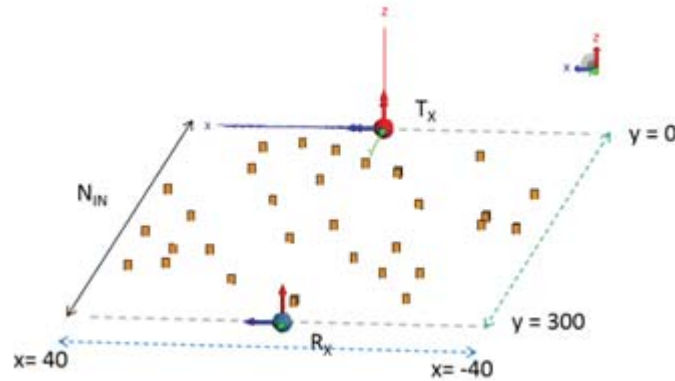


Figure 3-20: An example of a rural configuration simulated with FEKO

The first configuration was developed to reproduce the channel properties of a rural scenario. In this configuration, we locate 33 N_{IN} scatterers equally spread over 11 consecutive lines ($M=5$), each separated by a distance of 8 m. The y -coordinates of the location of the scatterers are drawn, with a uniform distribution, from the interval $y \sim [20, 280]$. As may be noticed from Figure 3-20, there are three scatterers in each lines between the transmitter and the receiver. We recall that in our suggested configuration, the T_x and R_x are made to move longitudinally without any lateral movement, i.e., the direction of motion is limited only in the y -axis. Here, scatterers are distributed in a transversal way without there being any N_{OUT} scatterers which leads to a low multipath contribution. The initial T_x - R_x separation is set at 300 m. The transmitter and receiver, representing the vehicles are assigned a speed of 19.4 m/s and both move in the positive y -direction. The parameters of the geometry of the scattering environment representing a rural area are given in Table 3-7.

Table 3-7 : Geometry parameters of a rural propagation channel

Total number of scatterers		33
Type of scatterers	N_{IN}	33
	N_{OUT}	0
Number of lines		11
Random distribution of scatterers	N_{IN}	$U [20 , 280]$ m

3.4.1.2 Analytical method and FEKO simulation results

In this subsection, the channel parameters obtained from our simulation methods are presented. The RMS delay spread and the angular spread for the emulated rural scenario retrieved from both the analytical and FEKO simulation models are compared to results obtained from measurement campaigns, available in the open literature. Moreover, the delay-Doppler spectrum, obtained from FEKO simulations, is also given.

RMS delay spread

The delay spread is calculated from the reconstructed PDP obtained from the dynamic scenario simulated in our analytical tool. Figure 3-21(a) represents the cumulative distribution of ten different realizations of the preselected configuration obtained analytically whereas Figure 3-21(b) illustrates the delay-spread of ten configurations simulated in FEKO. Several realizations of each configuration, containing random variables with their associated probabilistic distribution, must be simulated to verify the repeatability of our results.

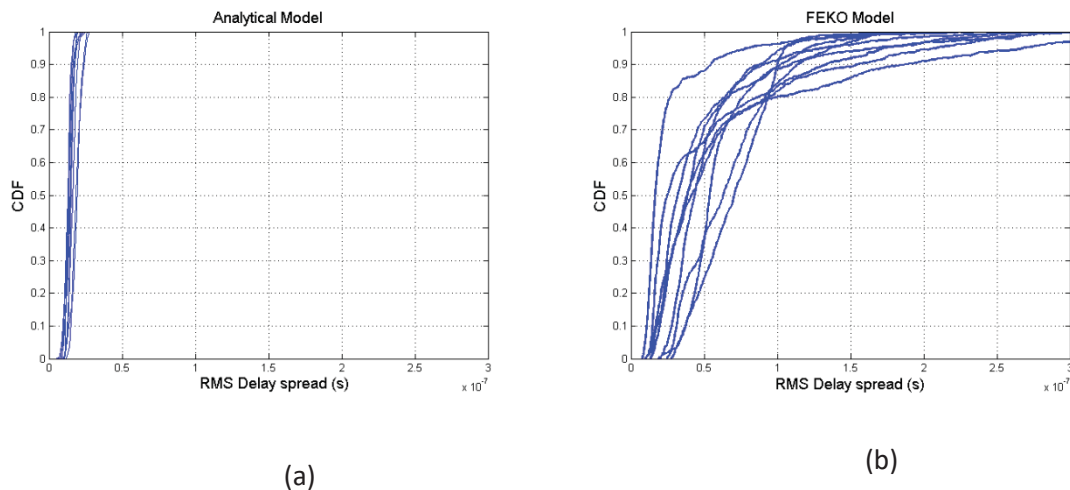


Figure 3-21: RMS delay spread distributions for rural configurations obtained with (a) Analytical method and (b) FEKO simulations

From those distribution curves we can derive the minimum and maximum values of the quantiles at 10% and 90% as well as the mean RMS-ds of this simulated setting. For the set of curves obtained from the analytical tool, the minimum quantile at 10% is 9 ns whereas its maximum is 15 ns. The quantile at 90% ranges from 15 ns to 25 ns while the values of mean RMS-ds are between 13 ns to 19 ns. These RMS-ds are slight underestimates of the delay spreads obtained from results of measurement campaigns carried out in rural areas with values ranging from 20 ns to 150 ns. In particular, higher value of RMS delay spread are less probable since the analytical model is a “one-interaction” model only.

The cumulative distributions of the RMS delay spread of ten different realizations of rural-like environment, from FEKO simulations, are extracted from their corresponding power-delay profiles and presented in Fig. 3-21(b). The minimum RMS-ds value at 10% quantile extracted from the cumulative curves in Figure 3 is 11 ns. The maximum value retrieved from the same set of curves at this quantile is 37 ns. The mean RMS-ds bears values from 26 ns to 87 ns. The quantile at 90% ranges from 55 ns to 187 ns. According to Table 3-3, we can notice that for rural environment, we have good concordance between results from our simulations, performed with the EM simulator,

and results from measuring campaigns carried out in such an environment. Let us take a look at the angular spread obtained from this configuration.

Angular spread

The angular spread is given as the distribution of the angles of arrival (AoA) at the receiver. The AoAs are obtained from geometric construction of each ray.

In the rural configuration, the absence of N_{OUT} scatterers leads to a low angular spread (see Figure 3-22(a)) which corresponds to a typical rural environment. For instance, in a rural scenario, there are few or no buildings. The main propagation mechanism in an NLOS rural scenario can be multiple reflections on the car body.

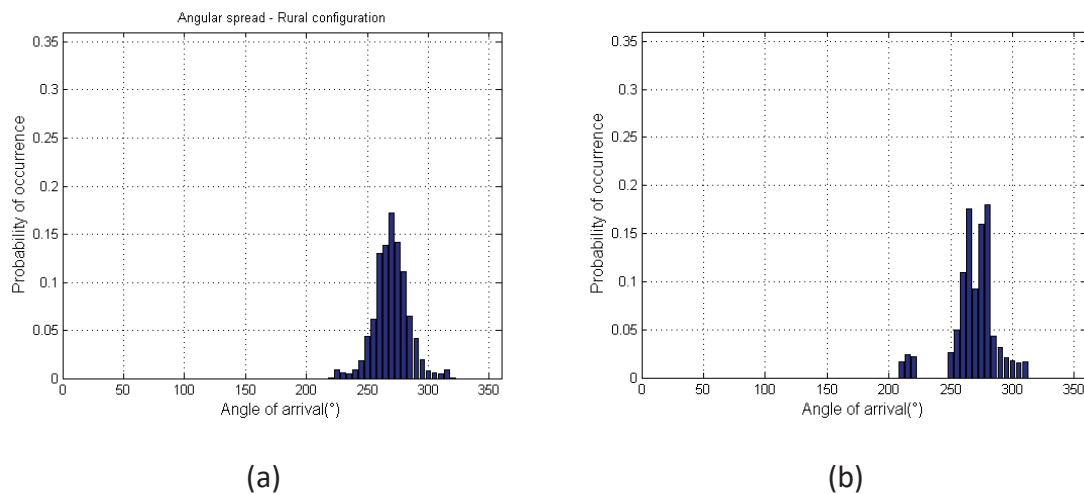


Figure 3-22: Angular spread distributions for rural configurations obtained with (a) Analytical method and (b) FEKO simulations

Due to scarcity of measurement campaigns that dealt with angular distribution in V2X context, we decided to compare to results obtained in a 3D deterministic narrowband ray-tracing simulator software (Winprop from AWE communications). For sake of brevity, those deterministic scenarios will not be presented here but are described in appendix B.

The angular spread from FEKO are obtained by the post-processing method described in section 3.2.3.2. We can see that the distribution of AoAs, presented in Figure 3-22 bears a fair resemblance with those earned from our analytical method and the narrowband deterministic ray-tracing tool commercialized from AWE communications.

Doppler spectrum

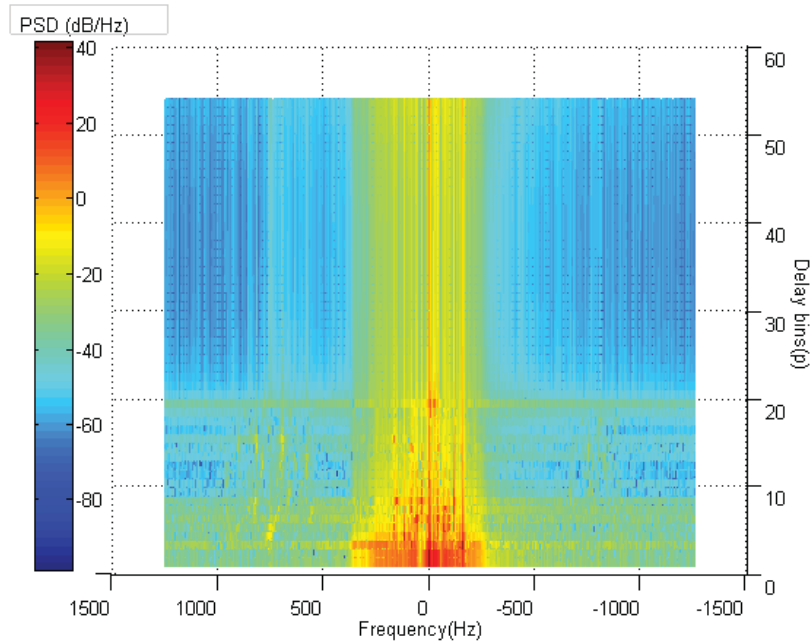


Figure 3-23 : Delay-Doppler spectrum for a rural configuration obtained from FEKO simulations

The delay-Doppler spectrum for the simulated rural propagation channel is depicted in Figure 3-23. In the rural scenario, both the T_x and the R_x move at a speed of 19.4 m/s while the speeds of scatterers are made to vary between [16.7-19.4] m/s. The scatterers placed in lines found to the left of the T_x - R_x axis (lines L_2 to L_{2M}) and those found in this axis itself (line L_1) move in the same direction as the T_x and the R_x . The others (lines L_3 to L_{2M+1}) go in the opposite direction. The first and strongest component arriving on the R_x will contribute to the Doppler shift associated with the relative velocity of the T_x and R_x . For simulated configurations, we notice a strong dominant frequency component that remains at the origin (0 Hz) as the T_x and the R_x are moving with the same speed.

Let us evaluate the maximum Doppler shift for a first order interaction that can occur in this scenario. To begin let us recall the Doppler shift formula given in Eq. 3.16. Given this equation and taking T_x and R_x moving in the same direction with a scatterer moving in the opposite direction with the lowest speed considered in the scenario. We make an assumption that the signal arrives with an angle close to zero, maximizing the cosine function. Thus the Doppler shift obtained for a first order interaction is 1.49 KHz. Eventually, having a sampling time of 400 μ s leads us to a maximum resolvable Doppler shift of 1250 Hz. This is the reason why we cannot display on our spectrum the maximum shift.

On the other way round, the first interaction maximum Doppler shift occurring when a ray scattered on a diffracting object having a velocity of 16.7 m/s moving in the same direction as the T_x - R_x system, the Doppler shift is 106 Hz. For a given 3rd order interaction, this Doppler shift can occur twice or thrice in the same scenario as the total Doppler shift is the sum of all Doppler shifts of each segment of that propagating ray.

Table 3-8: Geometry parameters of a highway propagation channel

Total number of scatterers		55
Type of scatterers	N_{IN}	33
	N_{OUT}	22
Number of lines		11
Random distribution of scatterers	N_{IN}	$U [20 , 280]$ m
	N_{OUT}	$U [-220 , -20]$ m
	N_{OUT}	$U [320 , 520]$ m

3.4.2.2 Analytical method and FEKO simulation results

RMS- delay spread

The time dispersive characteristics of the emulated highway configuration are evaluated in terms of RMS delay spread. The latter is calculated using the square root of the second central moment of the constructed PDP obtained from the dynamic scenario simulated in our analytical tool and FEKO model. Figure 3-25(a) represents the cumulative distribution of ten different realizations of the preselected configuration. A higher dispersion between the numerous realizations can be observed in this setting as compared to the rural one. This is eventually due to the higher number of scatterers in the scenario thus contributing to greater randomness in the positions of the diffracting obstacles.

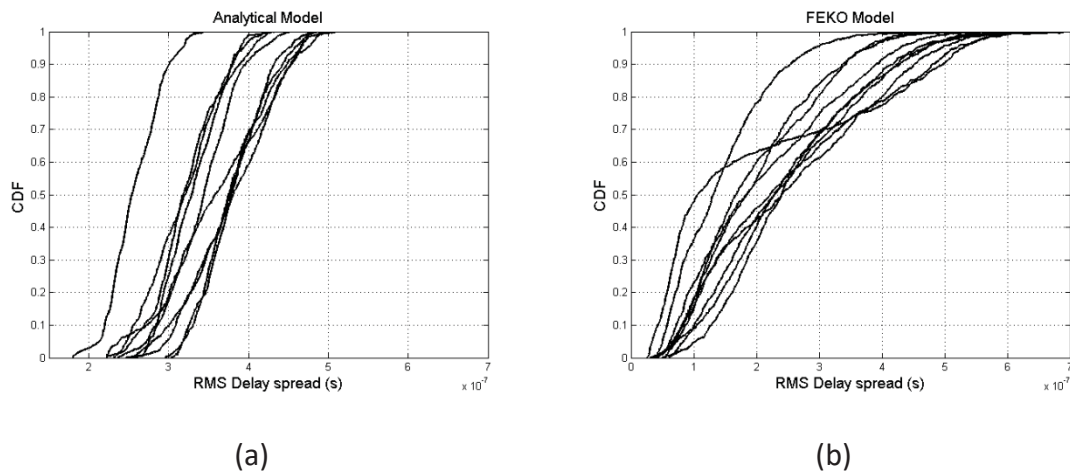


Figure 3-25: RMS delay spread distributions for highway configurations obtained with (a) Analytical method and (b) FEKO simulations.

From those cumulative distribution functions we extract the minimum and maximum values of the quantiles at 10% and 90% as well as the mean RMS-ds of this simulated setting. The minimum quantile at 10% is 220 ns whereas its maximum is 331 ns. The quantile at 90% ranges from 300 ns to 453 ns while the values of mean RMS-ds are between 258 ns to 379 ns. The mean RMS delay spread results of measurement campaigns undergone in different highway environments and

identified in the literature are 30-340 ns. Taking into account the fact that the sounded propagation channels are not the same and given the fact that repeatability of these campaigns are difficult to verify, we deemed that the time-dispersive character of our proposed channel can be associated to a highway configuration.

The preselected configurations are then modeled in the electromagnetic simulator FEKO where ray-tracing is performed using the Uniform Theory of Diffraction (UTD) module, with a maximum of three interactions. On the basis of the study and preselection made from our analytical method, multipath components with higher delays are expected in the scenario. This can be observed in the PDP obtained from FEKO simulations. Due to the high mobility of the virtual vehicles in the scenario, the channel fluctuations are much more important. From FEKO simulations, the minimum RMS-ds value at 10% quantile extracted from the cumulative curves in Figure 3 is 43 ns. The maximum value retrieved from the same set of curves at this quantile is 128 ns. The mean RMS-ds bears values from 144 ns to 271 ns. The quantile at 90% ranges from 254 ns to 553 ns. We can notice, for this highway environment, a good match between results from our simulations and results from measuring campaigns carried out in such an environment.

Besides, in Fig. 3-26, we compare the 10 simulated realizations of the highway configuration with results from three different measuring campaigns carried out on a highway environment [10]. We can notice a good match between the distributions.

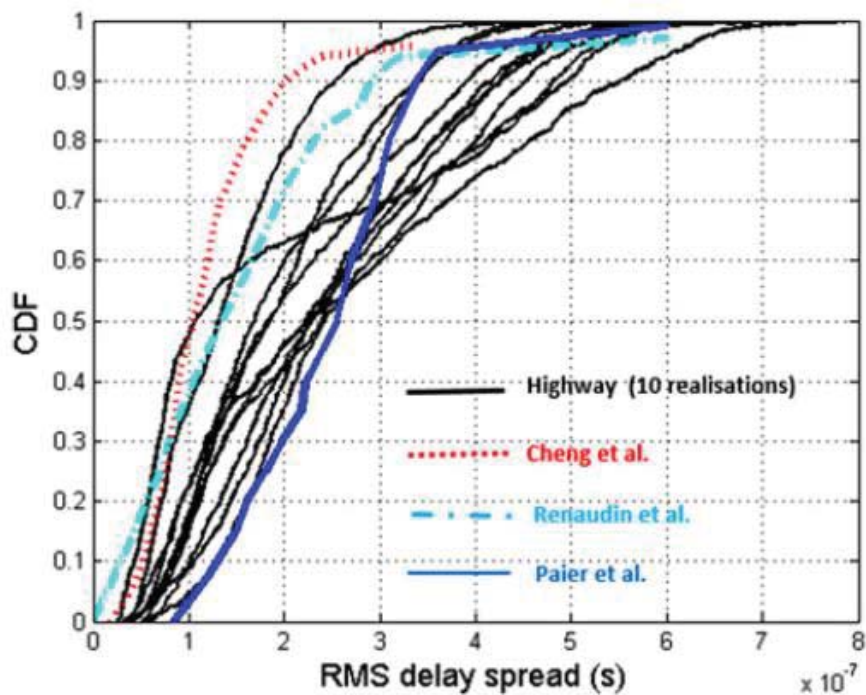


Figure 3-26 : RMS-delay spread comparisons for highway configurations

Angular spread

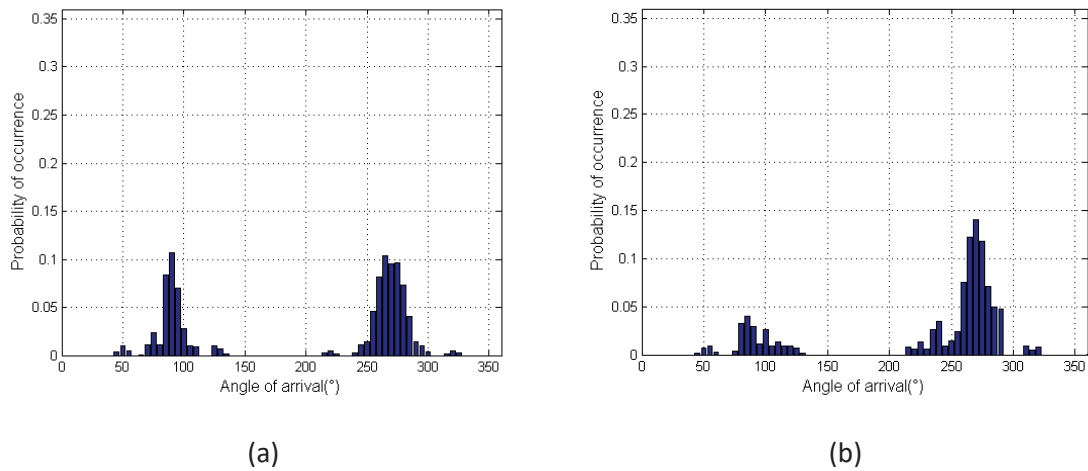


Figure 3-27: Angular spread distributions for highway configurations obtained with (a) Analytical method and (b) FEKO simulations

In a highway configuration we have a high angular spread due to the presence of the 22 N_{OUT} scatterers as we can notice in Figure 3-27(a) and Figure 3-27(b). Typically, in a highway environment, elements contributing to multipath are numerous (high traffic density, presence of billboards, guardrails and even middle wall separating lanes). Therefore, the angular spreads obtained from our simulated configurations give a good representation of a realistic highway environment. We can see that the distributions of AoAs, retrieved from both simulation models, bear fair resemblance with those earned from the narrowband deterministic ray-tracing tool commercialized from AWE communications (see Appendix B).

Doppler spectrum

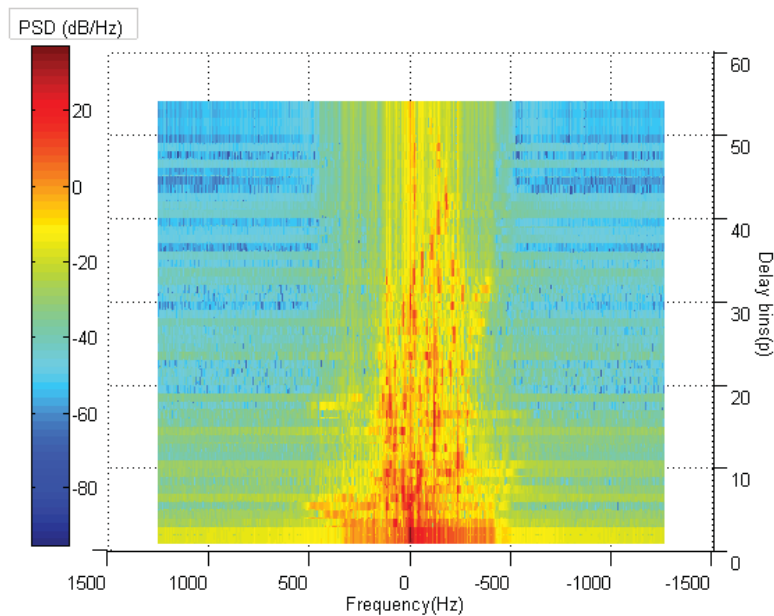


Figure 3-28 : Delay-Doppler spectrum for a highway configuration obtained from FEKO simulations

The same displacement principle is applied to the highway scenario otherwise the TX and RX moving with speed of 30 m/s. Also, the scatterers are assigned speeds between [30-36] m/s. In the highway configuration (Figure 3-28), the base of the spectrum remains wider in late delay bins due to strong angular spread of the multipath components arriving with larger delays.

3.4.3 Configuration for urban-like channel

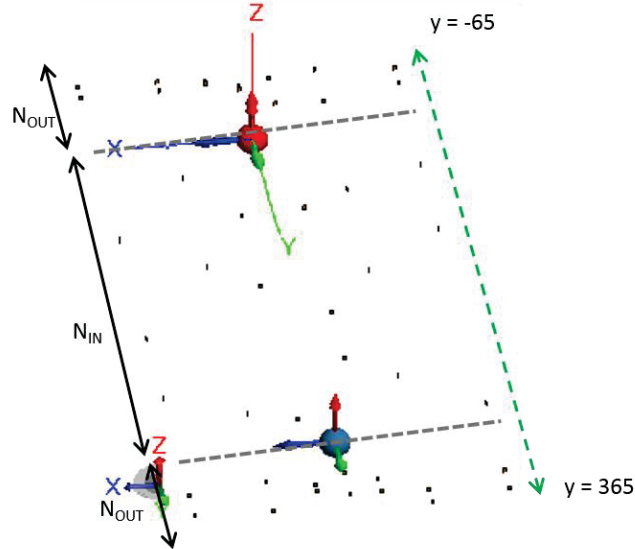


Figure 3-29 : An example of an urban configuration simulated with FEKO

3.4.3.1 Suggestion of the number and laws of distributions of the scatterers

In the latter, 46 scatterers are spread over 7 lines. Lines with the following indices were used: (L_i , where $i = 1, 4, 5, 10, 11, 20$ and 21). Hence, the perpendicular distance between the lines where scatterers are placed and Line 1 (the TX – RX axis) is increased. There are 18 N_{IN} scatterers. 28 N_{OUT} scatterers were equally dispatched over the 7 lines. In Figure 3-29, we illustrate a particular configuration aiming to mimic channel parameters pertaining to an urban environment. It is important to notice that in this proposed configuration the Tx-Rx axis (L_1) is free of N_{IN} scatterers. So the receiver is found in a perfect line of sight condition. N_{OUT} scatterers found in the Tx-Rx axis induce specular reflections with greater propagation distances, thus carrying the expectancy of late arrival on the receiver. Here also, the initial Tx-Rx separation is set at 300 m. The transmitter and receiver, representing the vehicles move in the same direction with a speed of 9.7 m/s. The parameters of the geometry of the scattering environment destined to represent an urban scenario are given in Table 3-9.

Table 3-9: Geometry parameters of an urban propagation channel.

Total number of scatterers		46
Type of scatterers	N_{IN}	18
	N_{OUT}	28
Number of lines		7

Random distribution of scatterers	N_{IN}	$U [20 , 280]$ m
	N_{OUT}	$U [-60 , -30]$ m
	N_{OUT}	$U [330 , 365]$ m

3.4.3.2 Analytical method and FEKO simulation results

RMS- delay spread

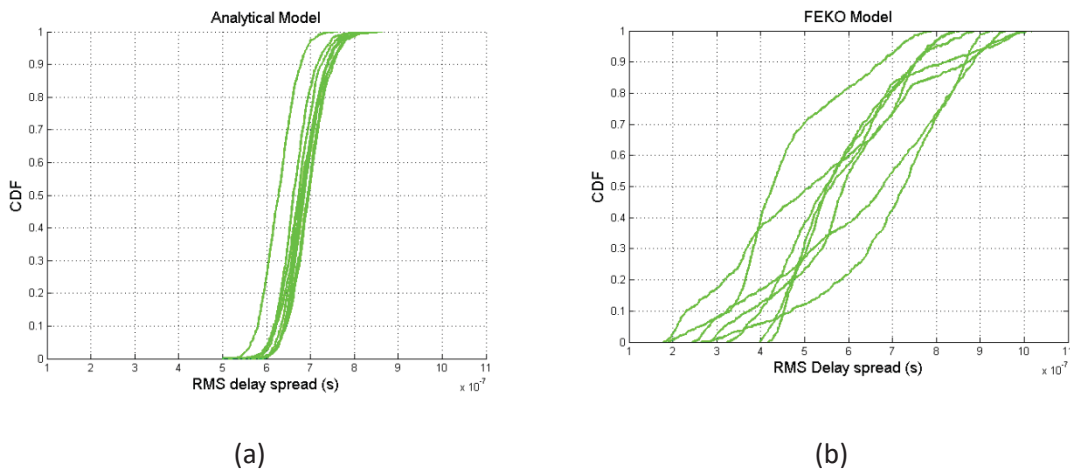


Figure 3-30: RMS delay spread distributions for urban configurations obtained with (a) Analytical method and (b) FEKO simulations

The RMS delay spread distributions are plotted in Figure 3-30(a) and Figure 3-30(b). We expect higher RMS delays as compared to rural and highway configuration. From those distribution curves, we can derive the minimum and maximum values of the quantiles at 10% and 90% as well as the mean RMS-ds of this simulated setting. The minimum quantile at 10% is 580 ns whereas its maximum is 645 ns. The quantile at 90% ranges from 678 ns to 753 ns while the values of mean RMS-ds are between 627 ns to 697 ns. These 10% quantile of RMS-ds are slight overestimates as compared to the delay spreads obtained from results of measurement campaigns carried out in some urban areas with values ranging from 50 ns to 1100 ns.

The same comparative procedure is applied for FEKO simulated configurations. The time dispersive character of the urban-like channel response is displayed as a cumulative distribution of the RMS-ds obtained over the whole dynamic (1000 snapshots). The minimum value for the quantile at 10% is 267 ns while the 90th % threshold value is 470 ns. The mean values of the RMS-ds are situated between 459 ns and 676 ns. The upper criteria fixed at 90% of the cumulative distribution ranges from 754 ns to 884 ns.

Angular spread

An increase in the perpendicular distance of the scatterers from the vehicles enabled us to significantly enrich the angular spread thus approaching a fair representation of such an urban scenario where presence of buildings and high traffic density ensures rich multipath. Figure 3-31(a) depicts the angular spread obtained from the “one-interaction” ray-tracing performed with the developed analytical model. Upon comparison against results obtained from Winprop (c.f Appendix B), we confirmed the choice of the number and positioning of scatterers. Moreover, a correct representation of the distribution of the directions of arrival of multipath components in an urban environment was reproduced in FEKO simulations as illustrated in Figure 3-31(b).

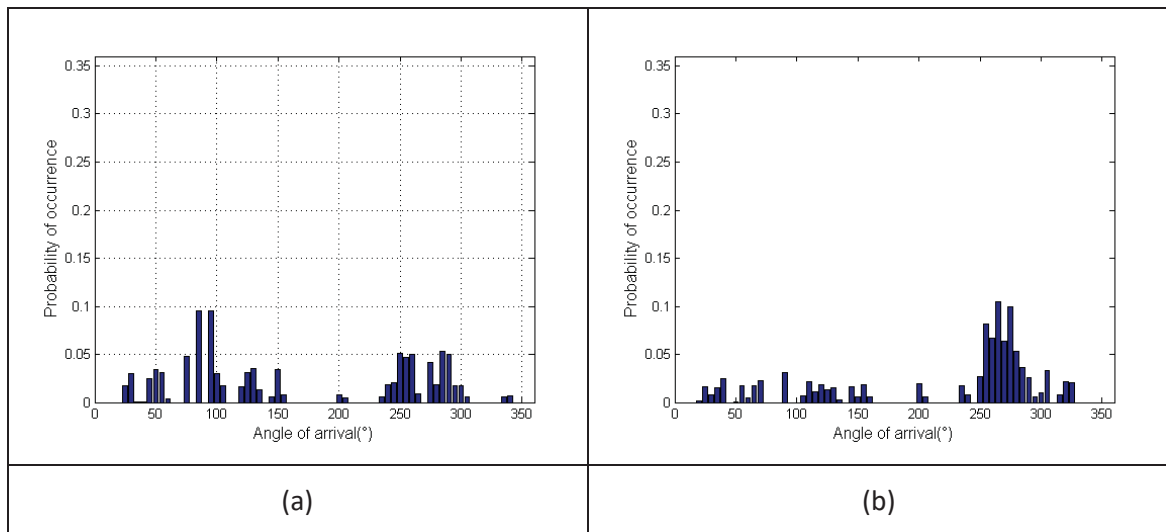


Figure 3-31: Angular spread distributions for urban configurations obtained with (a) Analytical method and (b) FEKO simulations

Doppler spectrum

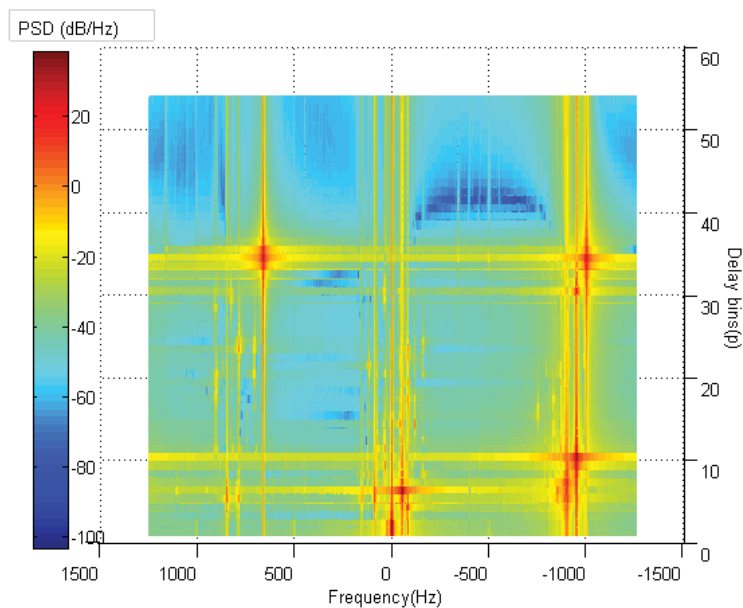


Figure 3-32 : Delay-Doppler spectrum for an urban configuration obtained from FEKO simulations

In the third configuration, representing an urban scenario, a speed of 9.7 m/s is chosen for both TX and RX while the speed of the scatterers vary from 8-13 m/s. In this third scenario also, the scatterers found in the axis of the TX-RX and those found in the two lines left of the TX-RX axis move in the same direction while the remaining scatterers move in the opposite way. Finally, the same principle as the previous configuration is applied to the new urban configuration. The three lines left of the TX-RX axis move in the same direction as the transmitter and receiver while those on the right of the TX-RX axis travel in the opposite direction. We can clearly see a multipath component with a high power spectral density arriving in delay bin 31 (contributing to a larger RMS-ds).

3.5 SUMMARY OF THE SIMULATION RESULTS

In this section, an overview of the simulated results, in terms of delay spread, obtained from our analytical model (Table 3-10) and FEKO simulations (Table 3-11) will be presented. Furthermore, the different results extracted from measurement campaigns that were available in the open literature are also recalled here, in Table 3-12. The range of values of the quantiles at 10 % and 90 % as well as the mean RMS delay spread obtained for all simulated configurations is tabulated below.

For the rural configuration, we can observe an underestimation of the RMS-ds results obtained as compared to those obtained from FEKO simulations. The ray-tracing strategy in our analytical model is based on a single bounce interaction. Also, the masking effect of different scatterers of multipath components is neglected in the analytical tool. This phenomenon is taken into account in the EM simulator. Therefore, increasing the maximum number of interactions to 3, in FEKO software, allows us to obtain RMS-ds results that pertain good concordance with measurement results.

The 10th percentile of the RMS-delay results for preselected configurations from the analytical tool are higher than that obtained from FEKO. The only explanation for the high estimation of the RMS-ds is the increase importance of the masking effect in the presence of a larger number of scatterers in the scenario. Therefore, results obtained from our chosen EM simulator, provides better correlation with measurement results.

For the urban scenario, both simulation models contribute to an overestimation of the RMS-ds results at the 10th percentile and the mean delay.

Table 3-10 : Statistics on the delay-spread obtained from our analytical model

RMS-ds (ns)	Rural	Highway	Urban
10th percentile	9 -15	220 – 331	580 – 645
Mean RMS-ds	13 -19	258 - 379	627 – 697
90th percentile	15 -25	300 - 453	678 – 753

Table 3-11 : Statistics on the delay-spread obtained from FEKO simulations

RMS-ds (ns)	Rural	Highway	Urban
10th percentile	11 – 37	43 - 128	444 – 691
Mean RMS-ds	26 – 87	144 - 271	803 – 959
90th percentile	55 -184	254 - 553	996 – 1340

Table 3-12 : Summary of RMS-ds results extracted from different measurement campaigns (reproduction of table 3.3).

RMS-ds (ns)	Rural	Highway	Urban
10th percentile	20 [32]	30 [34]	30 [34]
Mean RMS-ds	22 [31]-52 [25]	41 [25] – 247 [33]	47 [25]-373 [34]
90th percentile	150 [32]	340 [33]	1100 [34]

3.6 CONCLUSIONS

In this paper, we have introduced a methodology, associated with the GBSCM models, to produce impulse channel responses that look like those encountered in typical environments for V2V communications. Rather than elaborating sophisticated channel modelling approaches based on channel sounding experiments, we suggest that these experiments may be virtually reproduced at least in a behavioral sense. We have shown with our three configurations that we are able to parameterize channel characteristics such as RMS-delay spread and AOA distribution and delay-Doppler spectrum with simple adjustments on the number and position of scatterers. The three arrangements of scatterers show to have good correlations with the channel properties extracted from measuring campaigns encountered in the literature. Moreover, an analytical model, based on UTD method, is proposed in order to quickly design the arrangement of simple scatterers to emulate targeted propagation channel. This preselection is then used to perform a driving scenario using an electromagnetic ray-tracing simulator. In next chapters, these configurations would be used to integrate realistic antenna pattern (including the effect of the vehicle) into our channel propagation models. These new models will be used as test cases to evaluate the communication performance in terms of BER/PER after the integration of the PHY layer of the IEEE 802.11p standard dedicated to V2V communications. Hence, this complete simulation tool will be able to guide our choice of antenna technology and integration on the vehicle.

3.7 REFERENCES

- [1] T. S. Rappaport, *Wireless communications: principles and practice*. NJ: Prentice Hall, 2002.
- [2] J. D Parsons, *The mobile Radio Propagation Channel*, second Edition, John Wiley & Sons, 2000.
- [3] C. A. Balanis, *Antenna theory: analysis, and design*, third edition, New York: John Wiley & Sons, 2005.
- [4] O. Landron, M. J. Feuerstein, T. S. Rappaport, "A comparison of theoretical and empirical reflection coefficients for typical exterior wall surfaces in a mobile radio environment", *IEEE Trans. Antennas Propag.*, vol. 44, no. 3, pp. 341-351, Mar. 1996.
- [5] J. Deygout, "Multiple knife-edge diffraction of microwaves", *IEEE Trans. Ant. & Prop.*, vol. 14, no. 4, pp. 480-489, 1966.
- [6] J. B. Keller, "Geometrical Theory of Diffraction," *Journal of Optical Society of America*, 52, 1962, pp. 116-130.
- [7] R. G. Kouyoumjian and P. H. Pathak, "A Uniform Geometrical Theory of Diffraction for an Edge in a Perfectly Conducting Surface," *Proceedings of the IEEE*, 62, 11, November 1974, pp. 1448-1461.
- [8] P. Stoica, R. L. Moses, "Spectral analysis of signals" 1st Edition, Prentice-Hall, Mar. 2005.
- [9] P. Welch, "The Use of Fast Fourier Transform from the Estimation of Power Spectra: A Method Based on Time Averaging Over Short, Modified Periodograms," *IEEE Transactions on Audio and Electroacoustics*, vol. 15, no. 2, 1967.
- [10] A. Molisch et al., "A survey on vehicle-to-vehicle propagation channels", *IEEE Wireless Communications*, vol.16, no.6, pp.12 - 22, Dec. 2009.
- [11] L. Bernadó et al., "Non-WSSUS vehicular channel characterization at 5.2 GHz—Spectral divergence and time-variant coherence parameters", *Proc. Assembly URSI*, pp. 9-15, Aug. 2008.
- [12] L. Bernadó, T. Zemen, F. Tufvesson, A. F. Molisch and C. F. Mecklenbrauker "Time-and frequency-varying-factor of non-stationary vehicular channels for safety-relevant scenarios", *IEEE Trans. Veh. Technol.*, vol. 63, no. 1, pp.82 - 93, Jan. 2014.

- [13] L. Bernado, T. Zemen, F. Tufvesson, A. Molisch, and C. Mecklenbräuker, "The (in-)validity of the WSSUS assumption in vehicular radio channels," in Proceedings of Personal Indoor and Mobile Radio Communications (PIMRC), 2012, pp. 1757-1762.
- [14] A. Paier, T. Zemen, L. Bernadó, G. Matz, J. Karedal, N. Czink, C. Dumard, F. Tufvesson, A. F. Molisch, C. F. Mecklenbräuker, "Non-WSSUS vehicular channel characterization in highway and urban scenarios at 5.2GHz using the local scattering function", Proc. Int. WSA, pp. 9-15, 2008.
- [15] P. Bello "Characterization of randomly time-variant linear channels", IEEE Trans. Commun. Syst., vol. 11, no. 4, pp. 360-393, 1963.
- [16] I. Sen and D. Matolak, "Vehicle-Vehicle channel models for the 5-GHz band", [IEEE Trans. Intell. Transp. Syst., vol. 9, no. ,pp. 235–245, Jun. 2008.
- [17] L. Cheng et al., "Mobile Vehicle-to-Vehicle Narrow-Band Channel Measurement and Characterization of the 5.9 GHz Dedicated Short Range Communication (DSRC) Frequency Band," IEEE JSAC, vol. 25, 2007, pp. 1501–16.
- [18] L. Cheng et al., "Doppler Component Analysis of the Suburban Vehicle-to-Vehicle DSRC Propagation Channel at 5.9 GHz," Proc. IEEE Radio and Wireless Symp., 2008, pp. 343–46.
- [19] J. Maurer, T. Fugen, and W. Wiesbeck, "Narrow-band measurement and analysis of the inter-vehicle transmission channel at 5.2 ghz," in Vehicular Technology Conference, 2002. VTC Spring 2002. IEEE 55th, vol. 3, 2002, pp. 1274-1278 vol.3.
- [20] A. Paier, J. Karedal, N. Czink, H. Hofstetter, C. Dumard, T. Zemen, F. Tufvesson, C.Mecklenbrauker, and A.Molisch, "First results from car-to-car and car-to-infrastructure radio channel measurements at 5.2GHz," in Proc. IEEE 18th Int. Symp. Personal, Indoor Mobile Radio Comm. PIMRC, pp. 1–5, 2007.
- [21] Rubio, L., Reig, J., & Fernández, H. (2011). Propagation aspects in vehicular networks, Vehicular technologies. Miguel Almeida (Ed), InTech.
- [22] Green, E. & Hata, M. (1991). Microcellular propagation measurements in an urban environment. IEEE Personal, Indoor and Mobile Radio Communications International Symposium, pp. 324-328, London, UK, Sep. 1991.
- [23] Xia, H. H.; Bertoni, H. L.; Maciel, L. R.; Lindsay-Stewart, A. & Rowe, R. (1993). Radio propagation characteristics for line-of-sight microcellular and personal communications. IEEE Transactions on Antennas and Propagation, Vol. 41, No. 10, pp. 1439-1447.

- [24] J. Karedal, N. Czink, A. Paier, F. Tufvesson, and A. Molisch, "Path loss modeling for vehicle-to-vehicle communications, " *Vehicular Technology, IEEE Transactions on*, vol. 60, no. 1, pp. 323-328, Jan 2011.
- [25] J. Kunisch and J. Pamp, "Wideband Car-to-Car Radio Channel Measurements and Model at 5.9 GHz," *Proc. IEEE VTC 2008 Fall*, 2008.
- [26] L. Cheng, B. Henty, F. Bai, and D. Stancil, "Highway and rural propagation channel modeling for vehicle-to-vehicle communications at 5.9 ghz, " in *Antennas and Propagation Society International Symposium*, 2008. AP-S 2008. IEEE, July 2008, pp. 1-4.
- [27] Okechukwu Onubogu, Karla Ziri-Castro, Dhammika Jayalath, Keyvan Ansari, Hajime Suzuki, "Empirical vehicle-to-vehicle pathloss modeling in highway suburban and urban environments at 5.8 GHz", *Signal Processing and Communication Systems (ICSPCS) 2014 8th International Conference on*, pp. 1-6, 2014.
- [28] L. Rubio, H. Fernandez, V. M. Rodrigo-Pefiarrocha, "Path loss characterization for vehicular-to-infrastructure communications at 700 MHz and 5.9 GHz in urban environments", *Antennas and Propagation & USNC/URSI National Radio Science Meeting*, 2015 IEEE International Symposium on, Issue Date: 19-24 July 2015.
- [29] R. Chen, Z. Zhong, "Analysis on V2V connectivity under dual-slope path loss model in urban scenarios", *General Assembly and Scientific Symposium (URSI GASS), 2014 XXXIth URSI*, Aug. 2014.
- [30] Lin Cheng and R. Shakya. Vanet adaptive power control from realistic propagation and traffic modeling. In *Radio and Wireless Symposium (RWS), 2010 IEEE*, pages 665-668, 2010.
- [31] I.Tan, W. Tang, K. Laberteaux, and A. Bahai, "Measurement and analysis of wireless channel impairments in dsrc vehicular communications," in *Communications*, 2008. ICC '08. IEEE International Conference on, May 2008, pp. 4882-4888.
- [32] L. Cheng et al., "Multi-Path Propagation Measurements for Vehicular Networks at 5.9 GHz," *Proc. IEEE Wireless Commun. Net. Conf.*, 2008, pp. 1239-44.
- [33] A. Paier, J. Karedal, N. Czink, H. Hofstetter, C. Dumard, T. Zemen, F. Tufvesson, A. F. Molisch, and C. F. Mecklenbräuker, "Car-to-car radio channel measurements at 5 GHz: Pathloss, power-delay profile and delay-Doppler spectrum," in *Proc. IEEE ISWCS*, Trondheim, Norway, Oct. 2007, pp. 224-228.
- [34] O. Renaudin, V. M. Kolmonen, P. Vainikainen, and C. Oestges, "Wideband MIMO car-to-car radio channel measurements at 5.3 GHz", in *Proc. IEEE Veh. Technol. Conf.*, 2008.

- [35] L. Bernado, T. Zemen, F. Tufvesson, A.F. Molisch, C. Meck-lenbrauker, "Delay and doppler spreads of non-stationary vehicular channels for safety relevant scenarios", *IEEE Transactions on Vehicular Technology*, vol. 63, no. 1, pp. 82-93, 2014.
- [36] J. Maurer, T. Schafer, and W. Wiesbeck, "A Realistic Description of the Environment for Inter-Vehicle Wave Propagation Modeling," *Proc. IEEE VTC 2001 Fall*, 2001, pp. 1437–41.
- [37] J. Maurer et al., "A New Inter-Vehicle Communications (IVC) Channel Model," *Proc. IEEE VTC. 2004 Fall*, 2004, pp. 9–13.
- [38] L. Reichardt, T. Fugen, and T. Zwick, "Influence of Antennas Placement on Car to Car Communications Channel," *Proc. Euro. Conf. Antennas Prop.*, 2009.
- [39] AWE Communications website, <http://www.awe-communications.com>.
- [40] R. Wahl, G. Wölfle, R. Weigel, "Prediction of spatial channel impulse responses for time variant wireless ad-hoc networks using a 3D ray tracing model with radar cross sections," *IEEE Veh. Techn. Conf, VTC 2007 Fall*, Oct. 2007, Baltimore, pp. 2204 – 2208.
- [41] J. Nuckelt, M. Schack, and T. Kürner, "Deterministic and stochastic channel models implemented in a physical layer simulator for Car-to-X communications," *Advances in Radio Science*, Vol. 9, pp. 165-171, September 2011.
- [42] T. Mangel, O. Klemp, and H. Hartenstein. 5.9 GHz Inter-vehicle Communication at Intersections: a Validated Non-line-of-sight Path-loss and Fading Model. *EURASIP Journal on Wireless Communications and Networking*, 2011(1):182, 2011.
- [43] T. Abbas, J. Nuckelt, T. Kurner, T. Zemen, C.F. Mecklenbrauker, and "F. Tufvesson, "Simulation and Measurement-Based Vehicle-to-Vehicle Channel Characterization: Accuracy and Constraint Analysis," *IEEE Transactions on Antennas and Propagation*, vol. 63, no. 7, pp. 3208- 3218, 2015.
- [44] G. Acosta-Marum and M. A. Ingram, "Six time- and frequency-selective empirical channel models for vehicular wireless LANs," *IEEE Vehicular Technology Magazine*, vol. 2, no. 4, pp. 4 - 11, Dec. 2007.
- [45] L. Bernadó, T. Zemen, F. Tufvesson, A. F. Molisch and C. F. Mecklenbrauker "Time-and frequency-varying-factor of non-stationary vehicular channels for safety-relevant scenarios", *IEEE Trans. Veh. Technol.*, vol. 63, no. 1, pp.82 - 93, Jan. 2014.
- [46] J. Maurer , T. Fügen , T. Schäfer and W. Wiesbeck "A new inter-vehicle communications (IVC) channel model", *Proc. IEEE 60th VTC*, vol. 1, pp.9 - 13, . (VTC'04-Fall), 2004.

- [47] L. Bernadó, T. Zemen, F. Tufvesson, A. F. Molisch and C. F. Mecklenbrauker "Time-and frequency-varying-factor of non-stationary vehicular channels for safety-relevant scenarios", *IEEE Trans. Veh. Technol.*, vol. 63, no. 1, pp.82 - 93, Jan. 2014.
- [48] J. Maurer , T. Fügen , T. Schäfer and W. Wiesbeck "A new inter-vehicle communications (IVC) channel model", *Proc. IEEE 60th VTC*, vol. 1, pp.9 - 13, . (VTC'04-Fall), 2004.
- [49] J. Karedal , F. Tufvesson , N. Czink , A. Paier , C. Dumard , T. Zemen , C. F. Mecklenbräuker and A. F. Molisch "A geometry-based stochastic MIMO model for vehicle-to-vehicle communications", *IEEE Trans. Wireless Commun.*, vol. 8, no. 7, pp.3646 - 3657, July 2009
- [50] Soltani, M. D, Alimadadi. M., and Mohammadi, A., "Modeling of Mobile Scatterer Clusters for Doppler Spectrum in Wideband Vehicle-to-Vehicle Communication Channels," *IEEE Comm. Letters*, vol. 18, no. 4, pp.628 - 631, Apr. 2014.
- [51] X. Cheng et al., "An adaptive geometry-based stochastic model for non-isotropic MIMO mobile-to- mobile channels," *IEEE Trans. Wireless Commun.*, vol. 8, no. 9, pp. 4824 - 4835, Sep. 2009.
- [52] A. G. Zajic and G. L. Stuber, "Three-dimensional modeling and simulation of wideband MIMO mobile-to-mobile channels," *IEEE Trans. on Wirel. Commun.*, vol. 8, no. 3, pp.1260 - 1275, Mar. 2009.
- [53] A. G. Zajic, "Impact of Moving Scatterers on Vehicle-to-Vehicle Narrow-Band Channel Characteristics," *IEEE Trans. on Veh. Technol.*, vol. 63, no. 8, pp.3094 - 3106, Sep. 2014.
- [54] O. Renaudin, V.-M. Kolmonen, P. Vainikainen, and C. Oestges, "Wideband Measurement-Based Modeling of Inter-Vehicle Channels in the 5-GHz band," *IEEE Trans. Veh. Technol.*, vol. 62, no. 8, pp.3531 - 3540, Oct. 2013.
- [55] D. W. Matolak, Q. Wu, "Channel Models for V2V Communications: A Comparison of Different Approaches," *Proc. European Conf. on Antennas & Propagation*, Rome, Italy, 11 - 15, April 2011.
- [56] F. A. Sikta, W. D. Burnside, T. T. Chu, and L. Peters Jr., "First-Order Equivalent Current and Corner Diffraction Scattering from Flat Plate Structures," *IEEE Transactions on Antennas and Propagation*, AP-31, July 1983, pp 584-589.
- [57] A. Michaeli, "Comments on first-order equivalent current and corner diffraction scattering from flat plate structures", *IEEE Trans. Antennas Propag*, vol. 32, no. 9, pp. 1011-1012, Sept. 1984.

Chapter 4 : ANTENNA INTEGRATION

Antennas have high impact on the performance of the communication. Automotive antennas are subjected to vehicle design, aesthetical, profile and cost constraints. Fortunately, vehicular antenna development is a topic that has not been left behind and is under constant evolution. Recent advances and innovative solutions are contributing to aesthetical low-priced antennas that can still meet their technical requirements. The radiofrequency services offered in the automotive field are following an increasing trend, leading to the integration of numerous antennas. Figure 4-1 gives an overview of the different RF services provided by Renault with their corresponding potential antenna locations. These various systems cover a large frequency spectrum starting from 125 kHz for keyless entry to 77 GHz radar systems.



Figure 4-1 : Frequency ranges of the multiple RF automotive services.

4.1 COMPUTATION ELECTROMAGNETIC TECHNIQUES

Due to the ever-growing number of vehicle models and short development time, electromagnetic simulations are of utmost importance in the automotive industry. Numerical simulation approaches can be very helpful to guide our choice of antenna configurations and antenna placement in upstream studies prior to prototyping. The computation and analysis of the different electromagnetic characteristics of antennas implemented on a vehicle rely upon the discretized solution of Maxwell's equations. Numerous software tools have been developed to study electromagnetic simulations. It can be tackled using different numerical approaches or computation electromagnetic (CEM) techniques.

For a complete survey of available techniques the reader may refer to [1], [2], [3], [4], [5] and [6]. CEM is roughly classified into two main categories: the rigorous methods based on the discretization of Maxwell's equations and high-frequency methods based on an asymptotic version of these equations. Rigorous methods can be subdivided into frequency domain methods (such as

the method of moments – MoM, and the finite element method) and time domain methods (e.g. the finite-difference time domain method – FD-TD, and the transmission line modeling method - TLM). Tools involved in that category solve systems of equations related to the discrete version of Maxwell’s equations either in their differential or integral formulation. High-frequency methods can be subdivided into field-based methods (the geometrical optics method) and current-based methods (the physical optics method). High-frequency methods are suitable for structures much larger than the wavelength, while rigorous methods are more suitable for smaller structures. They are based on an asymptotical (high-frequency) approximation of Maxwell’s equations yielding to the laws of geometrical optics and further to the uniform theory of diffraction.

4.1.1 FEKO software tool

Our choice for FEKO is only dictated by two main features. It uses a rigorous solver in the frequency domain to solve problems at a few wavelength scale, and also offers an asymptotic method to deal with large scales (with regard to wavelength) electromagnetic scenes. FEKO software is an electromagnetic simulation tool developed by the EMSS society [7]. The name FEKO is an abbreviation derived from the German phrase FEldberechnung bei K rpern mit beliebiger Oberflache. (Field computations involving bodies of arbitrary shape.) It is based on the method known as method of moments, formalized by Harrington [8], which solves Maxwell equations in their integral form and in the frequency domain.

The strength of FEKO resides in its capacity to propose numerous numerical methods to the user following the electrical size of the model, its geometrical complexity and available computational resources. Figure 4.3 sums up the different appropriate numerical analysis techniques and hybridization methods to solve electromagnetic simulations regarding dimensions and complexity of the simulated model.

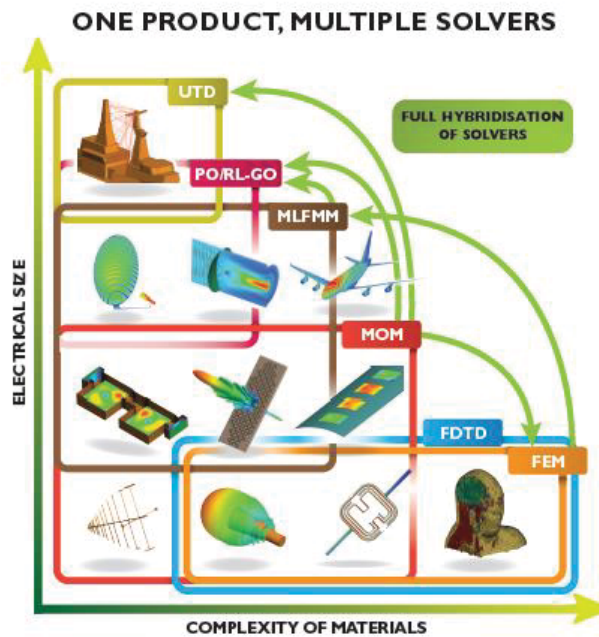


Figure 4-2 : Illustration of the numerical analysis techniques in FEKO [7]

4.1.1.1 MoM and MLFMM

MoM consists in resolving the equations of Maxwell in their integral form. In its most common used version, this method adopts a frequency-domain formulation and requires determination of the unknowns only at the model's boundaries (surface meshing). The MoM is applied on discretized model of the simulated object. The latter is split into sub-domains such as linear triangles for metallic surfaces, segments for wired elements and cubes for dielectric structures.

The current density \vec{J} on a geometry G can be expressed as,

$$L(\vec{J}) = \vec{g} \quad (\text{Eq. 4.1})$$

where L is a linear operator and \vec{g} is an excitation. As suggested, in classical MoM, the discretization of the geometry leads to the expansion of the current density in a set of linear functions known as basis functions, approximated by the finite series:

$$\vec{J} = \sum_{n=1}^N I_n \vec{f}_n \quad (\text{Eq. 4.2})$$

where \vec{f}_n are the set of basis functions, I_n are the unknown current coefficients and N represents the total number of unknowns. Substituting (Eq. 4.2) in (Eq. 4.1) and applying a testing procedure with weighting functions $\vec{W}_1, \vec{W}_2, \dots, \vec{W}_N$, transforms (Eq. 4.1) into a set of linear equations that can be written as:

$$[Z][I] = [V] \quad (\text{Eq. 4.3})$$

In (Eq. 4.3), Z is the impedance matrix of size (N x N), V is the voltage matrix vector with their respective elements: $Z_{in} = \langle \vec{W}_i, L \vec{f}_n \rangle$ and $V_i = \langle \vec{W}_i, \vec{g} \rangle$. I is the vector of unknown coefficients I_n of the basis functions. Eventually, I is obtained after the inversion of the Z matrix. This inversion of the impedance matrix results in a scaling of N^2 of the memory requirements and N^3 computational time to solve the linear set of equations.

Consequently, if the numerical model is large compared to the wavelength, the methods of moment can rapidly become too greedy in computational resources, both in terms of memory and computational time requirements. In this case, FEKO includes the Multi-Level Fast Multipole Method (MLFMM) [9], a method for optimizing computation time when handling large simulation models while keeping the accuracy of the traditional MoM. The MLFMM is also based on the inversion of the impedance matrix. However, on the opposite of the MoM which computes the interaction between individual basis function, the MLFMM groups the basis functions and computes the interaction between clusters of basis functions. With respect to classical MoM, the MLFMM allows to reduce the memory cost to $N \cdot \log(N)$ and computational time duration to $N \cdot \log(N) \cdot \log(N)$. In our work, due to numerical complexity, we chose to simulate antenna integration on car body with the MLFMM.

4.1.1.2 Meshing criteria

With numerical techniques, based on the Method of Moments, the meshing quality of the numerical model is crucial to guarantee optimal results. We must ensure ourselves that the maximal dimension of the meshes satisfies the condition presented in (Eq. 4.4). The latter provides a fair trade-off between accuracy of the estimation of the surface currents and an acceptable computation time.

$$\text{Triangle edge} \leq \frac{\lambda}{10} \quad (\text{Eq. 4.4})$$

As a consequence, the higher the frequency range of the investigated computation problem, the more precise the numerical model should be. This can be quite problematic from the computational point of view. This means that simulations at very high frequencies are often very time consuming and are very demanding in memory capacity. The number of mesh cells for an accurate simulation model can reach several millions depending on the geometry size and on the frequency range of interest. In order to save computation time, compromises between accuracy of the results and the geometry area considered in simulation have to be made.

4.1.2 Numerical model of the vehicle

In addition to the precision of different numerical simulation techniques, the most important aspect for the accurate approximation of the antenna under investigation is the correct consideration of the antenna environment once installed on-board a vehicle, which should be taken into account in order to ensure the best possible realistic simulation model. Inclusion of geometrical details in the numerical model of the vehicle will improve the accuracy of simulation results. However, we have seen in previous paragraphs of this chapter that at high frequencies, the model accuracy (large number of mesh cells) can have a huge impact on the computational requirements in terms of available memory or time-duration of the simulation. This is the reason why a tradeoff in complexity of the simulated model must be made at the expense of the precision of the simulated results. In our work, we chose to simplify our numerical models to fit in the maximum computation resources available.

4.1.3 Measurement facility

In order to characterize antennas mounted on vehicles, Renault makes use of a semi-spherical multi probe chamber situated in the EMC/RF laboratory in the Renault's technical center in Aubevoye (CTA, standing for Centre Technique d'Aubevoye in French). This chamber (Figure 4-3) was developed by the Satimo society in 2006 and is based on an indoor hemispherical nearfield range. Antenna measurements must in general be carried out in free-space and this requirement is met in the chamber as it is fully anechoic. The dimensions of the chamber are the following: a height of 12 m, a width of 16m and is 18 m long.

The measurement facility consists of an arch divided into two bipolarised probe arrays. Each array is distributed along each half of the arch whose radius is 6 m. The first one covers the 70 to 500 MHz range, and the second one the 400 MHz to 6 GHz range. The acquisition of complex tangential electric-field on a hemisphere is achieved by scanning a probe array in the elevation axis combined with the rotation of a turntable to cover the azimuth.



Figure 4-3 : Full anechoic measuring facility

Table 4-1 : Technical characteristics of both probe arrays.

Frequency range (MHz)	Arch Radius (m)	Probes number	Angular coverage (°)	Angular step
70- 400	6	31	-9.64 to 86.79	3.21
400-6000	6	101	-10,00 to 90,00	1.00

4.2 A STATE OF THE ART ON V2X ANTENNA INTEGRATION

One of the most challenging aspects of car to car communication is the integration of the antenna systems in the vehicle itself. In this section, a brief state-of-the-art on V2X antenna integration will be provided. Some works on antenna design at 5.9 GHz covering the dedicated band were identified while others dealt on the impact of the vehicle body on the antenna radiation pattern. V2X communication performance analysis for different antenna designs and implementation on vehicles were performed using either ray-tracing channel simulators or field tests.

4.2.1 Antenna design at 5.9 GHz

Authors in [10] shed light on the integration aspects especially regarding antenna design and more precisely on the effect of the radome of a roof-top shark-fin antenna. They showed that with modification of the thickness of the radome, nulls in the radiation pattern situated in the direction of travel can be eliminated. The results of this study were based on simulation and were validated by measurements in an anechoic chamber. In [11], a simple microstrip patch antenna that resonates at 5.9 GHz is presented. This antenna has a return loss of -48.5 dB at the resonating frequency with a directivity of 7.6 dBi and a radiation efficiency of -1.3 dB. Besides in [12], two car-to-car antennas were integrated in a conventional roof-top antenna containing a GPS patch and a dedicated UMTS services radiating element. The first C2C antenna is a printed monopole and the second one is a short-circuited patch working in the TM_{01} mode. This study was carried out by the Calero society. Measurement showed that antennas were well matched and decoupled on both horizontal and vertical planes.

Furthermore, in [13] authors designed a new shark-fin rooftop C2C multi-band antenna for automotive applications. It is a single-feed wideband antenna that covers the LTE frequency band as well as that of V2X communications. Integration on the roof of the vehicle was performed only in simulation with an internal software using a specialized solver for electrically large simulations based on the Methods of Moments. It was shown that the novel antenna design works better than a $\lambda/4$ monopole situated at the same feeding point. Moreover, authors in [14] present a compact module consisting of two identical LTE antennas and a pair of V2X antennas working at 5.9 GHz. The overall dimensions of the radiating module is 290 mm x 40 mm x 7.6 mm. Simulations and measurement results show that the V2X antennas were well-matched for ITS services at the dedicated frequency band. Besides, the antenna is suitable for a rear-spoiler mounting position.

Moreover in [15], authors analyze in Renault a three-element patch antenna resonating at 5.8 GHz. From the reflection coefficient measurement result, it can be clearly deduced that the antenna covers the V2X communication band as defined by ETSI. The antenna was integrated in a simplified canonical structure half a size of a car. The half-scaled car structure is simulated with the actual 5.8 GHz patch antenna without performing any frequency scaling. The goal, here, was to reduce the number of meshes for its simulation compared to a real car, keeping a representative shape. Good agreement was found between simulated results obtained with different electromagnetic tools and with measurement results. It can be noted, that this antenna will be used later on in this thesis for field test purposes.

4.2.2 Numerical methods to integrate V2X antennas

In this subsection, a focus will be maintained on the different numerical techniques to integrate V2X dedicated antenna mounted on vehicles. In [16], simulation results for different antenna mounting positions on personal use vehicles and trucks were presented. A monopole antenna placed on the rear roof of an Audi car model was simulated with EMPIRE XPU FDTD simulation software. It was shown that the radiation pattern at this antenna position achieves better backside coverage due to the curvature of the roof. Besides, the authors also put forward simulation results for a truck cabin and a truck cabin with a tarpaulin container for different turn positions. In both cases, two electrical monopoles were mounted inside the truck plastic spoiler situated on the roof the cabin. The authors did not take into account the material and conductor losses of the plastic spoiler in this case as they were targeting only a rough estimation of the radiation patterns. The impact of the rotation of the tarpaulin container on the radiating performance of the monopole antennas were studied. The FDTD method was used to simulate large structure for high frequencies. The time of simulation for a model constituting of 7000 million FDTD cells needing up to 170 GB was about 1 day.

Furthermore, in [17] an emphasis on high-frequency asymptotic methods like uniform theory of diffraction (UTD) and physical theory of diffraction was made to examine the impact on a radiation pattern of antennas when integrated on the roof, side mirrors and bumpers. In order to validate the asymptotic solver, the author proceeded with a comparison study of a full wave analysis considering only a metallic roof structure. Due, to limited computational resources they had to resign to consider solely a reduced structure of the vehicle. In a second step, they considered the complete car which can only be solved with reasonable computational effort by an asymptotic solver. Furthermore, electric field distribution was used as a criterion to identify dispensable parts of the car to speed up numerical computations keeping an acceptable level of accuracy. In the second part of this work, full wave analysis, taking account for wave guidance, diffractions and creeping waves, was required to correctly characterize the influence of glass roof on the radiation pattern. The authors showed that the good correlation found between measurement and the simulation results, was only possible with a rigorous technique in the presence of a glass roof. Moreover, in [18] the effects of the car body on radiation pattern of a half-wavelength dipole placed on the side mirror were investigated. The FDTD method was used as a simulation technique to investigate the change in the radiation pattern upon simplification of the numerical model of the car structure. Authors indicated same tendencies in radiation patterns obtained with both the complete model and the simplified one.

In [19], the authors examined the implementation of two monopoles on the car's roof and dipole antennas situated on the lateral mirrors, front and rear bumpers respectively. The simulation was performed using REMCOMs' XFDTD solver [20]. Focus was also made on the contribution of diversity techniques such as Maximum Ratio Combining between the different antennas.

4.2.3 Impacts of antenna on V2X communication performance

To ensure best performance of communication between two vehicles, the optimal antenna configuration must be found. This task can be done via the basis of measurement campaigns but they are often expensive, time-consuming and are not prone to provide repeatability. This is the reason why many researchers channel this study towards ray-tracing simulations. In this

subsection, we will enumerate some works found in the literature that englobe the investigation of the impact of antenna configuration or antenna placement on the quality of service.

In [22], a tool called Virtual Drive, developed in the University of Karlsruhe, consisting of an environment and a traffic model, is used to compute the multi-path wave propagation between the transmitter and receiver. Although, a detailed description of the environment is included in this 3D ray-tracing method, antennas are represented by their radiation pattern if previously measured patterns are available or placed on canonical representation of a vehicle. In [22], the authors also used Virtual Drive to determine the influence of various antenna positions on the narrowband and wide band characteristics of two different motorway environments. Six antenna positions were chosen: front bumper, rear bumper, lateral mirrors, the roof and under the car respectively. The antennas were represented by their radiation pattern and placed at their corresponding positions on either the transmitting car or the receiving car. No near-field interactions between the radiating element and the vehicle are taken into account. According to the authors, the side mirror antenna positions present a considerable alternative when we are under design constraints. Also, simulation results obtained suggested that antennas under the cars can be an adequate solution as they have good line of sight probabilities in common road traffic and they are not design critical.

4.2.4 Conclusions

In this state-of-the art section on V2X antenna integration we have covered the aspects of antenna design, presented an overview of the numerical methods used to tackle antenna integration problematics and exposed a brief literature review of how antennas were represented in ray-tracing tool to investigate their performance. In the light of what we have seen, it can be deduced that the complex shape and huge electrical size of a car at 5.9 GHz yield an important challenge for the numerical modeling.

In this chapter, we want to demonstrate the alterations of the radiation pattern of an integrated antenna on-board a car given the interactions between the car and the corresponding antenna. Ideally, a full wave simulation with a complete description of the vehicle shall be executed. Unfortunately, due to computational limitations, a trade-off on the accuracy of simulated results must be made in order to reduce computation time and to fulfill memory requirements.

Besides, to implement the representation of the integrated antenna on the vehicle in a propagating environment, we must have recourse to asymptotic methods as the scale of a complete driving scenario is very large compared to the wavelength. In this case, the accuracy of the source representation has a strong influence on the accuracy of the results. To our knowledge, no previous work has been done to investigate on the accuracy of using directly a far-field radiation pattern in a propagation channel. The substitution of the antenna system by merely its radiation pattern should be handled with care especially in cases where interacting elements are found in the vicinity of the radiating element. Thus, a technique to establish or to maintain correct interactions with near-field elements should be found. This would be the subject of the second part of this chapter.

4.3 REPRESENTATION OF THE ANTENNA ON THE VEHICLE

In this subsection, we will focus on the integration of antenna on the vehicle's body. As seen in chapter 3, propagation channels were characterized using a perfect dipole antenna radiation pattern because of its isotropic characteristic in the azimuthal plane. Nevertheless, in order to simulate realistic propagating scenario, we must take into account far-field radiation pattern of the antenna mounted in the car-body.

For this study, we possess the CAD of two vehicle structures as shown in Figure 4-4 : A canonical vehicle structure and the CAD of the Mégane IV. The characteristics in terms of numerical size of each model is given in Table 4-2.

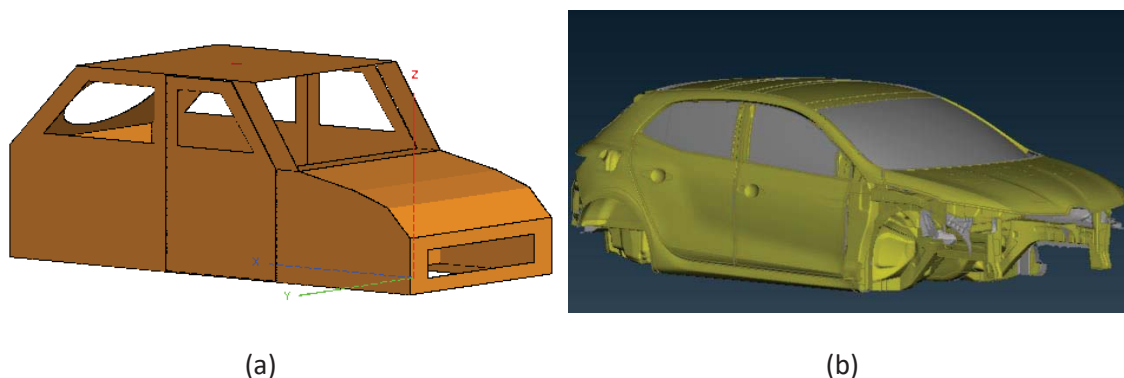


Figure 4-4 : (a) The canonical vehicle model (b) The digital mock-up of the Mégane IV car

The canonical vehicle model is made of flat polygonal plates and hence has a uniform meshing structure. Besides, the benefit of this model is that it can be easily handled and can be downsized or upsized to different scale. This will prove to be a major advantage when investigating the impact of the effective electrical size of a mounted antenna on the near-field to far-field boundary conditions.

The CAD of the Mégane IV will be used to simulate antenna implemented on the vehicle body. Of course, due to computational restrictions, a preliminary selection of the necessary parts of the vehicle having huge impact on the radiation pattern of the antenna must be done. Therefore, depending on the antenna position and configuration, dispensable parts of the vehicle can be left out in order to reduce the numerical complexity of our model. Antenna simulation results with this digital mock-up of the Mégane IV will be compared to measured radiation antenna pattern performed in our facility in Aubevoye using the same car model.

All antenna integration simulations were carried out on a HPC (High Performance Computing) server. This machine possesses 32 processing cores with 248 GB of RAM. With the MLFMM method the memory limitation is reached with a numerical model consisting of approximately 7 million unknowns, i.e., about 3.5 million triangles (meshed cells).

Table 4-2 : Characteristics of available numerical models

Numerical model	Mesh size (Number of triangles)
Canonical vehicle model	2 200 000
CAD of the Mégane IV	10 450 000

4.3.1 Roof- antenna case

Roof-top antenna remains the most common antenna position even if the trend in automotive designs is imposing more and more constraints and is pushing towards no-roof antenna vehicles. Nevertheless, the location on the roof offers an unobstructed condition and is the optimal position to obtain an omnidirectional radiation pattern in the azimuthal plane. We may also guess that the inner structure of the vehicle has a negligible impact on the radiation pattern. This opens the door for a huge simplification of the CAD of the vehicle to examine it. In subsection 4.3.1, we will focus on the impact of simplifying our numerical models for roof-antennas.

4.3.1.1 Canonical vehicle structure

In the first place, the scenario of a quarter-wavelength monopole placed at the center of the roof of the canonical model is considered. The aim, here, is to simplify at most the numerical model and to observe the change in the respective radiation patterns for each level of simplification. The distribution of the surface currents is evaluated. It gives us a clear view of dispensable parts of the numerical model with respect to the antenna's location.

Centre of the roof

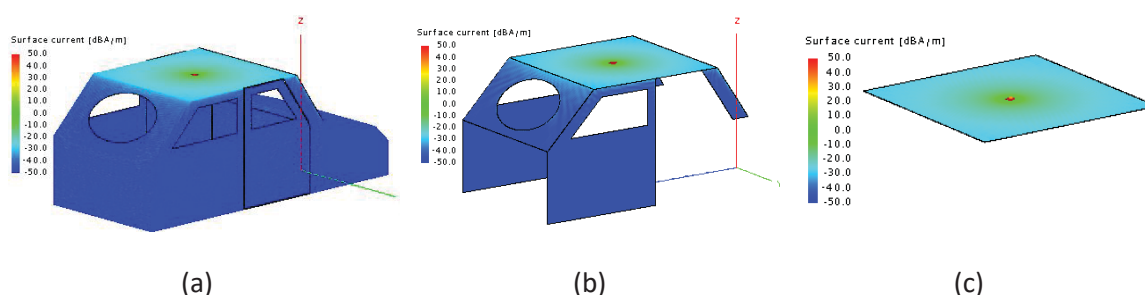


Figure 4-5 : The distribution of the surface currents on (a) the whole vehicle structure (b) the roof and the edges and (c) the roof only

In Figure 4-5, the 3 states of simplification under investigation are presented. In Figure 4-5(a), the whole vehicle structure is simulated while in Figure 4-5(b), only the roof with its corresponding edges is taken into account. Finally, in Figure 4-5(c) only the roof of the model, considered as the highest level of simplification is simulated. The distribution of the surface current (in A/m) is shown

with a dynamic range of 90 dB. It can be observed, from the current distribution, that even the edges of the roof have minimum impact on the radiating element. Let us take a look at the radiation pattern in the three cases.

In Figure 4-6, the radiation patterns in the azimuthal plane ($\theta = 90^\circ$) and in the elevation plane ($\phi = 0^\circ$) are plotted. The three far-field patterns show quasi-identical behavior except for some minor ripples for the lowest and mild level of simplification. We can thus infer from this study that for the case of an antenna situated at the center of the roof, the simulation model containing merely the roof structure deemed to be sufficient.

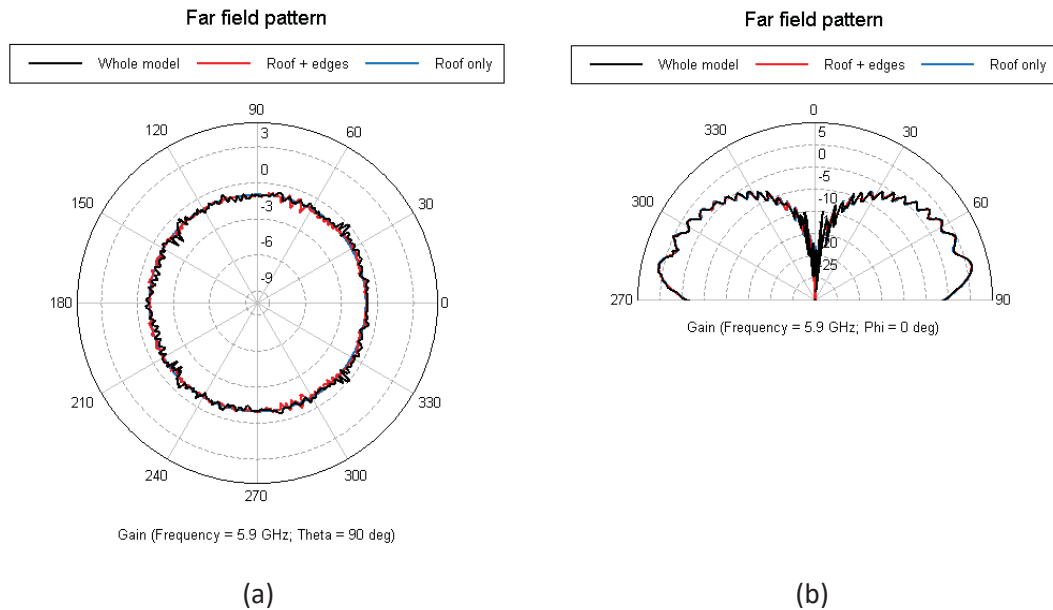


Figure 4-6 : Radiation patterns for the three levels of simplification in (a) the azimuthal plane and (b) the elevation plane.

Back of the roof

In the situation where the antenna is placed at the center of the roof, inclusion of the roof structure only provides accurate simulation results. Now, we want to verify if this approximation still stands if the $\lambda/4$ monopole is positioned near the back end of the roof.

Here also, the canonical vehicle structure with the same levels of simplification is used for this investigation. Observing the distribution of the current density, we can see an increase in the impact of the back edges and tailgate. This statement is also confirmed when we take a look at the far-field pattern in the azimuthal plane in Figure 4-8 (a). We can clearly see discrepancies in the direction of the roof edges. Hence, it can be problematic in certain cases where the antenna is positioned away from the center of the roof to consider only the roof structure in the simulated model. In order to ensure accurate results, it may be advised to consider at least the edges in simulations.

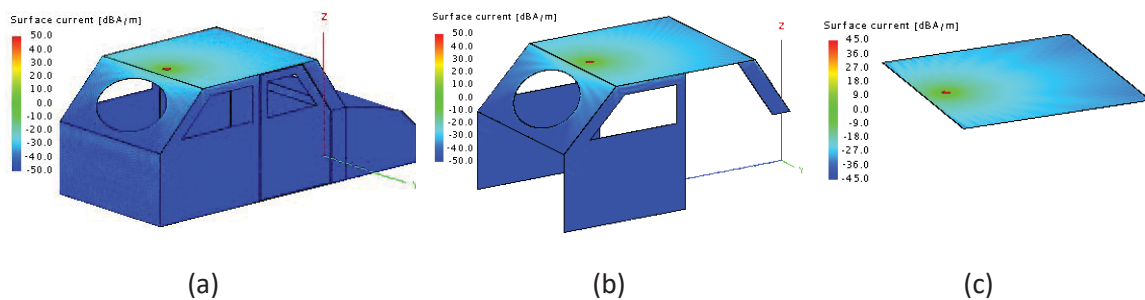


Figure 4-7 : The distribution of the surface currents on (a) the whole vehicle structure (b) the roof and the edges and (c) the roof only

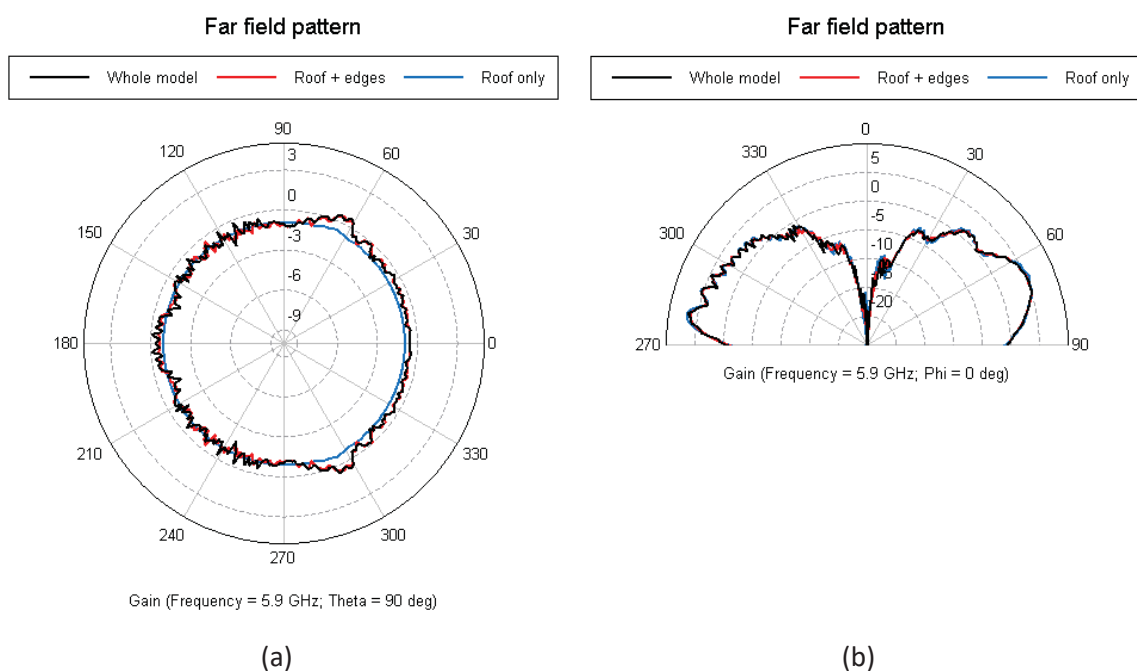


Figure 4-8 : Radiation patterns for the three levels of simplification in (a) the azimuthal plane and (b) the elevation plane.

4.3.1.2 The Mégane IV numerical model

The Mégane IV has been selected by Renault to be used in the Scoop@f project dedicated to the V2X communications. The digital mock-up of the vehicle is quite bulky and exceeds the memory limitations of our available processing tools. Considering rigorous simulating method, such as MLFMM, simplification process of our model is necessary.

In substance, the case of a simple monopole on the rooftop of the Mégane car will be studied. The simulated results will be confronted with measurements in terms of radiation patterns.

Centre of the roof

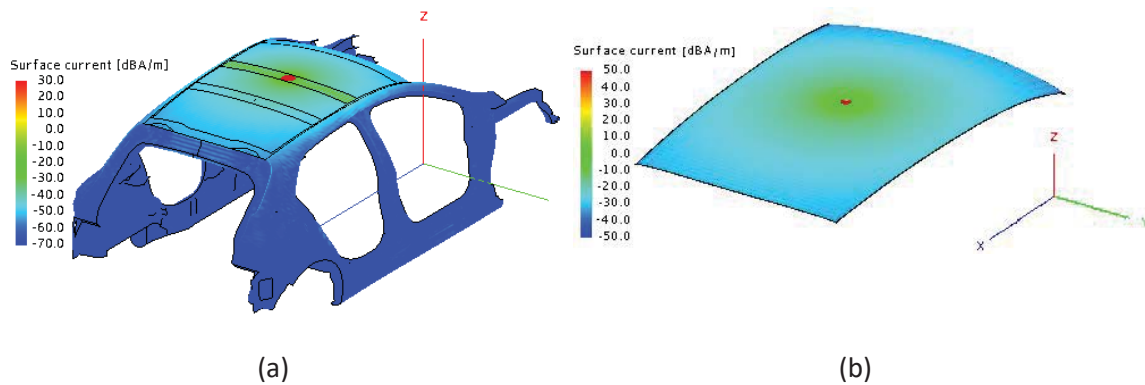


Figure 4-9 : The surface current distribution on (a) a simplified CAD of the Mégane IV and (b) the CAD of the only the roof of the Mégane IV

In Figure 4.9, the radiating element is mounted on the centre of the roof. We analysed two levels of simplification as shown in Figure 4.9 (a) and Figure 4.9 (b) respectively. According to the surface current distribution we can predict that the simplest representation consisting of the roof only can be acceptable.

Back of the roof

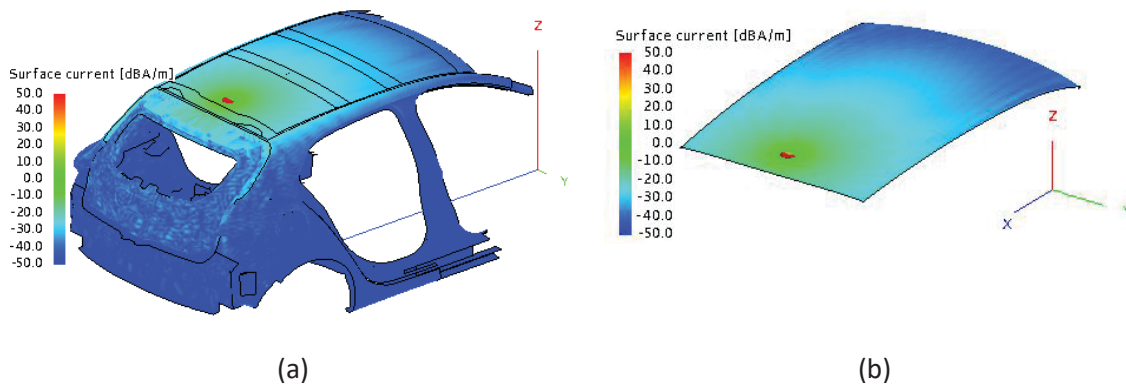


Figure 4-10 : The surface current distribution on (a) a simplified CAD of the Mégane IV and (b) the CAD of the only the roof of the Mégane IV

Upon consideration of the $\lambda/4$ monopole placed on the rear roof, the tailgate was included in the simplified model. Figure 4-10, representing the distribution of the surface current, supports this fact. Indeed, we can see that the current is spread on the tailgate for this particular antenna location.

4.3.1.3 Measurement of a $\lambda/4$ monopole antenna of the roof of the Mégane IV

In a need to confront our simulated results with measurements, a $\lambda/4$ monopole antenna was crafted in our laboratory. A semi-rigid cable was used for this purpose. The inner conductor was stripped of its dielectric and outer conductor. It was carefully bent to be as much perpendicular as possible to the ground plane. The outer conductor was filed down at the proximity of the monopole antenna to reduce capacitive effect forming in between. The gap between the monopole antenna and the ground plane can be estimated as the radius of the semi-rigid cable. The latter was grounded to the plane using conductive copper tape. The length of the inner conductor or monopole was trimmed in order to fine tune the antenna.



Figure 4-11 : A crafted monopole using a semi-rigid cable

In Figure 4-12, reflection coefficient of our fabricated a $\lambda/4$ monopole is plotted. The antenna is well adapted as we obtained $S_{11} = -24$ dB at the frequency of 5.9 GHz.

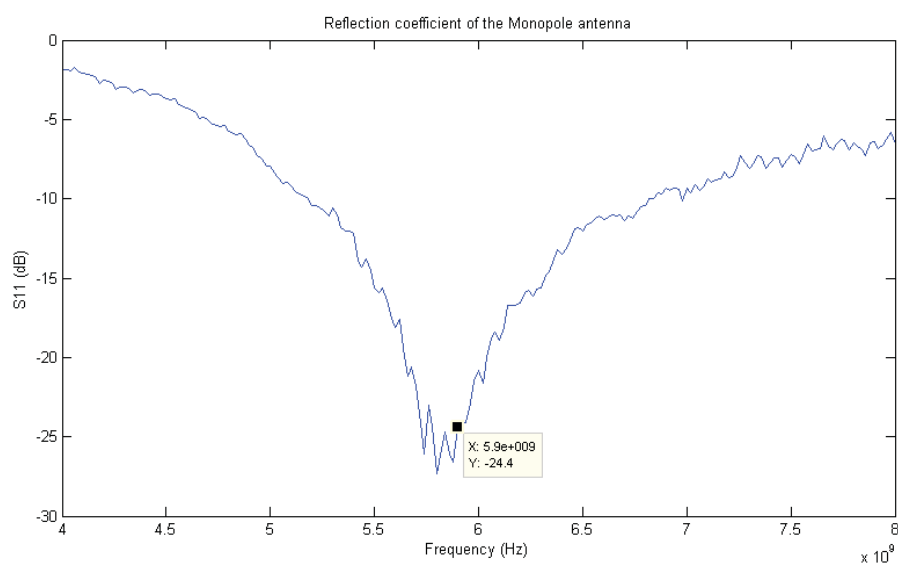


Figure 4-12 : Reflection coefficient of the crafted $\lambda/4$ monopole.

Center of the roof

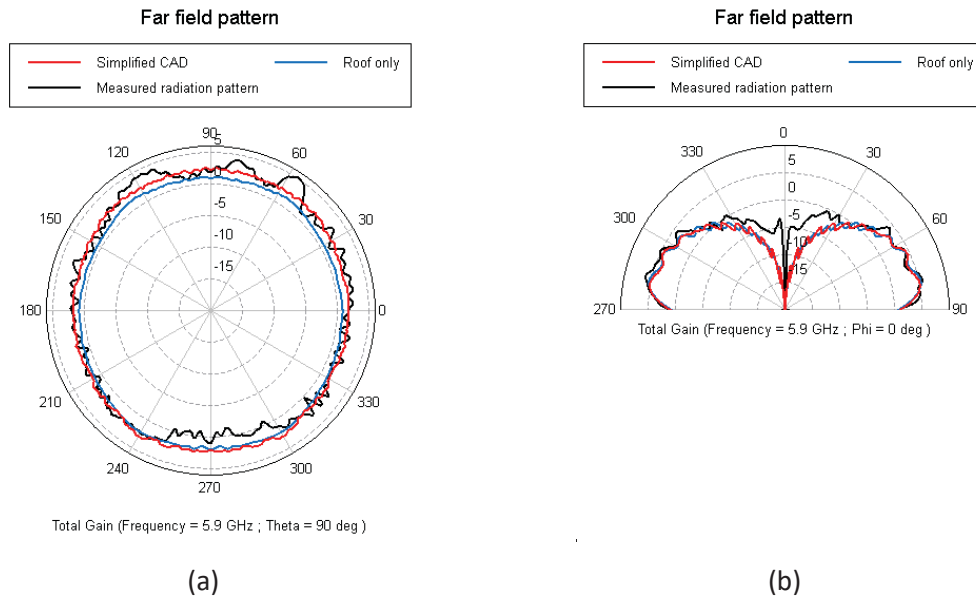


Figure 4-13 : Radiation patterns of an antenna situated at the center of the roof in (a) the azimuthal plane and (b) the elevation plane.

The radiation pattern for the simplified CAD, the roof-only case and the measured radiation pattern is plotted in both the azimuthal and elevation plane. A good correlation between the measured radiation pattern and that obtained with the simplified CAD can be observed except for the region $270^\circ < \varphi < 300^\circ$. We can observe slight fluctuation 60° and 120° in the azimuthal plane. Moreover, the null in the radiation pattern in the elevation plane is not correctly reproduced in simulation even if it will not have strong influence in further studies.

Back of the roof

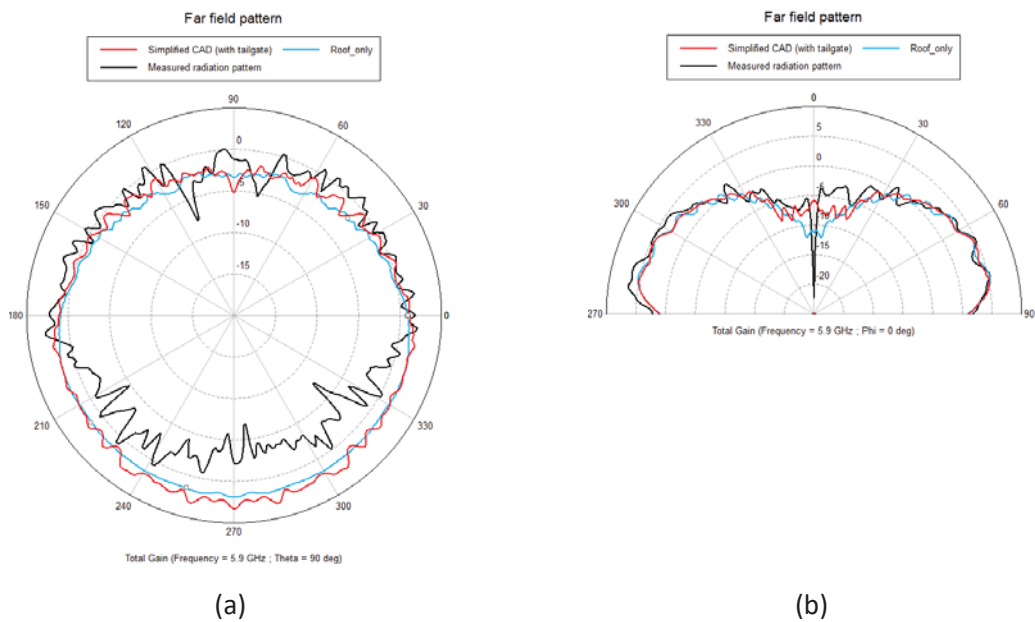


Figure 4-14 : Radiation patterns of an antenna situated at the back of the roof in (a) the azimuthal plane and (b) the elevation plane.

Greater differences can be found between the measured radiation pattern and the simulated one at the back of the car. A plausible cause of this difference can be the gap between the radiating element and the actual ground plane (the roof on the car). Thus, the roof curvature has a moderate impact on the radiation pattern in the azimuthal plane. However, a fair correlation is observed between the 3 patterns in the elevation plane.

4.3.2 On-board antenna case

Until now, only roof antennas were investigated. We will now analyze the instance of an on-board antenna. The patch antenna, developed in [15], was used for this scope. The radiating element was positioned vertically on the rear window. The numerical model, shown in Figure 4-15, considering the tailgate was used in our simulation. The rear windscreen was represented as glass with a permittivity of 4.5. Figure 4-15 shows the dispersion of surface currents displayed with a dynamic of 90 dB with two different point of view.

4.3.2.1 Simulation

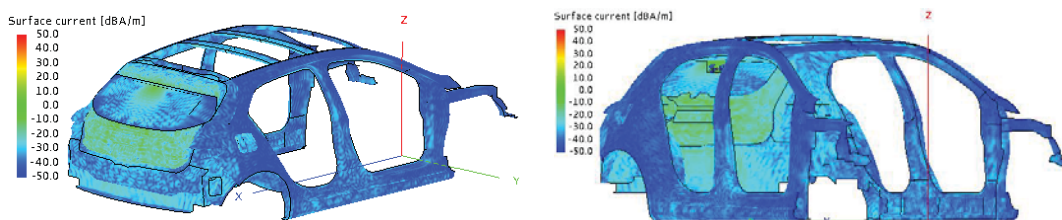


Figure 4-15 : Surface current distributions of a patch antenna situated at the rear window.

4.3.2.2 Measurement



Figure 4-16 : Measuring configuration of a patch antenna on the rear window

The measuring configuration is shown in Figure 4-16. The location of the patch antenna is framed in red. A layer of styrofoam was used as support to ensure that the patch antenna remains in a vertical position with the major lobe pointing the azimuthal plane.

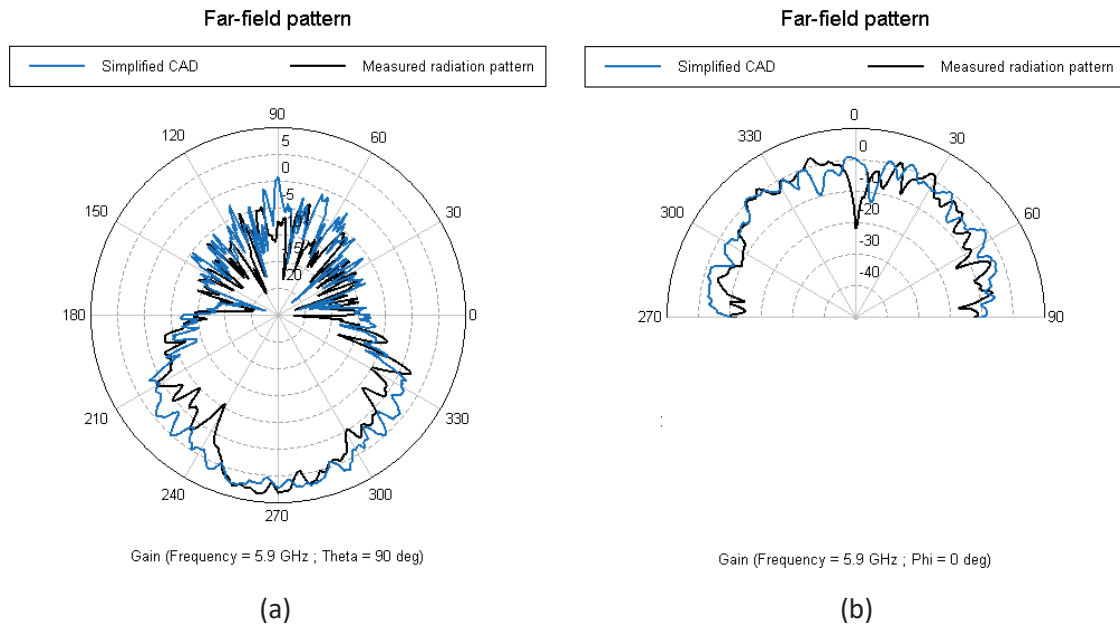


Figure 4-17 : Radiation patterns of a patch antenna situated on the rear windscreen in (a) the azimuthal plane and (b) the elevation plane.

There is a good correlation between the radiation patterns in both azimuthal and elevation plane. It must be noted that the measured antenna radiation pattern, in our semi-spherical anechoic chamber characterizes the field only in the upper hemisphere. In automotive applications, it is not of great interest characterizing radiation field towards the ground.

4.3.3 Conclusions

In this section, a focus on antenna integration simulation was presented. Two vehicles model were considered: a canonical vehicle structure made of flat polygonal plates and secondly the digital mock-up of the Mégane IV vehicle meshed according to a frequency of 5.9 GHz. In the first part, we investigated the degree of the impact of simplifying the numerical model on the radiation pattern. We deduced that roof structure is sufficient when considering the situation of an antenna placed around the center point of the roof. However, the influence of the other parts of the car body such as the tailgate become important when the antenna is placed at the back-end of the roof.

Moreover, the simulation results obtained with the simplified numerical model of Mégane IV were compared with measured radiation pattern. Fair correlations between measurement and simulations were found. In the next subsection, we will analyze the impact of having near-field scatterers in our propagation channel bearing in mind that we use directly the far-field pattern to represent the integrated antenna and vehicle system.

4.4 COMPLETE EM SIMULATION INCLUDING THE INFLUENCE OF NEAR-FIELD ELEMENTS

As we have seen in the previous sections, the antenna-to-vehicle interactions are not negligible and must be considered to reach better accuracy on radiation pattern estimation. As a matter of fact, the distribution of the surface currents on the vehicle models clearly suggests the effective size of the antenna does not solely rely on the radiating element. Due to diffracting and scattering parts of the vehicles we have the presence of coupling effects between the antenna and the vehicle body leading to an increase of the size of the equivalent radiating source. Increasing the size of the radiating element means that the considered far-field zone approximation governed by the Fraunhofer distance (see equation 3.2) will also increase (together with the modification of the radiation pattern as investigate in the above section 4.3).

Ray-tracing tools are usually based on GTP or UTD which correspond to an approximation of the Maxwell equations under the following basic assumptions:

- The frequency of communication must be high enough to fulfil the asymptotic approximation.
- Scatterers must be found in the far-field region of the radiating source.

If we have seen in the chapter 3 that the first condition is met at 5.9 GHz, the second condition remains unanswered. In the next subsections we will try to elucidate if this condition is met and how to mitigate its effect in the presence of scattering element in the near-field zone of the radiating element.

4.4.1 Defining the far-field zone

In the first place, a criterion to find the minimum distance for which it is acceptable to suppose far-field condition should be found. This distance, noted D_{min} , will be a reference radius around the radiating element covering the near-field zone. Therefore, the following procedure has been performed without the need of simulating the propagating scenario:

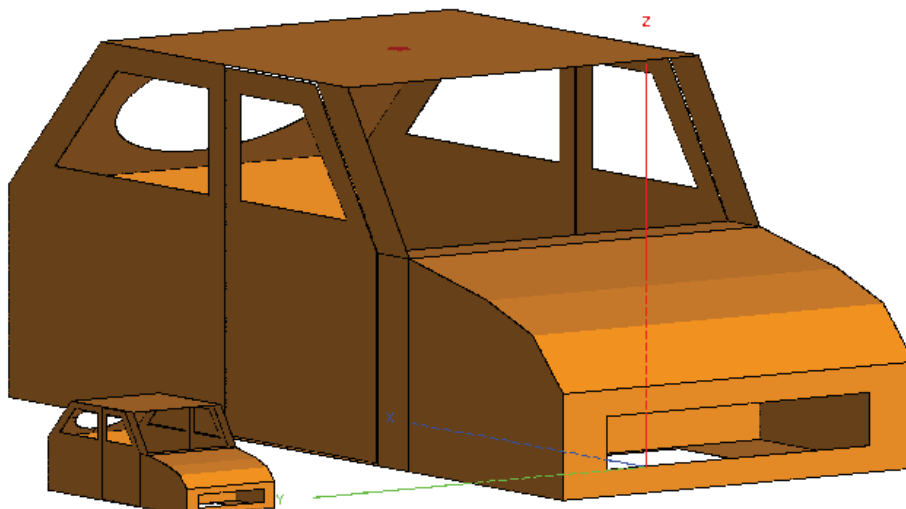


Figure 4-18 : The quarter-scale and full-scale canonical vehicle structure.

- Estimation of the distance for which the electric field level match the far-field radiation pattern within a fixed criteria
- The estimation is performed following a basic dichotomy rule starting with the largest dimension of the vehicle structure.
- The reason of changing the scale of the vehicle model is to study the impact of its size on the electric field formation in the far field.

The electric-field level is evaluated for each considered distance and normalized to $V = E \times D$ and is expressed in volt (or dBV). This corresponding normalized electric-field strength is compared to the radiating normalized electric-field of the far-field pattern. The two measurable characteristics should of course be exactly the same beyond the far-field boundary. An acceptability criterion of ± 1 dBV is fixed to determine this minimum distance D_{\min} .

The 99normalized electric-field level for a far-field radiation pattern can be written as follows:

$$V_{FF} = E_{FF} \times 1 \text{ m} \quad (\text{Eq. 4.5})$$

V_{FF} is the normalized electric-field provided by FEKO simulations. Equation 4.6 represents the expression of the 99normalized near-field electric-field, expressed in volt, for a given distance d in meters, where the near-field distribution is observed.

$$V_{NF} = E_{NF} \times d \text{ m} \quad (\text{Eq. 4.6})$$

Thus, beyond the far-field to near-field boundary $V_{FF} \approx V_{NF}$. According to the following criterion, the average difference over each considered plane should not be greater than 1 dB.

$$\text{Acceptability criteria : } 20 \log \left(1 + \frac{\sum_{i=0}^n \left| \frac{V_{NF}(\theta_i, \varphi_i) - V_{FF}(\theta_i, \varphi_i)}{V_{FF}(\theta_i, \varphi_i)} \right|}{n} \right) \leq 1 \text{ dB} \quad (\text{Eq. 4.7})$$

The latter will be evaluated for the full-scale and quarter-scale vehicle model. Once the location of the far-field zone is pinpointed, we shall elaborate a complete scenario to evaluate eventual discrepancies in terms of received power in the case of near-field scatterers.

A quarter-wavelength monopole is made to radiate at the center of the roof of the vehicle. The total electric-field of the far-field pattern is hence evaluated. The pattern is compared to that of the electric-field value of a sphere with different radii corresponding to the distances under evaluation.

4.4.1.1 Full-scale model

Considering the largest dimension of vehicle structure in figure 4-18 as the effective electrical size of our radiating object, the approximated Fraunhofer distance is situated at 320 m. Therefore, for this model we shall start our comparison at twice the Fraunhofer distance to ensure being well beyond the far-field boundary. Then, we proceed by dichotomy to find, with a precision of 1 dB difference, the correct far-field zone limitation. The comparison is made for $\theta = 90^\circ$ for each evaluated distance. In the following figures, we shall lead our investigation at two extreme distances 640 and 20 m respectively before displaying in-between points. The disparity resulting between the patterns is also plotted.

In Figure 4-19 (a), the polar representation of the normalized electric-field strength at a distance of 640 m is given. It is compared to the far-field pattern of the $\lambda/4$ monopole placed on the roof of the vehicle structure. As expected, there is practically a perfect match between the patterns as proved in Figure (4-20) (a) where the relative difference between the two plots is given for each angle in the horizontal plane. The mean difference for the azimuthal cut at 640 m is only 0.12 dB and thus satisfies the acceptability criterion. On the opposite, there is a complete mismatch between the plots at 20 m as shown in Figure 4-19(b). The mean difference between the plots is 2.43 dB and is well beyond our acceptable criterion of 1 dB.

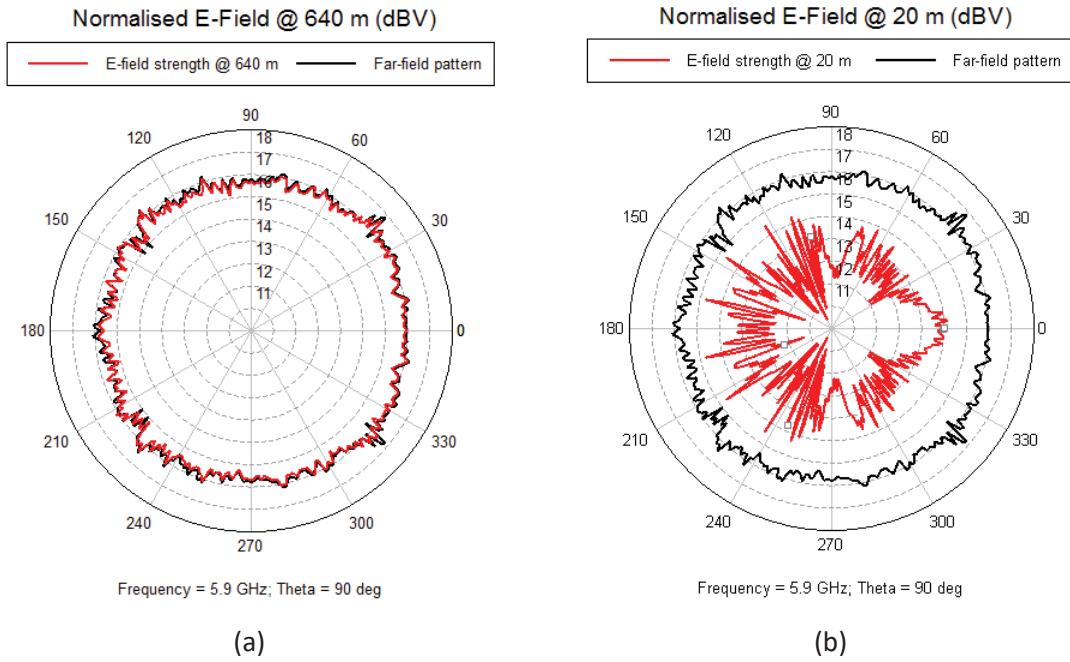


Figure 4-19 : The normalized E-field of the FF pattern compared to the E-field strength of the NF at (a) 640m and (b) 20 m.

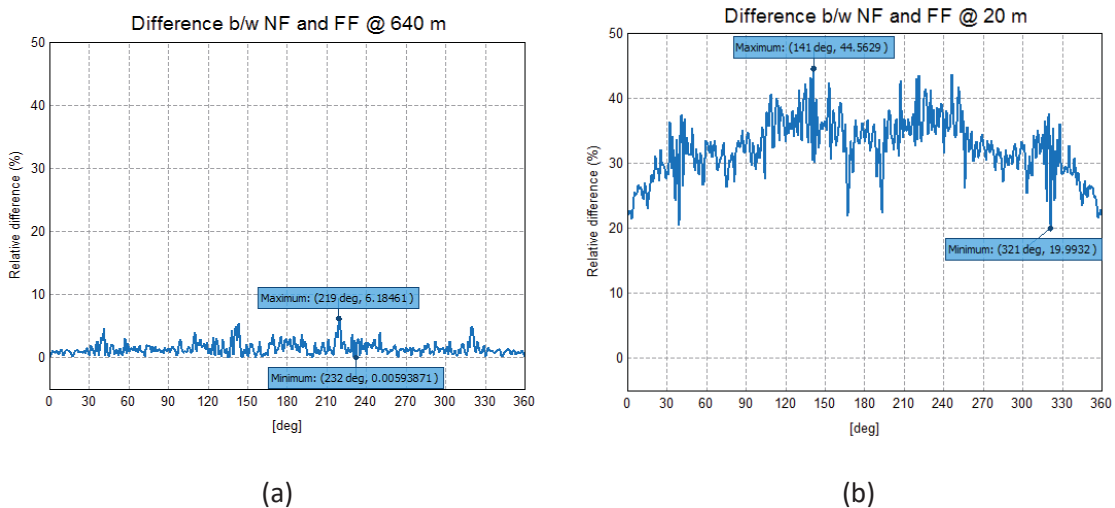


Figure 4-20 : Relative percentage difference for each angle of the between the normalized E-field of the FF pattern compared to the E-field strength of the NF at (a) 640m and (b) 20 m.

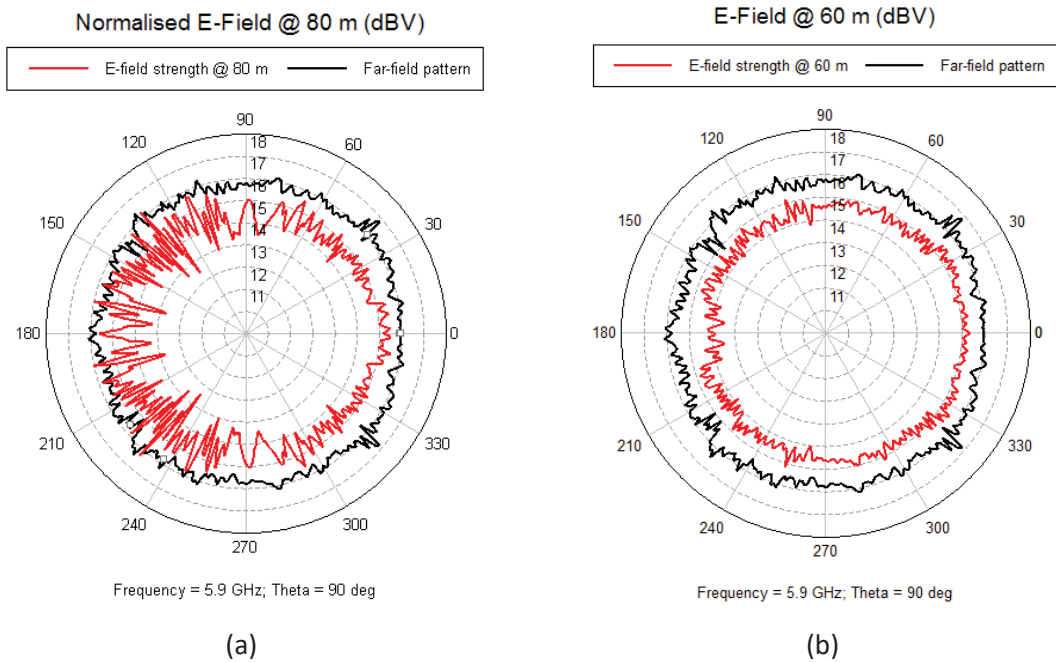


Figure 4-21 : The normalized E-field of the FF pattern compared to the E-field strength of the NF at (a) 80 m and (b) 60 m.

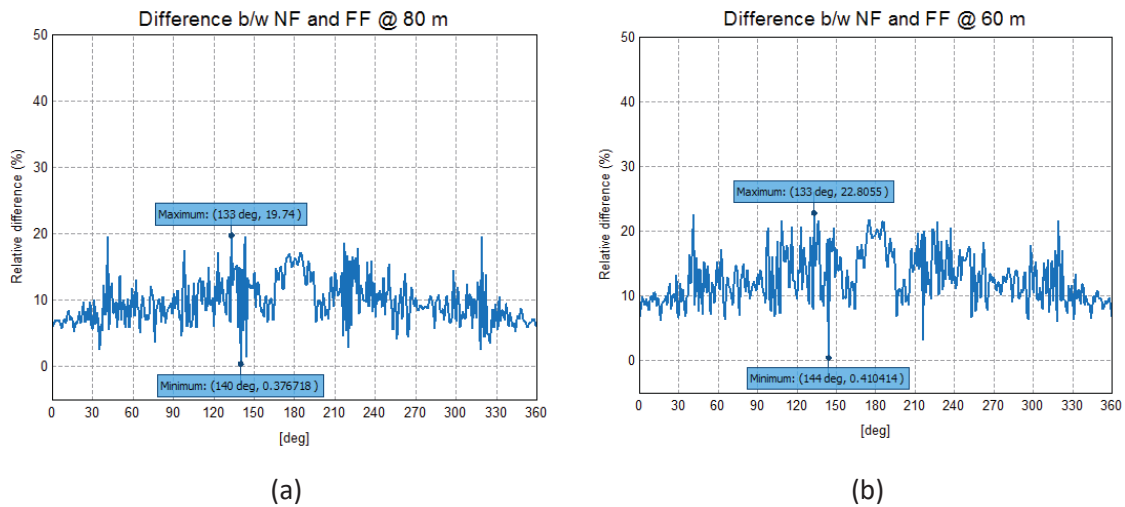


Figure 4-22 : Relative percentage difference for each angle of the between the normalized E-field of the FF pattern compared to the E-field strength of the NF at (a) 80 m and (b) 60 m.

The comparison is then performed at distances of 80 m and 60 m. The radiation patterns and the electric-field strength at these corresponding distances are plotted in Figure 4-21. The average discrepancies for a distance of 80 m and 60 m is 0.80 dB and 1.03 dB respectively. From the point of view of a very restrictive interpretation), at distances smaller than 60 m from the radiation source, we can consider ourselves within the near-field boundary.

4.4.1.2 Quarter-scale model

Henceforth, the previous study shall be applied to the same canonical model brought, this time, to a quarter-scale. The aim of downsizing the vehicle structure is to observe the impact of the car size on the near-field to far-field boundary. Moreover, the reduced dimensions lead to a lighter numerical model and can, hence, be included in a simulated propagation channel model to investigate the effect of near-field elements without exceeding the memory limitations. According to the Fraunhofer expression, we expect the far-field region to be situated beyond 5 m in the quarter-scale scenario.

The far-field radiation pattern is plotted both in the horizontal (cut $\theta=90^\circ$) and vertical plane (cut $\phi=0^\circ$). The electric-field strength, expressed in dBV is compared to the radiation pattern at 20 m and 5 m respectively. Here also, the difference between the two plots for every single angle is measured and plotted. This mean of discrepancies in the patterns must be below the acceptability criterion of 1dB for us to consider that the far-field boundary is reached. The average difference between the near electric-field strength and the normalized far-field pattern for a distance of 10 m and 5 m is 0.7 dB and 1.3 dB respectively. We can infer, from these results, that elements found within sphere of 5 m radius should be considered as near-field scatterers.

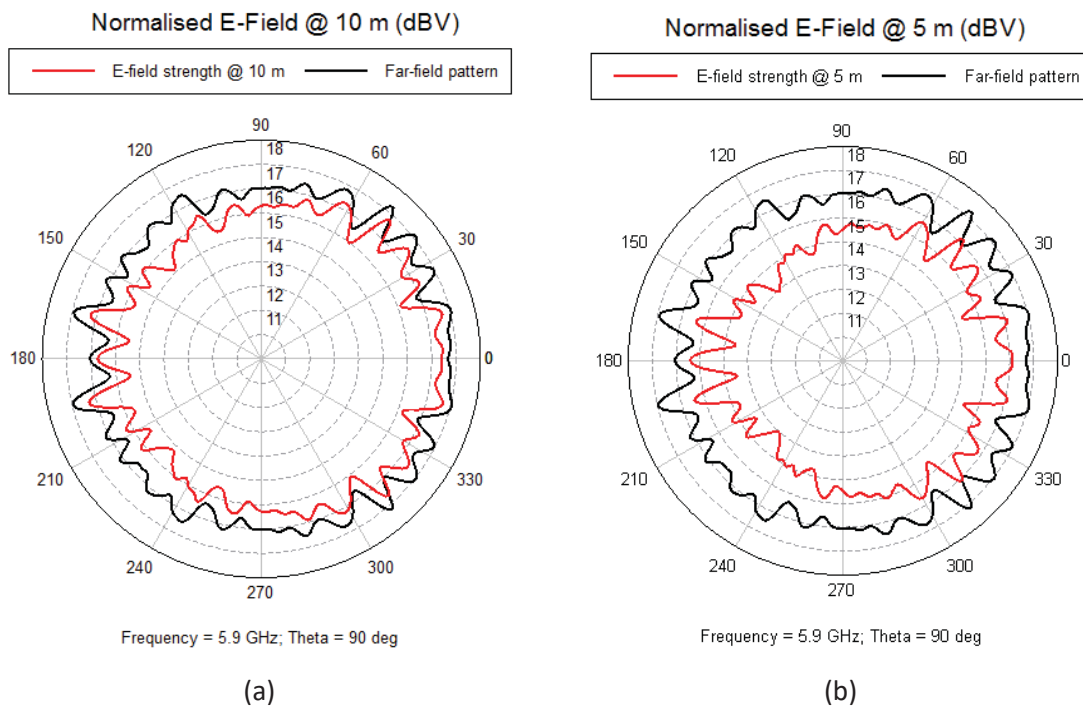


Figure 4-23 : The normalized E-field of the FF pattern compared to the E-field strength of the NF at (a) 20 m and (b) 5 m for a quarter-scale scenario.

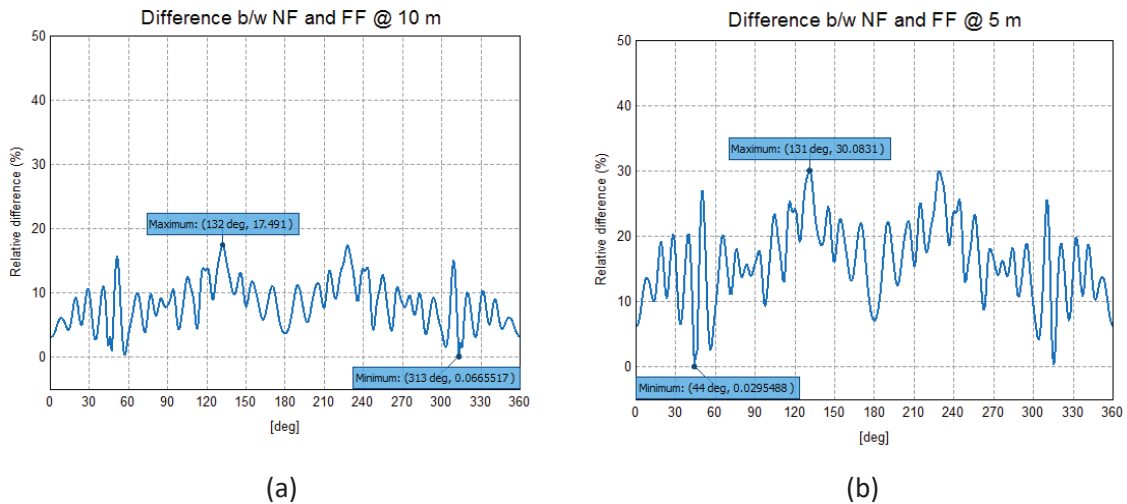


Figure 4-24 : Relative percentage difference for each angle of the between the normalized E-field of the FF pattern compared to the E-field strength of the NF at (a) 20 m and (b) 5 m for a quarter-scale scenario.

4.4.1.3 Conclusions

In the light of what we have seen in this section, we can infer that the electrical size of the antenna increases due to the coupling effect with the vehicle body. Therefore, the radiating element is not merely the antenna but the antenna and neighboring part of the vehicle where the antenna is implanted. The distribution of the surface current gives us a good idea of how electrically large is our effective antenna. In this work, we have only considered the case where the antenna is placed on the roof on a vehicle structure. For in-body integrated antenna, an increase in the electrical size of the vehicle and antenna system is expected and can be worth a study. Nevertheless, from what we have seen, a good estimation of the far-field delimitation zone can be obtained. For the full-scale scenario, we predict the far-zone to be situated at a distance of 60 to 80 m while it would be between 10 m and 5 m for the quarter-scale scenario. For simplification purposes, we set the near-field to far-field field boundary at 5 m for the quarter-scale scenario.

Henceforth, the impact of having scattering elements in the near field zone of a radiating element will be evaluated. The quarter-scale vehicle structure will be considered in the next section due to limited computational resources since an integral propagation scenario with diffracting scatterers will be treated.

4.4.2 Limitations of using far-field pattern in the presence of near-field elements and a proposed method to mitigate their effect

Knowing how to assess the far-field to near-field boundary, we shall now find a liable method to represent at best an integrated antenna on the vehicle in our simulated propagation channel model. The most precise simulation result would of course be obtained if the vehicles on which the antennas are mounted are included in the whole propagating environment. This would be of course too demanding in computational resources and this is the reason why the choice of representing the radiating elements by their far-field radiation pattern is maintained. In this section, we will present the limitations of this method when scatterers are found in the near-field zone of the effective antenna and propose a mechanism to mitigate the impact of the received power differences in the presence of the so-called “near-field scatterers”.

A generic propagation scenario containing 25 diffracting elements as shown in figure 4-25 is developed to highlight the posed problem.

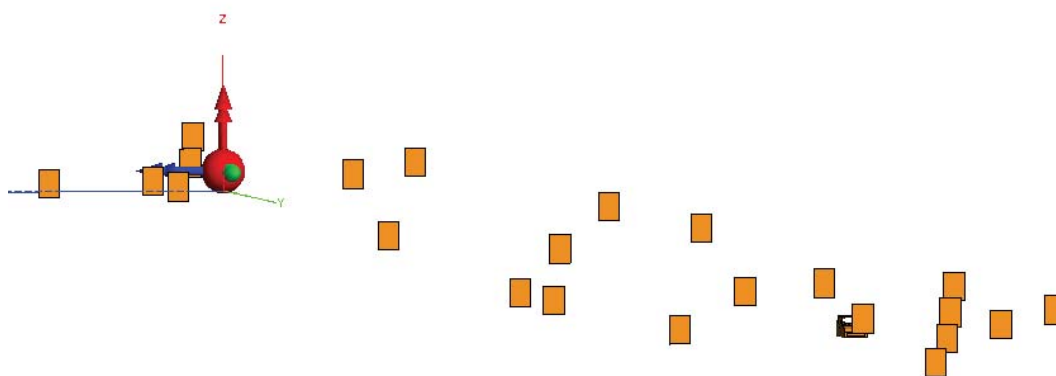


Figure 4-25 : Generic propagation scenario downsized to quarter scale

In this case no limitation in the positioning of the scatterers, with respect to antenna positions, was made and hence some can be found in the close vicinity of the radiating elements. 20 configurations of scatterers were chosen with a random positioning of the diffracting elements between the transmitting and receiving antenna. The characteristics, listed in table 4-3 were chosen for this particular generic scenario.

Table 4-3 : Characteristics of the generic propagation scenario

Total number of scatterers		25
Type of scatterers	N_{IN}	15
	N_{OUT}	10
Number of lines		5
Random distribution of scatterers	N_{IN}	U [0 , 75] m
	N_{OUT}	U [-15 , 0] m
	N_{OUT}	U [75, 90] m

The complete scenario was downsized to a quarter scale to fit to computation resources limitations as in this section, all simulations will be performed with the rigorous method MLFMM. Our methodology to investigate the influence of near-field elements when using far-field radiation pattern is described as follows:

- Case 1: MLFMM with both Tx and Rx represented by radiation patterns

In the first case, we use the transmitter as point source and the receiver as a perfectly-matched receiving antenna. The pair is characterized by their respective radiation pattern. The far-field pattern is obtained by simulating a monopole at the center of the rooftop of quarter-scale vehicle structure. We are in the same configurations as in propagation channel characterization in the previous chapter. Hence, the received power is directly obtained in the output files generated by FEKO.

- Reference case: MLFMM with the Tx modelled with its radiation pattern and the Rx with the antenna mounted on the vehicle structure

In the reference case, only the transmitting antenna is represented by its far-field pattern. On the other hand, at the receiving end the complete radiating element consisting of the vehicle structure with a monopole antenna mounted on its rooftop is included in the scenario. The monopole is loaded with its conjugate impedance such that all power dissipated in it provides us with the receiving power without any mismatch. Hence, results from case 1 can be directly compared to those obtained in case 2. This will be our reference scenario as presence of near-field elements is directly taken into account.

- Case 2: MLFMM with Tx modelled by its radiation pattern and the Rx with a radiation pattern including near-field elements

As in the previous cases, the transmitter is modelled by a point source represented by the radiation pattern of a quarter wavelength monopole mounted on a car. At the receiving end, all diffracting scatterers that are found within the near-field zone are spotted and simulated along with the car structure and antenna system. The resulting radiation pattern would of course differ from the one simulated with only the vehicle model and antenna in free-space. This modified pattern, taking into account the impact of near-field elements, is used as a perfectly matched receiving antenna. The power received from this configuration will allow us to verify if the preliminary inclusion of near-field elements during the simulation of the radiation pattern can help to reduce the gap relative to the reference case.

Table 4-4 : Summary of the received power in dB for the three cases

Scenario No.	Case 1	Reference case	Case 2	Difference in dB (Case 1-Reference case)	Difference in dB (Case 2- Reference case)
1	-91.9	-85.2	-81.9	-6.7	3.3
2	-82.5	-83.4	-83.4	0.9	0
3	-83.3	-81.9	-82.6	-1.4	-0.7
4	-86.8	-81.9	-84.0	-4.9	-2.1
5	-81.5	-86.8	-85.7	5.3	1.1
6	-88.1	-83.0	-82.8	-5.1	0.2
7	-87.9	-81.5	-82.2	-6.4	-0.7
8	-82.8	-83.3	-83.3	0.5	0
9	-88.7	-83.9	-82.9	-4.8	1
10	-90.4	-84.0	-82.3	-6.4	1.7
11	-89.1	-83.9	-82.3	-5.2	1.6
12	-92.0	-82.1	-78.2	-9.9	3.9
13	-86.1	-89.9	-88.1	3.8	1.8
14	-87.0	-85.4	-83.6	-1.6	1.8
15	-87.9	-84.1	-83.0	-3.8	1.1
16	-82.5	-83.4	-83.4	0.9	0
17	-86.1	-85.2	-85.2	-0.9	0
18	-88.6	-81.5	-79.4	-7.1	2.1
19	-88.8	-83.7	-82.4	-5.1	1.3
20	-88.4	-85.1	-84.6	-3.3	0.5

In Table 4-4, the results obtained from the 20 randomly selected propagation channels are listed. The received power for case 1, case 2 and the reference case are expressed in dB. The power ratio of case 1 against the reference case and case 3 against the reference case are also tabulated after being expressed in dB. In perfect conditions, i.e, in the absence of near-field scatterers, we expect

the power ratio between case 1 and the reference case to approach 1 (0 in dB). The lines in the table highlighted in blue are particular scenarios where the near-field elements were absent. By the way, we can notice that the power ratio, as expected, for case 1 against the reference case for these scenarios are intrinsically small as the near-field interactions are minor. Globally, our method to limit the errors due to near-field interactions is effective as we considerably reduce the power ratio when we simulate our propagation channels with case 3 with scenario 14 making the sole exception.

4.4.2.1 Conclusions

In this subsection, we have seen that when substituting directly the antenna mounted on a vehicle with its radiation pattern, the interactions with the elements in the near-field will no longer be valid. If we consider near-field scatterers in our simulations of (antenna + vehicle system) with a rigorous method (MLFMM), we re-establish the correct interactions between the simulated vehicle and the NF-field elements. Thus, we obtain a radio link that approaches the right one. It, for sure, makes the simulation a bit more complicated. On the other side, it all depends on the degree of approximation that we are ready to tolerate. Another solution is to apply the following constraints to all of our propagation channels such that none of the scatterers are positioned within the near-field to far-field boundary, but it would be equivalent to not account for a possible scenario.

4.5 REFERENCES

- [1] H. Tazi. "Integration of Numerical Simulation Approaches in the Virtual Development of Automotive Antenna Systems:" PhD. Thesis, Technische Universität München, 2012.
- [2] R. F. Harrington. Field Computation by Moment Methods. Wiley-IEEE Press, 1993.
- [3] A. Taflov and S. C. Hagness. Computational Electrodynamics: The Finite-Difference Time-Domain Method, Third Edition. Artech House, 2005.
- [4] J. M. Jin. The Finite Element Method in Electromagnetics, 2nd Edition. Wiley-IEEE Press, 2002.
- [5] P. H. Pathak. High-frequency techniques for antenna analysis in Proceedings of the IEEE, vol. 80, pages 44–65, Jan. 1992.
- [6] Xin-Qing Sheng; Wei Song, "Hybrid Methods," in Essentials of Computational Electromagnetics , 1, Wiley-IEEE Press, 2012, pp.243-276
- [7] FEKO user manual, v7.0, www.feko.info.
- [8] R. F. Harrington, "Matrix methods for fields", Proc. IEEE, vol. 55, no. 2, pp. 136-149, Feb. 1967.
- [9] J. M. Song, C. C. Lu, W. C. Chew, "Multilevel fast multipole algorithm for electromagnetic scattering by large complex objects", IEEE Trans. Antennas Propagat., vol. 45, no. 10, pp. 1488-1493, 1997.
- [10] L. Ekiz, T. Patelczyk, O. Klemp, C. F. Mecklenbrauker, "Compensation of vehicle-specific antenna radome effects at 5.9 GHz", Industrial Electronics Society IECON 2013 – 39th Annual Conference of the IEEE, pp. 6880-6884, 2013.
- [11] D. Sharma, V. N. Saxena and P. Singh, "A simple plasmonic based rectangular microstrip patch antenna resonating at 5.9 GHz," 2015 International Conference on Signal Processing and Communication (ICSC), Noida, 2015, pp. 386-389.
- [12] M. Gallo, S. Bruni and D. Zamberlan, "Design and measurement of automotive antennas for C2C applications," 2012 6th European Conference on Antennas and Propagation (EUCAP), Prague, 2012, pp. 1799-1803.

- [13] M. A. Bueno Diez and S. Lindenmeier, "A Highly Efficient Car2Car-multiband rooftop automotive antenna," 2015 IEEE International Symposium on Antennas and Propagation & USNC/URSI National Radio Science Meeting, Vancouver, BC, 2015, pp. 1606-1607.
- [14] E. Condo Neira, J. Carlsson, K. Karlsson and E. G. Ström, "Combined LTE and IEEE 802.11p antenna for vehicular applications," 2015 9th European Conference on Antennas and Propagation (EuCAP), Lisbon, 2015, pp. 1-5.
- [15] M. Ibambe Gatsinzi, F. Jouvie, X. Bunlon and A. Azoulay, "Study of a 5.8 GHz frequency band patch antenna integrated into a vehicle for automotive DSRC applications," 2007 International Conference on Electromagnetics in Advanced Applications, Torino, 2007, pp. 543-546.
- [16] C. Oikonomopoulos-Zachos, W. Simon, E. Stavrou, J. Siemons, J. Kunisch and M. Geissler, "Efficient EM-simulation of large vehicles for Car2Car communication," 2016 10th European Conference on Antennas and Propagation (EuCAP), Davos, 2016, pp. 1-5.
- [17] M. B. Diez, P. Plitt, W. Pascher and S. Lindenmeier, "Antenna placement and wave propagation for Car-to-Car communication," 2015 European Microwave Conference (EuMC), Paris, 2015, pp. 207-210.
- [18] S. Imai, K. Taguchi, T. Kashiwa and T. Kawamura, "Effects of car body on radiation pattern of car antenna mounted on side mirror for inter-vehicle communications," 2014 IEEE Antennas and Propagation Society International Symposium (APSURSI), Memphis, TN, 2014, pp. 601-602.
- [19] D. Quack, M. Meuleners, S. Hommen and Christoph, "Simulation-based evaluation of MIMO antenna systems in car-to-car communication," The 8th European Conference on Antennas and Propagation (EuCAP 2014), The Hague, 2014, pp. 3049-3052.
- [20] Remcom Inc., "<http://www.remcom.com>".
- [21] L. Reichardt, J. Maurer, T. Fugen and T. Zwick, "Virtual Drive: A Complete V2X Communication and Radar System Simulator for Optimization of Multiple Antenna Systems," in Proceedings of the IEEE, vol. 99, no. 7, pp. 1295-1310, July 2011.
- [22] L. Reichardt, T. Fugen and T. Zwick, "Influence of antennas placement on car to car communications channel," 2009 3rd European Conference on Antennas and Propagation, Berlin, 2009, pp. 630-634.

Chapter 5 : MODELLING OF THE IEEE 802.11P PHY LAYER

System performance evaluation and accurate comparison of different antenna integration efficiency on the quality of communication implies a correct description and implementation of the physical layer (PHY layer) of the communication system. Performance evaluation of V2X systems can be carried out by measurements with field operational tests, on-bench channel emulation together with physical modems and finally computer simulation. In this chapter, a computer-based simulation of the physical layer of the IEEE 802.11p standard, developed in [1], will be described to complete the communication chain constituting of the propagation channel and the radiation pattern of the mounted antennas of the transmitter and receiver. It should be noted that the investigation of the validation and the reliability of the PHY layer simulation used in this work will not be detailed here as it is out of scope of this thesis. Nevertheless, readers can refer to [1], [2] [3] to obtain additional information.

Performance achieved with perfect receiver design, under influence of various propagation channel parameters and different antennas on the overall system behavior will be demonstrated based on numerical simulation results.

5.1 DESCRIPTION OF THE PHY LAYER

The PHY layer constitutes an interface between the MAC layer and the physical RF support that allows to send and receive packets. The PHY layer of the IEEE 802.11p standard can be divided into two sub-layers, namely the Physical Layer Convergence Protocol (PLCP) which grants the possibility of communicating with the MAC layer. Besides, it includes a convergence process that transforms the Packet Data Unit relayed through the MAC layer to compose the transmitted OFDM frame, called the Protocol Packet Data Unit (PPDU). The second sub-layer is known as the Physical Medium Access which is responsible for transmitting the data packets into the wireless channel. It manages data encoding and performs modulation [4], [5].

5.1.1 The transmitted packet structure

The PPDU includes the preamble, the signal field and the DATA field as depicted in Figure 11 in chapter 2. The preamble, marking the beginning of the packet, consists of 10 short training symbols (STS) and two repetitions of a long training sequence (LTS). They are separated by a Guard interval, increasing their robustness to Inter-Symbol Interference (ISI). The STS are responsible for appropriate antenna selection in case of antenna diversity and to correct timing and frequency offset. The long training symbols are used for channel estimation and for fine tuning of the frequency acquisition in the receiver.

The signal field is used to carry information pertaining to the data rate and the length of the packet. It is composed of the Rate, Length and Tail fields which determine the coding data rate, the number of octets in the PSDU (PHY layer Service Data Unit), and a six bits field respectively. The latter,

usually set to zero, are used to synchronize the descrambler in the receiver and to return the convolutional encoder to its zero state. Finally, the data field represents the encapsulated data transmitted over the wireless channel. It is composed of four fields: Service, PSDU, Tail and padding bits fields.

5.1.2 Architecture of the transmitter

In this section, an overview of the transmission structure will be given. The block diagram of the transmitter is depicted in chapter 2. In a first place, the binary source of data is scrambled to prevent a long bit sequence. The scrambler uses the polynomial generator $S(x)$ to produce a sequence of 127 bits as follows:

$$S(x) = x^7 + x^4 + 1 \quad (\text{Eq. 5.1})$$

The output of the scrambler is passed through the convolutional encoder, with $\frac{1}{2}$ coding rate, to introduce a forward error correction (FEC). Adding redundancy to the transmitted bit stream can help to reduce error induced by ICI and ISI. In order to reduce the number of transmitted bits and increase encoder bit rate, a puncturing element is applied to the convolutional encoder output, resulting in coding rates of $\frac{3}{4}$ and $\frac{2}{3}$. Puncturing resides in omitting on purpose some of the coded bits on the transmitting sides and replacing them by “zeros” in the convolutional decoder on the receiving side. The coded data are then interleaved using a process that composes of a redistribution of the coded bits in time or frequency in order to achieve desirable bit error distribution after demodulation. Interleaving is used to cope with the correlated channel noise such as burst errors and fading.

Afterwards, the interleaved data stream is modulated to complex symbols, using binary phase shift keying (BPSK), quadrature phase shift keying (QPSK), 16- and 64-quadrature amplitude modulation (QAM) as defined by the standard. The choice of mapping and coding affects directly the data rate of the transmitted signal which can vary from 3 MB/s to 27 MB/s (as indicated in Table 3 in section 2.2.3). The total number of available subcarriers is 64 but only 52 information carriers are used for mapping. Before applying IFFT, 4 carriers out of 52 are selected to carry the pilot signal. The pilot symbols are used to estimate the channel and examine the changes made to the transmitted signal. Pilot subcarriers are used to make a robust detection in receiver against frequency offsets and phase noise. To transmit the data on the subcarriers, the OFDM symbols are converted from the frequency domain to the time domain using the IFFT. A simplified structure of the transmitter block is illustrated in Figure 5-1.

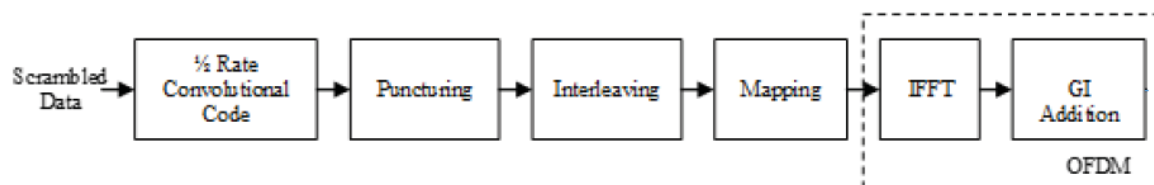


Figure 5-1: Structure of the transmitting block

5.1.3 Receiving process

In this section, we will take a closer look at the main receiver blocks and describe how they are implemented in our case. The receiver, basically reverses the processing performed at the transmitter besides time and frequency synchronization, equalization and the channel estimation. The outlines of the receiver blocks are given in Figure 5-2.

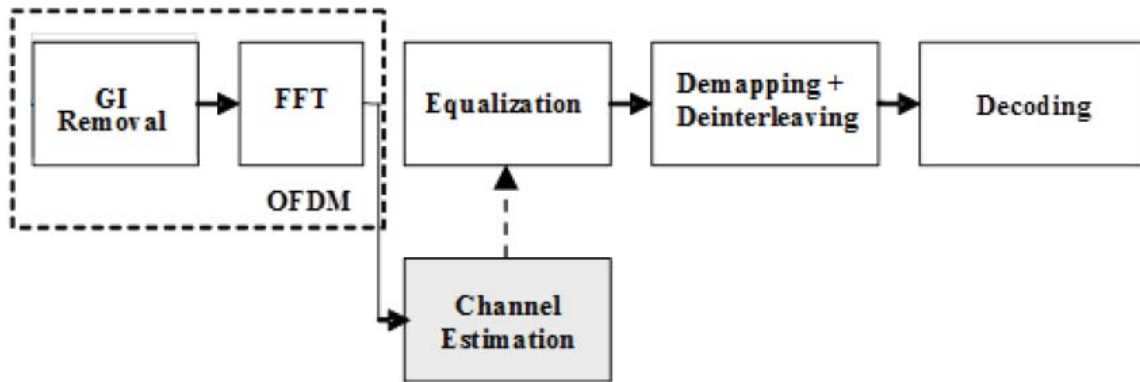


Figure 5-2: The structure of the receiving block

According to the frame structure of IEEE 802.11p, the whole signal processing in the receiver can be divided into two parts: processing of the preamble field to estimate the channel and decoding of the signal and data fields. In the first place, a serial-to-parallel conversion is performed to separate the preamble and the signal field from the receiving signal. The short training symbols and the long training symbols, from the preamble, are used to perform coarse and fine time as well as frequency synchronization.

In order to demodulate the signal, the time-domain symbols have to be converted into the frequency domain to yield the 64 parallel subcarriers by applying a 64-FFT. Prior to that, the cyclic prefix (CP), situated at the beginning of each OFDM symbol is removed. CP is used to eliminate ISI between consecutive OFDM symbols. Afterwards, the channel is estimated before the equalization step to perform accurate detection. Channel estimation technique plays an important role for the design of any communication systems. Therefore, generally speaking, the accuracy of the channel estimation decides system performance. However, the radio propagation channels in a V2V context can be easily influenced by the rapidly changing environment. It is thus hard to foresee the variation of channels. Accurately and efficiently estimating vehicular channels is very challenging. Several tracking algorithms are proposed in the literature [6], [7]. In the next step, the estimated channel is used for equalization. Generally, techniques such as zero-forcing equalization or MMSE (Minimum Mean Square error is used) before the signal is again parallel-to-serial converted. Then, the complex symbols are demapped to binary data in order to determine the most likely transmitted bits. Afterwards, the data is deinterleaved by the deinterleaver block, which performs the inverse operation of the interleaver block on the transmitting side. Recommended by the IEEE 802.11 standard, the Viterbi decoder is then used to decode the convolutional cods. There exists two types of Viterbi decoder: the soft decision and hard decision version. Finally, descrambling can be performed before comparing the received data with the transmitted data to evaluate the quality of service in terms of packet or bit error rate.

5.1.4 Computer implementations

After a brief description of both the transmitting side and the receiving side of the 802.11p physical layer, the computer implementation of both of them with Matlab will be depicted. Moreover, a focus on simplifications and assumptions considered in simulation will be made in this section. As we consider perfect synchronization at the receiver and known transmission parameters, the packets are generated with neither the short-training sequence (STS) nor the SIGNAL field. Consequently, the preamble of the simulated transmitted packet consists only of the long-training sequence (LTS) $[T_1, T_2]$ and the guard interval (G12).

The first step to generate the DATA symbols is to set the PSDU length, L_{PSDU} (in number of bytes). Afterwards, we compose the DATA field from the 16 SERVICE bits (which are generally set to zero), the PSDU, the tail bits, and the pad bits. The number of DATA symbols, N_{DATA} , transmitted is a function of the packet length and the data rate and is given by:

$$N_{DATA} = \lceil (16 + 8 \times L_{PSDU} + 6) / N_{DBPS} \rceil \times N_{DBPS}, \quad (\text{Eq. 5.2})$$

where N_{DBPS} is the data bits per OFDM symbol and is reported in Table B in section 2.2.3 for each modulation scheme. Also, the " $\lceil \cdot \rceil$ " function, called the ceiling function, denotes the smallest integer greater than, or equal to the parameter.

The PSDU is composed of a binary random sequence of length $8 \times L_{PSDU}$. The tail field represents six bits of zero, which are required to return the convolutional encoder to the zero state. To complete the last OFDM symbol, a number of pad bits composed of zero bits are appended after the tail bits. The number of pad bits, N_{PAD} , can be determined from the number of OFDM symbols, the PSDU length, L_{PSDU} , the number of SERVICE bits ($N_{SERVICE}=16$), and the number of tail bits ($N_{TAIL}=6$):

$$N_{DATA} = N_{SERVICE} + 8 \cdot L_{PSDU} + N_{TAIL} + N_{PAD} \quad (\text{Eq. 5.3})$$

The number of OFDM symbol, N_{SYM} is given by:

$$N_{SYM} = \frac{N_{DATA}}{N_{DBPS}} \quad (\text{Eq. 5.4})$$

For instance, a transmitted packet in Mode 3 (data rate of 6Mb/s) with a packet length of 100 bytes will have 18 DATA symbols.

Besides, on the receiving side, the frequency and time synchronization were considered perfect in the simulated PHY layer. In addition, to reduce computational complexity, single-tap, ZF equalizer, hard decision demapping and Viterbi decoder with hard decision were employed. Advanced channel tracking algorithms in recent receiving modems are equivalent to the performance of simulated receivers considering perfect channel State Information (pCSI). Such a receiver was taken into account in our simulation tool. This channel estimation scheme can be considered as best case scenario.

5.2 TIME SEQUENCES GENERATION

As mentioned earlier, the packets generated contain neither the short-training sequence (STS) nor the SIGNAL symbol. The number, N , of OFDM symbols constituting the transmitted data is calculated as per Eq. 5.4. So, considering the two training symbols of the LTS, the time duration of the preamble is $16 \mu\text{s}$. According to our implementation, the time duration of a whole packet is:

$$T_{packet} = 16 \mu\text{s} + (8 * N_{SYM}) \quad (\text{Eq. 5.5})$$

Thus, together with the preamble, the duration of the transmitted packet in Mode 3, with a frame length of 100 bytes, is $160 \mu\text{s}$ ($16 \mu\text{s} + 18 \times 8 \mu\text{s}$).

To evaluate the impact of different antenna configurations and PHY layer system parameters on the performance of V2V communication, we use the time-varying channel responses, obtained in chapter 3, to evaluate the PER. In fact, the time sequences obtained from FEKO propagation channel simulations were sampled at $T_s = 400 \mu\text{s}$. However, the sampling period, T_{V2X} , of V2X communications working within a 10 MHz bandwidth is $T_{V2X} = 1/10 \text{ MHz} = 100\text{ns}$. Consequently, an interpolation must be performed in order to obtain the correct sampling rate, leading to a total time duration of the sequence of 0.4 s as 1000 snapshots were considered. Following interpolation, we divide the time-sequence into smaller sequences corresponding to the duration of the desired packet length. For a frame with a packet length of 100 bytes transmitted in Mode 3, we obtain 2497 independent channel sequences of $160 \mu\text{s}$ each.

To evaluate the quality of the communication in terms of PER, only the short-time fading was used. Furthermore, the average received power of each independent packet is evaluated before being subtracted to the sensitivity level to calculate the SNR of each transmitted packet at the receiver. The sensitivity level as a function of the transmitting mode is fixed, here, according to data obtained in the data sheet of the modem that will be used for field trials in the next chapter. Here, the sensitivity, which is the minimum power level required for the receiver to detect transmitted packets is fixed at -92 dBm . Then, the Monte Carlo algorithm is used to estimate the PER performance of each received packet for the entire driving scenario. Each packet is passed 2000 times in the PHY simulator providing a significant result for PER above the order of 5×10^{-3} . The procedure is depicted in Figure 5-3.

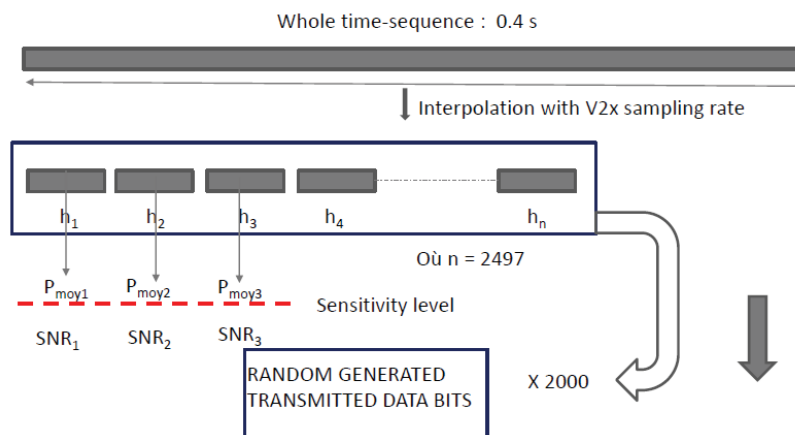


Figure 5-3: Steps of the process to obtain independent channel sequences (Example of a communication in Mode 3 with a packet length of 100 bytes)

5.3 SIMULATION RESULTS WITH DIFFERENT ANTENNAS

After a succinct description of the PHY layer and its implementation in simulation, we will analyze the contribution of different antenna configurations on the performance of the V2V communication. The developed simulation tool is, hereafter, completely constituted with all the three core blocks forming the communication chain: the propagation channel, the integrated antenna radiation patterns and the PHY layer of the transmitter and receiver. Therefore, in this section, antenna configurations will be tested in all simulated type of propagation channels. This investigation should enable us to guide our choice of antenna technology and their integration on vehicles.

This part of the manuscript will be subdivided into three parts. In a first place, a presentation of the different antenna configurations in terms of their radiation patterns will be taken into consideration. Afterwards, the performance in terms of received power in each propagation environment (rural, highway and urban) will be given. Finally, the quality of communication in terms of PER will be given for the overall configuration.

5.3.1 Antennas under test

Antenna placement has a significant importance on the performance of the communications. With the help of simulations, antenna positioning and technology can be optimized. Their performance can be thus assessed and anticipated. In this subsection, six different antenna patterns will be overviewed. In the first subsection, relatively directive patch antennas will be analyzed followed by antennas with rather omnidirectional patterns. For all antenna configurations, measured radiation pattern will be used in our propagation channels.

5.3.1.1 Patch antennas

The same patch antenna, presented in chapter 4 in section 4.2.1 and 4.3.2, is characterized in two different positions inside the vehicle. In the first configuration, the antenna was placed on the front windscreen, with its primary lobe pointing in the driving direction. In the second configuration, the patch antenna was positioned in such a way that the radiation pattern points away from the driving direction. The radiation pattern in both elevation and in the azimuthal plane is shown in Figure 5-4. It should be noted that according to our defined references in our simulated propagation channel, the axis of travel is in $\theta = 90^\circ$. For simplification purposes, the antenna placed on the rear window will be referred to as "Patch 1" whereas the one stuck on the front windscreen will be indicated as "Patch 2". All antenna references will be summarized in Table 5-1 later in this section anyway.

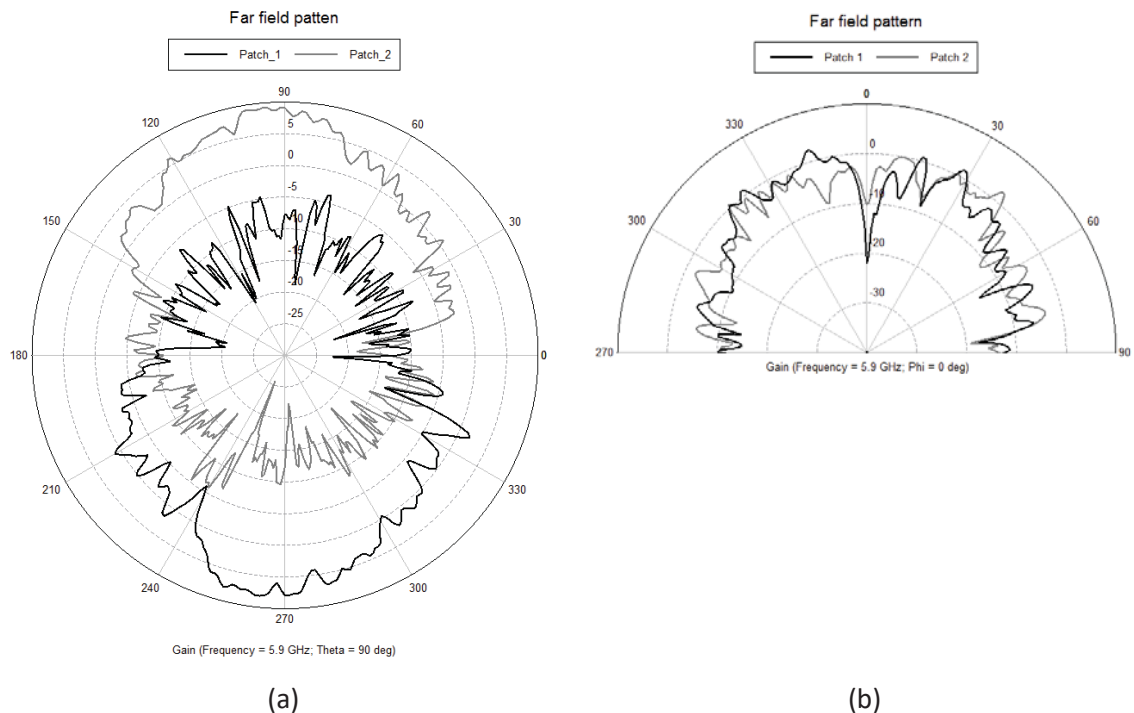


Figure 5-4: Radiation patterns of Patch 1 and Patch 2 antennas both in (a) Azimuthal plane (Theta=90°) and (b) in the elevation plane (Phi=0°).

5.3.1.2 Omnidirectional antennas

In this section, two different shark-fin antennas provided by our supplier will be studied. In each antenna, there were 2 monopole-typed radiating elements dedicated to V2X communications. The main reason behind having two integrated antennas in one shark-fin module was to dedicate the best performing one to the control channel which conveys security-prone messages whereas the other one shall be used for the service channel. The monopoles in the first shark-fin will be referred to as “Omni 1” and “Omni 2” respectively while the other pair of V2X antennas will be, henceforth, called “Omni 3” and “Omni 4”. It must be noted, that in the first shark fin component, a non-grounded metallic wall was placed between the two “Omni1” and “Omni2” V2X antennas with the goal to increase their gain in corresponding directions. It was initially designed and thought in order to anticipate antenna diversity contributions. The metallic wall between the two V2X antennas is the only changing factor between the two shark-fin components. Thus Omni 1 antenna will tend to have higher gain in the driving direction (phi=90°) as compared to Omni 3 antenna whereas Omni 2 antenna is expected to bear higher performance in the opposite direction of motion than Omni 4 in that particular direction.

The measured radiation pattern of both V2X antennas of the first shark-fin module is presented Figure 5-5 in the horizontal (theta = 90°) and vertical (phi=0°) cut respectively. Although, meant to produce an omnidirectional pattern, these two antennas contain strong ripples and nulls in some directions.

First shark-fin module (Omni 1 & Omni 2)

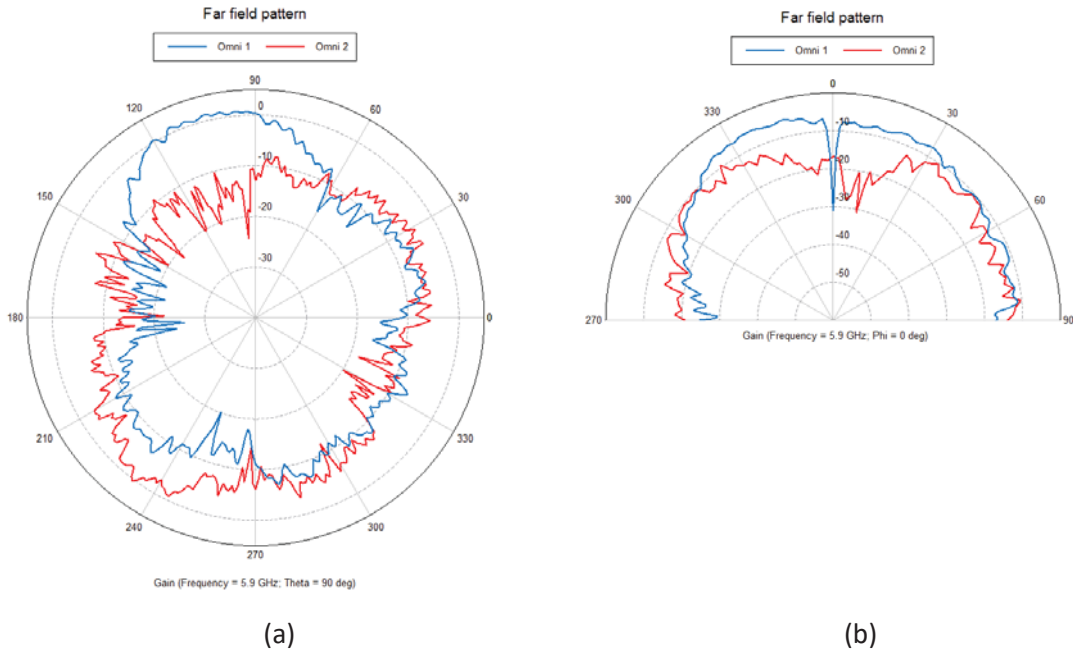


Figure 5-5: Radiation patterns of Omni 1 and Omni 2 antennas both in (a) azimuthal plane (Theta=90°) and (b) in the elevation plane (Phi=0°).

Second shark-fin module (Omni 3 & Omni 4)

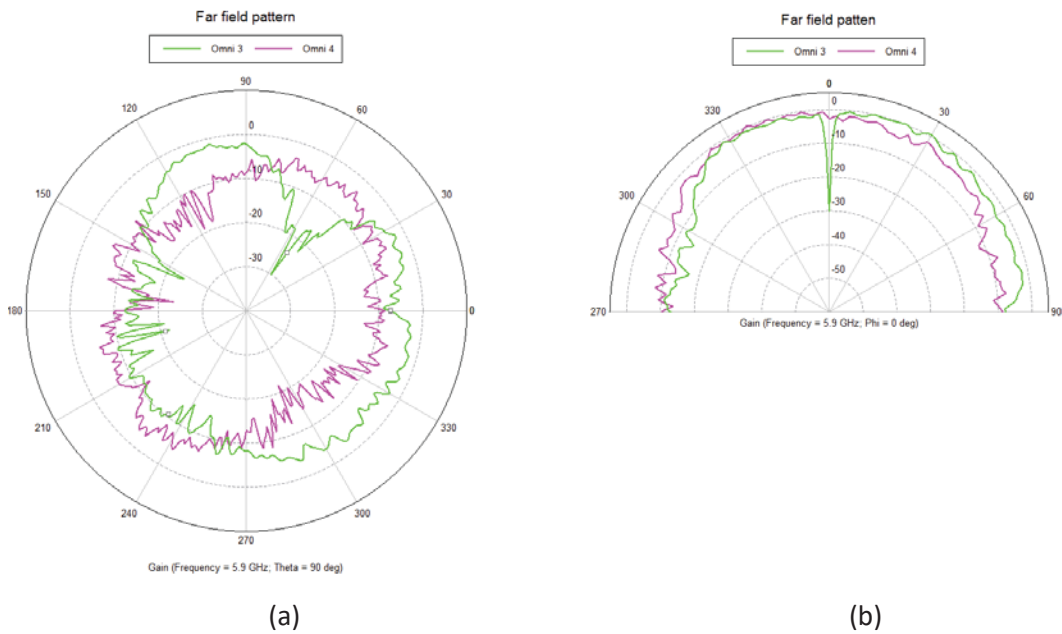


Figure 5-6 : Radiation patterns of Omni 3 and Omni 4 antennas both in (a) azimuthal plane (Theta=90°) and (b) in the elevation plane (Phi=0°).

5.3.1.3 Antenna configurations and use cases

In this subsection, we will describe the different configurations that will be used to test antenna performance in terms of received power or PER after the embodiment of the PHY layer. In all cases, except in configuration 1, the transmitting and the receiving antennas are the same. Indeed, in the first case, the patch antenna fixed on rear windscreen is used as the Rx and the one pointing the driving direction is used as the Tx. In all of our driving use cases, the transmitting and receiving vehicles move in the same direction (as suggested by a + sign in the velocity column in Table 5-2) with the Rx always in front of the Tx. Table 5-1 and 5-2 resume the antenna configurations and the driving use cases under investigation.

Table 5-1 : Antenna configurations

Configuration	Tx antenna	Rx antenna
Config. 1	Patch 2	Patch 1
Config. 2	Omni 1	Omni 1
Config. 3	Omni 2	Omni 2
Config. 4	Omni 3	Omni 3
Config. 5	Omni 4	Omni 4

Table 5-2 : Use cases and velocities of Tx and Rx

Use cases	Tx velocity	Rx velocity
Rural (NLOS)	+ 70 Km/h	+ 70 Km/h
Highway(NLOS)	+ 110 Km/hr	+ 110 Km/h
Urban (LOS)	+ 35 Km/h	+ 35 Km/h

5.3.2 Performance in terms of received power

In this subsection, we will study how different antenna patterns, presented earlier in this chapter, influence the quality of the received signal. This investigation will be carried out in the three propagating scenarios, characterized in chapter 3. The 5 antenna configurations, listed in Table 5-1, are tested under the three use cases, summarized in Table 5-2. The transmitting power is fixed at 23 dBm for each configuration. In fact, the maximum power allowed as per the ETSI requirements for the control channel (CCH) is 33 dBm EIRP. Therefore, the input power transmitted to the Tx antenna will depend on the gain of the antenna used. Hence, we chose the transmitting power of 10 dB less than the maximum allowed as the patch antennas have a relatively high gain of about 8 dB in the main lobe.

The received power is thus given for the three propagating scenarios: rural, highway and urban environment respectively.

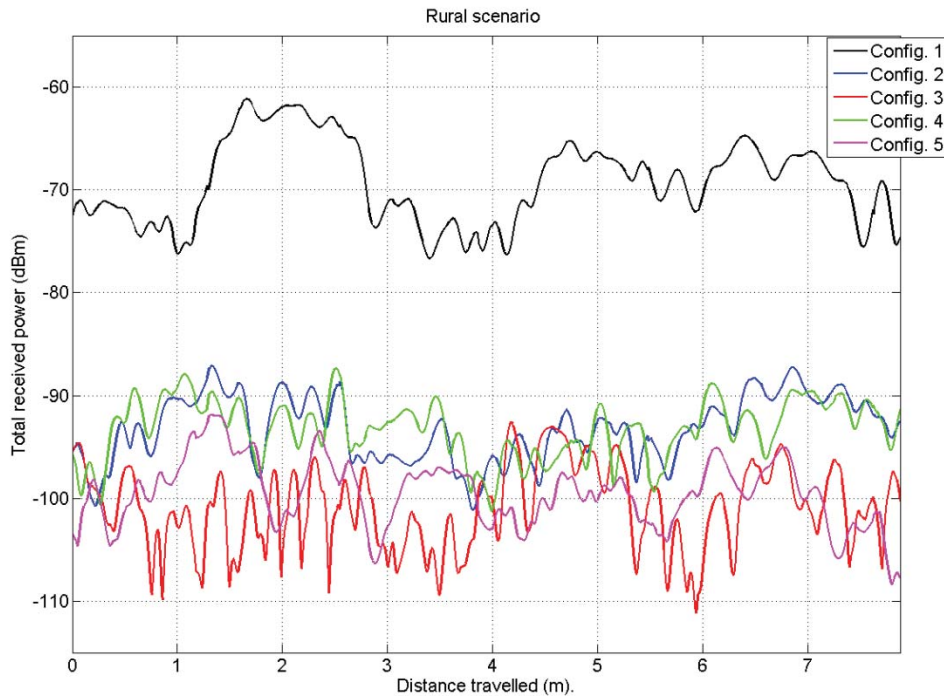


Figure 5-7 : Total received power for the 5 antenna configurations against travelled distance in a rural scenario.

The performance of the 5 antenna configurations in a rural scenario was the first use case to be studied. In Figure 5-7, the total received power is presented against distance travelled by the Rx. As in this situation, the Tx and the Rx have the same speed, they both travel about 8 m, considering the time-duration of the 1000 snapshots simulated. The rapid fluctuations in the received power prove the dynamic nature of the propagating environment. As expected, the best performance eventually belongs to the directive patch antenna pointing towards each other. For a rural scenario, with constraint angular spread, the front to back ratio of each of the pseudo-omnidirectional antennas' radiation pattern will be the predominant factor contributing to the performance of communication.

In Figure 5-8, the total received power for the 5 antenna configurations are plotted for the highway simulated propagation channel. We can notice Config. 2 performs better than the other omnidirectional antennas as the gap in terms of received power has considerably increased. The presence of a higher number of multipath components arriving in different directions contributes to an increase in the average received power for the 4 omnidirectional antennas as compared to the rural environment.

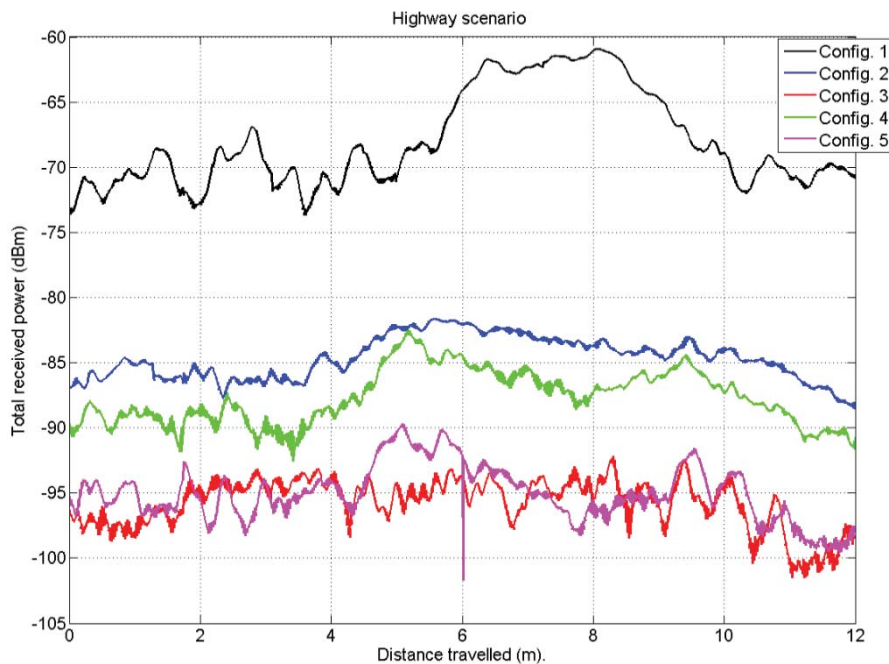


Figure 5-8 : Total received power for the 5 antenna configurations against travelled distance in a highway scenario.

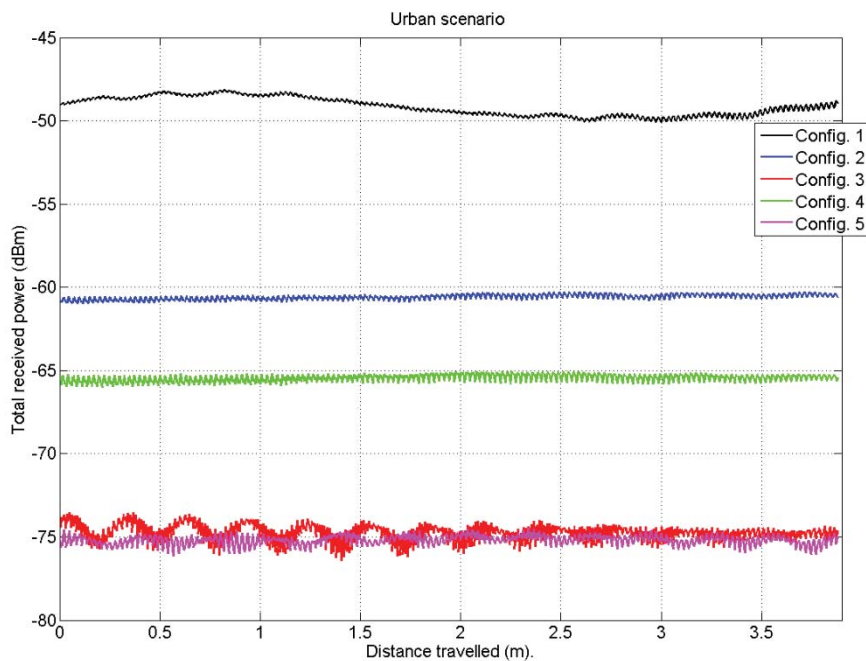


Figure 5-9 : Total received power for the 5 antenna configurations against travelled distance in a urban scenario.

In the urban configurations simulated in chapter 3, there is occurrence of a direct path from the transmitter to the receiver. The strong contribution of a line of sight makes the

received power to remain more or less constant throughout the whole simulated dynamic scenario as it can be noticed in Figure 5-9. The received power can be approximated by the Friis equation.

In this section, we have seen the performance of five different antenna configurations in terms of received power. The importance of characterizing antennas in different propagating scenario can be highlighted here. In section 5.3.3, the performance of the communications will be given in terms of packet error rate for different use cases and PHY layer parameters.

5.3.3 Performance in terms of PER

The results from the last block that remained to be considered in order to complete our simulated communication chain will be the heart of the subject in the rest of this chapter. Indeed, in this subsection, an example of a V2V communication in mode 3 with a packet length of 200 bytes will be given. Each of the 5 antenna configurations will be evaluated in a particular highway environment. In mode 3, we have a QPSK mapping and a coding rate of $\frac{1}{2}$, leading to a data rate of 6 Mb/s. With a packet length of 200 bytes, the duration of the transmitted packet is 288 μ s, obtaining thus 1387 independent channel sequences from the global simulated time-sequence of 0.4 s. Afterwards, each packet is passed through the PHY layer simulator 2000 times and PER henceforth evaluated.

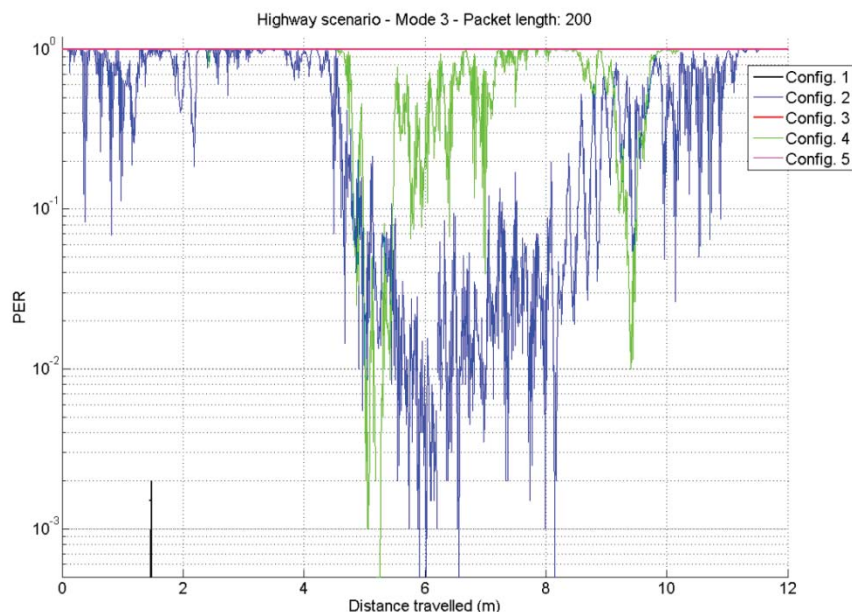


Figure 5-10 : PER results for the 5 antenna configurations in a highway scenario with a communication in Mode 3 and packet length of 200 bytes.

Figure 5-10 represents the PR estimation for the 5 antenna configurations for a distance of 12 m covered by the transmitter and receiver. As expected, Config. 1 with the patch antennas performs best as the average received power is well over the sensitivity level of -92 dBm using this modulation scheme. For the patch antennas, an average PER of almost 0 (except for 2 independent packets at a travelled distance of 1.5 m approximately) is obtained for the whole communication duration. We obtained an average PER of 0.52 with Config. 2 while Config. 4 gave rise to a mean

PER of 0.81 over the 12 m covered. Config. 3 and Config. 5 revealed to be the worst performing set of antennas as communication was impossible between the transmitter and receiver at an inter-vehicular distance of 300m, obtaining average PER of 1 with both of them.

In this study, we emit the hypothesis that a successful transmission occurs when the PER is less or equal to 0.1. A possible indication for system performance evaluation is to calculate the probability for which the PER is less than 0.1 for each antenna configuration on the considered period of time. Therefore, in the above example, we can deduce that Config. 1 has almost 100 % of success, followed by Config. 2 and Config. 4 with 32 % and 6 % of success respectively. According, to simulation results, Config. 3 and Config. 5 will both lead to unsuccessful communication.

5.4 SIMULATION RESULTS WITH DIFFERENT PHY LAYER PARAMETERS

In this section, the influence of the different parameters of the PHY layer, such as the data rate and the packet length, on the communication performance will be studied. For the sake of this study, the example presented in the previous subsection will be used as the reference case.

In the first place, we will study the effect of increasing the transmitted packet length to 1000 bytes. The results in terms of PER are plotted in Figure 5-11 for the 5 antenna configurations. We can observe an overall degradation of the performance of communication with an increase in the average PER except for Config. 1 which still has an optimal performance in this condition. Indeed, the mean PER for Config. 2 and Config. 4 have risen to 0.70 and 0.92 respectively. This results correspond to a decrease in the probability of success, falling from 32 % to only 11 % for the second antenna configuration.

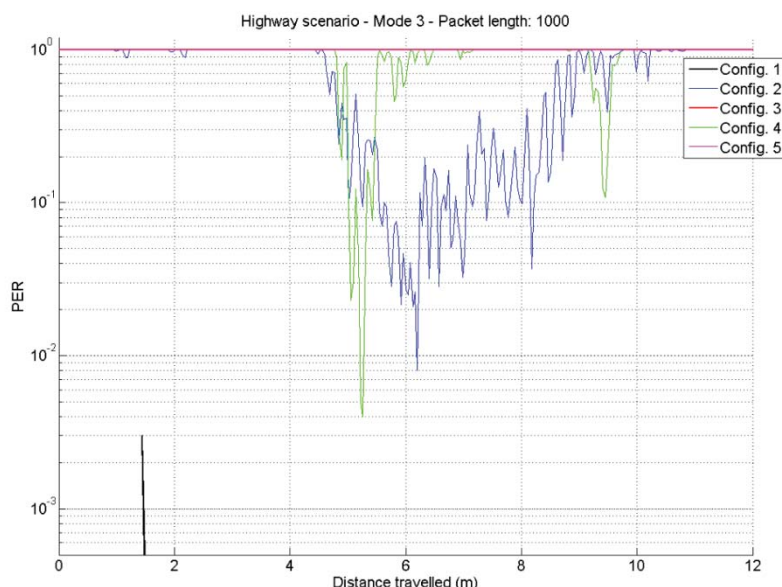


Figure 5-11 : PER results for the 5 antenna configurations in a highway scenario with a communication in Mode 3 and packet length of 1000 bytes.

This behavior is expected, since considering identical transmission parameters, a large packet is more likely to contain an erroneous bit than a small one.

In the next simulated configuration, we decided to investigate the antenna performance with a lower mode. Hence, the packets were transmitted in Mode 1 (mapping with BSPK and coding rate of $\frac{1}{2}$) and a packet length of 200 bytes. The corresponding PER results obtained is displayed in Figure 5-12. A smaller data rate should lead to better performance with same antenna and propagation conditions. Following our expectation, we can observe an increase in the probability of success for Config. 2 as it now pertains 90 % of success. It should be noted that the considered sensitivity of the receiver in mode 1 condition is -94 dBm. This decrease in the minimum received signal level reflected also on the boost in the probability of success of Config. 4. With a data rate of 3 Mb/s and a frame length of 200 bytes, we have 47 % chance of maintaining the communication if we are using the Omni 3 antennas. Unfortunately, even in this moderate condition (low data rate, small packet length), the communication between the transmitter and receiver under Config. 3 and Config. 5 is almost impossible.

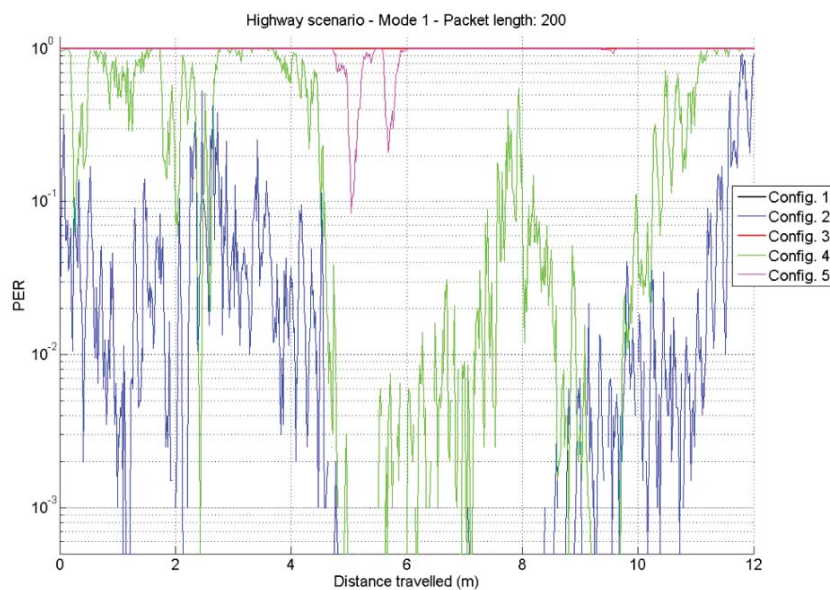


Figure 5-12 : PER results for the 5 antenna configurations in a highway scenario with a communication in Mode 1 and packet length of 200 bytes.

Now, we will consider the case where the data are still transmitted in mode 1 but this time with a packet length of 1000 bytes. The results in terms of PER are plotted in Figure 5-13 for the 5 antenna configurations. We can observe an overall degradation of the performance of communication with an increase in the average PER except for Config. 1 which still has an optimal performance even on a longer packet length. Eventually, the average PER for Config. 2 and Config. 4 are 0.13 and 0.54 respectively. This results correspond to a decrease in the probability of success, falling from 90 %, for communication with transmitted packet length of 200 bytes, to only 68 % for the second antenna configuration. Conf. 4 also suffers a decrease in performance upon the increase of the size of the transmitted packet. It has, now, only 33% chance of success.

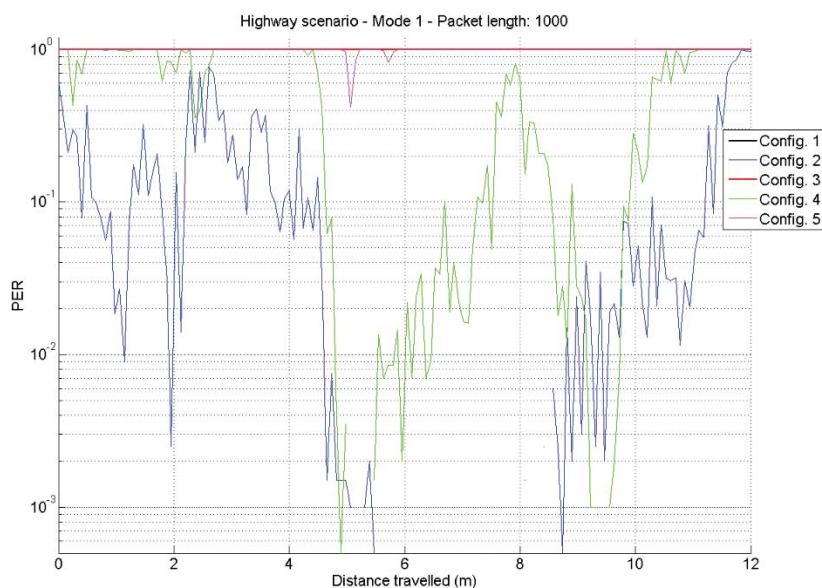


Figure 5-13 : PER results for the 5 antenna configurations in a highway scenario with a communication in Mode 1 and packet length of 1000 bytes.

In the last two simulations, focus will be made on the limit of using patch antennas on the highway configurations under relatively harsh physical layer conditions. The five antenna configurations will be tested with higher modes of transmission. In this part, we chose to transmit in mode 5 using a QAM-16 mapping together with a coding rate of $\frac{1}{2}$. This leads to a data rate of 12 Mb/s. The investigation will be performed with a packet length of 200 and 1000 respectively.

Consequently, good performance is only expected from Config. 1 as the considered sensitivity level for mode 5 is -87 dBm. Figure 5-14 and 5-15 illustrate the PER results for the 5 antenna configurations with the above mentioned PHY layer parameters. As predicted, Config. 2 to Config. 5 are unfavorable to V2V communications as their probability of success, according to simulation results, is zero.

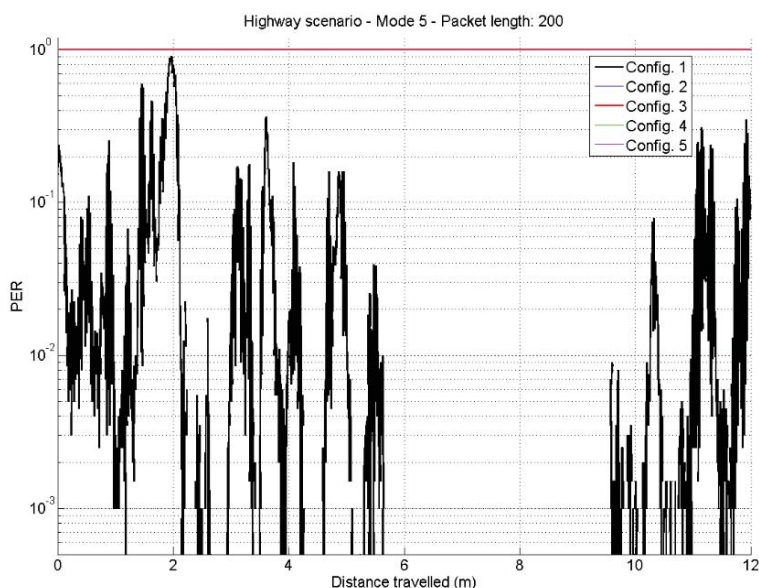


Figure 5-14 : PER results for the 5 antenna configurations in a highway scenario with a communication in Mode 5 and packet length of 200 bytes.

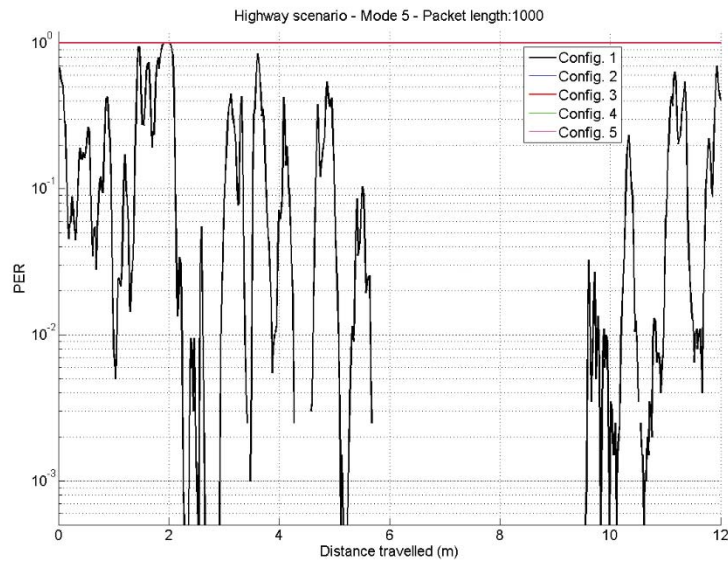


Figure 5-15 : PER results for the 5 antenna configurations in a highway scenario with a communication in Mode 5 and packet length of 1000 bytes.

In mode 5 and a packet length of 200, the first antenna configuration (with two relatively high gain patch antennas pointing towards each other) has 91 % of success. The latter has only a probability of 74 % of decoding correctly the received packet. Therefore, Config. 1 is favorable to even higher data rate compared to the other antennas.

5.5 CONCLUSIONS

In this chapter, a brief description of the physical layer of the protocol of communication dedicated to V2X communications was presented. The simplifications and assumptions taken into account during the implementation in Matlab was depicted. Indeed, in this work, we assumed perfect channel state information on the receiving side.

In section 5.3, the measured radiation patterns of 5 different antennas were given. A relatively high gain patch antenna was characterized in two different locations on the vehicle: the front windscreen and the rear window. Furthermore, two shark-fin module containing each a pair of V2X antennas were measured in the full anechoic chamber presented in chapter 4. The performance of each antenna configuration was tested on the three simulated propagation channel (rural, highway and urban) emulated in chapter 3. Eventually, we noticed that the highly directive patch antennas outperform the other pseudo-omnidirectional radiating elements in the 3 considered use cases. The same trend was observed when the physical layer of the receiver was embodied with the independent transmitted channel sequences.

Afterwards, a parametric study with varying data rate and packet length was made to investigate their impact of the performance of communication for each antenna configuration in a particular highway environment. Table 5-3 gives a summary of the simulated results obtained in terms of probability of success for each modulation scheme and packet length in bytes. From the table, we can clearly conclude that the most predominant factor is the data rate as compared to packet length.

Table 5-3 : Summary of the simulated results of all antenna configurations under the considered use cases

Highway-like propagation channel						
	Mode 1, 200 bytes	Mode 1, 1000 bytes	Mode 3, 200 bytes	Mode 3, 1000 bytes	Mode 5, 200 bytes	Mode 5, 1000 bytes
Config. 1	100 %	100 %	100 %	100 %	91 %	74 %
Config. 2	90 %	68 %	32 %	11 %	0 %	0 %
Config. 3	0 %	0 %	0 %	0 %	0 %	0 %
Config. 4	47 %	33 %	6 %	3 %	0 %	0 %
Config. 5	0 %	0 %	0 %	0 %	0 %	0 %

From the light of our simulated results, the patch antenna is the most favorable configuration under the considered use cases. However, we must not hide the fact that this antenna solution has not been submitted to any design constraints as opposed to the other 4 antennas. Nevertheless, similar solutions (directive radiating element) can be integrated in the rear spoiler and interior rear-view mirror.

In this chapter, we considered only highway configurations. In fact, the next chapter deals with a measurement campaign that has been carried out in rural environments. Hence, the results obtained from rural configurations will be presented and confronted to those obtained from the functional tests in chapter 6.

5.6 REFERENCES

- [1] I. Ivan, "Vehicle to Vehicle communication systems performance evaluation: A simulation approach combining physical layer implementation, propagation channel model and antenna properties", PhD dissertation, Renault SAS – IETR, INSA de Rennes, 2012.
- [2] I. Ivan, P. Besnier, M. Huard, L. Le Danvic, M. Crussière, and M. Drissi, "Physical layer performance analysis of V2V communications in high velocity context," 9th International Conference on Intelligent Transport Systems Telecommunications, ITST 2009, Lille, France, Oct. 2009.
- [3] I. Ivan, P. Besnier, X. Bunlon, L. Le Danvic, M. Crussière, and M. Drissi, "Influence of propagation channel modeling on V2X Physical Layer performance," European Conference on Antennas and Propagation, EuCAP 2010, Barcelona, Spain, May 2010.
- [4] A.M.S. Abdelgader, W. Lenan, "The Physical Layer of the IEEE 802.11p WAVE Communication Standard: The Specifications and Challenges", Proc. of World Congress on Engineering and Computer Science 2014, 22-24 October, 2014, San Francisco, USA.
- [5] A. Sassi, F. Charfi, L. Kamoun, Y. Elhillali and A. Rivenq, "The impact of mobility on the performance of V2X communication," 2011 4th International Conference on Logistics, Hammamet, 2011, pp. 434-438.
- [6] Z. Zhao, X. Cheng, M. Wen, B. Jiao and C. X. Wang, "Channel Estimation Schemes for IEEE 802.11p Standard," in IEEE Intelligent Transportation Systems Magazine, vol. 5, no. 4, pp. 38-49, winter 2013.
- [7] M. Hermansson, V. Skoda, "Evaluating channel estimation methods for 802.11p systems", MSC dissertation, Division of Communication Systems and Information Theory, Chalmers University of Technology, 2011.

Chapter 6 : FIELD TESTS

This last chapter is dedicated to a measurement campaign with the objective to check the performance and usefulness of our dedicated simulation tool to predict the best choice and location of antenna for V2V communications. This measurement campaign is not an experimental validation of the model itself, since propagation channels encountered are not quantified or modelled in a way or the other. We only expect a rough representation of it through a rural-like model as described in above chapters. On the contrary, we expect that the trends in communication performance in terms of PER are predictable from the model. The description of the measurement campaigns that were carried out is presented. The goal of these field tests was to test the operability of V2X communications under different antenna configurations and physical layer parameters such as data rate and packet length. We rode on the trend carried by the Scoop@f [1] project, dedicated to the evaluation of the performance of V2X communications, to undergo our field tests. In the next section, a brief outline of this national project is depicted. The same antennas, studied in chapter 5, were used during the measurements. First and foremost, a complete description of the experimental setup will be given together with a presentation of the different environments where the functional tests were performed. Afterwards, results in terms of maximum distance coverage, RSSI and packet error rate will be analyzed and presented. Finally, comparative studies between results obtained from simulations and measurements will be performed.

6.1 PRESENTATION OF THE SCOOP@F PROJECT

SCOOP@f is a national pilot project responsible for the deployment of Cooperative Intelligent Transport Systems (C-ITS) launched in 2014 by the Ministry of Ecology, Sustainable development and Energy in France. It is the continuation of the SCORE@f [2] project launched in 2010 for a duration of 30 months. Following on from several European research projects (such as CVIS, COOPERS, SAFESPOT,..) and field operation tests like SCORE@f, the SCOOP@f project aims at demonstrating the feasibility and significance of a large-scale deployment of C-ITS across 5 test sites.

The 5 test sites considered are:

- Intercity roads in Ile-de-France,
- Brittany,
- Highway between Paris and Strasbourg : A4,
- Bordeaux city and its ring road,
- County roads in the Isère County.

The ministry manages this project which involves partners such as local authorities, State services in charge of national road management, automotive industries, automotive suppliers and research centers. This is the largest experiment in Europe, with the deployment of approximately 3,000 intelligent vehicles over 2,000 km of connected roads. Six service groups will be tested (2016-2018) to prepare their national deployment by 2020. In addition to the technical aspects, the project will

study the legal aspects of data exchange (protection of Privacy, ownership of data, etc.) and the security of information systems.



Figure 6-1 : Partners participating in the SCOOP@f project

The objectives of the SCOOP@f project can be summarized as follows:

- Improve road safety and reduce accidents through the exchange of information from vehicle to vehicle and between vehicles and infrastructure.
- Optimize traffic management and traffic information so as to reduce congestion and thereby contribute to the reduction of greenhouse gas emissions.
- Optimize infrastructure cost management while providing new services to the user.
- Prepare the vehicle of tomorrow: the cooperative ITS sector offers significant growth potential and job creation in the service of road users' safety.

6.2 TECHNICAL EQUIPMENT IN THE RENAULT CAR

Renault decided to equip by the end of mid-2017, two thousand vehicles dedicated to ITS testing for the Scoop@f project. The Mégane IV was the vehicle chosen and will be accustomed to V2X equipment such as the vehicle transceiver unit (VXU) developed by LG electronics. The VXU consists of the chipset of the modem supplier Autotalks [3] and relay all the information received by the antenna to the multimedia display interface. The antenna was supplied by the Italian society Calearo [4].

6.3 EXPERIMENTAL SETUP

In our conducted field trials, we overlooked the VXU developed by LG electronics and used directly a modem provided by the second rank supplier, Autotalks, using the same chipset and processor. The Modem, called PANGEA5, is provided with an android based user-interface tablet for device management and real-time monitoring which is of great use during measurement campaigns. The PANGEA5 modem was chosen thanks to its numerous advantages listed in section 6.3.3. Furthermore, our field tests allowed us to make a choice between 2 different antenna configurations developed by Calearo and a directive antenna characterized in Renault. These studies leave us many future prospects concerning antenna strategies in forthcoming ITS projects.

In this subsection, each part constituting the communication chain will be described. The outlines of the vehicles used in the field are given in the first place followed by the description of the different antennas under test.

6.3.1 Vehicles

For our entire field tests, two Mégane IV vehicles were employed, each one equipped with a V2X-dedicated antenna and a modem. The car equipped with the receiving modem was always in front and was followed by the transmitting car. The vehicles blueprint and dimensions are illustrated in Figure 6-2.



Figure 6-2 : Blueprint and dimensions of the Mégane IV

To summarize, the vehicle's length is 4.35 and has a height of 1.45 m. The rooftop, entirely made of metal, is of size 0.9 x 1.1 m. As shown in figure 6-2, the roof is slightly curved with a rear bending.

6.3.2 Antennas

As mentioned in the introduction of this section, two types of antenna will be used in our measurement campaigns: shark fin antennas from Calero and relatively directive antennas developed in Renault. The characteristics of all the antennas and their mounting strategies will be presented in the following sections.

6.3.2.1 Shark-fin antennas

In order to equip the fleet of vehicles dedicated to SCOOP@f project, a shark-fin typed antenna was designed. A prototype of that antenna mounted on the rooftop of a white Mégane IV is illustrated in Figure 6-3. It consists of a rod antenna, which is committed to FM services, screwed to the shark-fin module. Within the latter, a GPS patch and two printed monopole antennas are located. These monopole antennas are dedicated to V2X communications. The two ITS-dedicated antennas possess Fakra connectors with red and pink color. It was decided to devote the monopole antenna showing the best performance to the control channel as it is vowed to send security-prone messages. The second one will hence be used for the service channel although we are allowed to convey security messages through this channel in case of emergencies.

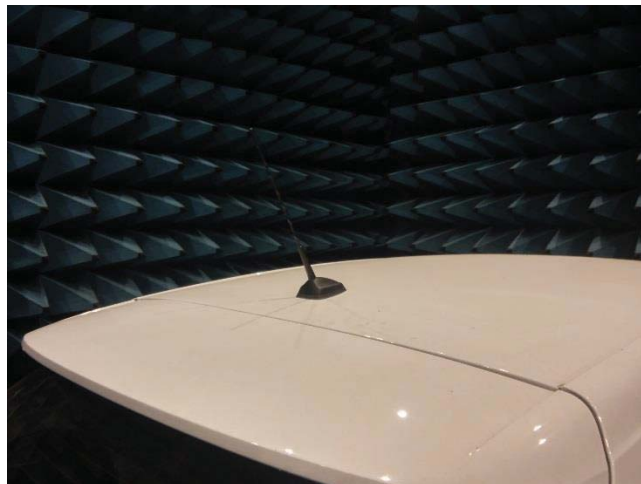


Figure 6-3 : Shark-fin antenna mounted on the roof of a Mégane IV

Two shark-fin antennas (Calaero W3 and Calero STD) were designed by CALAERO with two different approaches in the implementation of the V2X antennas inside the radome. Due to confidentiality reasons, we are unable to detail the two design aspects in this manuscript. Each of these two shark-fin antennas may be used either on the Tx or Rx vehicle. As measurement campaigns are greedy in time consumption, only 3 configurations out of 4 will be tested. Table 6-1, presented at the end of this subsection, resumes all the considered antenna configurations in our different campaigns. The configuration name associated to each set of antennas listed in chapter 5 will be recalled facilitating comparative studies and hence improving the reader's understanding.

6.3.2.2 Patch antenna

The 3-patch antenna developed by [15] was illustrated in chapter 4. The antenna was mounted either on the front windscreen or the rear window. Mounting procedures, with the help of Styrofoam layers, ensured the vertical positioning of the patch, without any tilt. As a matter of fact, the main lobe of the radiation pattern should point in or opposite of the driving direction.



Figure 6-4 : Mounted configuration of the patch antenna on the front windscreen

For best conditions, the vehicle, be it in transmitting or receiving mode, situated in front needs to have the excited patch antenna at the back of its window pointing towards the other patch antenna situated on the front windscreen of the second vehicle following. The middle patch is connected to the modem while the two other patches are loaded with 50 ohm resistances.

6.3.2.3 Summary of antenna used in the measurement campaigns

In this subsection, we will summarize the 4 antenna configurations that were used in our field trials to conduct a comparative study between not only the antennas themselves but also different configuration parameters such as packet length and data rate. Due to time constraints, we limited ourselves to those 4 different antenna configurations. The antenna radiation patterns were illustrated in chapter 5.

Table 6-1 : Antenna configurations

Configuration	Tx antenna	Rx antenna
Config. 1	Patch 2	Patch 1
Config. 2	Omni 1	Omni 1
Config. 3	Omni 2	Omni 2
Config. 4	Omni 3	Omni 3

6.3.3 Modem

In this section, a description of the modem used for performance evaluation will be given. The chosen supplier is an Israeli society, named Autotalks. This company provides a ready-to-use, automotive-qualified chipset that supports V2X communication solutions.

6.3.3.1 Physical description



Figure 6-5 : Modem provided by Autotalks used during measurement campaigns

A representation of the modem is shown in Figure 6-5. The physical dimensions of the product are 12.5 cm in length, 7 cm wide and has a height of 1.8 cm. Magnetic supports are available at the back of the modem to facilitate mechanical setup. Two DSRC antenna connectors are available, at port A and B respectively. The GNSS port is also available to connect the GPS antenna in order to obtain geolocalized data. The modem is powered via the 12 V cigarette lighter socket available in the car. All available logs obtained during measurements are stored in real-time in an external SD Card inserted in the slot provided for.

6.3.3.2 Sensitivity of the modem

Before evaluating the performance of the modem in different scenarios and configurations, it is important to evaluate the receiver sensitivity. Evaluating the receiver sensitivity means determining the minimum received signal level for which a specified PER is obtained. Normally, this level is fixed at 10 % of the PER. Sensitivity values for data rate of 3, 6 and 12 Mb/s are respectively tabulated in Table 6-2.

Table 6-2 : Sensitivity level according to different transmitting mode available in the manufacturers' datasheet

Modulation	Coding rate	Data Rate (Mb/s)	Sensitivity (dBm)
BPSK	1/2	3	-94
QPSK	1/2	6	-93
16-QAM	1/2	12	-87

6.3.4 Global setup

The global set-up is illustrated in the diagram presented in Figure 6-6. Antennas are connected using low-loss cables. A transition element between the Fakra connector to the SMA female port of the modem is used. The same procedure is performed for the GPS antenna. The PANGEA5 is connected to the tablet via Wi-Fi signal. For this reason, we need to connect a WIFI-dongle to the modem in order to have a correct Wi-Fi connection with the tablet. The dongle is connected to 5V auxiliary port available on the modem box for power supply.

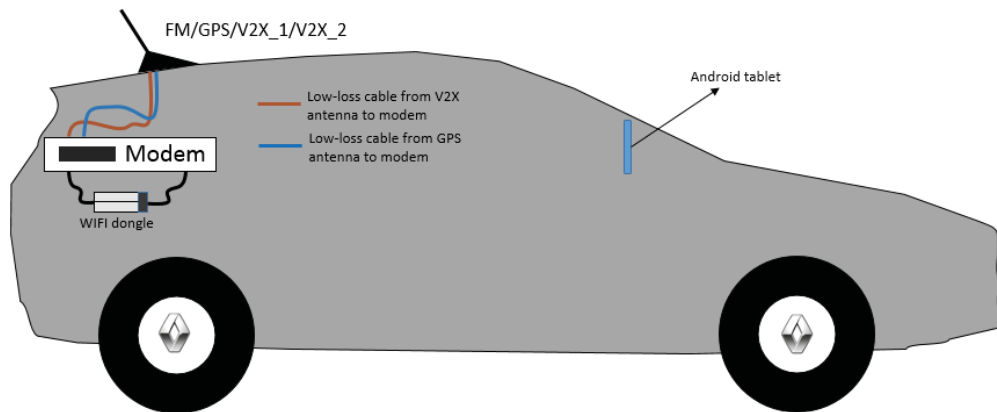


Figure 6-6 : Representation of the on-board setup.

The tablet is placed in the front such that the driver is able to take repetitive glances in order to be aware of the evolution of the real-time results or parameters such as distance between the transmitting and receiving vehicles. The tablet possesses an intuitive graphical user interface that helps the user to obtain information on the current state of the PANGEA5. The main screens of this GUI application are shown in Figure 6-7. The MAP tabs, illustrated in Figure 6-7(a), display real-time information which is very useful during outdoor field tests. Once the V2X and GPS antennas are connected, we can obtain the vehicle positioning on the map. The latter is based on Google Maps, which requires network connection. As network connection is not always available, during field trials, it is recommended to preload test area maps. Besides, information pertaining to the distance between the vehicles, as well as their speed, are also displayed. Furthermore, packet reception quality is also obtained in terms of Received Signal Strength Indicator (RSSI) and the Packet Error Rate calculated for the last second.

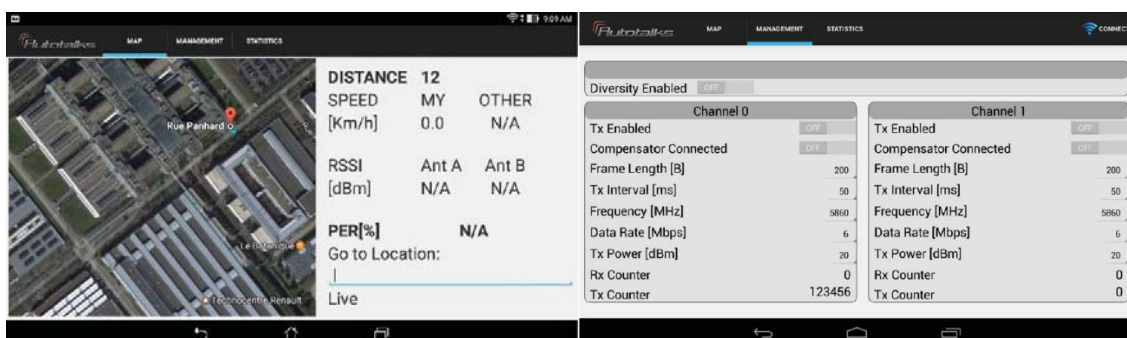


Figure 6-7 : Snapshot of (a) the MAP tab and (b) the MANAGEMENT tab of the Graphical User Interface of the tablet

Figure 6-7 (b) shows the management tab through which the user can control the PANGEA5 parameters. Channel 0 and channel 1 are dedicated to the port A and B respectively. All communication parameters affecting the packet of data transferred such as frame length can be changed between 200, 400 and 1000 bytes. Moreover, the time interval between emitted packets can be fixed to either 10 ms, 50 ms or 100 ms. Besides, the options for frequency are 5860 MHz to 5920 MHz by steps of 10 MHz. In all of our field tests, we set the frequency to 5900 MHz dedicated to the control channel as set by the ETSI standard. Both the Tx and Rx need to be exactly tuned to the same frequency for connection between them to be established. Data rate can be made to vary between 3 Mb/s, 6 Mb/s and 12 Mb/s. Furthermore, the output power at the antenna port can be set to 0, 10, 20 or 23 dBm. We chose to fix the output power to the maximum allowed, i.e., 23 dBm. The summary of all the available parameters in the management tab is given in Table 6-3.

Table 6-3 : Parameter settings in the management tab

Control	Description
Diversity Enabled	Enable/Disable diversity mode
Tx Enabled	Transmit packets
Frame Length	Packet length. Options: [200, 400, 1000] Bytes
Tx Power	Transmit signal strength. Options: [0,10,20,23] dBm
Data Rate	Transmitted packets data rate. Options: [3,6,12] Mbps
Tx Interval	Inter-packet interval. Options: [20,50,100]ms
Frequency	Operating frequency. Options: [5860,5870,5880,5890,5900,5910,5920] MHz

6.4 LOG DATA PROCESSING

All measurement data are collected in a special *.vca Ascii format and can be converted into *.csv files to ease post-treatment. Three types of data are stored in the logs. Firstly, there are the “Navigation_fix” data which give the navigation coordinates when the GPS is locked. The latter means that communication between the Tx and Rx have been correctly made. Only then, we have information about the corresponding speed of each vehicle. The “Navigation_fix” data are timestamped in epoch time¹ and bear also the latitude, longitude and altitude coordinates of the position of the vehicle. It is sent or received every 100 ms. In the case communication is well established between the vehicles, 10 “Navigation_fix” packets are received each second. Furthermore, the “Transmitted_packet”, as its name suggests, consists of all information about transmitted packets which are also timestamped in epoch time. These data contain the sequence number and the message count of the packet which are unique to each and every packet. They are used to identify the packets that are correctly received at the other end. Besides, they contain the GPS coordinates and the information about the current vehicle’s speed. Finally, the third packets are the received ones called “Received_packet”. They consist of a sequence number and message count which can relate them to transmitted packets. Moreover, they carry information about the RSSI of each received packet, the GPS coordinates and the corresponding speed.

Segments of routes to be considered are tracked down using either timestamping or GPS coordinates location. In this way, selected environment can be extracted from the whole measurement campaigns and can be thus used for comparative studies as they are more apt to show repeatability. It must, also, be noted that we fixed the time interval between each transmitted packet to 10 ms.

6.4.1 Evaluation of PER and distance in post-processing

PER is calculated for packets received over the last past second. Considering a time interval of 10 ms between emitting salves leads to 100 packets being sent each second. So, in the perfect condition of communication we are expecting to receive at most 100 packets. Non-null PER are not measurable below 1% since the PER is defined as follows:

$$PER (\%) = \frac{\text{Number of packets not received}}{\text{Number of packets sent}} \times 100 \quad (\text{Eq. 6.1})$$

Furthermore, the Haversine formula [6] is used to calculate the distance between the transmitting and receiving vehicle. The goal of this formula is to calculate the shortest great circle distance between two points on the globe designated by latitude and longitude coordinates. It is important to note that this calculation does not take into account the non-spheroidal shape of the earth but give nonetheless accurate results at short distances.

¹ The Epoch time or Unix time is the number of seconds that have elapsed since January 1, 1970 (midnight UTC/GMT), not counting leap seconds.

6.5 SCENARIO

The field trials were conducted in a 10 km circuit near the town of Gometz-la-ville. Depending on traffic conditions, the time taken to complete the whole circuit was 12 to 16 minutes. It comprises mainly departmental and suburban routes as shown in Figure 6-8. A satellite version of google map covering the whole lap is illustrated. 3 zones pertaining to rural environment were identified and framed in yellow as well as 2 urban/suburban zone pointed out with red boxes.



Figure 6-8 : Measurement circuit chosen for field trials

The rural routes were 2-lane roads with clear landscape on both sides except for trees and scattered housing. Street views of the 3 identified rural scenarios are displayed in Figure 6-9. Presence of bends and uneven level of the road does have important impacts on observed real-time results.



Figure 6-9 : Street views of the 3 identified rural scenarios

In our post-processing approach, we will consider only the rural sections of this measurement circuit as the time spent in the urban segments were too small to be significant. Besides, in these regions, we were too often influenced by traffic lights and thus observed that under these conditions no repeatability was provided.

6.6 PERFORMANCE RESULTS

In this part of the manuscript, post-processed results will be shown and discussed. In the logs of the receiving modems, we are provided with the information concerning the measured power for each received packet. This piece of information is available even though the packet is not correctly decoded. This is the reason why we may record RSSI levels below than the indicated sensitivity level. A mean RSSI is therefore calculated over each second for all the packets arriving at the receiver. In figure 6-10, we plotted, as an example, the RSSI for the rural environment with the following configurations: antenna configuration 3, a packet length of 200 and a data rate of 3 Mb/s.

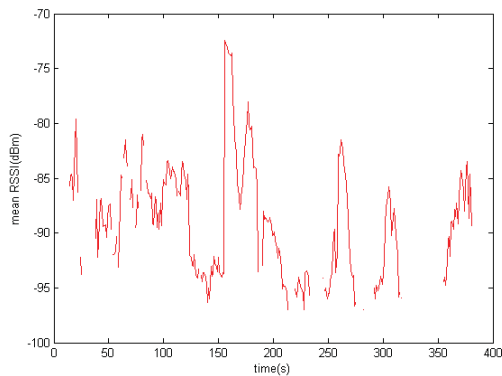


Figure 6-10 : Mean RSSI against time for a section of a rural environment.

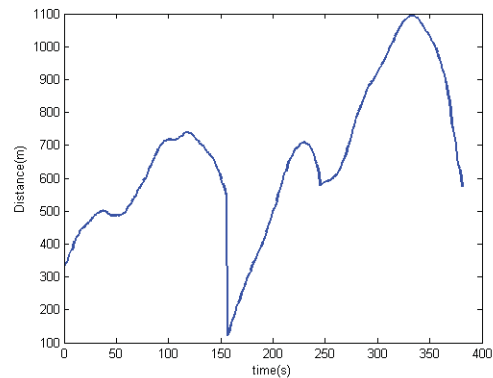


Figure 6-11 : Evolution of the inter-vehicular distance against time

The whole scenario lasted about 6 minutes (exactly 361 seconds). Next to the RSSI plot (Figure 6_11), we displayed the evolution of the inter-vehicle distance for this particular test. We observe a good correlation between the two plots as the RSSI decreases at high distances. We also tend to lose communication at distances higher than 850 m. In Figure 6-12, is an example plot of the PER against time in order to visualize the communication performance. Corresponding PER of 0 % are plotted at a value of 10^{-3} to ease the visual aspect of the figure.

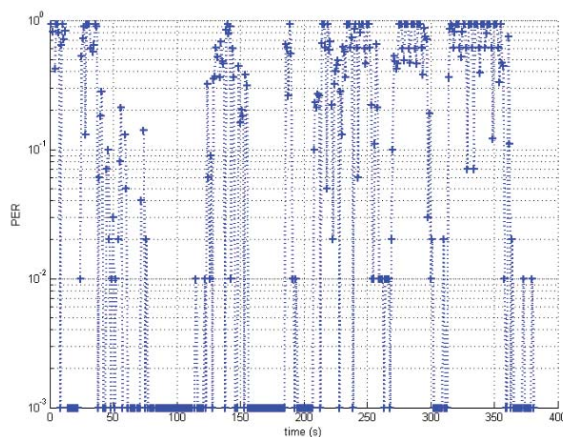


Figure 6-12 : PER against time

Now, after showing that we are able to post-process the logs obtained from measurements correctly and handle the different results, we will push further the study by comparing in the first place the RSSI against inter-vehicle distance for different antenna configurations. The latter are

summarized in Table 6.1 in section 6.3.3. Moreover, a comparative study with varying parameters such as data rate and packet length will be made and following conclusions will be drawn.

6.6.1 Changing parameters: Antennas

The measured radiation patterns of the 4 antennas, integrated on-board vehicles, used in this measurement campaign are illustrated in Figure 5-1 to Figure 5-3 in chapter 5. The objective of this subsection is to show the performance in terms of received power against distance for each of the antenna configurations. Some statistics concerning the time duration of field tests for each set of antenna are given in Figure 6-13. Only two complete laps were performed with the third antenna configuration as real-time observations suggested bad results with these radiating elements configuration and was therefore put aside in order to devote more time to better antenna configurations.

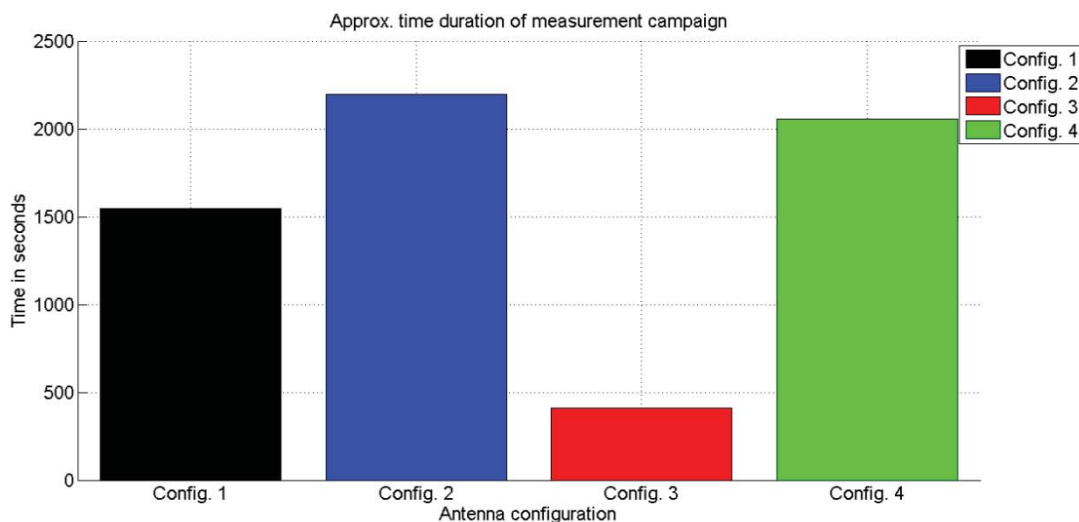


Figure 6-13 : Time duration of the measurement campaign for each antenna configuration

The RSSI results were extracted for all configurations regardless of the varying parameters such as data rate and packet length since these variables do not influence the received power. However, we did verify that in all cases, the transmitting power was fixed at 23 dBm. The RSSI against distance is plotted, in Figure 6-14, for our 4 antenna configurations. As expected, the worst-case scenario is obtained with Config. 3. We have a RSSI of only -90 dBm for distances around 200 m. Config. 2 and Config. 4 tend to have the same performance. This can be deduced from their radiation patterns which show almost the same front to back ratio in the driving direction ($\varphi=0^\circ$). Maximum received power of -70 to -75 dBm can be reached at distances of 200 m with Config. 2 and Config. 4. Directive patch antennas pointing towards each other confirm their anticipated performance. An offset of around 20 dBm is reproduced for nearly all inter-vehicular distances.

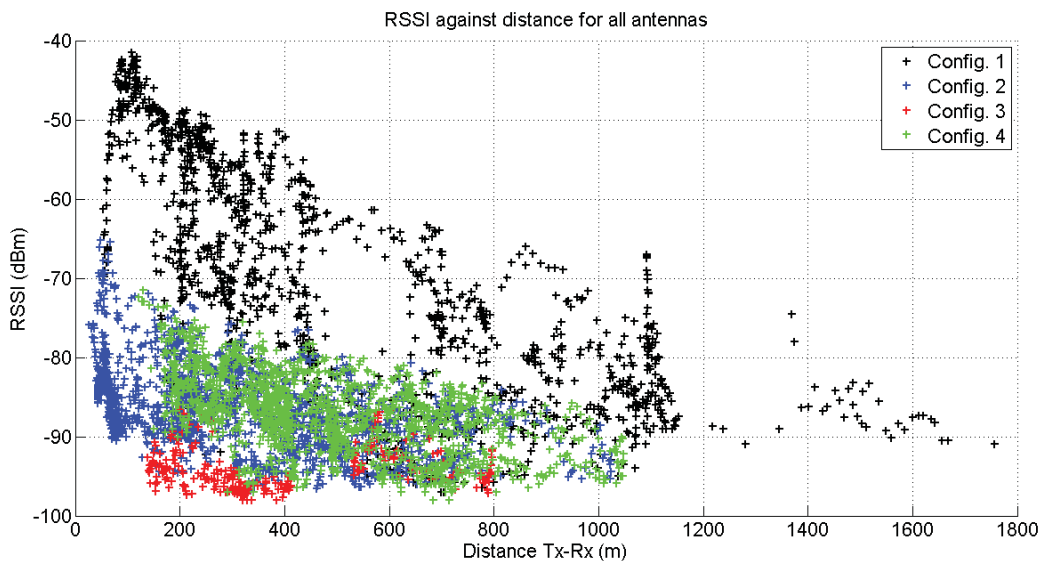


Figure 6-14 : RSSI against distance for all antenna configurations

Taking look at Figure 6-14, we can suggest a maximum coverage distance of 1750 m for Config. 1. Maximum distances reached for Config. 2 and Config. 4 approach the kilometer. We must bear in mind, even if communication is established at this distance, it does not necessarily mean that the packet is correctly decoded with a low PER and thus does not give us information about the quality of communication. As a matter of fact, the next section deals with the analysis of PER for different modem parameters.

6.6.2 Changing parameters: DATA rate and packet length

In this section, quality of service in terms of PER will be analyzed. The maximum coverage distance will also be under investigation for different packet length and data rate. In doing so, the most influential parameter on the communication performance can be pinpointed. This analysis will be made only for configuration 1, 2 and 4 as measurement with antenna configuration 3 was carried out only in best case condition (packet length =200 and data rate = 3 Mb/s).

The 4 different combinations of data rate and packet length that will be measured for each considered antenna configuration are as follows:

- Mode 1, 200 bytes - Data rate : 3 Mb/s, Packet length = 200 bytes
- Mode 5, 1000 bytes - Data rate : 12 Mb/s, Packet length = 1000 bytes
- Mode 1, 1000 bytes - Data rate : 3 Mb/s, Packet length = 1000 bytes
- Mode 5, 200 bytes - Data rate : 12 Mb/s, Packet length = 200 bytes

Antenna configurations Config. 1, Config. 2 and Config. 4 are used for the field trials described in this subsection. The probability of occurrence of distances for which the PER is less than 10 % is extracted and plotted as grouped histograms for each combination of physical layer parameters in Figure 6-15. We can deduce, as expected, a better performance for the best-case conditions, i.e., short packet length and low data rate. Higher occurrences of the mode 1, 1000 bytes (Data rate: 3 Mb/s, Packet length = 1000) can be observed in Figure 6-15 to 6-17. The maximum coverage obtained with antenna configurations 2 and 4 in successful receiving conditions are just under 1 km. Intuitively, we obtained better coverage distances with antenna configuration, Config. 1. Distances neighboring the 1600 m were achieved under the least severe condition (Mode 1 with a packet length of 200 bytes). From the results presented in Figure 6-15 and 6-17, we can clearly see that the maximum coverage distances are obtained when transmitting in lower modes. We can, thus, suggest that except in Figure 6-16, where there are occurrences of successful communication in mode 5 at high inter-vehicular distances, that the most influential physical layer parameters is the modulation scheme.

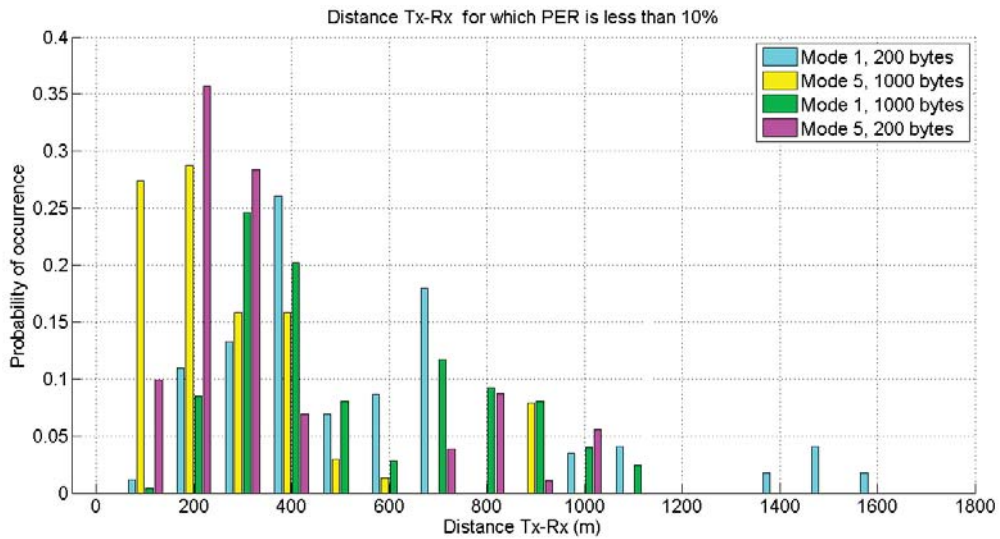


Figure 6-15 : Probability of occurrences of inter-vehicular distances with successful communication using antenna configuration Config. 1

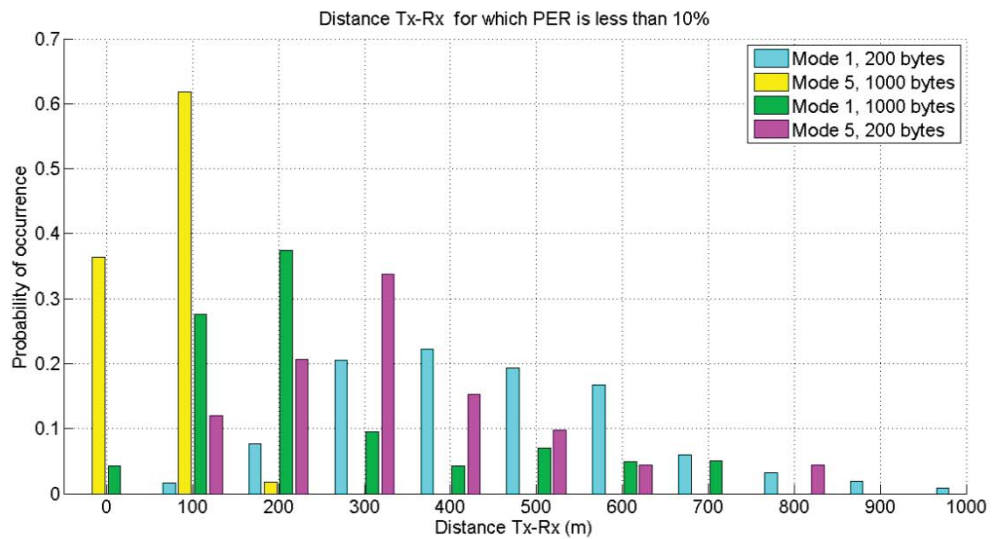


Figure 6-16 : Probability of occurrences of inter-vehicular distances with successful communication using antenna configuration Config. 2

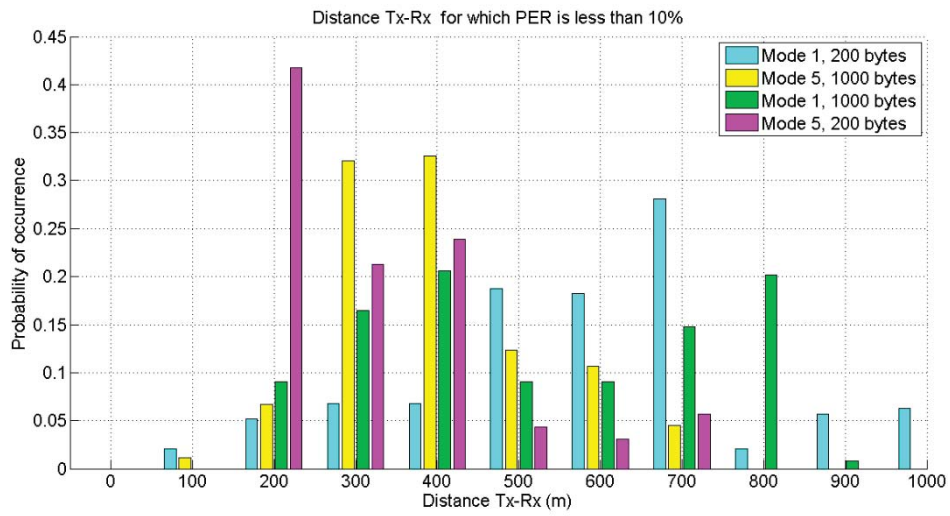


Figure 6-17 : Probability of occurrences of inter-vehicular distances with successful communication using antenna configuration Config. 4

6.7 COMPARISON BETWEEN SIMULATION AND MEASUREMENTS

In this final part of this chapter, effort will be focused on comparative studies between simulation results and measurements obtained from the field trials performed. It is important to recall that simulations were carried out for typical propagation scenarios where the distance between the transmitting vehicle and the receiving one was at 300 m. However, the strategy adopted during field trials was focused principally on obtaining the maximum coverage distance while having a successful communication, i.e., a PER less than 10 %. Therefore, in order to compare outdoor field tests' results with that obtained from our complete simulation chain we chose to extract data for which the distance inter-vehicle was between 275 m and 325 m. This range of distance can be considered close enough to the targeted distance of 300 m.

Here, comparisons will be made only for rural environments. Most measurement conditions are not under control (e.g. traffic conditions, vehicle relative speed, surrounding environments) and are, thus, not reproducible. Indeed, we noticed that traffic conditions have high impact on real-time results we obtained during measurements. Unfortunately, the chosen measurement circuit is no exception to this rule as traffic can be very dense during peak hours that is mainly at 16hr30 to 18hr30 in the afternoon. Field trials with antenna configurations 2 and 4 were carried out when the flow of traffic was fluid. On the other hand, Config. 1 and config. 3 performance evaluations were done after work hours and hence in the presence of a dense traffic. Hence, it is important to differentiate between two types of propagating environments: a rural scenario with a high density of scatterers between the Tx and the Rx and a second one representing a rural scenario with a lighter traffic. As a matter of fact, we kept the simulated rural configuration defined in chapter 3 as the representation of a denser rural propagating scenario. Besides, we described a second rural configuration with a reduced number of scatterers in the scenario in order to better emulate a rural environment with a lighter traffic.

Antenna performance results obtained from field trials, expressed in terms of RSSI, will be confronted to the power received from each antenna configurations driven in simulations. This first comparison element will give us an idea of the degree of correlation between the two sets of results. Afterwards, results in terms of PER will be given in terms of the different communication parameters such as data rate and packet length for the three antenna configurations.

6.7.1 Configuration for the new rural scenario

In this section, we will briefly describe the new propagation environment which is more representative of a rural scenario with a less dense traffic as compared to the one presented in chapter 3 (section 3.4.1). Indeed, we noticed, thanks to instantaneous results in terms of RSSI obtained during trials, that the latter were traffic-intensity dependent.

Table 6-4 : Geometry parameters of a new rural propagation channel

Total number of scatterers		22
Type of scatterers	N_{IN}	22
	N_{OUT}	0

Number of lines		11
Random distribution of scatterers	N_{IN}	$U [20 , 280]$ m

In this configuration, reproducing a rural environment with a lighter traffic, we located only 22 N_{IN} scatterers spread over 11 consecutive lines. In the Tx-Rx axis, only one scatterer was placed so as to increase the global received power. Consequently, a reduction of the RMS delay-spread is noted, as expected, though the angular spread remains practically the same as the geometry of the emulated scenario has not changed.

6.7.2 Measurement results: RSSI for each antenna configuration

In this subsection, the received power obtained at the range of distance neighboring the 300 m will be presented. The probability of occurrence for the RSSI extracted for inter-vehicular distances between 275 and 325 is plotted in Figure 6-18. The same trend, as seen in previous analysis, is observed here also. Indeed, the patch antennas configuration works better as the RSSI from -80 dBm to -45 dBm with most occurrences around -65 dBm. The received power for Config. 2 and Config. 4 fluctuates mostly between -85 to -80 dBm. Config. 3 shows, as expected, the worst performance with RSSI ranging from -100 dBm to -95 dBm.

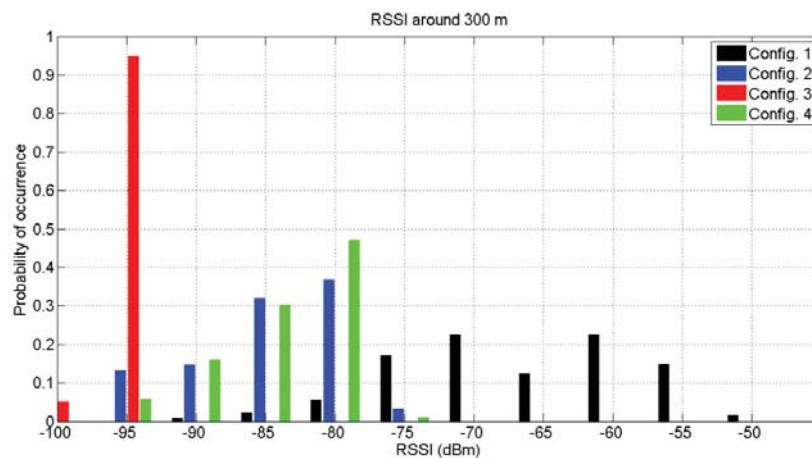


Figure 6-18 : RSSI for inter-vehicular distances around 300 m for all antenna configurations

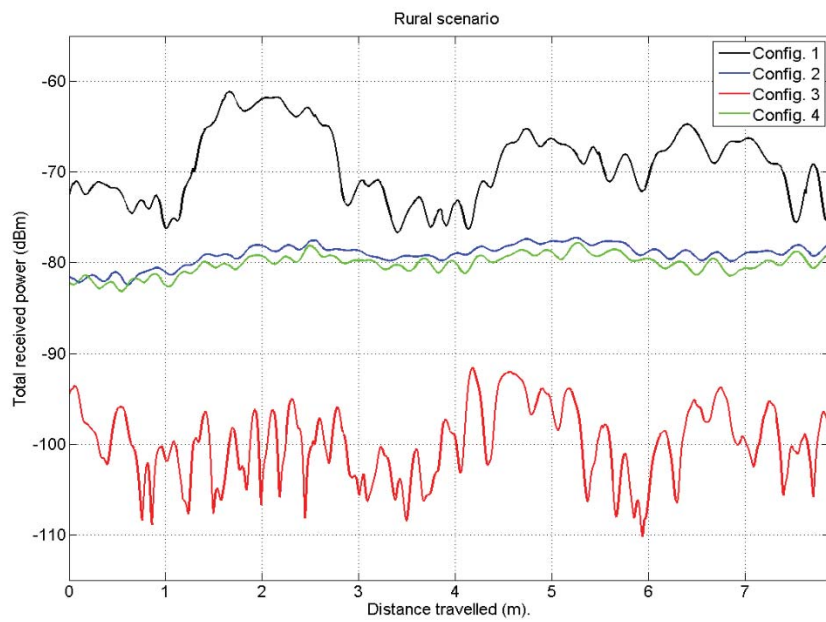


Figure 6-19 : Received power for the 4 antenna configurations in their corresponding rural environment

In figure 6-19, the received power is plotted for the simulated antennas configurations Config. 1, Config. 2, Config. 3 and Config. 4 respectively. The results are shown for the 1000 snapshots corresponding to a distance of 12m. The histogram representation is illustrated in Figure 6-20 with a bar width of 5 dBm. Confronting the latter with figure 6-18, we can see that there is a good correlation between the RSSI obtained in outdoor field trials and the simulation results retrieved from FEKO simulations. These promising results foreshadow positive prospects for further analysis.

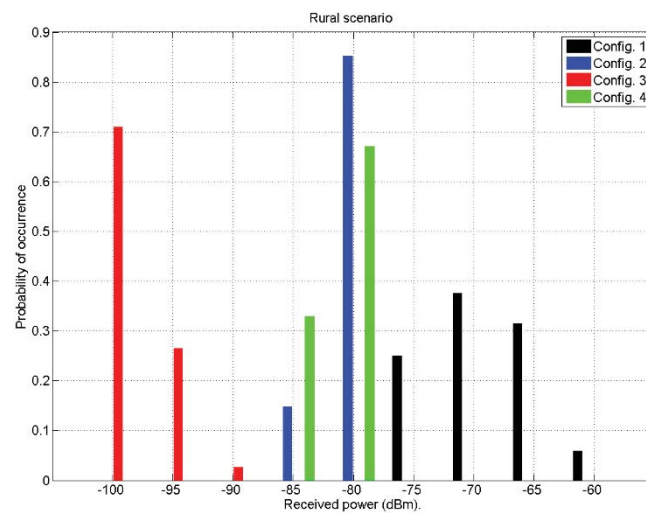


Figure 6-20 : Probability of occurrence of the received power for the 4 antenna configurations in their corresponding rural environment

6.7.3 Measurement results: PER results for each antenna configuration under different PHY layer parameters

The PER results for the 4 considered antenna configurations will be calculated using data obtained from the measurement campaign as described in section 6.4.1. They will be confronted with simulation results obtained from their respective emulated rural propagation environment as presented earlier in this section. Table 6-4 and 6-5 summarize these two sets of results. The average PER is evaluated for communications that occurred at inter-vehicular distances around 300 m (275 m to 325 m). Moreover, the probability of successful communication (tabulated in between brackets) is also calculated, abiding by the assumption that a PER of less than 10 % is favorable to a good communication between the transmitter and receiver. Moreover, it must be noted that the chosen measurement circuit for each antenna configuration and physical layer set of parameters (data rate and packet length) lasted only ten minutes and the number of occurrences for which the inter-vehicular distance was around 300 m can be scarce. For measurement configurations for which the average PER was evaluated using less than ten field trials outcomes will be highlighted in light blue.

6.7.3.1 Measurement results

From Table 6-5, it can be noticed that the patch antennas (Config. 1) has obviously the best performance, as we obtained negligible values of PER even when communicating in Mode 5 (16-QAM mapping and coding rate of $\frac{1}{2}$) with a packet length of 1000 bytes. Although, we have a relative high probability of success with Config. 1 when transmitting in Mode 1 (89 % and 93 % with frame size of 200 bytes and 1000 bytes), better results were expected under these physical layer parameters.

Measured results obtained with Config. 2 follow the expected trend. Better performance was observed in lower transmission modes and smaller packet size. Indeed, with Mode 1 and a packet length of 200 bytes and 1000 bytes the percentage of a successful communication are 84 % and 83 % respectively. In Mode 5, there is a significant deterioration of the quality of service, obtaining 63 % with a packet length of 200 bytes and 0 % chance of communicating with a longer transmitted frame size.

Measurement with the third antenna configuration (Config. 3) was performed only in mode 1 with a packet length of 200 bytes. Even with the least harsh physical layer parameters, the mean PER obtained is important, leading to a probability of success of only 14 %.

Furthermore, practically the same observation, as for Config. 2, can be applied to measurement results obtained with Config. 4 though we were somehow expecting better results with Config. 2 in this particular driving scenario. Besides, we retrieved a rather astonishing performance when transmitting in Mode 5 and 1000 bytes.

6.7.3.2 Simulation results

Results obtained from our simulation tool are presented in Table 6-6. They are, here also, expressed in terms of mean PER and percentage of successful communication during the lapse of time considered. Config. 1, Config. 2 and Config. 4 are all favorable to V2V communications with

transmission Mode 1, at an inter-vehicular distance of 300 m. Indeed, under these conditions, the receiver can perfectly decode all the received packets be it short (200 bytes) or long (1000 bytes).

Config. 1 confirms the measurement results though the simulation results show poorer performance when transmitting in higher mode. Nevertheless, Config. 1 is clearly the best performing antenna configuration, whether in simulation or field trials.

Under Config. 2, Config. 4, simulation results do not allow us to distinguish the performances between these two configurations. During, measurements, these two antenna configurations show different performance following the transmission mode, though they exhibit the same weaknesses as in simulations.

The third antenna configuration, Config. 3, displays the worst communication performance both in the measurement campaigns and in simulation. Besides, in the latter, this configuration is not favorable to V2V communications when the inter-vehicular distance is at 300 m whatever the transmitting mode.

Table 6-5 : Measured results obtained with 4 antenna configurations. Average PER and in between parenthesis rate of transmission with PER <10 %

Rural-like propagation channel. Measured results.				
	Mode 1, 200 bytes	Mode 1, 1000 bytes	Mode 5, 200 bytes	Mode 5, 1000 bytes
Config. 1	0.04 (89 %)	0.04 (93 %)	0.00 (100 %)	0.01 (100 %)
Config. 2	0.08 (84 %)	0.11 (83 %)	0.20 (63%)	0.86 (0 %)
Config. 3	0.54 (14 %)	-	-	-
Config. 4	0 (100 %)	0.11 (84 %)	0.36 (39 %)	0.17 (70 %)

Table 6-6 : Simulated results obtained with 4 antenna configurations. Average PER and in between parenthesis rate of transmission with PER <10 %

Rural-like propagation channel. Simulation results.				
	Mode 1, 200 bytes	Mode 1, 1000 bytes	Mode 5, 200 bytes	Mode 5, 1000 bytes
Config. 1	0.00 (100%)	0.00 (100%)	0.15 (79%)	0.21 (76%)
Config. 2	0.00 (100%)	0.00 (100%)	1.00 (0 %)	1.00 (0 %)
Config. 3	1.00 (0 %)	1.00 (0 %)	1.00 (0 %)	1.00 (0 %)
Config. 4	0.00 (100%)	0.01 (100%)	1.00 (0 %)	1.00 (0 %)

In the light of this comparison study between simulation and field test results, obtained in a rural-like propagation channel, we can infer that the overall performance of antenna configurations in terms of PER or percentage of successful communication can be anticipated with the simulation tool. The expected trends in communication performance in terms of PER are globally predictable from our model. The principal hitch is that we are not able to distinguish between the performance of Config. 2 with respect to Config.4 in our simulation model. Their operating points are too close to each other to allow a clear discrimination between their respective results. Also, a surprising low average PER value has been found when using Config. 4 in Mode 5 and a packet length of 1000 bytes. The only explanation to this phenomenon is that potentially the occurrence of communications under these particular physical layer parameters at inter-vehicular distance of 300 m, were performed in clear line of sight conditions. Further investigation is required to find a clear and valid explanation.

We must bear in mind that only a rough representation of the results was expected since the propagation channels encountered in our measurement campaigns were neither sounded nor quantified. This reinforces our statement that measurement conditions, such as traffic conditions or vehicles' speed, are not controllable and hence are not reproducible. Hence, much more intensive measurement campaigns focusing on distance between transmitter and receiver of 300 m should be performed if better comparative results are expected.

6.8 REFERENCES

- [1] <http://www.developpement-durable.gouv.fr/SCOOP-F-Projet-de-deploiement.html>
- [2] <http://www.scoref.fr/>
- [3] <http://www.auto-talks.com/>
- [4] <http://www.calearo.com/ita/>
- [5] M. Ibambe Gatsinzi, F. Jovvie, X. Bunlon and A. Azoulay, "Study of a 5.8 GHz frequency band patch antenna integrated into a vehicle for automotive DSRC applications," 2007 International Conference on Electromagnetics in Advanced Applications, Torino, 2007, pp. 543-546.
- [6] Sinnott, RW, Virtues of the haversine. *Sky and Telescope*, 68(2):159, 1984.

GENERAL CONCLUSIONS

The promising potential of point-to-point wireless communications between vehicles and infrastructure to drastically reduce car accidents and to optimize traffic flow has already been identified. Thus, many research works on V2X communications were performed these recent years. These efforts were accompanied with standardization activities which led to a globally harmonized set of standards of the communication protocol in Europe and the United States.

The development of V2X solutions requires the understanding and merging of a number of techniques from several communication technology areas. Indeed, the performance of these systems are strictly related to three main blocks: the implementation of the modems, the antenna configuration and the fast varying environment surrounding the transmitter and the receiver. Therefore, finding the most favorable antenna configuration and location together with the best developed V2X modems to ensure optimal performance in different driving situations is a tedious task. A possible solution is to resort to intense measurement campaigns but they are expensive, time consuming and provide no repeatability. Consequently, the development of a robust and precise simulation tool can be helpful for equipment specifications in upstream development phase and to validate the performance of the communication systems in different driving conditions. This has been the principal objective of our thesis project.

Our Ph.D. thesis has dealt with Vehicle to Vehicle (V2V) communications. The purpose of this work was precisely to elaborate a design strategy to investigate and interface all the different blocks constituting the communication chain:

- 1) Representation of the transmitter and the receiver following the physical layer standard dedicated to the communication.
- 2) Simulation of a set of virtual driving scenarios emulating the propagation channel properties corresponding to typical environments such as highway, rural and urban ones.
- 3) Representation and integration of the antenna on or in the car-body to obtain realistic antenna patterns.

The first block of this chain has been deeply analyzed through a previous Ph. D. thesis in relation with the simulation of two specific propagation channels depicted in the literature. In consequence, this work has been mainly concentrated on the two last blocks raising numerous challenges.

Results provided from our work are decomposed in 4 main parts that are summarized below.

Simulation strategy of multiple types of propagation channels

We proposed a Geometry-Based Stochastic Channel Modeling (GBSCM) approach for V2V wireless communications. Our method help to develop dynamic scenarios and its flexibility allows us to parameterize the different characteristics of a propagation channel such as delay spread, angles of arrival distribution and even the Doppler signatures. It is shown that the most common propagation environments such as rural, highway or urban-like propagation channels are reached through adjustment of location and numbers of simple metallic plates. In a first place, we used an analytical method which aimed at defining the number and convenient distribution of scatterers in our generic physical setting based on the targeted RMS delay and angular spread. This analytical

calculation consists of an initial step towards a rough estimation of these parameters. Following this approximate evaluation of channel parameters, preselected configurations were then simulated in a 3D electromagnetic simulator FEKO using the Uniform Theory of Diffraction as ray-tracing method. Most importantly, we showed that the created channel responses pertained similar characteristics to results obtained from measurement campaigns that were available in the literature. Therefore, rather than elaborating sophisticated channel modeling approach based on channel sounding experiments or deterministic models, we suggested that our developed configurations may virtually reproduce these experiments or other ones at least in a behavioral sense.

Antenna pattern of antennas on-board vehicles

Antenna integration problems was the core subject of the study. At a working frequency of 5.9 GHz, the numerical model of vehicles tend to be bulky and very demanding in both time consumption and computational resources. This stimulated the investigation of how to simplify the CAD to speed up calculations without much deteriorations on the radiation pattern results. From first studies, it was deduced that roof structure is sufficient when considering the situation of an antenna placed around the center point of the roof. However, the influence of the other parts of the car body such as the tailgate became important when the antenna is placed at the back-end of the roof. Moreover, when the antenna is placed inside the car body, a more complete description of the model of the vehicle is required.

Our propagation models uses radiation patterns of antennas integrated on-board the vehicle, whether obtained from simulation or measurements. Therefore, it does not account for any modification of the source current / charge distribution and, moreover, supposes that only far-field interactions are considered. We have investigated the limit of validity of this approach due to possible interactions with elements found in the near-field zone of the antenna / car. A criterion was first identified to evaluate an acceptable boundary distance of the near-field to far-field zone when considering an integrated antenna on a car body. A strategy to alleviate the degree of error was found upon consideration of objects located nearer than the boundary distance in the a priori simulation of the antenna integrated on the vehicle. In this case, we are able to re-establish correct interactions between the simulated vehicle and the scatterers present in its vicinity.

Production of a complete simulation tool

The last objective of this work, was to present the performance of each considered antenna configurations under all propagation channel environments in terms of outputs such as packet error rate (PER). Thus, to complete the picture, the embodiment of the PHY layer of the IEEE 802.11p standard, dedicated to V2X communication, with the propagation channel responses including realistic antenna patterns was performed. Simulation results, for each antenna configurations, was given for several combinations of PHY layer parameters such as data rate and packet length. The importance of antenna performance was highlighted and the PHY layer parameter having the most impact on the quality of service was identified.

Validation of the simulation results through a measurement campaign

A measurement campaign was carried out in a rural driving environment. The aim of these field trials was to test the operability of V2X communications under different antenna configurations and physical layer parameters such as data rate and packet length. Results obtained from these functional tests were confronted with simulation results to demonstrate the strength of the latter to help the guidance towards a proper choice of antenna configuration and PHY layer parameters. We found that the expected trends in communication performance in terms of PER are globally predictable from our model though we obtained surprising results in some cases, needing further investigation. From our point of view, much more intensive field trials should be carried out for a better comparative study of the simulation against measured results.

PERSPECTIVES

In this thesis, we proposed a complete simulation tool to evaluate the performance of V2V communication systems. Although the tool is well underway, there is still room for improvement to obtain closer agreement with measurement results. In this section, we will put forward some future research directions that may enhance the simulation tool and to set foot on novel techniques of validating V2X communication performance.

Consideration of the influence of the ground

Many research works have been carried out to highlight the impact of the ground in V2X communications. In fact, in most channel models, the path loss is modelled using the well-known two-ray ground model. In our FEKO model, we suggest to insert a flat metallic plate below the cloud of scatterers at a representative height to emulate the influence of the ground plane.

Vehicle to infrastructure (V2I)

In this scope of work, we focused only on the V2V communication context. The V2I case must be studied, bearing in mind that road-side units' antennas are usually placed at a higher level as compared to the height of the vehicle. In such conditions, we should also take into account the elevation plane of V2X-dedicated radiating element.

Emulating V2X propagation channel in anechoic chamber

The objective is to reproduce the same propagation environments as the V2X systems would experience during a drive test in a controlled environment. Up to now, algorithms implemented in commercial channel emulators are limited to reproduce GBSC model in multiprobe anechoic chamber for "over-the-air" testing. Therefore, our simulated channel responses can be directly emulated. The difficulty lies in the adjustments of an existing anechoic facility to correctly mimic these channels. A number of antenna probes must be positioned in the azimuthal plane, from which most of the energy is arriving, especially for V2V communications.

APPENDIX. A MATLAB IMPLEMENTATION OF THE PHY LAYER

In this appendix, we present the performance evaluation technique employed, as well as the computer implementation method of the V2X transmission chain (PHY layer). It was mainly reproduced from the PhD report of Iulia Ivan. All simulations were performed in Matlab. The required Matlab toolboxes are:

- *Communication Toolbox*
- *Signal Processing Toolbox.*

Performance evaluation with Monte Carlo method

To estimate the bit error rate (BER) and the packet error rate (PER) performance of the system, we have employed the error estimation technique called the Monte Carlo (MC) method. Monte Carlo is a statistical simulation method, very useful to obtain numerical solutions to problems which are too complex to solve analytically. The algorithm we have employed for estimating the BER and PER for a given average SNR value (calculated for each independent channel packets), based on the MC method, is illustrated in Figure A-1.

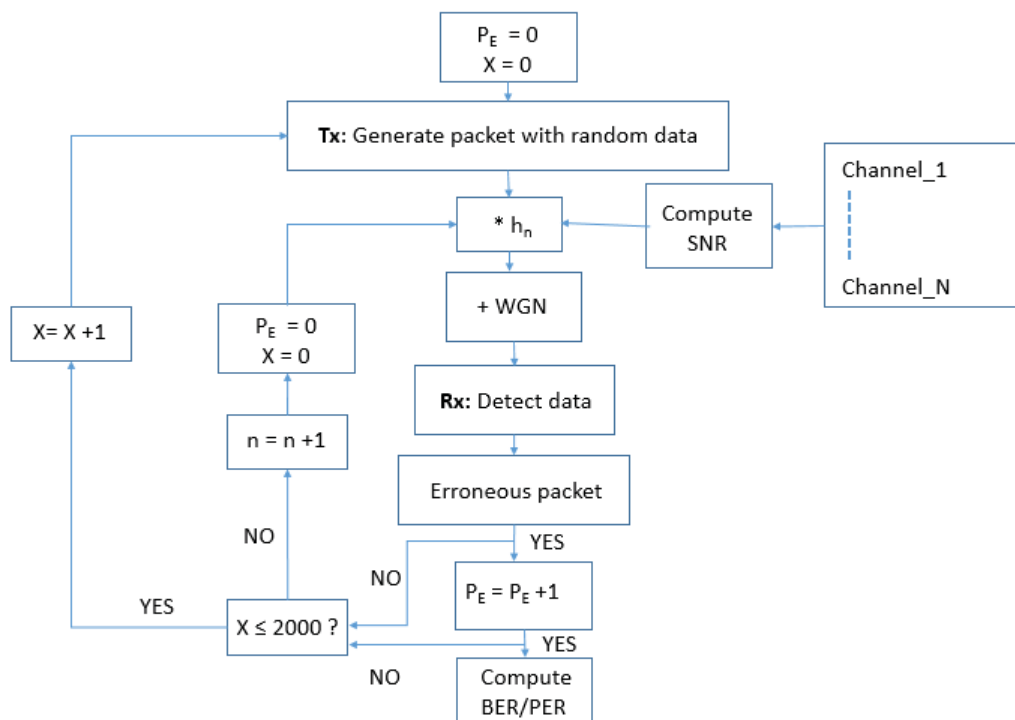


Figure A-1 : Algorithm to calculate BER/PER

We first initialize the number of erroneous packets ($P_E=0$) and the value of the index of the number of time ($X=2000$ at the end) the same independent channel is evaluated. We generate random binary data and we pass it through the transmission chain. The transmitted signal is then convoluted with a random, independent channel sequence, generated beforehand and stored in

The convolutional encoding and the puncturing are performed by using Matlab “convenc” function from Matlab Communication Toolbox. The interleaving, as well as the mapping, are implemented with several basic Matlab functions, since they are faster than the dedicated Communication Toolbox functions.

Before the IFFT, in each OFDM symbol are added the four BPSK modulated pilot symbols (as described in Section 2.1). Afterwards, the cyclic extension, or the cyclic prefix (CP), is appended at the beginning of each OFDM symbol. The obtained signal is then convoluted with channel coefficients loaded from the hard-disk computer memory, and WGN with variance N_0 is added.

Reception

The receiver basically performs the inverse operations, as described in Section 2.1. First, the CP is removed, the FFT of the obtained signal is computed, and afterwards the channel LS equalization is performed as in (B.29), Appendix B. Then, the pilots are removed, and hard demapping is performed. After the de-interleaving, the Matlab function “vitdec” served to perform the Viterbi decoding with hard decision. The detected bits are then compared to the transmitted bits, and the number of erroneous bits is computed. A packet is considered erroneous if at least one bit contained in the packet is erroneous.

Appendix. B WinProp results

WinProp is a 3-D ray-tracing simulation tool developed and commercialized by AWE Communications, initially designed for radio network planning in large-scale urban scenarios. Recently, a new software module was added, enabling to create and edit time variant scenarios. Therefore, the locations of transmitters, receivers, and obstacles are time-variant. See internet link for more details: <http://www.altairhyperworks.com/product/FEKO/WinProp-Propagation-Modeling>

Modeling of scenarios and vehicles

All objects modeled in the simulated scenario are composed of either planar polygons, either cylinders. To each polygon, an individual material property (permittivity, permeability and conductivity) can be assigned. The following table introduces the basic tools used in Winprop to simulate a time variant scenario:

Table B-1 : Short guide to introduce the basic tools used in Winprop

Software tool	Basic functions
WallMan	Generate the vector database describing the environment and the vehicles. We also assign the time-variant properties to all moving objects in the scenario.
ProjectMan	Set up a project with the parameters of the simulation
SiMan	Compute the prediction of ray paths
ProMan	Visualize the results

After the creation of the 3D model in WallMan, the properties of the transmitter and receiver can be set up in the the ProjectMan module. The frequency (in GHz) of the communication, the transmitted power (in dBm) and optionally a radiation pattern can be defined. The coordinates of the absolute position of the antenna must also be entered by the user. In case the user wants to assign the antenna to a moving vehicle, he should activate the checkbox: Assign to vehicle. Then, the transmitter or receiver will follow the same movements as the time-varying object. By default, an isotropic antenna is used as point source and perfectly-matched receiving antenna. Polarization of the antenna can be either fixed to horizontal or vertical

The computation of interaction losses along each ray is based on the Fresnel coefficients for reflections and transmissions, and on the Uniform Geometrical Theory of Diffraction (UTD) for diffractions. The algorithm supports an arbitrary number of reflections, diffractions and transmissions/penetrations for each ray path, but in practice only two reflections, one diffraction and zero transmissions are considered (more interactions did not show to considerably improve the computation accuracy). Scattering on rough surfaces is also included in the model.

Simulation results

In this section, we will briefly present the different deterministic scenario developed in Winprop. Three typical outdoor propagation channel were considered: Rural, Highway and Urban. The angular spread obtained from each simulated channel is presented.

Rural scenario

The rural scenario drawn in Winprop is shown in Figure B-1. It is a typical rural scenario with a curved road. There is presence of vegetation and a few buildings. The considered traffic scenario is very light with only 5 time-varying objects in the environment. The inter vehicular distance is 300 m.

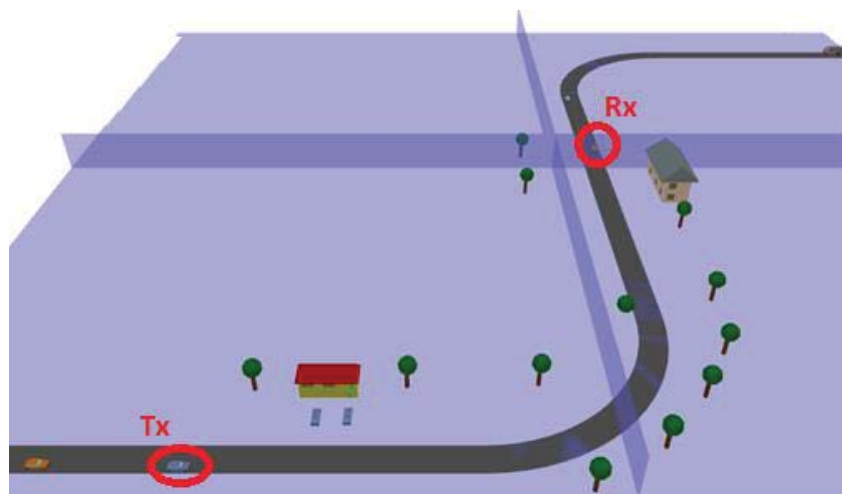


Figure B-1 : Rural scenario developed in Winprop

The angles of arrival at the receiver is directly obtained in the *.cir output files. It must be noted that the default isotropic radiation pattern has been used for both Tx and Rx. The probability of occurrences of the angles of arrival is presented in Figure B-2.

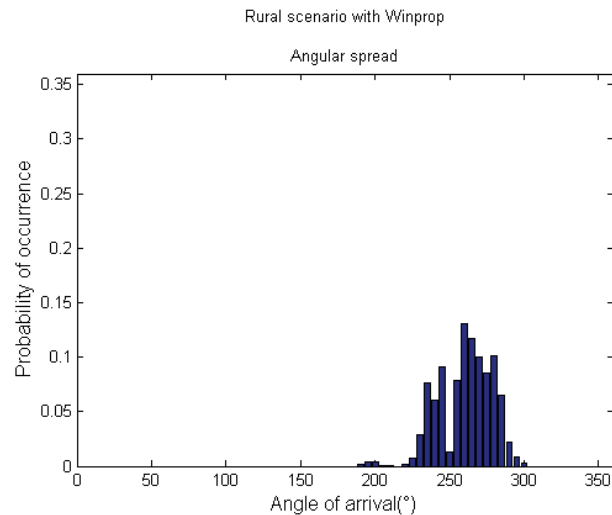


Figure B-2 : Angular spread in a rural scenario obtained with Winprop

Highway scenario

The configured highway scenario in Winprop is illustrated in Figure B-3. It is a typical highway environment with 4 lanes. There is presence of vegetation alongside the road. Guardrails have also been inserted on each side of the road. The traffic density is higher in that scenario as compared to the rural one. The inter-vehicular distance is fixed at 300 m.

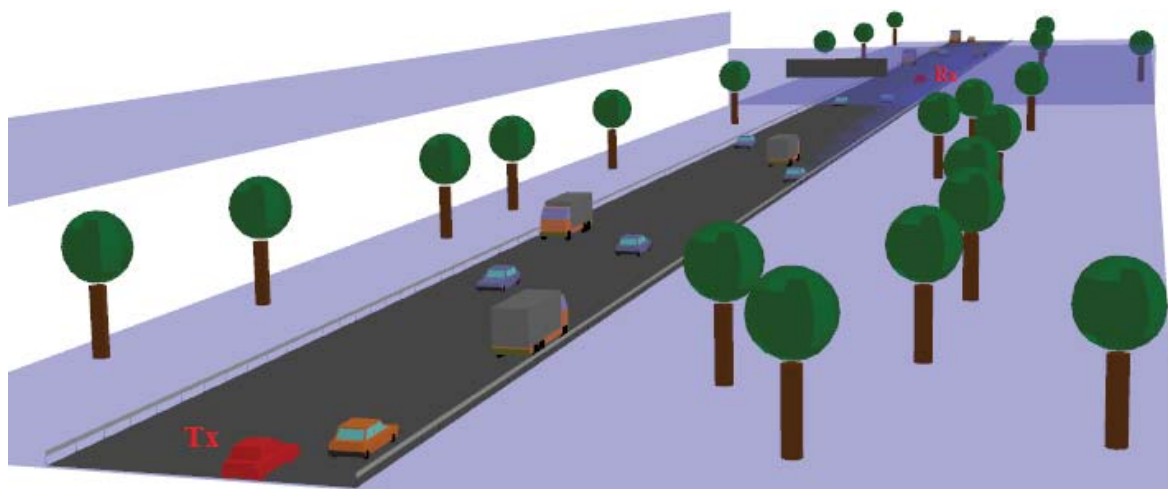


Figure B-3 : Highway scenario developed in Winprop

The angles of arrival at the receiver is directly obtained in the *cir output files. It must be noted that the default isotropic radiation pattern has been used for both Tx and Rx. The probability of occurrences of the angles of arrival is presented in Figure B-4.

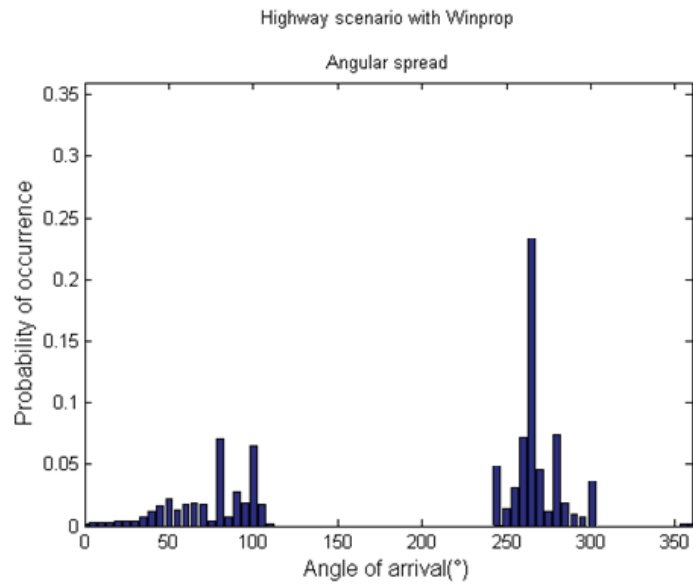


Figure B-4 : Highway scenario developed in Winprop

Urban scenario

A denser scenario was modelled in Winprop to represent an urban scenario as depicted in Figure B-5. We can notice the presence of a numerous building surrounding the Tx and Rx leading to the well-known urban-canyon scenario. This propagation channel is expected to lead to a higher number of multipath components. The traffic density is mild at the Tx-Rx distance is 200 m.

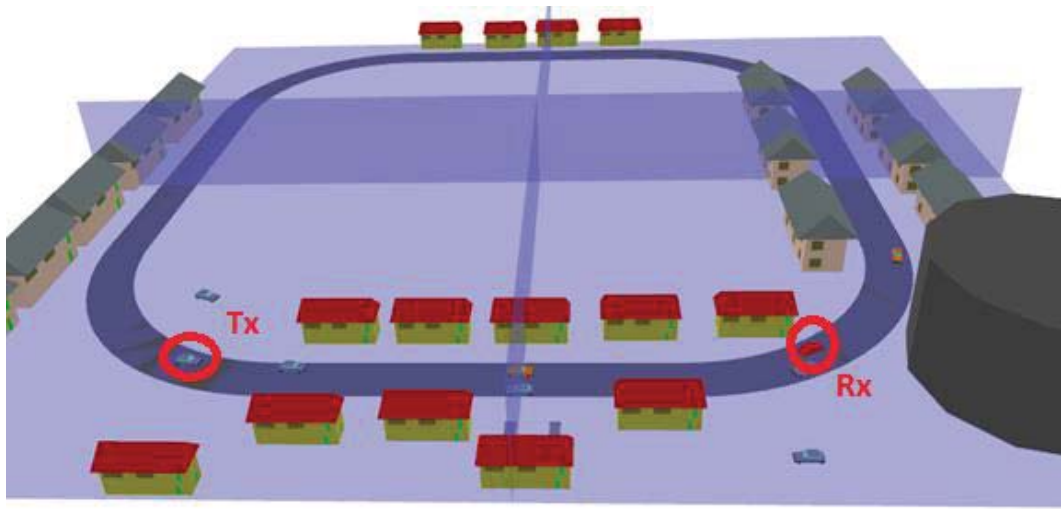


Figure B-5 : Urban scenario developed in Winprop

The angles of arrival at the receiver is directly obtained in the *.cir output files. It must be noted that the default isotropic radiation pattern has been used for both Tx and Rx. The probability of occurrences of the angles of arrival is presented in Figure B-4.

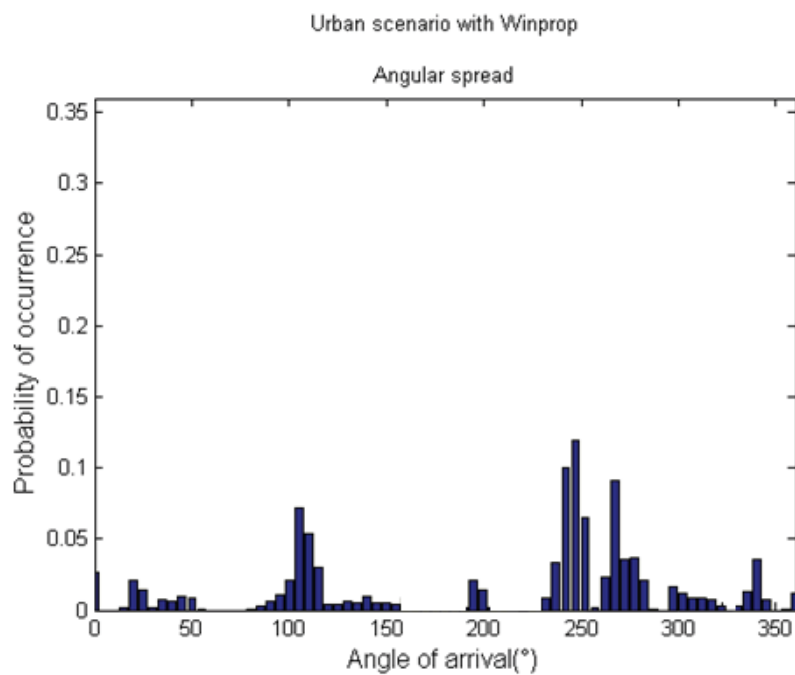


Figure B-6 : Urban scenario developed in Winprop

APPENDIX. C A SECOND MEASUREMENT CAMPAIGN

In this third appendix, the results of a second measurement campaign that was carried out in February 2017 are presented. Unfortunately, it was not possible to report them in chapter 6 as the manuscript was already submitted. Nevertheless, we deemed it judicious to show these results at least in an appendix.

Measurement results: PER results for each considered antenna configurations under different PHY layer parameters

In the second measurement campaign, we focused only on two antenna configurations. The main goal was to clear out the surprising result that we obtained with Config. 4 under a high data rate and a packet length of 1000 bytes. Furthermore, we were hoping to distinguish between the performance of Config. 2 with respect to Config. 4 and to show a hierarchization between them. The PER results for the 2 considered antenna configurations will be calculated using data obtained from the second measurement campaign as described in section 6.4.1. Table C-1 and C-2 summarize these two sets of results obtained from both campaigns. The average PER is evaluated for communications that occurred at inter-vehicular distances around 300 m (275 m to 325 m). Moreover, the probability of successful communication (tabulated in between brackets) is also calculated, abiding by the assumption that a PER of less than 10 % is favorable to a good communication between the transmitter and receiver.

Measurement results

Comparing the two sets of results, we can observe an overall decrease in the performance of both antennas in terms of percentage of successful rate of transmission. This can be due to a change in the total link budget between the two measurement campaigns that can have been affected due to weather conditions or electric connections. Nevertheless, in the second measurement campaign, it can be observed that Config. 2 works better than Config. 3, clearing off the surprising results obtained in the first measurement campaign.

Table C-1 : First set of measured results obtained with 2 antenna configurations in terms of successful rate of transmission with PER <10 %

Rural-like propagation channel. Measured results – Nov 2016			
	Mode 1, 200 bytes	Mode 1, 1000 bytes	Mode 5, 200 bytes
Config. 2	84 %	83 %	63%
Config. 4	100 %	84 %	39 %

Table C-2 : Second set of measured results obtained with 2 antenna configurations in terms of successful rate of transmission with PER <10 %

Rural-like propagation channel. Measured results – Feb 2017			
	Mode 1, 200 bytes	Mode 1, 1000 bytes	Mode 5, 200 bytes
Config. 2	44 %	49 %	8 %
Config. 4	24 %	23 %	0 %

If we take a look at the RSSI observed between the two measurement campaigns, the decrease in the overall performance is explained, revealing the RSSI predominant factor in the quality of the communication.

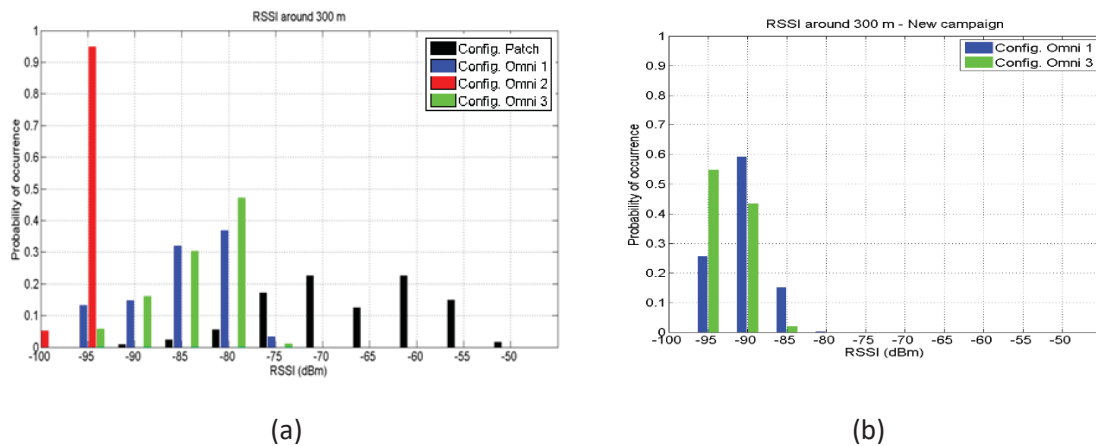


Figure C-1 : Probability of occurrence of the RSSI obtained for inter-vehicular distances around 300 m for (a) the first measurement campaign and (b) the second measurement campaign

LIST OF FIGURES

Figure 1 : Allocations de fréquences en Europe.....	VIII
Figure 2 : Schéma généralisé représentant l’environnement simulé.	X
Figure 3 : Résultat issus de la simulation FEKO pour la configuration rurale : (a) étalement des retards et (b) distribution angulaire.....	XI
Figure 4 : Résultat issus de la simulation FEKO pour la configuration autoroute : (a) étalement des retards et (b) distribution angulaire.....	XII
Figure 5 : Résultat issus de la simulation FEKO pour la configuration urbaine : (a) étalement des retards et (b) distribution angulaire.....	XIII
Figure 6 : Distribution des courants surfaciques.....	XV
Figure 7 : La configuration de mesure d’une antenne patch sur la lunette arrière.....	XV
Figure 8 : Diagramme de rayonnement d’une antenne patch intégrée sur la lunette arrière de la Mégane IV dans (a) le plan azimutal (b) et le plan d’élévation.....	XVI
Figure 9 : La structure du paquet transmis selon le standard IEEE 802.11p.....	XIX
Figure 10 : Puissances reçues, obtenues à partir de la campagne de mesure, pour des distances inter-véhicules avoisinant 300 m	XXI
Figure 11 : Puissances reçues, obtenues à partir de la simulation pour des distances inter-véhicules de 300 m.....	XXI
Figure 2-1 : Annual death toll due to road accidents in France.	4
Figure 2-2 : V2X ad-hoc network environment [4].....	5
Figure 2-3 : Main categories of ITS applications.....	6
Figure 2-4 : Example of Road Hazard Warning.....	7
Figure 2-5 : Examples of Cooperative collision warning: (a) merging traffic turn collision risk warning and (b) co-operative forward collision warning.....	7
Figure 2-6 : Example of Co-operative awareness warning.....	8
Figure 2-7 : Example of traffic management applications.	8
Figure 2-8 : ADAS applications developed by Renault.	9
Figure 2-9 : Dedicated frequency bands to V2X communications in Europe.....	10
Figure 2-10 : The Transmitter and Receiver block diagram.	15
Figure 2-11 : IEEE 802.11p transmitted packet structure.	15
Figure 2-12 : PER performance vs. SNR with perfect CSI for all considered scenarios in: (a) Model 1 (b) Model 2.	18
Figure 3-1 : Example of a wireless propagation channel	24
Figure 3-2 : Reflection and transmission.....	26
Figure 3-3 : Diffraction.	27

Figure 3-4 : Difference between specular reflection on a smooth surface (a) and scattering of a rough surface (b).	28
Figure 3-5 : Illustration of fast fading (short-term scale) and slow fading (long-term scale)	29
Figure 3-6 : Example of a time-varying channel impulse response [1].	31
Figure 3-7 : Power delay profile of a single snapshot	32
Figure 3-8 : Simulated configuration to test the precision of the UTD module.....	45
Figure 3-9 : Diagram outlining the general representation of the simulated configurations.....	47
Figure 3-10 : Frequency domain representation of an OFDM signal	50
Figure 3-11 : N=64 simulation frequencies.	50
Figure 3-12 : Power received on each subcarrier frequency (example).	51
Figure 3-13 : The channel response in time domain against the delay bins (example).....	51
Figure 3-14 : PDP of a simulated highway configuration.	52
Figure 3-15: PDP after the elimination of delay bins prior to the first arriving component.....	53
Figure 3-16 : Angular orientation of the Rx with respect to the Tx	54
Figure 3-17 Horizontal and vertical edge diffraction in UTD module of FEKO.....	59
Figure 3-18: Corner diffraction in UTD module of FEKO	59
Figure 3-19 : Flow chart of the steps to obtain virtual driving scenarios.....	61
Figure 3-20: An example of a rural configuration simulated with FEKO	62
Figure 3-21: RMS delay spread distributions for rural configurations obtained with (a) Analytical method and (b) FEKO simulations.....	63
Figure 3-22: Angular spread distributions for rural configurations obtained with (a) Analytical method and (b) FEKO simulations.....	64
Figure 3-23 : Delay-Doppler spectrum for a rural configuration obtained from FEKO simulations	65
Figure 3-24: An example of a highway configuration simulated with FEKO	66
Figure 3-25: RMS delay spread distributions for highway configurations obtained with (a) Analytical method and (b) FEKO simulations.....	67
Figure 3-26 : RMS-delay spread comparisons for highway configurations.....	68
Figure 3-27: Angular spread distributions for highway configurations obtained with (a) Analytical method and (b) FEKO simulations.....	69
Figure 3-28 : Delay-Doppler spectrum for a highway configuration obtained from FEKO simulations	69
Figure 3-29 : An example of an urban configuration simulated with FEKO	70
Figure 3-30: RMS delay spread distributions for urban configurations obtained with (a) Analytical method and (b) FEKO simulations.....	71
Figure 3-31: Angular spread distributions for urban configurations obtained with (a) Analytical method and (b) FEKO simulations.....	72
Figure 3-32 : Delay-Doppler spectrum for an urban configuration obtained from FEKO simulations	72

Figure 4-1 : Frequency ranges of the multiple RF automotive services.....	81
Figure 4-2 : Illustration of the numerical analysis techniques in FEKO [7].....	82
Figure 4-3 : Full anechoic measuring facility	85
Figure 4-4 : (a) The canonical vehicle model (b) The digital mock-up of the Mégane IV car.....	89
Figure 4-5 : The distribution of the surface currents on (a) the whole vehicle structure (b) the roof and the edges and (c) the roof only	90
Figure 4-6 : Radiation patterns for the three levels of simplification in (a) the azimuthal plane and (b) the elevation plane.	91
Figure 4-7 : The distribution of the surface currents on (a) the whole vehicle structure (b) the roof and the edges and (c) the roof only	92
Figure 4-8 : Radiation patterns for the three levels of simplification in (a) the azimuthal plane and (b) the elevation plane.	92
Figure 4-9 : The surface current distribution on (a) a simplified CAD of the Mégane IV and (b) the CAD of the only the roof of the Mégane IV.....	93
Figure 4-10 : The surface current distribution on (a) a simplified CAD of the Mégane IV and (b) the CAD of the only the roof of the Mégane IV.....	93
Figure 4-11 : A crafted monopole using a semi-rigid cable.....	94
Figure 4-12 : Reflection coefficient of the crafted $\lambda/4$ monopole.	94
Figure 4-13 : Radiation patterns of an antenna situated at the center of the roof in (a) the azimuthal plane and (b) the elevation plane.	95
Figure 4-14 : Radiation patterns of an antenna situated at the back of the roof in (a) the azimuthal plane and (b) the elevation plane.	95
Figure 4-15 : Surface current distributions of a patch antenna situated at the rear window.	96
Figure 4-16 : Measuring configuration of a patch antenna on the rear window.....	96
Figure 4-17 : Radiation patterns of a patch antenna situated on the rear windscreen in (a) the azimuthal plane and (b) the elevation plane.	97
Figure 4-18 : The quarter-scale and full-scale canonical vehicle structure.....	98
Figure 4-19 : The normalized E-field of the FF pattern compared to the E-field strength of the NF at (a) 640m and (b) 20 m.....	100
Figure 4-20 : Relative percentage difference for each angle of the between the normalized E-field of the FF pattern compared to the E-field strength of the NF at (a) 640m and (b) 20 m.	100
Figure 4-21 : The normalized E-field of the FF pattern compared to the E-field strength of the NF at (a) 80 m and (b) 60 m.....	101
Figure 4-22 : Relative percentage difference for each angle of the between the normalized E-field of the FF pattern compared to the E-field strength of the NF at (a) 80 m and (b) 60 m.	101
Figure 4-23 : The normalized E-field of the FF pattern compared to the E-field strength of the NF at (a) 20 m and (b) 5 m for a quarter-scale scenario.	102
Figure 4-24 : Relative percentage difference for each angle of the between the normalized E-field of the FF pattern compared to the E-field strength of the NF at (a) 20 m and (b) 5 m for a quarter-scale scenario.	103

Figure 4-25 : Generic propagation scenario downsized to quarter scale	104
Figure 5-1: Structure of the transmitting block.....	111
Figure 5-2: The structure of the receiving block	112
Figure 5-3: Steps of the process to obtain independent channel sequences (Example of a communication in Mode 3 with a packet length of 100 bytes)	114
Figure 5-4: Radiation patterns of Patch 1 and Patch 2 antennas both in (a) Azimuthal plane (Theta=90°) and (b) in the elevation plane (Phi=0°).	116
Figure 5-5: Radiation patterns of Omni 1 and Omni 2 antennas both in (a) azimuthal plane (Theta=90°) and (b) in the elevation plane (Phi=0°).	117
Figure 5-6 : Radiation patterns of Omni 3 and Omni 4 antennas both in (a) azimuthal plane (Theta=90°) and (b) in the elevation plane (Phi=0°).	117
Figure 5-7 : Total received power for the 5 antenna configurations against travelled distance in a rural scenario.	119
Figure 5-8 : Total received power for the 5 antenna configurations against travelled distance in a highway scenario.....	120
Figure 5-9 : Total received power for the 5 antenna configurations against travelled distance in a urban scenario.....	120
Figure 5-10 : PER results for the 5 antenna configurations in a highway scenario with a communication in Mode 3 and packet length of 200 bytes.	121
Figure 5-11 : PER results for the 5 antenna configurations in a highway scenario with a communication in Mode 3 and packet length of 1000 bytes.	122
Figure 5-12 : PER results for the 5 antenna configurations in a highway scenario with a communication in Mode 1 and packet length of 200 bytes.	123
Figure 5-13 : PER results for the 5 antenna configurations in a highway scenario with a communication in Mode 1 and packet length of 1000 bytes.	124
Figure 5-14 : PER results for the 5 antenna configurations in a highway scenario with a communication in Mode 5 and packet length of 200 bytes.	124
Figure 5-15 : PER results for the 5 antenna configurations in a highway scenario with a communication in Mode 5 and packet length of 1000 bytes.	125
Figure 6-1 : Partners participating in the SCOOP@f project.....	129
Figure 6-2 : Blueprint and dimensions of the Mégane IV	130
Figure 6-3 : Shark-fin antenna mounted on the roof of a Mégane IV.....	131
Figure 6-4 : Mounted configuration of the patch antenna on the front windscreen	132
Figure 6-5 : Modem provided by Autotalks used during measurement campaigns.....	133
Figure 6-6 : Representation of the on-board setup.	134
Figure 6-7 : Snapshot of (a) the MAP tab and (b) the MANAGEMENT tab of the Graphical User Interface of the tablet	134
Figure 6-8 : Measurement circuit chosen for field trials.....	137
Figure 6-9 : Street views of the 3 identified rural scenarios	137

Figure 6-10 : Mean RSSI against time for a section of a rural environment.	138
Figure 6-11 : Evolution of the inter-vehicular distance against time	138
Figure 6-12 : PER against time.....	138
Figure 6-13 : Time duration of the measurement campaign for each antenna configuration	139
Figure 6-14 : RSSI against distance for all antenna configurations	140
Figure 6-15 : Probability of occurrences of inter-vehicular distances with successful communication using antenna configuration Config. 1	141
Figure 6-16 : Probability of occurrences of inter-vehicular distances with successful communication using antenna configuration Config. 2	142
Figure 6-17 : Probability of occurrences of inter-vehicular distances with successful communication using antenna configuration Config. 4	142
Figure 6-18 : RSSI for inter-vehicular distances around 300 m for all antenna configurations	144
Figure 6-19 : Received power for the 4 antenna configurations in their corresponding rural environment.....	145
Figure 6-20 : Probability of occurrence of the received power for the 4 antenna configurations in their corresponding rural environment	145
Figure A-1 : Algorithm to calculate BER/PER.....	154
Figure B-1 : Rural scenario developed in Winprop	158
Figure B-2 : Angular spread in a rural scenario obtained with Winprop	159
Figure B-3 : Highway scenario developed in Winprop	159
Figure B-4 : Highway scenario developed in Winprop	160
Figure B-5 : Urban scenario developed in Winprop	161
Figure B-6 : Urban scenario developed in Winprop	161
Figure C-1 : Probability of occurrence of the RSSI obtained for inter-vehicular distances around 300 m for (a) the first measurement campaign and (b) the second measurement campaign.....	163

LIST OF TABLES

Table 1 : Statistiques sur l'étalement de retard obtenues à partir de la simulation	XIII
Table 2 : Statistiques sur l'étalement de retard obtenues à partir de la littérature.....	XIV
Table 3 : Résultat des puissances reçus (en dB) pour les 3 cas étudiés.....	XVIII
Table 4 : Résumé des résultats issus de la simulation pour les 5 configurations d'antenne selon différents paramètres de la couche PHY.....	XX
Table 5 : Résultats mesurés obtenus avec les 4 configurations d'antenne. TER moyen et entre parenthèses taux de transmission avec TER <10%	XXII
Table 6 : Résultats simulés obtenus avec les 4 configurations d'antenne. TER moyen et entre parenthèses taux de transmission avec TER <10%	XXII
Table 2-1 : Characteristics of V2X channels.	11
Table 2-2 : Comparison between the 802.11p and 802.11a PHY layer parameters.....	12
Table 2-3 : Modulation coding schemes as per IEEE 802.11p standard	14
Table 2-4 : Example of channel model in an Expressway-oncoming environment for V2V communications [11].	17
Table 3-1 : Path loss exponents in different propagating conditions	30
Table 3-2 : Path loss model (single and dual slope) parameters for typical V2X environments.....	39
Table 3-3 : Summary of RMS-ds results extracted from different measurement campaigns.	40
Table 3-4 : First set of simulation results of the parametric study to test the precision of the UTD module.	46
Table 3-5 Second set of simulation results of the parametric study to test the precision of the UTD module.	46
Table 3-6 : Simulation parameters of a highway configuration.....	49
Table 3-7 : Geometry parameters of a rural propagation channel.....	62
Table 3-8: Geometry parameters of a highway propagation channel.....	67
Table 3-9: Geometry parameters of an urban propagation channel.....	70
Table 3-10 : Statistics on the delay-spread obtained from our analytical model.....	73
Table 3-11 : Statistics on the delay-spread obtained from FEKO simulations	74
Table 3-12 : Summary of RMS-ds results extracted from different measurement campaigns (reproduction of table 3.3).....	74
Table 4-1 : Technical characteristics of both probe arrays.	85
Table 4-2 : Characteristics of available numerical models.....	90
Table 4-3 : Characteristics of the generic propagation scenario	104
Table 4-4 : Summary of the received power in dB for the three cases.....	106
Table 5-1 : Antenna configurations.....	118

Table 5-2 : Use cases and velocities of Tx and Rx.....	118
Table 5-3 : Summary of the simulated results of all antenna configurations under the considered use cases.....	126
Table 6-1 : Antenna configurations.....	132
Table 6-2 : Sensitivity level according to different transmitting mode available in the manufacturers' datasheet.....	133
Table 6-3 : Parameter settings in the management tab	135
Table 6-4 : Geometry parameters of a new rural propagation channel	143
Table 6-5 : Measured results obtained with 4 antenna configurations. Average PER and in between parenthesis rate of transmission with PER <10 %.....	147
Table 6-6 : Simulated results obtained with 4 antenna configurations. Average PER and in between parenthesis rate of transmission with PER <10 %.....	147
Table B-1 : Short guide to introduce the basic tools used in Winprop	157

PUBLICATIONS

Publications in peer-review journals

J. NARRAINEN, P. BESNIER, M. GATSINZI IBAMBE, “ A geometry-based stochastic approach to emulate V2V communications' main propagation channel metrics ”, International Journal of Microwave and Wireless Technologies, vol.8, Special Issue 03, May 2016, pp 455-461.

Communications in international conferences

J. NARRAINEN, P. BESNIER, P. BOUTIER, "Simulation of V2V Communications in Various Propagation Channels: Assessing Antenna Performance in Terms of PER", has been accepted for inclusion in the programme of EuCAP 2017 (Paris, France on 19-24 March 2017) (5 pages).

J. NARRAINEN, P. BESNIER, M. GATSINZI IBAMBE, “ Simple Electromagnetic Scenarios Emulating Typical Propagation Channel for V2V communications ”, IEEE-APS Topical Conference on Antennas and Propagation in Wireless Communications, Torino, 7-11 Sept. 2015, pp 557-560.

Communications in national conferences.

J. NARRAINEN, P. BESNIER, M. GATSINZI IBAMBE, “ Répartition de diffuseurs pour l’ajustement des caractéristiques d’un canal de propagation simulé dans un contexte V2V ”, Journées Nationales Microondes, Bordeaux, 1-3 juin 2015 (4 pages).

AVIS DU JURY SUR LA REPRODUCTION DE LA THESE SOUTENUE

Titre de la thèse:

Contribution à la modélisation des performances des systèmes de communications sans fil embarqués dans les véhicules automobiles

Nom Prénom de l'auteur : NARRAINEN JESSEN

Membres du jury :

- Madame LIENARD Martine
- Monsieur BESNIER Philippe
- Monsieur LAHEURTE Jean-Marc
- Monsieur VAUZELLE Rodolphe
- Monsieur D'ERRICO Raffaele
- Monsieur BOUTIER Philippe
- Monsieur BUNLON Xavier

Président du jury : *Madame Martine LIENARD*

Date de la soutenance : 07 Mars 2017

Reproduction de la these soutenue

Thèse pouvant être reproduite en l'état
~~Thèse pouvant être reproduite après corrections suggérées~~

Fait à Rennes, le 07 Mars 2017

Signature du président de jury

Le Directeur,

M'hamed DRISSI



[Handwritten signature]

Résumé

Le cadre général de cette thèse porte sur les communications véhicule à véhicule (V2V). L'objectif principal de ce type de communication est d'améliorer la sécurité routière et d'optimiser la fluidité du trafic. Les performances de systèmes de communication embarqués dépendent principalement de la configuration des antennes, du type de récepteurs utilisés (modem) et du canal de propagation. Le sujet de la thèse se concentre précisément sur l'élaboration d'un outil de simulation robuste et fiable pour optimiser les choix technologiques d'antennes et leurs implantations à bord. Il permettra de limiter ainsi le recours aux prototypes et aux essais de roulage.

Dans un premier temps, nous avons proposé une méthode de type géométrique-stochastique pour modéliser des canaux de propagation d'un système de communication V2V. Cette méthode permet de définir des scénarios dynamiques et sa flexibilité nous offre l'opportunité de paramétrer les caractéristiques d'un canal de propagation. Nous montrons pour l'essentiel de quelle manière l'agencement et le nombre de diffuseurs de forme simple peuvent contribuer à influencer les statistiques de l'étalement des retards, la distribution des angles d'arrivée et les spectres Doppler.

Dans la deuxième partie de ces travaux, nous nous focalisons sur la problématique d'intégration d'antenne. Il a été constaté qu'il est particulièrement utile de simplifier la maquette numérique du véhicule complet lors d'une simulation électromagnétique de l'antenne intégrée à bord de ce véhicule. De plus, dans cette section, nous avons étudié la limite de la validité de substitution d'une antenne intégrée à bord par son seul diagramme de rayonnement dans les modèles de canaux de propagation. A partir de cette étude, nous en avons déduit, que les interactions électromagnétiques avec les éléments se situant dans le champ-proche n'étaient plus valides. Ainsi, une stratégie de correction a été trouvée en considérant l'élément en champ proche dans la simulation initiale de l'antenne intégrée sur le véhicule.

L'évaluation des performances d'antennes, en termes de taux d'erreurs paquet, après l'implémentation de la couche physique du standard 802.11p, est au cœur de la troisième partie de cette thèse. Des résultats de simulation, pour chaque configuration d'antenne, ont été donnés pour plusieurs combinaisons de paramètres de couche PHY tels que le débit et la longueur de paquet.

La dernière partie de ce manuscrit traite de la présentation d'une campagne de mesure qui a été réalisée principalement dans un environnement de type rural. Les essais de roulage avaient pour but de démontrer la capacité des méthodes de simulation à faire un choix approprié d'installation d'antenne. Nous avons constaté que les tendances attendues des performances de communication en termes de PER sont globalement prévisibles à partir de notre modèle bien que nous ayons obtenu des résultats surprenants dans certains cas. Ce qui nécessitera une enquête plus approfondie.

Abstract

The general framework of this Ph.D. thesis deals with Vehicle to Vehicle (V2V) communications. This communication is principally dedicated to reinforce security through exchange of information between vehicles in case of unexpected events. The development of V2V solutions requires the understanding and merging of a number of techniques from several communication technology areas. Indeed, the performance of these systems are related to three main blocks: the implementation of the modems, the antenna configuration and the fast-varying electromagnetic environment surrounding the transmitter and the receiver. The purpose of this PhD thesis is precisely to elaborate a design strategy to investigate all the different blocks constituting the communication chain. The ultimate goal is to optimize antenna selection and location on board the vehicle.

In the first place, we proposed a geometry-based stochastic channel modelling approach to develop virtual dynamic scenarios. It was shown that the most common propagation environments such as rural, highway or urban-like propagation channels are reached through adjustment of numbers and location of simple metallic plates. Using this method, we can emulate the characteristics, such as the delay spread, angles of arrival distribution and the Doppler spectrum, of these typical driving scenarios.

Moreover, we dealt with antenna integration problems in the second part of this work. A study on the simplification of numerical models of vehicles was carried out. Furthermore, in this section, we investigated the limit of validity of representing the integrated antenna on board vehicle solely by its radiation pattern. We deduced from this study that the interactions with the elements present in the near-field is no longer valid. Thus, a strategy to alleviate the degree of error was found upon consideration of the near-field scatter in the a-priori simulation of the antenna integrated on the vehicle.

In the third part of this thesis, we evaluated the performance of different antenna configurations in terms of packet error rate after the embodiment of the PHY layer of the IEEE 802.11p standard. Simulation results, for each antenna configurations, was given for several combinations of PHY layer parameters such as data rate and packet length.

The last part of this manuscript is dedicated to the presentation of a measurement campaign that was carried out in a rural driving environment. Results obtained from these functional tests were confronted with simulation results to demonstrate the strength of the latter. We found that the expected trends in communication performance in terms of PER are globally predictable from our model though we obtained surprising results in some cases, needing further investigation.